UNIVERSITY OF CALGARY

Coherent Cavity Optomechanics in Wide-Band Gap Materials

by

Matthew John Mitchell

A THESIS

SUBMITTED TO THE FACULTY OF GRADUATE STUDIES

IN PARTIAL FULFILLMENT OF THE REQUIREMENTS FOR THE

DEGREE OF DOCTOR OF PHILOSOPHY

GRADUATE PROGRAM IN PHYSICS AND ASTRONOMY

CALGARY, ALBERTA

NOVEMBER, 2019

Abstract

The utilization of photon-phonon interactions for transducing, storing, and transmitting information holds great promise for linking disparate quantum technologies. Cavity optomechanics aims to enhance coherent phonon-photon interactions through co–localization of mechanical and optical resonances coupled via radiation pressure or other optical forces. Many on-chip demonstrations of optomechanical cavities have relied on silicon-on-insulator as a material platform, which suffers from large nonlinear absorption at the telecommunication wavelengths widely used in optical communication technologies. The optomechanical cooperativity, C, which describes the efficiency of exchange between photons and phonons, is proportional to the intracavity photon number, N. As such, there is great interest in circumventing nonlinear absorption in these cavities, where the approach taken in this thesis is to use wide-band gap materials, which do not exhibit nonlinear absorption at these wavelengths.

In this work, microdisk optomechanical cavities fabricated from gallium phosphide (GaP) and single-crystal diamond (SCD) were studied. The ability of these structures to support large N, while remaining thermally stable, enabled the demonstration of optomechanically induced self-oscillation and coherent processes such as optomechanically induced transparency and amplification with cooperativity $C > 1$. An advantage of microdisk cavities is that they support optical modes across the transparency window of the material, enabling the study of multimode optomechanics where multiple optical modes are coupled to the same mechanical mode of the microdisk. This resulted in the demonstration of optomechanically mediated wavelength conversion with internal conversion efficiency of $\sim 45\%$. These cavities hold great potential for applications in quantum networks, namely as a phonon mediated transducer of quantum information from visible or microwave photons to telecommunication wavelength photons. SCD microdisk cavities also have potential application as a hybrid-quantum system which can couple electron spins from defect centers in the diamond lattice to telecommunications wavelength photons via phonons in the optomechanical cavity.

Preface

Research is never done in isolation, or at least research that I am interested in doing. As such, I would like to use this section to outline the timeline and collaborations that I was a part of during my graduate student career at the University of Calgary as well as outline the structure of this thesis.

Origins

I started working for Paul as an undergraduate student in 2011, before he had moved to the University of Calgary and got to help build the lab from the ground up. My first task as an undergraduate was designing and building the tapered fiber pulling system that would be used to fabricate the fiber tapers essential to the lab for coupling light to and from our cavities. With the arrival of Paul and the first two graduate students Behzad Khanaliloo, and Marcelo Wu I continued this work and also helped build and organize our lab, which changed locations a few times in the first few years of Paul's arrival. This was a great opportunity for me to learn the in's and outs of dealing with vendors, university administration, and designing and building parts ranging in size from sample holders to the racks that hold the lab equipment above our optical tables.

Cavity optomechanics in gallium phosphide microdisks

My project as a graduate student in the group was to design, fabricate, and characterize cavity optomechanical cavities that could avoid nonlinear absorption in the telecommunications wavelength band. Paul had done a lot of work during his graduate studies examining the nonlinear absorptive properties of silicon nanocavities and was interested in finding a

way to circumvent this issue. The approach I was to take was to use wide-bandgap materials to avoid nonlinear absorption at telecommunications wavelengths. Paul's expertise working with gallium phoshpide (GaP) and the opportunity to take some high-quality GaP substrates from his time at HP labs made this a natural material to start with. I had some experience from my time as an undergraduate modelling the microdisk whispering gallery mode structures that I would be making using finite-difference-time-domain (FDTD) simulations which I expanded upon to predict the mode structure and radiation loss-limited optical quality factors I could expect to see.

All of my nanofabrication work was done at the National Research Council Nanotechnolgy (NRC-Nano) facility, formerly known as the National Research Council-National Institute for Nanotechnology (NRC-NINT) and the University of Alberta nanoFAB. I was essentially exclusively trained in all things fabrication by Aaron Hryciw, our postdoc stationed in Edmonton, who I tried my best to emulate. Much of the groundwork of developing the GaP fabrication process was done by Aaron, which I then used to fabricate and characterize the devices described in Chapter 3. After a few iterations of fabrication and testing I succeeded in demonstrating cavity optomechanical coupling in GaP microdisks [1]. Portions of Chapter 3 are used with permission from M. Mitchell et al. [1] of which I am first author. These devices were also used by my colleague David Lake to demonstrate efficient second harmonic generation [2]. I also had the opportunity to travel to the National Institute for Standards and Technology (NIST-Gaithersburg) to collaborate with Kartik Srinivasan's photonics and plasmonics group, where we measured optomechanically induced transparency in these structures. This training enabled our group to do these measurements in our lab, as discussed in Chapters 3 and 7.

Shift to working with single-crystal diamond

Around the time of my work with GaP, Behzad and Aaron had been working intensively on developing a recipe for fabricating free-standing nanobeam structures from bulk SCD. This is a technological challenge as high-quality SCD is not commercially available in a

heteroepitaxially grown thin-film form. As diamond has an even wider electronic bandgap, Young's modulus, and thermal conductivity, one could argue it is the ideal material to fabricate optomechanical structures from. Based on our groups' motivation to demonstrate stress-coupling to defect centers in a diamond optomechanical cavity I decided to shift my focus to SCD as a material platform. I collaborated with Behzad who trained me on the diamond fabrication process, and then extended that process to fabricate microdisk whispering gallery mode resonators with high optical quality, but had supporting pedestal diameters too large to observe optomechanical coupling. This work is presented in Chapter 4, portions of which are used with permission from B. Khanaliloo et al. [3] of which I am second author.

Cavity optomechanics in single-crystal diamond microdisks

After a few more iterations of fabrication and testing I demonstrated microdisk structures with supporting pedestal diameters small enough to reduce mechanical damping to the point that we were able to measure optomechanical coupling and optomechanically induced self-oscillation [4]. This work is presented in Chapter 5, and was my first of many collaborations with David Lake who contributed to the analysis of the data presented in Chapter 5. This work is presented in Chapter 5, portions of which are used with permission from M. Mitchell et al. [4] of which I am first author.

Optimizing the diamond fabrication process for coherent cavity optomechanics

While we were able to demonstrate optomechanically induced self-oscillation in the first generation of diamond optomechanical cavities there was significant linear absorption based heating present that prevented accessing the red-detuned side of the optical cavity at high input powers. This prevented the study of coherent optomechanical processes such as optomechanically induced transparency, wavelength conversion, and pulse storage. We attributed this to linear absorption in the material and a reduced thermal conductivity in the ~ 100 nm pedestals supporting the microdisks. In order to remedy this problem, an additional step was added to the fabrication process to tailor the pedestal shape, allowing for a larger pedestal diameter without negatively affecting the mechanical quality factor. These improvements en-

abled red-detuned laser operation at high power, and the demonstration of optomechanically induced transparency and optomechanical cooling [5]. This work is presented in Chapter 7, portions of which are used with permission from D.P. Lake et al. [5] of which David and I are both first authors.

During this time I also was working on optimizing the fabrication process to improve the optical quality factor of the microdisks by improving our material etches. This involved moving of some of our etch recipes from NINT to nanoFAB and lots of late night sessions in the nanoFAB. By optimizing our Si_3N_4 mask layer etch and diamond etch we were able to demonstrate optical $Q > 300\ 000$ [6]. This fabrication optimization work is presented in Chapter 6, portions of which are used with permission from M. Mitchell et al. [6] of which I am first author.

Multimode coherent cavity optomechanics

Optimization of the microdisk cavities allowed us to explore multimode optomechanical phenomena, where two optical modes are coupled to a single mechanical mode of the microdisk. This allowed the demonstration of optomechanically mediated and amplified wavelength conversion in the optical regime, for the first time. This work is presented in Chapter 7, which is used with permission from M. Mitchell et al. [7] of which I am first author. These devices were also used to demonstrate additional multimode applications, namely an all-optically tunable buffer, and double optomechanically induced transparency [8], the former of which is briefly discussed in Chapter 8.

Acknowledgements

I have had the pleasure of completing my BSc and PhD at the University of Calgary; I grew up in and around Calgary and am lucky to call it home. I was fortunate enough to be Paul Barclay's first student here as an undergraduate, and have greatly enjoyed my time helping to set up the lab, and pursing my PhD with him as a supervisor. I can't thank Paul enough for all the opportunities I have had while being a member of the lab. These include, but are not limited to, presenting at numerous conferences, receiving training in nanofabrication and characterization techniques in Edmonton at NRC-Nano and nanoFAB, studying for two years at the University of Alberta, and travelling to collaborate with Kartik Srinivisan's group at NIST. These opportunities, combined with the time and energy he donates to ensuring students success and development is not a luxury that all graduate students receive, and I am very grateful.

During my time here I have had the pleasure of working with many talented and brilliant people. Aaron Hryciw was an invaluable source of knowledge and inspiration not only in his skills in the nanoFAB but in organizing himself and his research; I have strived to be as organized and thorough as he is in and out of the lab. I have worked most closely with David Lake during my PhD and could not have asked for a better colleague and friend. His skill in the lab, and ability to understand and build upon state of the art research and theory in our field is inspiring. I have learned much from, and with him during my graduate career. Behzad Khanaliloo, Marcelo Wu, and Chris Healey were also invaluable sources of knowledge in the lab and I am grateful I had their support during the early days of my project. JP Hadden,

Nathanael Wu, Harishankar Jayakumar, Tamiko Masuda, Hamid Kamidreza, and Thomas Lutz, were also great colleagues, chapters could be written on the time spent together and things learned with the people listed above.

I would like to thank the BSc senior lab technician Pat Irwin for being, in my opinion, the best educator at the University of Calgary, and Alex Lvovsky for taking me on as a summer student. Being exposed to these research environments inspired me to pursue this path, and I am very grateful for that. While working in Alex's lab, Andrew MacRae, Connor Kupchak, Michael Förtsch, and Pierre Gobez taught me much about how to be a successful graduate student.

Outside the lab I am grateful to David for getting me into cycling and for all our resulting adventures. Tamiko, Behzad, David, and JP you have all been great friends and I won't forget the many great times we have spent together. During my time spent in Edmonton, Joel Hutchinson, Roshan Achal, and Hugh Ramp, showed me the ropes, and helped dispel some of the Calgary-Edmonton rivalry that had been ingrained in me as a Calgarian.

I couldn't have done this without my wife Emily, her support, encouragement, and understanding through all the late nights, crunch-times, and trips to Edmonton can not be overstated. My family and friends were always there to support me; their pride and encouragement was invaluable during this journey.

To my family and friends

Table of Contents

List of Figures and Illustrations

List of Tables

List of Abbreviations, Symbols and Nomenclature

Abbreviations	Definition
EBL	electron beam lithography
EBPVD	electron-beam physical vapor deposition
EOM	electro-optic modulator
FDTD	finite difference time domain
FEM	finite element method
ICP-RIE	inductively coupled plasma reactive ion etching
IQST	Institute for Quantum Science and Technology
MEMS	micro-electromechanical systems
NINT	National Institute for Nanotechnology
NV	nitrogen vacancy
PECVD	plasma enhanced chemical vapor deposition
PPE	personal protective equipment
PSD	power spectral density
RBM	radial breathing mode
RIE	reactive ion etching
RSA	real-time spectrum analyzer
SCD	single-crystal diamond
SEM	scanning electron microscope
SiV	silicon vacancy
TPA	two-photon absorption
U of A	University of Alberta
U of C	University of Calgary
VNA	vector network analyzer
WGM	whispering gallery mode
ZED	zeon electron-beam developer
ZEP	zeon electron-beam positive

Symbols	Definition
N	intracavity photon number
n_{th}	average phonon number in thermal equilibrium
ω_{m}	mechanical frequency
Γ_{m}	mechanical damping rate
Q_{m}	mechanical quality factor $Q_{\mathrm{m}} = \omega_{\mathrm{m}}/\Gamma_{\mathrm{m}}$
ω_{o}	optical cavity resonance frequency
κ	total optical cavity intensity decay rate
Q_{o}	total optical cavity quality factor $Q_{\mathrm{o}} = \omega_{\mathrm{o}}/\kappa$
ω_{l}	laser frequency
Δ	laser-cavity detuning $\omega_{\mathrm{l}} - \omega_{\mathrm{o}}$
g_0	single-photon optomechanical coupling rate
g	photon-assisted optomechanical coupling rate $g = g_0\sqrt{N}$
G	optomechanical coupling coefficient $G = \partial\omega_{\mathrm{o}}/\partial\alpha$
$\hat{a}$	photon annihilation operator
$\hat{b}$	phonon annihilation operator
x_{zpf}	mechanical zero-point fluctuation amplitude
$\delta\omega_{\mathrm{m}}$	optical spring shift
Γ_{opt}	optomechanical damping/anti-damping rate
P_{in}	input laser power

Chapter 1

Introduction

1.1 Radiation pressure

The idea of radiation pressure dates back to 1619 when Johannes Kepler suggested it as the reason that the tail of a comet always points away from the sun [9]. Although a theoretical exploration of radiation pressure was developed by James Clerk Maxwell in 1862, and Adolfo Bartoli in 1882 [10], it was not until 1901 that it was correctly measured by Pyotr Lebedev with a torsional balance [11] and confirmed by Ernest Fox Nichols and Gordon Ferrie Hull in 1903 with the Nichols radiometer [12]. Since that time, radiation pressure has found applications in spacecraft propulsion [13, 14, 15], and in optical tweezers [16]. The effects of radiation pressure also had to be taken into account in the detection of gravitational waves [17], and is an integral part of the field of cavity optomechanics [18].

To elucidate the magnitude of this force consider the magnitude of the imparted momentum to a perfectly reflective mirror when a photon from a green laser pointer is reflected by it. For a photon with a wavelength of 532 nm this corresponds to $\Delta p = 2h/\lambda = 1.25 \times 10^{-27}$kg·m/s, or approximately 24 orders of magnitude smaller than the momentum of a raindrop[1], which is quite small! If you take the power output of your laser pointer to be 1 mW, this corresponds to a radiation pressure force of ~ 6.67 pN. As this force is small,

[1] Assuming raindrop mass of 100 mg, falling at 10 m/s.

it is difficult to detect, making the early measurements of this force quite impressive. To date, the radiation pressure force of a single photon has yet to be measured, although work is progressing towards this goal [19]. However, by adding a second mirror and forming a cavity this force can become appreciable as a single photon can reflect multiple times and can influence the dynamics of cavity. It was not until the 1970's that Vladimir Braginsky recognized the effects that radiation pressure would play in systems of coupled mechanical and optical cavities [20, 21, 22].

1.2 Cavity optomechanics

As eluded to above, the field of cavity optomechanics studies the dynamics of coupled mechanical and optical cavities, where the coupling is mediated by the radiation pressure force. Early experimental demonstrations of cavity optomechanical systems in the microwave regime included Braginsky's work [20], but it was not until 1983 that such a system was demonstrated in the optical regime [23]. Researchers realized that in order to enhance the radiation pressure force, or coupling between the mechanical and optical cavities, it would be advantageous to shrink these systems down to smaller length scales. If these systems could be miniaturized and integrated with high density on a chip, the potential for interfacing these devices with photonic and electronic components would greatly increase. As such, the field experienced rapid growth with the improvement and development of nanofabrication techniques for the semiconductor electronics and micro-electromechanical systems (MEMS) industries. This enabled the fabrication of micro- and nano-scale optical cavities which also supported localized mechanical modes. This co-localization is a fortuitous result of the similar photon and phonon wavelengths in these structures, which results from the ~ 5 orders of magnitude smaller speed of sound compared to light. As shown in Fig. 1.1, optical confinement is typically achieved using total internal reflection within an optically thin film waveguide layer (to achieve strong confinement, and localization of the field), in combina-

tion with patterning of this layer to achieve lateral confinement. The structures studied in this work, and the vast majority of those studied to date, achieve phononic confinement by physically separating or releasing the waveguiding layer from the underlying substrate to prevent phonons from leaking into bulk or surface modes of the substrate. However, recent work has demonstrated that simultaneous confinement of photons and phonons in unreleased waveguides is also possible [24, 25], which could enable much easier integration with existing MEMS and semiconductor electronics fabrication processes [26].

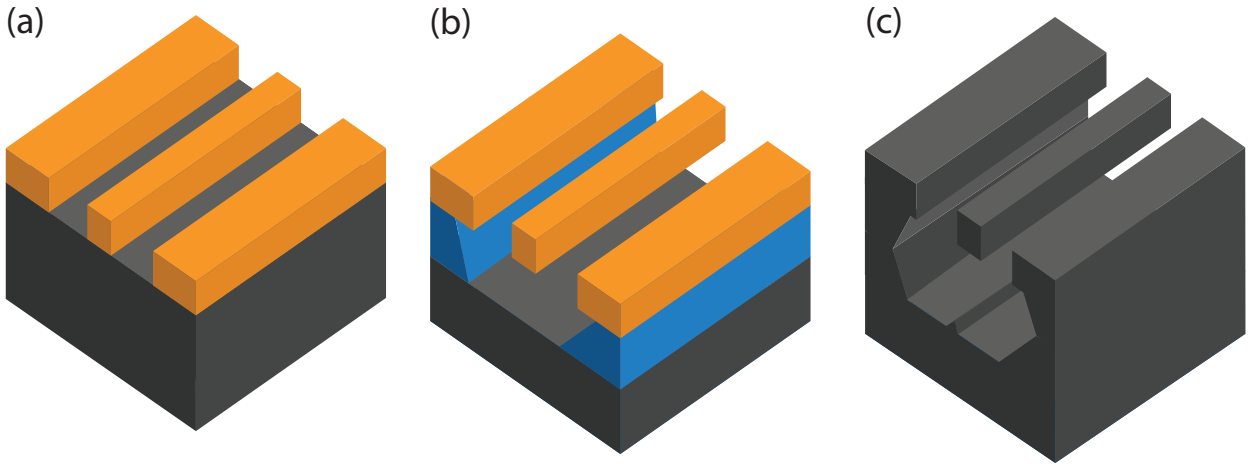

Figure 1.1: Schemes for planar confinement of photons on a chip, where lateral confinement is achieved by patterning the waveguiding layer to create waveguides or resonator structures. (a) To confine light on the chip via total internal reflection, the refractive index of the waveguiding layer (orange) must be greater than that of the underlying substrate (grey). (b) Alternatively, a multi-layer substrate may be used such that the material beneath the waveguiding layer (blue) can be selectively removed to achieve confinement. (c) When working with bulk material, such as SCD, vertical confinement is achieved by "carving" out the material beneath the waveguiding structure.

The first micro-scale optomechanical cavity was demonstrated in a ~ 60 μm diameter silica micro-toroid by Tal Carmon et al. [27], where many cavity optomechanical systems have followed, in a wide variety of form factors and materials ranging from macroscopic mirrors to single trapped atoms. Although these systems may appear drastically different in form, in function they can be described for the most part by a simple Fabry-Perot cavity where one mirror is fixed and one is free to vibrate, as illustrated in Fig. 1.2. To characterize this optomechanical cavity the following key parameters are required to describe the optical and mechanical resonators represented by this mass-spring system, and are described further

in Chapter 2:

- κ and ω_{o} are the optical cavity energy decay rate and resonance frequency, respectively, where the optical quality factor, $Q_{\mathrm{o}} = \omega_{\mathrm{o}}/\kappa$.
- Γ_{m} and ω_{m} are the mechanical resonator energy decay rate and resonance frequency, respectively, where the mechanical factor, $Q_{\mathrm{m}} = \omega_{\mathrm{m}}/\Gamma_{\mathrm{m}}$.
- g_0 - Single photon optomechanical coupling rate.
- N - Intracavity photon number.

The Fabry-Perot resonator will support standing wave optical modes when the length of the cavity, L is an integer multiple of the resonant half wavelength ($L = m\lambda/2$). As the free mirror moves it will modify L and cause a shift in ω_{o}. The shift in resonance frequency per small displacement is called the optomechanical coupling coefficient, G, as illustrated in Fig. 1.2, and is related to the single-photon optomechanical coupling strength by $g_0 = Gx_{\mathrm{ZPF}}$ where $x_{\mathrm{ZPF}} = \sqrt{\hbar/2m_{\mathrm{eff}}\omega_{\mathrm{m}}}$ is the zero point fluctuation amplitude of the mechanical resonator, and m_{eff} is its effective mass [18]. As photons reflect from the moving mirror they will impart some momentum to the mirror which also causes some displacement. These two effects will alter the phase and amplitude of the optical field in the cavity. As the lifetime of a photon in the cavity varies compared to the timescale of the mechanical oscillation there is a lag in the optical response, which results in dynamical back action between the optical field and mechanical resonator. In practice these dynamics are usually classified by the ratio of $\kappa/\omega_{\mathrm{m}}$ where $\kappa \gg \omega_{\mathrm{m}}$ is referred to as the sideband un-resolved regime and $\kappa \ll \omega_{\mathrm{m}}$ is the sideband-resolved regime. By choosing the detuning of the input field from the optical resonance appropriately, this back action can be utilized to damp or drive the mechanical oscillator, enabling cooling to its quantum ground state [28, 29] or optomechanically induced self-oscillations [27, 30, 31, 32, 33], respectively.

One can envision also using this system as a sensor: by fixing the input field detuned from the optical resonance at the point of highest slope, any modulation of the cavity resonance

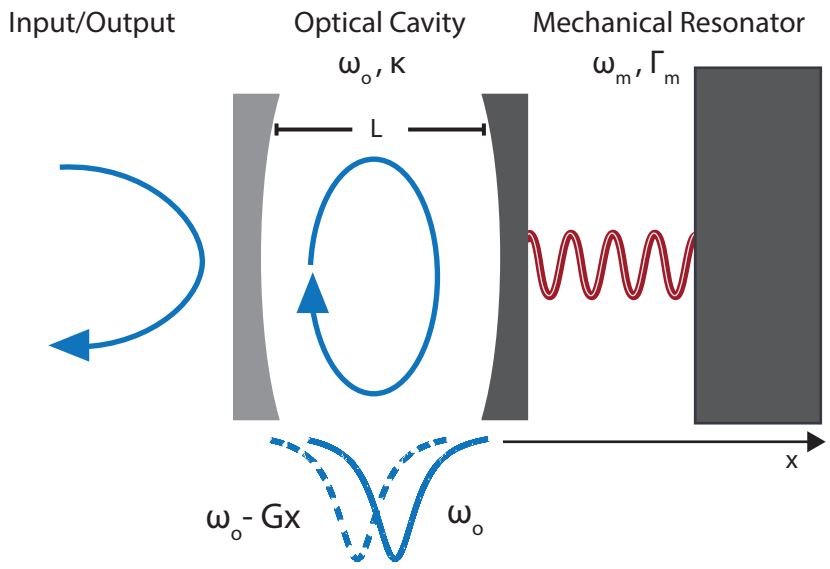

Figure 1.2: Canonical example of an optomechanical cavity.

frequency will in turn modulate intensity of the field in the cavity. This intensity modulation can then be directly detected by sending the light emitted from the cavity to a photodetector. This has proved a useful meterological tool where many sensors have been made from these systems such as accelerometers [34], magnetometers [35, 36], torque sensors [37, 38, 39], and environmental sensors [40].

Recent work has moved beyond the canonical system of Fig. 1.2 to study multimode optomechanical systems. By coupling multiple optical and/or mechanical [41, 42] modes via radiation pressure [42] optomechanically mediated wavelength conversion [43, 44, 45, 46], optical-microwave transduction [47], mechanical state transfer [48], and construction of optically non-reciprocal devices [49, 50, 51] which exhibit a direction dependent response, have been demonstrated. The field has also been trending towards optomechanical cavities that confine light to a volume $\sim$ 1 μm^3, coupled to GHz frequency mechanical modes. Larger ω_{m} has the advantage of lower thermal occupation and isolation from the thermal bath, resulting in lower input thermal noise. This has been enabled by rapid progress in engineering the mechanical properties of these structures, enhancing the ability to localize high frequency phonons [26]. Recent work has also focused on integrated phononic networks

where phonons may carry information and be routed on chip between optomechanical or electromechanical cavities [26].

1.3 Motivation

The efficiency of exchange between photons and phonons in these devices is often described by the optomechanical cooperativity parameter, $C = 4Ng_0^2/\kappa\Gamma_{\mathrm{m}}$, which for sufficiently large intracavity photon number, N, may exceed unity in several cavity optomechanics systems under investigation [18]. Increasing C (above, for example, the value of $C \sim 20$ demonstrated in optomechanical crystals [52]), would enable improved bandwidth of coherent wavelength conversion [44], observation of normal mode splitting [53], and faster optomechanical cooling [29]. Additionally, for multimode optomechanical systems the ability to handle large N is advantageous so that $C > 1$ for each coupled pair of modes. However, in these semiconductor-based large-g_0 devices, N is limited by two-photon absorption (TPA) [54, 55], which occurs when the energy of two photons is sufficient to excite an electron from the valence band to the conduction band as illustrated in Fig. 1.3, and scales quadratically with intensity, or N.

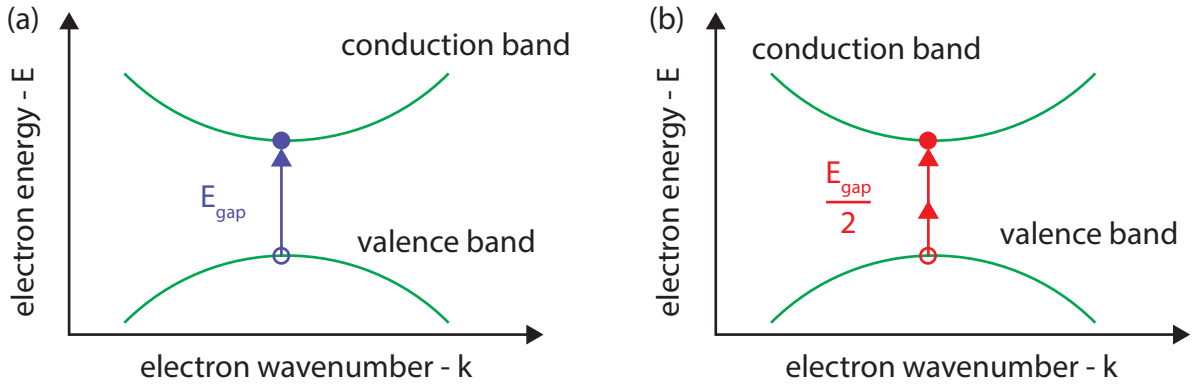

Figure 1.3: Illustration of linear (a) and two-photon (b) absorption in a direct band-gap semiconductor.

This results in absorption of the two photons, generation of free-carriers, and a degradation of the optical quality factor of the device [54]. The material heating accompanied by TPA alters the refractive index via the thermo-optic effect which in turn spectrally shifts the optical resonance, causing instability which can prevent access to the red-detuned side

of the optical resonance [56]. As TPA scales nonlinearly with optical power, a fundamental limit in the cooperativity of silicon optomechanical devices exists [54, 57]. By choosing a material with an electronic band gap energy greater than that of two telecom photons ($\lambda \sim 1550$ nm) the problem of TPA can be avoided for this range, allowing larger N, which removes a factor that currently limits C. As a result, many different wide-band gap materials are being considered for use, such as Si_3N_4 [58, 59, 60, 61], SiO_2 [62, 63, 64, 45], SiC [65], III-V semiconductors such as InGaP [66], AlGaAs [66], GaP [1, 67], and AlN [68], and diamond [4, 69, 70, 71].

The materials investigated in this work are GaP and SCD, whose ability to avoid TPA at telecommunications wavelengths enables large N, while remaining thermally stable, allowing the demonstration of optomechanically induced self-oscillations [4], and coherent processes such as optomechanically induced transparency [5] and amplification with cooperativity $C > 1$. The structures fabricated from SCD also enabled coherent multimode phenomena such as optomechanically mediated wavelength conversion [7]. While these phenomena have been studied in existing optomechanical structures the SCD microdisks studied here operate at room temperature and in ambient conditions, which offers a major technological advantage. These cavities hold great potential for application in a quantum network, namely as a phonon mediated way of transducing quantum information from visible or microwave photons to telecommunication wavelength photons. Lastly, diamond optomechanical cavities also have potential application as a hybrid-quantum system which can couple electron spins from defect centers in the diamond lattice to telecommunications wavelength photons via phonons in the optomechanical cavity.

1.4 Organization

In Chapter 2 I will lay the groundwork for understanding the microdisk mechanical and optical modes and the theoretical framework of cavity optomechanics required for interpreting

the later results. Chapter 3 will discuss the GaP microdisk optomechanical cavities that I fabricated and studied. In Chapter 4 the focus shifts to the fabrication of SCD microdisk cavities which exhibited high-Q optical modes but were not sufficiently undercut to detect the mechanical modes of vibration of the structures. Chapter 5 discusses the first microdisk SCD optomechanical cavities we successfully fabricated and characterized, where optomechanically induced self-oscillation of the mechanical motion was observed. In Chapter 6 the optimization of the SCD microdisk fabrication process is presented, which enabled stable operation in the red-detuned regime, with large N. This included re-optimizing the majority of the etch steps in the process and the introduction of a pedestal tailoring step, which improved the thermal properties of the device considerably. In Chapter 7 the optimized SCD microdisks are utilized to demonstrate coherent optomechanical process such as optomechanically induced transparency, and multimode phenomena such as optomechanically mediated and amplified wavelength conversion. Chapter 8 summarizes these results, and provides some outlook on current multimode experiments, and routes towards operation of the SCD microdisks in the quantum regime.

Chapter 2

Cavity optomechanics in microdisks

2.1 Optical whispering gallery modes

Microdisk optomechanical cavities are studied exclusively in this thesis, but are just one of many device geometries used today. Microdisks support optical whispering gallery mode (WGM) resonances which get their name from acoustic whispering galleries, the most famous of which is St. Paul's Cathedral in London, England. As the name suggests, when standing next to the wall of a whispering gallery a whisper can be heard across the gallery due to reflection of acoustic waves along the circumference, as illustrated in Fig. 2.1(a), and first correctly described by Lord Rayleigh in 1910 [72].

The optical analog of the whispering gallery confines light via total internal reflection, where photons can propagate around the circumference of a sphere [74, 75], disk [76, 77], or ring [78]. As with the Fabry-Perot resonator only wavelengths that exhibit constructive interference inside the structure will be resonant and form a whispering gallery mode (WGM), i.e. the condition $2\pi n_{\text{eff}} R \simeq m\lambda$ must be met. Here n_{eff} is the effective refractive index seen by the light, accounting for the fact that some of the field will exist as an evanescent wave outside of the structure which can become significant for optically thin structures; λ is the free space wavelength, and m is the azimuthal number of the WGM. The spatial profile of

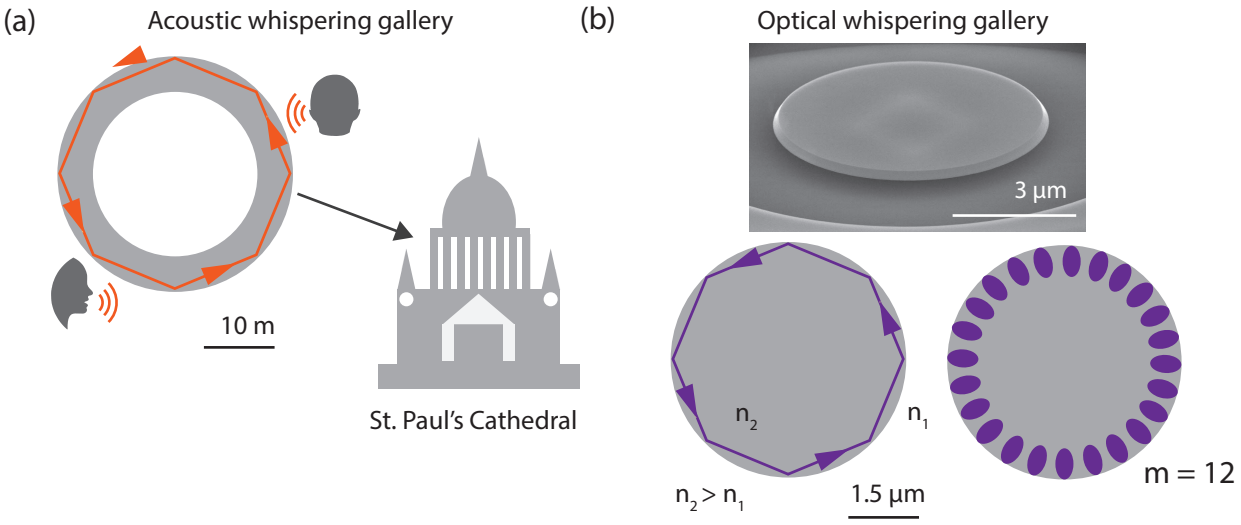

Figure 2.1: Illustration of acoustic and optical whispering galleries. (a) Acoustic whispering gallery in St. Paul's Cathedral and (b) optical whispering gallery resonator fabricated from GaP, and cartoon of azimuthal dependence of |E| for an $m = 12$ whispering gallery mode. This figure has been partially adapted from Ref. [73].

these modes are described as being either transverse electric (TE) or transverse magnetic (TM) polarized and are described by mode indices $\{m, n, q\}$ which describe the number of nodes in the azimuthal, radial, and vertical direction, as described in Appendix B.

2.1.1 Optical figures of merit

To compare and analyze the performance of an optical cavity it is useful to define some universal figures of merit that describe the optical properties of the cavity.

Optical quality factor

The quality factor is a commonly used parameter used to described damped harmonic oscillators. The optical quality factor, Q_o describes the temporal confinement of light in the cavity, and is defined as:

$$Q_o \equiv \omega_o \tau_o = \frac{\omega_o}{\Delta\omega_o}, \tag{2.1}$$

where $\Delta\omega_o$ is the full width at half maximum bandwidth of the cavity mode in frequency

space. As the Q_o is defined in terms of the field energy $\kappa = \Delta\omega_o = 1/\tau_o$ is the energy decay rate, which has units of radians/s. The stored energy in the cavity, $U(t)$, then dissipates according to $U(t) = U_o e^{-\kappa t}$, while the cavity amplitude will decay at a rate of $\kappa/2$. Lastly, Q_o represents, up to a factor of 2π, the number of oscillations the cavity field will undergo before $U(t)$ decays to $1/e$ of U_o.

In general, multiple mechanisms contribute to the total optical loss rate of the microdisks, such that the total Q_o or total loss rate, κ, is given by

$$\frac{1}{Q_o} = \omega_o \sum_n \frac{1}{Q_n} \qquad \text{and} \qquad \kappa = \sum_n \kappa_n. \tag{2.2}$$

Generally we can separate these contributions into losses that are intrinsic to the device and those that are extrinsic, such as coupling to a waveguide, and define an intrinsic quality factor, Q_i and an extrinsic quality factor Q_{ex} such that $1/Q_o = 1/Q_i + 1/Q_{ex}$ or $\kappa = \kappa_i + \kappa_{ex}$. For the microdisks studied in this work the intrinsic Q_i can be decomposed as

$$1/Q_i = 1/Q_{rad} + 1/Q_b + 1/Q_{ss} + 1/Q_{sa}, \tag{2.3}$$

where Q_{rad}, Q_b, Q_{ss}, and Q_{sa} relate to radiation loss via leakage into unbound modes, bulk absorption, surface scattering, and surface absorption, respectively. Etch smoothness impacts Q_{ss}, while etch chemistry and other processing that influences the microdisk surface can impact Q_{sa}. Q_b is determined by the bulk optical properties of the material, and Q_{rad} is defined by solutions to Maxwell's equations for modes of a device fabricated without any imperfections. The contributions of these factors to Q_o will be discussed in further detail throughout this thesis. Loss related to coupling with the fiber taper is accounted for in Q_{ex}, as discussed further in Section 2.2.

Free-spectral range, group velocity, and finesse

In WGM's the free spectral range (FSR) often refers to the spacing between the TE(TM)$_{m,n,q}$ and TE(TM)$_{m+1,n,q}$ modes in wavelength ($\delta\lambda_{\mathrm{FSR}}$) or frequency ($\delta\omega_{\mathrm{FSR}}$). As the cavities studied here are comprised of a dielectric material, the FSR will not be constant over all wavelengths due to material dispersion and device geometry. The FSR is a useful quantity for identifying mode families in the cavity resonance spectrum, as discussed in Chapter 3. An expression for ($\delta\omega_{\mathrm{FSR}}$) can be obtained by considering the resonance condition in the form of $\omega_{\mathrm{m}}T_{\mathrm{R}} = 2\pi m$, where $T_{\mathrm{R}} = 2\pi R n_{\mathrm{eff}}/c$ is the round-trip time. We can then describe two adjacent modes as

$$\omega_{\mathrm{m}}T_{\mathrm{R,m}} = 2\pi m \tag{2.4}$$

$$\omega_{\mathrm{m+1}}T_{\mathrm{R,m+1}} = 2\pi(m+1) \tag{2.5}$$

$T_{\mathrm{R,m}}$ depends on n_{eff}, which will exhibit dispersion, however, if we assume this is negligible for two adjacent modes then we get the simple expression

$$\delta\omega_{\mathrm{FSR}} = \omega_{m+1} - \omega_m \approx \frac{c}{R n_{\mathrm{eff}}}, \tag{2.6}$$

or

$$\delta\lambda_{\mathrm{FSR}} \approx \frac{\lambda_{\mathrm{m}}^2}{2\pi R n_{\mathrm{eff}}}, \tag{2.7}$$

as for small wavelength intervals $\Delta f = (c/\lambda^2)\Delta\lambda$.

The finesse, $\mathcal{F}$, of the cavity describes the sharpness of the resonance relative to the mode spacing, and up to a factor of 2π gives the number of round trips a photon will make before leaking out of the cavity [79]

$$\mathcal{F} = \frac{\delta\omega_{\mathrm{FSR}}}{\Delta\omega_{\mathrm{o}}} \approx \frac{Q}{m}, \tag{2.8}$$

Mode volume

The mode volume is an important quantity in nanophotonic structures which describes the volume that the optical mode occupies in the cavity and is commonly defined [80] as

$$V_{\mathrm{eff}} = \frac{\int \epsilon(\mathbf{r})|\mathbf{E}(\mathbf{r})|^2 d^3\mathbf{r}}{\max[\epsilon(\mathbf{r})|\mathbf{E}(\mathbf{r})|^2]} \tag{2.9}$$

where the volume integral is performed over the entire volume, including the field inside and outside of the disk, with the corresponding dielectric constant for that region of space, and is computed numerically here using finite difference time domain (FDTD) simulations as described in the following section, and is usually quoted as a number multiplying the ratio of free space wavelength to the structure's refractive index $(\lambda/n)^3$. Typically for the devices studied in this thesis $V_{\mathrm{eff}} \sim 10(\lambda/n)^3$, however photonic crystal structures can achieve $V_{\mathrm{eff}} < 1(\lambda/n)^3$ [70]. The mode volume combined with the intrinsic optical-Q_{i} provide the commonly used Q_{i}/V figure of merit. A technical challenge associated with reaching large Q_{i}/V, while reducing V, is to maintain high-Q_{i} due to increased sensitivity to fabrication imperfections as the mode is less effectively confined.

2.1.2 Simulations of microdisk whispering gallery modes

In practice FDTD or finite element method (FEM) simulations are commonly used to numerically solve Maxwell's equations for non-canonical dielectric structures such as microdisks. In this work, MEEP [81], an open source FDTD solver was utilized in the early design stage of the experiment. As FDTD is a well established technique and not the focus of this work, I will briefly summarize what it is and how it was utilized, but point the reader to MEEP's documentation for further details[1]. In MEEP, the FDTD simulation evaluates the

[1] https://meep.readthedocs.io/en/latest/

electromagnetic field propagated over a mesh grid of discrete distance points and through discrete time points with the evolution governed by Maxwell's equations. The size of this grid will ultimately limit the resolution of the simulation, where a finer grid requires more computational resources. An advantage of the microdisk geometry is that the simulation can be done in 2-dimensions instead of 3 by exploiting its cylindrical symmetry, reducing computation time significantly. The goal of these simulations were to put a lower bound on microdisk diameter that would be sufficient to observe modes whose Q_{i} were not limited by radiation or bending loss, i.e. $Q_{\mathrm{rad}} > Q_{\mathrm{i}}$. An advantage of using a FDTD method is that a large number of resonant frequencies can be obtained in a single simulation by analyzing the response of the system to a short time domain pulse. The basic prescription is to first run the simulation with a short duration excitation pulse which is centered at the wavelength of interest, and is relatively broadband (large enough to capture a handful of modes around the excitation frequency). After the source has turned off, the Harminv function in MEEP is used to identify resonant modes of the structure that were excited, for a user-input m number. We can then focus on a particular mode of interest by using a long excitation pulse (narrowband), centered at the mode frequency of interest, as outlined in detail in the MEEP documentation[2]. In FDTD the temporal resolution or time step, Δt is related to the grid spatial resolution, Δx, by $\Delta t = \mathcal{S}\Delta x$, where the Courant factor, $\mathcal{S} = 0.5$, by default in MEEP. Using the same methodology, MEEP was also used in simulating the FSR for various mode families observed in the GaP microdisks studied in Chapter 3.

Finite element method (FEM) simulations of the optical microdisk modes were also carried out with COMSOL Multiphysics, a commonly used FEM software suite. The goal of these simulations were to compute both the optical and mechanical modes of the microdisk such that the optomechanical coupling rate could be estimated, as described in Section 2.4.1. FEM simulations differ from FDTD in that approximating functions are specified on the mesh instead of the field on a grid of points and FEM directly solves for the eigenvectors

[2]https://meep.readthedocs.io/en/latest/Scheme_Tutorials/Ring_Resonator_in_Cylindrical_Coordinates/

and eigenmodes of the system. Here the field quantity is interpolated over a given element and connected to neighbouring elements at "nodes". The equations for each element are then assembled into a matrix which must be solved. As this matrix must be held in memory, FEM simulations are generally more computationally intensive compared to FDTD, which just needs to calculate the field's value at a specific mesh point in the next time step via Maxwell's equations. However, a major advantage of FEM is that the mesh size does not have to be uniform as it does in FDTD, which allows for greater resolution in areas of interest in the simulation. COMSOL solves systems of coupled nonlinear partial differential equations through the finite element method in one, two and three dimensions. For the work done here a full 3D model was utilized to solve for the optical and mechanical modes of the microdisk.

2.2 Fiber-taper coupling

A vital ingredient for studying an optical cavity is a method for coupling light to and from it. Traditional methods for coupling light to an in-plane waveguide or device includes prisms [82] and grating couplers [83, 84, 85], however, these typically have low coupling efficiency, and large footprints. This work utilizes a dimpled fiber taper, which is a tool pioneered by Oskar Painter's group at Caltech [86]. A fiber taper is a standard optical fiber which has been heated and stretched such that its diameter at the taper waist is about the wavelength of light passed through the fiber, as illustrated in Fig. 2.2(a). A portion of the guided field will exist as an evanescent field which can couple efficiently to a device for sufficient field overlap and phase matching, as discussed in the following section. In order to use this fiber taper to couple to a single device in an array of many, a dimpled shape is introduced to the tapered region as illustrated in Fig. 2.2(a). This is achieved by annealing the taper around a ceramic knife blade to give it sufficient radius of curvature to address a single device. I built the majority of the fiber tapering system used in the lab as an undergraduate

and Christopher Healey developed the ceramic knife dimpling technique, both of which are detailed in Refs. [87, 88].

2.2.1 Input-output formalism

In order to analyze the full cavity optomechanical system, knowing the rates at which light is coupled to and lost from the optical cavity is necessary. Input-output formalism is commonly used to achieve this goal and offers a quantum mechanical description of an optical cavity that is coupled to the environment and allows analysis of the light reflected or emitted from the cavity [18, 89, 90]. It is formulated in the Heisenberg picture and describes the evolution of the cavity field amplitude. Note that for the classical regime the photon anihilation operator, $\hat{a}$, is replaced by a properly normalized complex electric field amplitude for the cavity mode being analyzed. In this work the classical case of the following equations are obtained by taking the average of $\hat{a}$ such that $\hat{a} \rightarrow \langle \hat{a} \rangle \equiv a$, which is valid when N is large such that quantum fluctuations in N are negligible. We start by writing down the equation of motion for $\hat{a}$ for a travelling wave mode, pictured in Fig. 2.2(b) which occurs only for a perfectly azimuthally symmetric microdisk. Then we analyze the case of a standing wave or doublet mode, pictured in Fig. 2.2(c), where imperfections in the microdisk lead to splitting of the normally degenerate clockwise ($\hat{a}_{\mathrm{cw}}$) and counter-clockwise ($\hat{a}_{\mathrm{ccw}}$) propagating modes.

2.2.2 Travelling wave mode

For the travelling wave case we have

$$\frac{d\hat{a}_{\mathrm{cw}}}{dt} = \frac{i}{\hbar}[\hat{H}, \hat{a}_{\mathrm{cw}}] - \frac{\kappa}{2}\hat{a}_{\mathrm{cw}} + \zeta\hat{s} + \sqrt{\kappa_{\mathrm{i}}}\hat{f}_{\mathrm{in}}, \tag{2.10}$$

where the Hamiltonian for the bare cavity is given by $\hat{H} = \hbar\omega_o \hat{a}^{\dagger}_{\mathrm{cw}}\hat{a}_{\mathrm{cw}} + 1/2$. Here the input field $\hat{s}$ is normalized such that $\langle \hat{s}^{\dagger}\hat{s} \rangle$ is the rate at which photons arrive at the cavity and $P = \hbar\omega_{\mathrm{l}}\langle \hat{s}^{\dagger}\hat{s} \rangle$ is the input power [18] for an input laser of frequency ω_{l}. The input quantum

noise, $\hat{f}_{\mathrm{in}}$, is defined as

$$\hat{f}_{\mathrm{in}}(t) \equiv \frac{-1}{\sqrt{2\pi}} \int_{-\infty}^{\infty} d\omega e^{-i\omega(t-t_0)} \hat{f}_{t_0}(\omega) \tag{2.11}$$

where $\hat{f}_{t_0}(\omega)$ is the value of the bath anhiliation operator, $\hat{f}(\omega)$ at $t = t_0$ [91]. The relationship between the input and output fields can be determined by first moving to a frame rotating with the input laser frequency, ω_{l}, such that the Hamiltonian is given by $\hat{H} = -\hbar\Delta\hat{a}^{\dagger}_{\mathrm{cw}}\hat{a}_{\mathrm{cw}} + 1/2$, where $\Delta = \omega_{\mathrm{l}} - \omega_{\mathrm{o}}$. We then compute the Heisenberg equation of motion part of Eqn. 2.10, and work in the classical regime by taking the average quantity of the input field, $\hat{s}$, and cavity field amplitude, $\hat{a}_{\mathrm{cw}}$, as described above, and ignore input vacuum fluctuations:

$$\frac{da_{\mathrm{cw}}}{dt} = \left(i\Delta - \frac{\kappa}{2}\right) a_{\mathrm{cw}} + \zeta s. \tag{2.12}$$

In order to determine the coupling coefficient, ζ we can assume that the transmitted signal past the cavity will have the form

$$t = \eta_1 s + \eta_2 a_{\mathrm{cw}}, \tag{2.13}$$

and use a power conservation argument, where we equate the change in the cavity's internal energy to the power input to the cavity, minus the dissipated power [92]:

$$\frac{d|a_{\mathrm{cw}}|^2}{dt} = |s|^2 - |t|^2 - \kappa_{\mathrm{i}}|a_{\mathrm{cw}}|^2. \tag{2.14}$$

By substituting Eqn. 2.13 and Eqn. 2.12 into Eqn. 2.14, we find that one solution to this set of equations is $\eta_1 = 1$ and $\eta_2 = -\sqrt{\kappa_{\mathrm{ex}}}$, where κ_{ex} is the total decay rate from the cavity to the waveguide, which gives $t = s - \sqrt{\kappa_{\mathrm{ex}}}a_{\mathrm{cw}}$, and $\zeta = \sqrt{\kappa_{\mathrm{ex}}}$. Equation 2.12 is then

$$\frac{da_{\mathrm{cw}}}{dt} = \left(i\Delta - \frac{\kappa}{2}\right) a_{\mathrm{cw}} + \sqrt{\kappa_{\mathrm{ex}}}s. \tag{2.15}$$

We can then solve for a_{cw} in the steady state ($da_{\mathrm{cw}}/dt = 0$),

$$a_{\mathrm{cw}} = \frac{\sqrt{\kappa_{\mathrm{ex}}}s}{\kappa/2 - i\Delta}, \tag{2.16}$$

where the steady state normalized transmission can then be calculated as

$$T = \left|\frac{t}{s}\right|^2 = \left|\frac{(\kappa_{\mathrm{i}} - \kappa_{\mathrm{ex}})/2 - i\Delta}{(\kappa_{\mathrm{i}} + \kappa_{\mathrm{ex}})/2 - i\Delta}\right|^2. \tag{2.17}$$

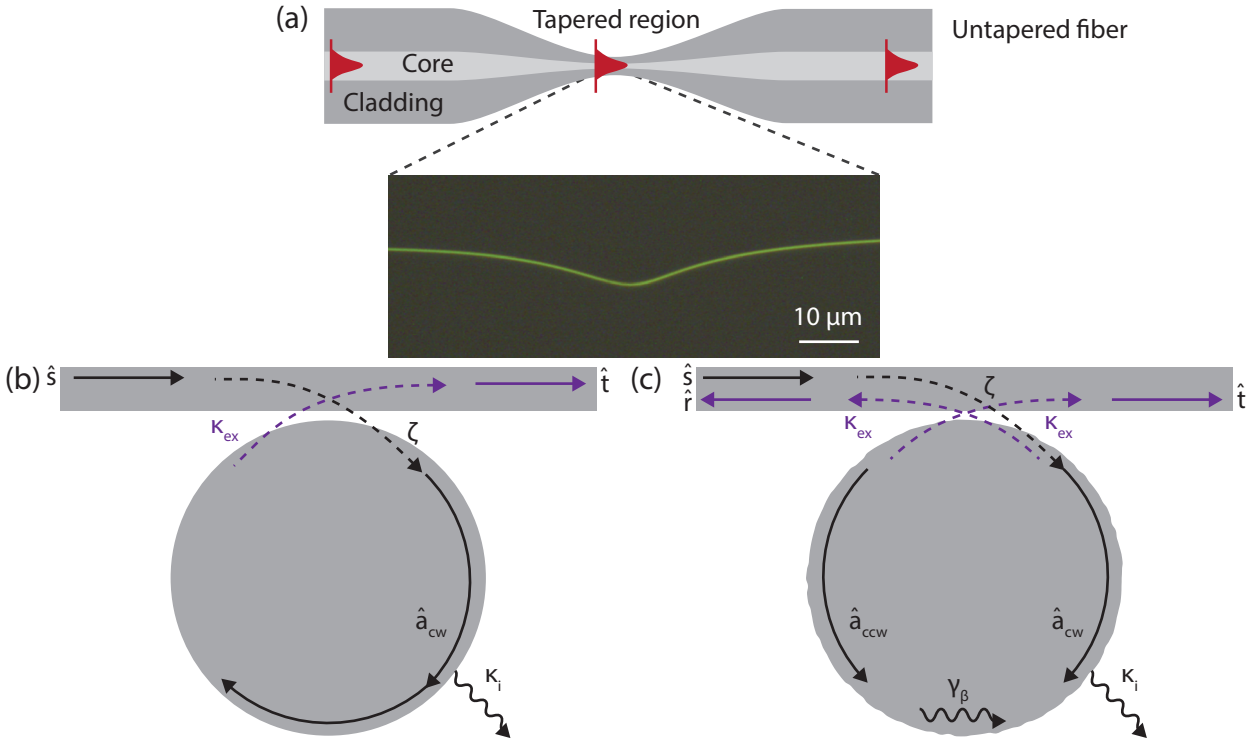

Figure 2.2: Schematic of fiber taper waveguide and coupling to a microdisk cavity. (a) Illustration of fiber taper shape and optical micrograph of a dimpled fiber taper. (b) Schematic of the fiber taper waveguide coupled to a microdisk where only a travelling wave mode is excited. κ_{i} is the cavity's intrinsic energy decay rate, and κ_{ex} is the energy decay rate into the fiber taper waveguide. Here the clockwise-propagating mode, $\hat{a}_{\mathrm{cw}}$, is excited by the waveguide input field $\hat{s}$, which is coupled to the microdisk with coupling rate ζ. Some light is coupled back to the waveguide and transmitted through the fiber with amplitude $\hat{t}$. (c) For a disk that is not perfectly azimuthally symmetric photons in the $\hat{a}_{\mathrm{cw}}$ mode will be scattered into the counter-clockwise propagating mode, $\hat{a}_{\mathrm{ccw}}$, at a rate of γ_β. Now photons will be transmitted and reflected from the cavity, with amplitude $\hat{r}$. Here a_{cw} and, a_{ccw} are normalized to energy and $\hat{s}, \hat{r}$, and $\hat{t}$ are normalized to power.

On resonance this reduces to

$$T|_{\Delta=0} = \left(\frac{1 - \kappa_{\mathrm{ex}}/\kappa_{\mathrm{i}}}{1 + \kappa_{\mathrm{ex}}/\kappa_{\mathrm{i}}}\right)^2 = \left(\frac{1-K}{1+K}\right)^2, \tag{2.18}$$

where $K = \kappa_{\mathrm{ex}}/\kappa_{\mathrm{i}}$ is the coupling parameter for a travelling wave mode. This allows us to define three regimes that characterize the degree of coupling between the waveguide and microdisk, listed below, and illustrated in Fig. 2.3(a).

- Under coupled: $K < 1$. Here $\kappa_{\mathrm{ex}} < \kappa_{\mathrm{i}}$ such that loss from the cavity is dominated by intrinsic loss in the cavity. All of the data presented in this thesis was taken in the under coupled regime. This is sub-optimal as not all of the photons coupled to the cavity are read out effectively.

- Critically coupled: $K = 1$. Here $\kappa_{\mathrm{i}} = \kappa_{\mathrm{ex}}$ and on resonance $T = 0$ as the power input to the microdisk is equal to the power dissipated in the cavity. This case results in the maximum stored energy in the cavity.

- Over coupled: $K > 1$. Here $\kappa_{\mathrm{ex}} > \kappa_{\mathrm{i}}$ such that photons coupled into the cavity have a high probability of being coupled back into the waveguide before leaking out of the cavity due to its intrinsic losses. In the limit $\kappa_{\mathrm{ex}} \gg \kappa_{\mathrm{i}}$ this results in $T \sim 1$ and a broadening of the resonance linewidth due to the increased total κ.

In general, the goal of the experiment will dictate which regime is preferential to be in. For example, when trying to measure Q_{i}, the under coupled regime is preferable as to perturb the system the least, while the over coupled regime can be advantageous when wanting to recover as many photons from the cavity as possible.

2.2.3 Doublet modes

As no device we fabricate will have perfect azimuthal symmetry, some light will be backscattered into the counter-clockwise propagating mode, as illustrated in Fig. 2.2(c) at rate γ_β

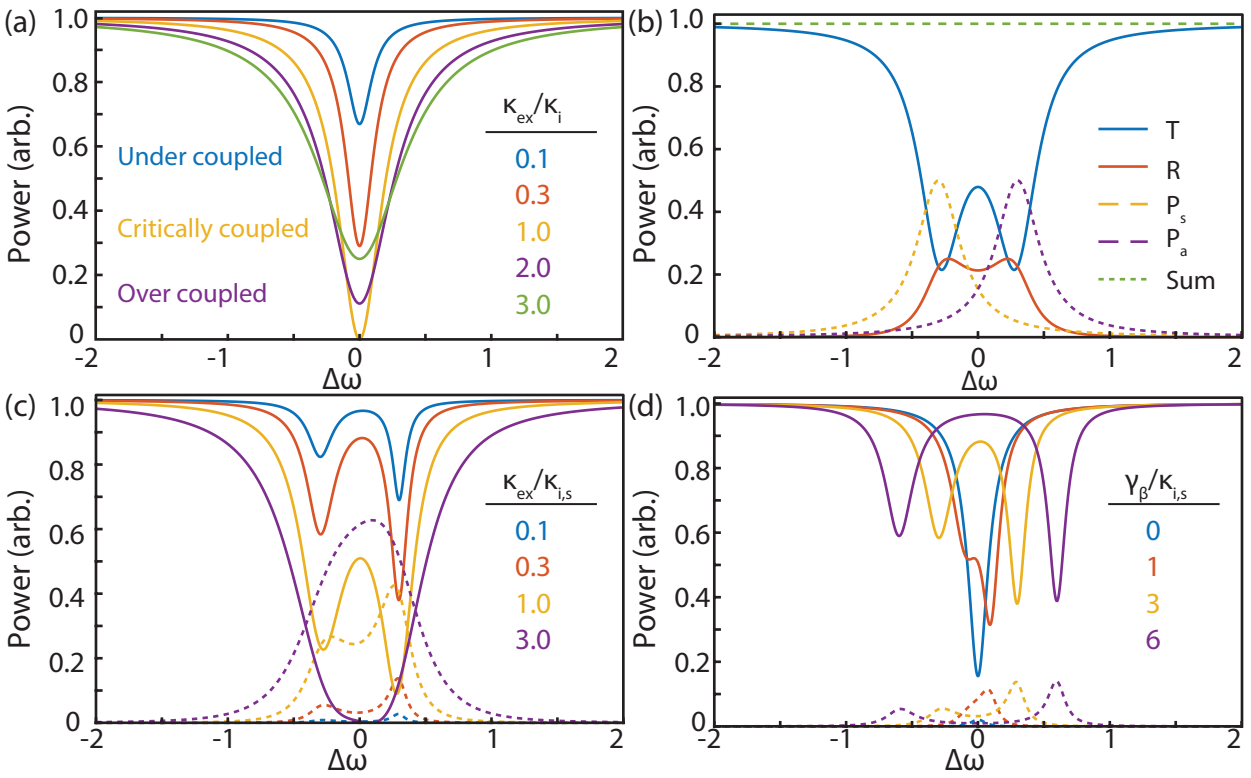

Figure 2.3: Coupling regimes for a waveguide-microdisk system. (a) Theoretical normalized transmission, T, for a singlet or travelling wave whispering gallery mode for various coupling regimes as labelled, with $\kappa_{\rm i} = 0.2$. (b) Normalized transmission and reflection, R, for a doublet whispering gallery mode with equal intrinsic loss rates for each standing wave mode, $\kappa_{\rm i,s} = \kappa_{\rm i,a} = 0.2$ and $\gamma_\beta = 3\kappa_{\rm i,s}$. The dissipated power from $a_{\rm s}$, and $a_{\rm a}$ is also shown as $P_{\rm s} = \kappa_{\rm i,s}|a_{\rm s}|^2$, and $P_{\rm a} = \kappa_{\rm i,a}|a_{\rm a}|^2$, respectively. The sum of $T, R, P_{\rm s}, P_{\rm a}$ illustrates the conservation of power. (c) The doublet mode transmission (solid) and reflection (dashed) spectrum as a function of $\kappa_{\rm ex}$ illustrating the regimes of under-, critical- and, over-coupling as in (a). Here $\kappa_{\rm i,a} = 0.1$, $\kappa_{\rm i,s} = 0.2$ and $\gamma_\beta = 3\kappa_{\rm i,s}$. (d) The doublet mode transmission (solid) and reflection (dashed) spectrum as a function of coupling between $a_{\rm cw}$ and $a_{\rm ccw}$, i.e. γ_β is also shown for reference.

[93]. The equations of motion then become

$$\frac{da_{\rm cw}}{dt} = \left(i\Delta - \frac{\kappa}{2}\right) a_{\rm cw} + i\frac{\gamma_\beta}{2} a_{\rm ccw} + \sqrt{\kappa_{\rm ex}} s, \tag{2.19a}$$

$$\frac{da_{\rm ccw}}{dt} = \left(i\Delta - \frac{\kappa}{2}\right) a_{\rm ccw} + i\frac{\gamma_\beta}{2} a_{\rm cw}, \tag{2.19b}$$

where $\zeta = \sqrt{\kappa_{\rm ex}}$ as $\kappa_{\rm ex}$ represents the coupling rate from the cavity to the waveguide as experienced by a clockwise or counter-clockwise propagating photon, as illustrated in Fig. 2.2(c). Following the work of Gorodetsky et al. [93] and Borselli [94], these equations can

be orthogonalized by working in a standing wave basis made up of symmetric ($a_{\rm s}$) and anti-symmetric ($a_{\rm a}$) combinations of the travelling wave modes, which are defined as

$$a_{\rm s} = \frac{1}{\sqrt{2}}(a_{\rm cw} + a_{\rm ccw}) \qquad \longleftrightarrow \qquad a_{\rm cw} = \frac{1}{\sqrt{2}}(a_{\rm s} + a_{\rm a}), \tag{2.20a}$$

$$a_{\rm a} = \frac{1}{\sqrt{2}}(a_{\rm cw} - a_{\rm ccw}) \qquad \longleftrightarrow \qquad a_{\rm ccw} = \frac{1}{\sqrt{2}}(a_{\rm s} - a_{\rm a}). \tag{2.20b}$$

The equations of motion then become

$$\frac{da_{\rm s}}{dt} = \left(i\Delta + i\frac{\gamma_\beta}{2} - \frac{\kappa_{\rm s}}{2}\right) a_{\rm s} + \sqrt{\frac{\kappa_{\rm ex}}{2}} s, \tag{2.21a}$$

$$\frac{da_{\rm a}}{dt} = \left(i\Delta - i\frac{\gamma_\beta}{2} - \frac{\kappa_{\rm a}}{2}\right) a_{\rm a} + \sqrt{\frac{\kappa_{\rm ex}}{2}} s, \tag{2.21b}$$

where to generalize these equations a bit more we allow each standing wave to have its own intrinsic decay rate ($\kappa^{\rm s,a} = \kappa_{\rm i}^{\rm (s,a)} + \kappa_{\rm ex}$). Note that we have taken $\kappa_{\rm ex}$ to be the same for each mode which does not have to be the case, but describes the situations encountered in this work. As $a_{\rm cw}$ and $a_{\rm ccw}$ have an $e^{im\phi}$ and $e^{-im\phi}$ azimuthal dependence, the $a_{\rm s}$ and $a_{\rm a}$ modes are standing waves with $\cos(m\phi)$ and $\sin(m\phi)$, up to a phase factor. Again we can find the steady state amplitude of $a_{\rm s,a}$ as

$$a_{\rm s,a} = \frac{-\sqrt{\kappa_{\rm ex}/2}s}{-\kappa^{\rm s,a}/2 + i(\Delta \pm \gamma_\beta/2)} \tag{2.22}$$

The transmission and reflection probabilities can then be computed as $T = \left|\frac{t}{s}\right|^2$, and $R =$

$\left|\frac{r}{s}\right|^2$, where $t = s - \sqrt{\kappa_{\rm ex}}a_{\rm cw}$ and $r = -\sqrt{\kappa_{\rm ex}}a_{\rm ccw}$, such that

$$T = \left|1 - \sqrt{\frac{\kappa_{\rm ex}}{2}}\left(\frac{a_{\rm s}}{s} + \frac{a_{\rm a}}{s}\right)\right|^2 \tag{2.23a}$$

$$R = \left|\sqrt{\frac{\kappa_{\rm ex}}{2}}\left(\frac{a_{\rm s}}{s} - \frac{a_{\rm a}}{s}\right)\right|^2 \tag{2.23b}$$

The doublet mode spectra for various conditions is shown in Fig. 2.3(b–d). In Fig. 2.3(b) the normalized reflection and transmission is shown, where the power dissipated from the disk for the standing wave modes $a_{\rm s}$, and $a_{\rm a}$ is also shown to illustrate that power is conserved in the system. The dependence of the doublet mode on $\kappa_{\rm ex}$ and γ_β is shown in Fig. 2.3(c,d) for reference.

2.3 Mechanical modes

Any mesoscopic object will have modes of vibration; we refer to excitations of these modes as mesoscopic phonons, or phonons for short. In addition to these modes, bulk phonon modes with wavelengths on the order of the atomic spacing also are present [95], but are not studied here. Rather, we focus on the continuum solid model to describe the mechanical modes of the structure. These modes still represent a collective excitation of atoms making up the object but are constrained by the imposed boundary conditions. Another way to imagine these modes are as a combination of standing wave phonons, constrained by the device geometry. In the continuum limit the deformations in the structure can be described via the fourth rank elasticity tensor, $\overleftrightarrow{c}$, and a time-dependent vector displacement field, $\mathbf{Q}(\mathbf{r},\mathrm{t})$, accounting for the structure's motion. Treating the material as a linear isotropic solid allows us to describe the material making up the structure by two material constants, namely the Young's modulus, E, and Poisson's ratio, σ. The relation between the relative displacement vector $\mathbf{q}(\mathbf{r})$ and the second rank strain tensor $\overleftrightarrow{S}$ by [96]

$$S_{ij} = \frac{1}{2}\left(\frac{\partial q_i}{\partial x_j} + \frac{\partial q_j}{\partial x_i}\right) \tag{2.24}$$

As the amplitude of vibration of these modes are much smaller than any geometric dimension of the microdisk, the motion follows linear elastic theory, i.e. the material obeys Hooke's law where deformation of the material is linearly proportional to the applied force such that the second rank stress tensor, $\overleftrightarrow{T}$, is related to $\overleftrightarrow{S}$ by

$$T_{ij} = \sum_{k=1}^{3}\sum_{l=1}^{3} c_{ijkl} S_{kl}. \tag{2.25}$$

where c_{ijkl} are the components of the elasticity tensor. Via Newton's second law, the equation of motion for a linear isotropic solid that is not subject to any external forces is [96]

$$\rho\frac{\partial^2 \mathbf{q}}{\partial t^2} = (\lambda+\mu)\nabla(\nabla\cdot\mathbf{q}) + \mu\nabla^2\mathbf{q}, \tag{2.26}$$

where ρ is the material density, and $\lambda = E\sigma/(1+\sigma)(1-2\sigma)$, $\mu = E/2(1+\sigma)$ are the Lamé constants, and

$$\Delta = \nabla\cdot\mathbf{q} = \frac{\partial q_1}{\partial x_1} + \frac{\partial q_2}{\partial x_2} + \frac{\partial q_3}{\partial x_3}, \tag{2.27}$$

is the dilatation of the displacement. By assuming that the displacement field has a form of $\mathbf{q} = \mathbf{q}(\mathbf{r})e^{-i\omega t}$ we find the eigenvector equation

$$(\lambda+\mu)\nabla(\nabla\cdot\mathbf{q}(\mathbf{r})) + \mu\nabla^2\mathbf{q}(\mathbf{r}) = -\rho\omega^2\mathbf{q}(\mathbf{r}), \tag{2.28}$$

where each eigenfrequency ω_j corresponds to a eigenvector $\mathbf{q}_j(\mathbf{r})$.

In this work we focus primarily on one type of mechanical mode, namely the radial breathing mode (RBM) of the microdisk, as it exhibits the strongest dispersive optomechanical coupling, as discussed in the following section. To get a feel for how the frequency of the RBM depends on the material parameters and structure's size we can use the approximation

of a free, thin circular plate, which is described by Love's theory of elasticity [97, 98, 99]. Love [97] gives the solutions for an infinitely thin isotropic circular plate with free edges, while Onoe [98] extends Love's analysis to show the character of the modes and numerical estimates of their frequencies. For the case of a circular plate that has vanishing stress at the outer radius, the solution for the mode with purely areal dilatation in cylindrical coordinates is given by $\Delta^{'} = Ah^2 J_1(hr)$, where A is a normalization factor, J_n is a Bessel function of first kind of order n, and h is a constant defined as [98]

$$h = \omega_0 \sqrt{\frac{\rho}{\frac{E}{1+\sigma} + \frac{E\sigma}{1-\sigma}}}. \tag{2.29}$$

Here ρ is the material density, and ω_0 is the angular frequency of the RBM. We then focus on the solution for the purely radial modes, of which there are an infinite number of higher order modes consisting of purely radial motion, which intrinsically have some dispersion [100]. Effectively this is due to each mode "seeing" a different speed of sound, due to how the structure is deformed in each case. The natural frequencies for the radial breathing modes can be found by numerically solving the following system of equations [98]

$$\frac{\zeta}{\xi} \frac{J_0(\zeta/\xi)}{J_1(\zeta/\xi)} = 1 - \sigma, \tag{2.30}$$

where

$$\zeta = \omega_0 R \sqrt{\frac{\rho(2+2\sigma)}{E}} \qquad \text{and} \qquad \xi = \sqrt{\frac{2}{1-\sigma}}. \tag{2.31}$$

These equations are derived by considering only vibrations that involve no transverse displacement of points of the middle plane by evaluating the appropriate stress-resultants and enforcing that at the free edge of the plate the stress-resultants vanish [97]. Equation 2.30 illustrates that the solutions are periodic, which will give the higher order modes of the

RBM. Onoe gives a more intuitive look at how ω_0 depends on the material parameters with the following expression for the p^{th} order RBM

$$\omega_0 = \frac{\zeta}{R}\frac{1}{\sqrt{2+2\sigma}}\sqrt{\frac{E}{\rho}}, \tag{2.32}$$

where ζ is found by numerically solving Eqn. 2.30, which will depend on the order of the RBM solved for.

The presence of a small diameter pedestal has a minimal effect on the frequencies of the RBM's as there is little displacement of the disk where the pedestal intersects it. However, the pedestal supporting the microdisk can not always be considered small, especially in the case of the diamond microdisks studied here. As such, finite element method (FEM) simulations of the mechanical mode spectrum are generally more accurate and can be used to solve for the full spectrum of eigenmodes of the structure efficiently. By simulating the optical and mechanical field distribution, an estimation of the optomechanical coupling rate can be calculated as well. COMSOL FEM simulations of the mechanical mode spectra for the microdisks studied here were used exclusively in this work, which solves differential equations for the normalized spatial displacement field, $\mathbf{q}(\mathbf{r})$ [101] subject to the appropriate boundary conditions, where $\max(|\mathbf{q}(\mathbf{r})|) = 1$. Here we model all of our structures as isotropic linear elastic solids that obey Eqn. 2.26. This displacement field describes the motion of the mechanical mode in question, however, the simulation gives no value to the amplitude of the motion which must be calibrated unless the specific damping and driving force information is known. There are many eigenmodes supported by the microdisk, some of which are shown in Fig. 2.4 where the directionality of $\mathbf{q}(\mathbf{r})$ is indicated by the superimposed arrows. However, the mode that exhibits the largest dispersive optomechanical coupling is the RBM, as shown in Fig. 2.4(f), and discussed as follows.

A single mechanical mode's equation of motion for the time dependent displacement field, $\mathbf{Q}(\mathbf{r},\text{t})$, can be described using the unit spatial displacement field, $\mathbf{q}(\mathbf{r})$, and a time varying amplitude, $x(t)$ such that $\mathbf{Q}(\mathbf{r},t) = x(t)\cdot\mathbf{q}(\mathbf{r})$. Here $x(t)$ is scaled by the maximum

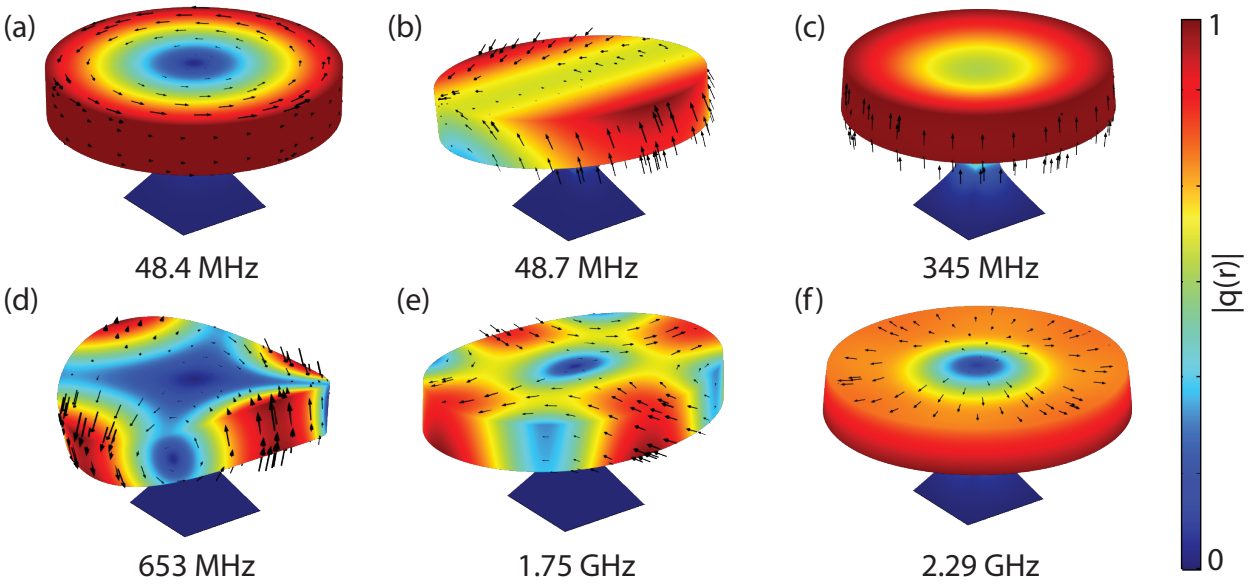

Figure 2.4: Selection of simulated first order mechanical normal modes for a diamond microdisk with radius of 2.65 μm, and a thickness of 940 nm. The normalized displacement field, $\mathbf{q}(\mathbf{r})$ is shown where the superimposed arrows indicate the directionality of the field. These modes are commonly referred to as (a) torsional, (b) cantilever, (c) sombrero (I made this one up) (d) crown, (e) wine-glass, and (f) radial breathing mode(RBM), where each family possesses higher order modes.

amplitude of oscillation, α, such that in the simplest case $x(t) = \alpha\cos(\omega_{\mathrm{m}}t)$. This allows us to reduce the equation of motions for the mechanical mode to a simple harmonic oscillator of single dimension and effective mass, m_{eff}, which describes the mass associated with the mechanical mode [18]. The mass of a mechanical resonator that is not isolated is non-trivial due to its connection to a substrate or larger supporting structure, i.e. the pedestal for the case of microdisk resonators. As such, an effective mass is utilized to measure the amount of mass that is ascribed to the mechanical resonator. This is done by weighting the mass such that larger mass is given to regions with larger displacement [101], and is calculated as

$$m_{\mathrm{eff}} = \rho \int \left(\frac{|\mathbf{Q}(\mathbf{r})|}{\max(|\mathbf{Q}(\mathbf{r})|)} \right)^2 dV, \tag{2.33}$$

where ρ is the material density which is taken to be isotropic, and the volume of integration corresponds to the volume of the disk.

By modelling these modes as one dimensional driven, damped harmonic oscillators in the time domain,

$$\ddot{x}(t) + \Gamma_{\rm m}\dot{x}(t) + \omega_{\rm m}^2 x(t) = \frac{F(t)}{m_{\rm eff}}, \tag{2.34}$$

we can easily characterize their properties in the frequency domain, where a mode's power spectral density is characterized by a Lorentzian with full width half maximum given by $\Gamma_{\rm m}$. In frequency space its displacement $x(\omega)$, as driven by some force $F(\omega)$ can be described as $x(\omega) = \chi_{xx}(\omega)F(\omega)$, where $\chi_{xx}(\omega)$ is the mechanical response function:

$$\chi_{xx}(\omega)^{-1} = m_{\rm eff}\left[\left(\omega_{\rm m}^2 - \omega^2\right) - i\omega\Gamma_{\rm m}\right]. \tag{2.35}$$

2.4 Cavity optomechanics in microdisks

The types of cavity optomechanical coupling can be lumped into either dispersive (cavity frequency modulation) or dissipative coupling (cavity loss rate modulation), as illustrated in Fig. 2.5. In the dispersive case, the cavity resonance frequency is modulated by a change in refractive index or cavity size as shown in Figs. 2.5(a,b). By parking a laser on the sloped section of the optical resonance this modulation is converted to amplitude modulation in the transmission of the fiber taper as illustrated in Fig. 2.5(c). Dissipative coupling arises from a modulation of the loss rate from the cavity, an example of which is shown in Figs. 2.5(d,e), where a highly absorptive element is brought close to the microdisk optical field and modulates the total cavity loss rate which again can be transduced as an amplitude modulation of an appropriately detuned laser. These amplitude modulations can then be detected with a high-speed photodetector whose output RF signal can then be Fourier transformed to reveal the mechanical mode power spectral density, as illustrated in Fig. 2.5(f).

The linear optomechanical coupling coefficient, G, describes the change in cavity frequency for a given displacement, $G = -d\omega/d\alpha$, where $G/2\pi$ has units of Hz/m. The microdisk cavities studied here exhibit primarily dispersive optomechanical coupling, which can be further decomposed into contributions due to moving dielectric boundaries, $G_{\rm MB}$, and

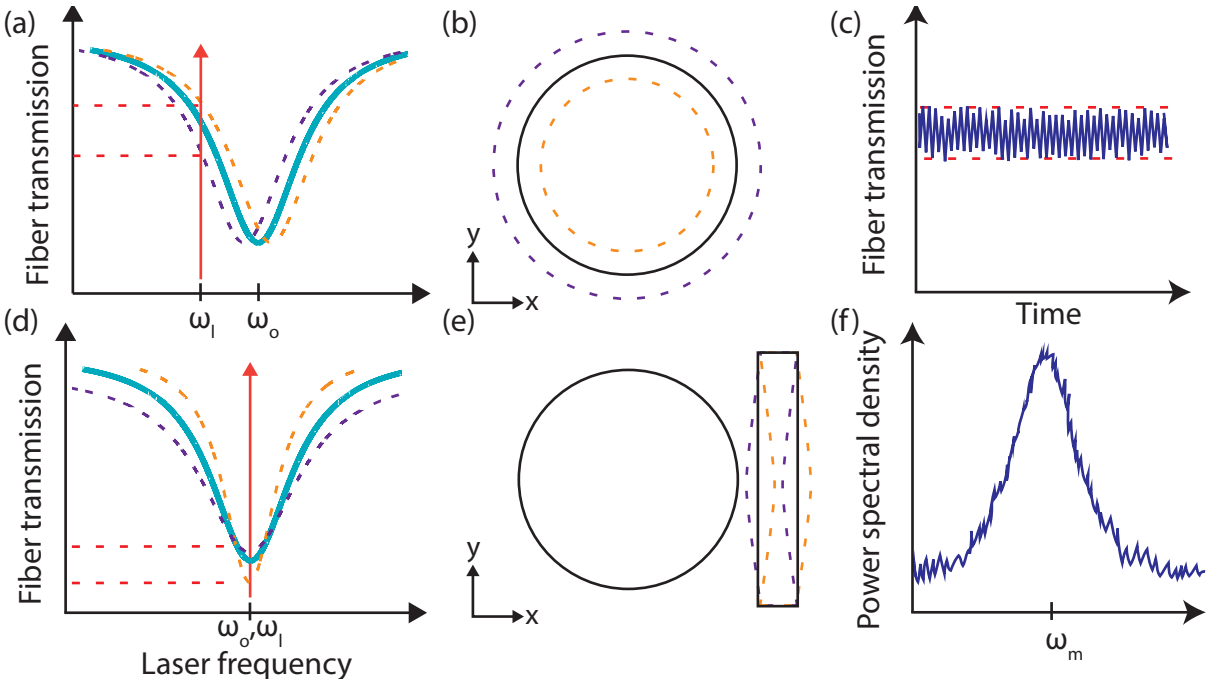

Figure 2.5: Dispersive versus dissipative optomechanical coupling. (a) Modulation of cavity resonance frequency occurs for a change in refractive index or cavity length as illustrated in (b). This modulation can be transduced by placing a laser detuned from ω_o which converts frequency modulation to amplitude modulation of the field transmitted by the cavity, as illustrated in (c). Dissipative coupling arises from a modulation of the cavity loss rate (d), an example of which is placing a highly absorptive element vibrating in the near field of the optical cavity (e). Here the modulation is transduced by placing a laser on resonance with the cavity. (f) By Fourier transforming the photodetected transmitted signal the mechanical mode spectrum or power spectral density can be found, which is a Lorentzian with FWHM, $\delta\omega_m = \Gamma_m$.

the photoelastic effect, G_{PE}. We can also define the single-photon optomechanical coupling rate $g_0 = Gx_{zpf}$, where $G = G_{MB} + G_{PE}$.

2.4.1 Simulation of optomechanical coupling coefficient

The optomechanical coupling coefficient can be calculated in COMSOL by first performing a simulation to identify the mechanical eigenmodes and displacement profiles of the structure, followed by a simulation to identify the optical eigenmodes and field profiles of the structure, which allows the computation of the following integrals; this procedure is now fairly standard in the field, and is outlined in detail in Marcelo Wu's thesis [88].

Moving boundary contribution

The contribution of the moving dielectric boundary to G_{MB} can be calculated via perturbation to Maxwell's equations [52, 101, 102], and is given by

$$G_{\mathrm{MB}} = -\frac{\omega_{\mathrm{o}}}{2} \frac{\oint_A (\mathbf{q} \cdot \hat{\mathbf{n}}) \left[\Delta\epsilon |\mathbf{E}_{||}|^2 - \Delta(\epsilon^{-1}) |\mathbf{D}_{\perp}|^2 \right] dA}{\int \epsilon |\mathbf{E}|^2 dV} \tag{2.36}$$

where $\mathbf{D} = \epsilon \mathbf{E}$, $\hat{\mathbf{n}}$ is the unit normal vector on the surface of the unperturbed cavity, $\mathbf{E}_{||}$ and $\mathbf{D}_{\perp}$ are the field components parallel and perpendicular to the dielectric boundary, respectively, and the displacement is normalized to the maximum displacement such that $\max|\mathbf{q}| = 1$. The integral is carried out over the disk surface, where ϵ_1 and ϵ_2 are the dielectric constants of the structure, and surrounding medium. Here $\Delta\epsilon = \epsilon_1 - \epsilon_2$, $\Delta(\epsilon^{-1}) = \epsilon_1^{-1} - \epsilon_2^{-1}$, and the volume integral encompasses the disk and surrounding medium.

Photoelastic contribution

The electric field inside the disk also leads to an induced strain due to electrostriction, which unlike the piezoelectric effect is present in all dielectric materials, and scales quadratically instead of linearly with the electric field. As the electric field here is oscillating at THz frequencies, the time averaged induced strain due to the piezoelectric effect is zero, while that due to electrostriction is non-zero owing to its quadratic dependence. The relationship between the change in refractive index due to strain can be written generally as

$$\delta\epsilon(\mathbf{r}) = -\overleftrightarrow{\epsilon} \left(\frac{\overleftrightarrow{p}\,\overleftrightarrow{S}}{\epsilon_0} \right) \overleftrightarrow{\epsilon}, \tag{2.37}$$

where $\overleftrightarrow{\epsilon}$, $\overleftrightarrow{p}$, and $\overleftrightarrow{S}$ are the dielectric, photoelastic, and strain tensors, respectively [103]. In an optically isotropic medium, which is the case for all of the materials studied in this thesis this can be simplified to

$$\delta\epsilon(\mathbf{r}) = -\epsilon_0 n^4 \overleftrightarrow{p}\overleftrightarrow{S}. \tag{2.38}$$

By inserting the appropriate photoelastic tensor for a cubic crystal, and assuming that x and y are in the [100] and [010] crystal directions, the photoelastic contribution to the optomechanical coupling coefficient can be calculated as [52]

$$G_{\mathrm{PE}} = -\frac{\omega_{\mathrm{o}}}{2}\frac{\langle E|\frac{d\epsilon}{d\alpha}|E\rangle}{\int \epsilon|\mathbf{E}|^2 dV} \tag{2.39}$$

$$= -\frac{\omega_{\mathrm{o}}\epsilon_0 n^4}{2}\int_{\mathrm{disk}} [2\mathrm{Re}\{E_x^* E_y\}p_{44}S_{xy} \tag{2.40}$$

$$+ 2\mathrm{Re}\{E_x^* E_z\}p_{44}S_{xz} + 2\mathrm{Re}\{E_y^* E_z\}p_{44}S_{yz} \tag{2.41}$$

$$+ |E_x|^2(p_{11}S_{xx} + p_{12}(S_{yy}+S_{zz})) + |E_y|^2(p_{11}S_{yy} + p_{12}(S_{xx}+S_{zz}))$$

$$+ |E_z|^2(p_{11}S_{zz} + p_{12}(S_{xx}+S_{yy}))]dV \;/\; \left[\max(|\mathbf{Q}(\mathbf{r})|)\int \epsilon|\mathbf{E}|^2 dV\right],$$

where the numerator is integrated only over the volume of the disk, the denominator is integrated over all space. This expression is also normalized by the maximum displacement given by the simulation ($\max(|\mathbf{Q}(\mathbf{r})|)$). To summarize: strain leads to change in refractive index according to the photoelastic effect, which leads to a change in the stored electromagnetic energy. Conversely, electrostriction induces some strain in the disk according to the time averaged electric field in the structure. As with the moving boundary case, the different time scales of mechanical vibrations and the optical energy decay rate leads to dynamical back-action in the system.

The vibration induced strain is minimized at the microdisk periphery, as shown in Fig. 2.6, which limits G_{PE} as the optical field is confined to the periphery of the microdisk. Here the simulated displacement field, $\mathbf{Q}(\mathbf{r})$ is normalized by a scaling factor A such that $\mathbf{Q}(\mathbf{r})/A = x_{\mathrm{th}}$, where the thermally driven amplitude, $x_{\mathrm{th}} = \sqrt{k_B T/m_{\mathrm{eff}}\omega_{\mathrm{m}}^2}$, which is computed via the equipartition theorem. To illustrate the normalized magnitude of normal stress in the

structure $\bar{\sigma}_n/\alpha = \sqrt{\sigma_{xx}^2 + \sigma_{yy}^2 + \sigma_{zz}^2}/\alpha$ is shown in Fig. 2.6(b), and the normalized σ_{xx} stress tensor component is shown as a function of radial distance and height inside the microdisk in Fig. 2.6(c,d). This illustrates that the normal stress in the microdisk falls to zero at the edge of the disk where the optical field is most strongly confined. Despite this fact, G_{PE} can still be significant in microdisks [104], and in some structures G_{PE} can exceed G_{MB} and become the dominant coupling mechanism [52, 105]. Note that G_{PE} can also have different sign from G_{MB} and negate each other in certain instances.

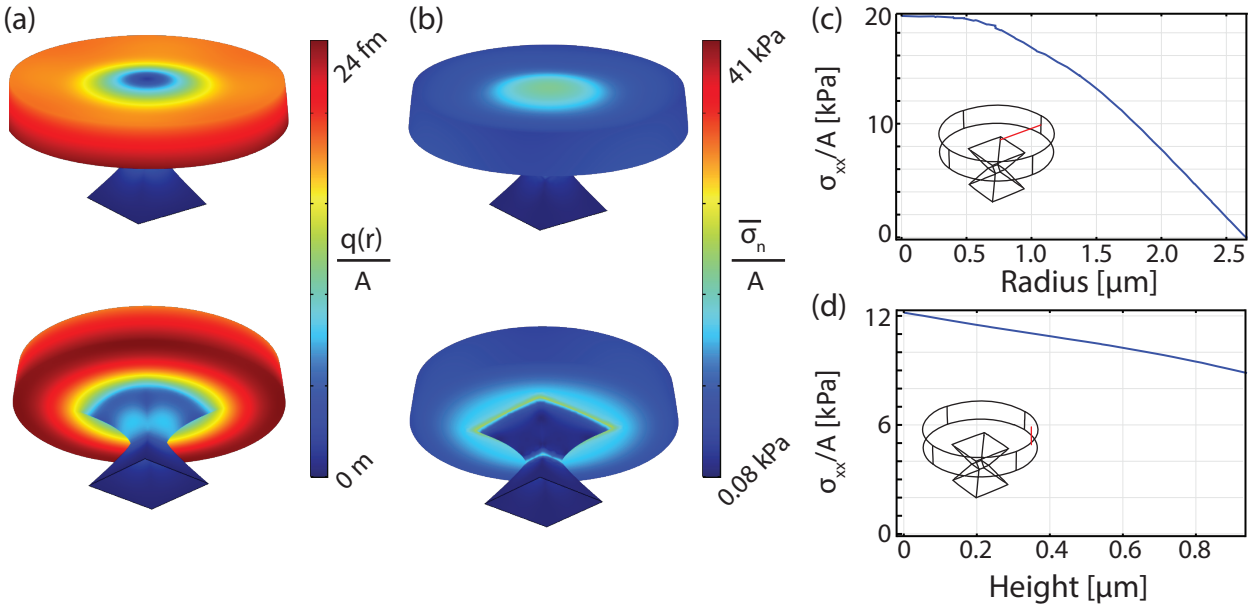

Figure 2.6: (a) Displacement profile of the RBM normalized to the thermally driven amplitude, x_{th} as discussed in the main text. (b) Normal stress profile ($\bar{\sigma}_n = \sqrt{\sigma_{xx}^2 + \sigma_{yy}^2 + \sigma_{zz}^2}$), which has also been normalized to the thermally driven amplitude. (c) Normalized σ_{xx} as a function of radial distance from the center of the disk. (d) Normalized σ_{xx} as a function of height near the edge of the disk.

2.4.2 Hamiltonian for cavity optomechanical cavity

The Hamiltonian describing the vast majority of cavity optomechanical cavities can be built up as follows, where we begin with the Hamiltonian for two uncoupled harmonic oscillators,

$$\hat{H}_0 = \hbar\omega_{\mathrm{o}}\hat{a}^\dagger\hat{a} + \hbar\omega_{\mathrm{m}}\hat{b}^\dagger\hat{b}. \tag{2.42}$$

Here $\hat{a}^\dagger, \hat{a}$ and $\hat{b}^\dagger, \hat{b}$ are the creation and annihilation operators for the optics and mechanics, respectively, and the zero-point energy contributions, $\hbar\omega/2$, are typically not explicitly written out. These terms do not enter the equations of motion for $\hat{a}$ and $\hat{b}$, and as all of the results presented in this thesis are firmly in the classical regime, these terms can be safely ignored for convenience. In this work we will only consider dispersive optomechanical coupling where $\omega_{\rm o}(\hat{x}) = \omega_{\rm o} + \hat{x}\partial\omega_{\rm o}/\partial x + ...$ such that when expanding to first order in x,

$$\hbar\omega_{\rm o}(\hat{x})\hat{a}^\dagger\hat{a} \approx \hbar(\omega_{\rm o} - G\hat{x})\hat{a}^\dagger\hat{a} \tag{2.43}$$

where $\hat{x} = x_{\rm zpf}(\hat{b}^\dagger + \hat{b})$ and $G = -\partial\omega_{\rm o}/\partial x$. The total system Hamiltonian, neglecting any input fields and coupling to the environment, is then

$$\hat{H} = \underbrace{\hbar\omega_{\rm o}\hat{a}^\dagger\hat{a} + \hbar\omega_{\rm m}\hat{b}^\dagger\hat{b}}_{\hat{H}_0} \underbrace{- \hbar g_0\hat{a}^\dagger\hat{a}(\hat{b} + \hat{b}^\dagger)}_{\hat{H}_{\rm int}} + ..., \tag{2.44}$$

where the ... represents the input field term that will be added later [18]. For convenience we can write this Hamiltonian in a frame rotating at the same frequency of our input laser, $\omega_{\rm l}$,

$$\hat{H} = -\hbar\Delta\hat{a}^\dagger\hat{a} + \hbar\omega_{\rm m}\hat{b}^\dagger\hat{b} - \hbar g_0\hat{a}^\dagger\hat{a}(\hat{b}^\dagger + \hat{b}) + \ ..., \tag{2.45}$$

where $\Delta = \omega_{\rm l} - \omega_{\rm o}$. From this point, terms such as a laser input field or environmental noise may be added to Eqn. 2.45 to model the experiment conditions. When examining $\hat{H}_{\rm int}$ we see that the photon-phonon interaction is nonlinear due to the $\hat{a}^\dagger\hat{a}\hat{b}^\dagger$ and $\hat{a}^\dagger\hat{a}\hat{b}$ terms which are cubic in the creation and annihilation operators. This leads to coupled equations of motion as calculated from the Heisenberg equations of motion. To make the equations of motion more tractable we can linearize this Hamiltonian about an average coherent cavity amplitude, $\bar{\alpha} = \sqrt{N}$, where N is the average cavity photon number, and focus on small fluctuations in cavity amplitude, $\delta\hat{a}$ by substituting $\hat{a} = \bar{\alpha} + \delta\hat{a}$ into Eqn. 2.45. This linearization is

valid for the large majority of optomechanical systems that have been demonstrated to date, but relies on the assumption that the fluctuations are small compared to the average cavity amplitude ($\delta\hat{a} \ll \bar{\alpha}$). However, if $\delta\hat{a} > \bar{\alpha}$, this assumption does not hold, which is the case for optomechanical cavities driven into the large amplitude or self-oscillation regime [4, 18, 106]. Recent work has even demonstrated an optomechanical cavity that exhibits $\delta\hat{a} > \bar{\alpha}$ from thermally driven oscillations alone [107].

Pressing on with the linearized Hamiltonian we note that expanding $\hat{a}^\dagger\hat{a}$ will give the following terms

$$\hat{a}^\dagger\hat{a} = |\bar{\alpha}|^2 + \bar{\alpha}(\delta\hat{a}^\dagger + \delta\hat{a}) + \delta\hat{a}^\dagger\delta\hat{a}. \tag{2.46}$$

The first term is indicative of an average radiation pressure force which may be neglected by shifting the origin of the mechanical oscillator's displacement [18]. As the third term is an order smaller in $|\bar{\alpha}|$ we neglect it and keep only the second term, resulting in the linearized Hamiltonian

$$\hat{H} = -\hbar\Delta\delta\hat{a}^\dagger\delta\hat{a} + \hbar\omega_{\mathrm{m}}\hat{b}^\dagger\hat{b} - \hbar g(\delta\hat{a}^\dagger + \delta\hat{a})(\hat{b} + \hat{b}^\dagger) + \ ..., \tag{2.47}$$

where $g = g_0\sqrt{N}$ is referred to as the photon-assisted optomechanical coupling rate. Although the optical and mechanical resonators have vastly disparate frequencies, (THz vs. GHz, respectively) by examining Eqn. 2.47 we see that the optical field fluctuations ($\delta\hat{a}$) couple to the mechanics, where the frequency of the optical field fluctuations ($\delta\hat{a}, \delta\hat{a}^\dagger$) are comparable to ω_{m}. As a quick digression we can examine the form of the Hamiltonian for red and blue laser detunings by moving into the interaction picture via the unitary $\hat{U} = e^{i\hat{H}_0 t/\hbar} = e^{-i(\Delta\delta\hat{a}^\dagger\delta\hat{a} - \omega_{\mathrm{m}}\hat{b}^\dagger\hat{b}t)}$, where $\hat{H}_0 = -\hbar\Delta\delta\hat{a}^\dagger\delta\hat{a} + \hbar\omega_{\mathrm{m}}\hat{b}^\dagger\hat{b}$. Then

$$\hat{H}_{\mathrm{int}} = -g(\delta\hat{a}^\dagger e^{-i\Delta t} + \delta\hat{a}e^{i\Delta t})(\hat{b}e^{-i\omega_{\mathrm{m}}t} + \hat{b}^\dagger e^{i\omega_{\mathrm{m}}t}), \tag{2.48}$$

which can be simplified depending on the laser detuning, Δ via the rotating wave approxi-

mation. Moving back out of the interaction picture, for $\Delta = -\omega_{\rm m}$ we find

$$\hat{H}_{\rm int} \approx -\hbar g(\delta\hat{a}^{\dagger}\hat{b} + \delta\hat{a}\hat{b}^{\dagger}), \tag{2.49}$$

which has the form of a beamsplitter Hamiltonian, and enables swapping quanta between photons and phonons in the system [18]. For $\Delta = \omega_{\rm m}$ we find

$$\hat{H}_{\rm int} \approx -\hbar g(\delta\hat{a}\hat{b} + \delta\hat{a^{\dagger}}\hat{b}^{\dagger}), \tag{2.50}$$

which has the form of a 'two-mode squeezing' interaction that allows for parametric amplification of the mechanical mode and driven optical mode, and entanglement of the optical and mechanical mode [18].

Utilizing input-output theory [18] the equations of motion for the linearized optomechanical cavity may be written as

$$\dot{\delta\hat{a}} = \left(i\Delta - \frac{\kappa}{2}\right)\delta\hat{a} + ig(\hat{b} + \hat{b}^{\dagger}) + \sqrt{\kappa_{\rm ex}}\delta\hat{a}_{\rm in}(t) + \sqrt{\kappa_{\rm i}}\hat{f}_{\rm in}(t), \tag{2.51}$$

$$\dot{\hat{b}} = \left(-i\omega_{\rm m} - \frac{\Gamma_{\rm m}}{2}\right)\hat{b} + ig(\delta\hat{a}^{\dagger} + \delta\hat{a}) + \sqrt{\Gamma_{\rm m}}\hat{b}_{\rm in}(t). \tag{2.52}$$

These equations of motion have the form of quantum Langevin equations which include input optical and mechanical fluctuation terms ($\hat{f}_{\rm in}(t), \hat{b}_{\rm in}(t)$). For the optical frequencies studied here we ignore $\hat{f}_{\rm in}(t)$ due to the low thermal occupation of the optical mode, however, the thermal occupation of the mechanical mode is significant ($n_{\rm th} \sim k_B T/\hbar\omega_{\rm m}$).

One method of solving for the dynamical optomechanical backaction is to first write Eqn. 2.51 and Eqn. 2.52 in frequency space by taking the Fourier Transform of both sides:

$$-i\omega\delta\hat{a}[\omega] = \left(i\Delta - \frac{\kappa}{2}\right)\delta\hat{a}[\omega] + ig(\hat{b}[\omega] + \hat{b}^{\dagger}[\omega]) + \sqrt{\kappa_{\mathrm{ex}}}\delta\hat{a}_{\mathrm{in}}[\omega], \tag{2.53}$$

$$-i\omega\hat{b}[\omega] = \left(-i\omega_{\mathrm{m}} - \frac{\Gamma_{\mathrm{m}}}{2}\right)\hat{b}[\omega] + ig(\delta\hat{a}^{\dagger}[\omega] + \delta\hat{a}[\omega]) + \sqrt{\Gamma_{\mathrm{m}}}\hat{b}_{\mathrm{in}}[\omega]. \tag{2.54}$$

To solve for the backaction effects of the mechanics on the optical cavity fluctuations we can ignore the $\delta\hat{a}_{\mathrm{in}}[\omega]$ input fluctuation term and solve for $\delta\hat{a}[\omega]$ and $\delta\hat{a}^{\dagger}[\omega]$ in terms of $\hat{b}$, taking care that $(\delta\hat{a})^{\dagger}[\omega] = (\delta\hat{a}[-\omega])^{\dagger}$:

$$\delta\hat{a}[\omega] = \frac{ig(\hat{b}[\omega] + \hat{b}^{\dagger}[\omega])}{-i(\Delta + \omega) + \kappa/2}, \tag{2.55}$$

$$\delta\hat{a}^{\dagger}[\omega] = \frac{-ig(\hat{b}[\omega] + \hat{b}^{\dagger}[\omega])}{i(\Delta - \omega) + \kappa/2}. \tag{2.56}$$

Subbing Eqns. 2.55 and 2.56 into Eqn. 2.54 allows us to write

$$-i\omega\hat{b}[\omega] = -i\omega_{\mathrm{m}}\hat{b}[\omega] - \frac{\Gamma_{\mathrm{m}}}{2}\hat{b}[\omega] + ig\left(\frac{ig(\hat{b}[\omega] + \hat{b}^{\dagger}[\omega])}{-i(\Delta + \omega) + \kappa/2} - \frac{ig(\hat{b}[\omega] + \hat{b}^{\dagger}[\omega])}{i(\Delta - \omega) + \kappa/2}\right) + \sqrt{\Gamma_{\mathrm{m}}}\hat{b}_{\mathrm{in}}[\omega]. \tag{2.57}$$

We can then set the $\hat{b}^{\dagger}[\omega]$ terms to zero via the rotating wave approximation, as they will oscillate at 2ω in a frame rotating with $\hat{b}[\omega]$, and identify the imaginary and real parts of the optomechanical coupling contribution such that

$$-i\omega\hat{b}[\omega] = -i\left(\omega_{\mathrm{m}} + \delta\omega_{\mathrm{m}}\right)\hat{b}[\omega] - \left(\frac{\Gamma_{\mathrm{m}}}{2} + \frac{\Gamma_{\mathrm{opt}}}{2}\right)\hat{b}[\omega] + \sqrt{\Gamma_{\mathrm{m}}}\hat{b}_{\mathrm{in}}[\omega], \tag{2.58}$$

or

$$\left(\chi_{\mathrm{m}}^{-1}+\underbrace{|g|^2\left(\frac{1}{-i(\Delta+\omega)+\kappa/2}-\frac{1}{i(\Delta-\omega)+\kappa/2}\right)}_{\Sigma[\omega]}\right)\hat{b}[\omega]=\sqrt{\Gamma_{\mathrm{m}}}\hat{b}_{\mathrm{in}}[\omega]. \tag{2.59}$$

where the bare mechanical response is defined as $\chi_{\mathrm{m}}^{-1}(\omega)=[i(\omega_{\mathrm{m}}-\omega)+\Gamma_{\mathrm{m}}/2]$ in the context of linear response theory, and the term in the bracket describes the added optomechanical response, defined as $\Sigma[\omega]$. From here, the optomechanical modifications to the mechanical decay rate and frequency can be computed as $\Gamma_{\mathrm{opt}}(\Delta)=2\mathrm{Re}(\Sigma(\omega))$ and $\delta\omega_{\mathrm{m}}(\Delta)=\mathrm{Im}(\Sigma(\omega))$, respectively. For the weak coupling regime, $g\ll\kappa$, as is the case for all of the studies in this work, it is sufficient to evaluate these expressions at the original mechanical frequency, ω_{m}, such that the perturbed mechanical resonance is shifted in frequency and linewidth, but still a Lorentzian. For the strong coupling regime, $g\gg\kappa$ this is not the case, where for sufficient g, normal mode splitting may be observed. The modification to the mechanical damping rate and frequency are then determined by the real and imaginary parts of $\Sigma[\omega]$, respectively:

$$\delta\omega_{\mathrm{m}}(\Delta)=\mathrm{Im}(\Sigma(\omega_{\mathrm{m}}))=g^2\left[\frac{\Delta+\omega_{\mathrm{m}}}{(\Delta+\omega_{\mathrm{m}})^2+\kappa^2/4}+\frac{\Delta-\omega_{\mathrm{m}}}{(\Delta-\omega_{\mathrm{m}})^2+\kappa^2/4}\right], \tag{2.60}$$

$$\Gamma_{\mathrm{opt}}(\Delta)=2\mathrm{Re}(\Sigma(\omega_{\mathrm{m}}))=g^2\left[\frac{\kappa}{(\Delta+\omega_{\mathrm{m}})^2+\kappa^2/4}-\frac{\kappa}{(\Delta-\omega_{\mathrm{m}})^2+\kappa^2/4}\right]. \tag{2.61}$$

Equations 2.60 and 2.61 will be used throughout this thesis primarily as a method for measuring the optomechanical coupling rate, g_0. This method relies on careful calibration of N as a function of Δ as well as the high quality measurements of κ and ω_{m}.

2.4.3 Power spectral density

In a typical measurement the dynamics of our cavity optomechanical system is measured by monitoring the optomechanically transduced mechanical motion of the microdisk. As mentioned above, fluctuations in cavity resonance frequency can be transduced to amplitude fluctuations in the output transmission of the fiber taper waveguide which can then be detected using a high speed photodetector. The radiofrequency (RF) output of the photodetector can be analyzed in either the time or frequency domain depending on the measurement. In most of the measurements presented in this thesis this analysis is performed in the frequency domain.

The standard method to analyze this data in the frequency domain is via a power spectral density (PSD) formalism which describes the power of a signal distributed across a frequency domain [108, 109]. The two sided power spectral density, $P_{xx}(\omega)$ of a continuous stationary and real function $x(t)$ is given by the Fourier transform of the autocorrelation function $R_{xx}(t)$ according to the Weiner-Kichner theorem

$$P_{xx}(\omega) = \int_{-\infty}^{\infty} R_{xx}(t) e^{i\omega t} dt, \tag{2.62}$$

where $R_{xx}(t)$ can also be computed as the inverse Fourier transform of $P_{xx}(\omega)$

$$R_{xx}(t) = \frac{1}{2\pi} \int_{-\infty}^{\infty} P_{xx}(\omega) e^{-i\omega t} d\omega, \tag{2.63}$$

and $R_{xx}(t)$ is defined as

$$R_{xx}(t) \equiv \lim_{T\to\infty} \frac{1}{T} \int_{0}^{T} x(\tau) x(\tau + t) d\tau. \tag{2.64}$$

Here P_{xx} is defined from negative to positive frequencies and to get the total power of the signal it must be integrated across this entire domain according to Parseval's theorem. By taking $t = 0$ in Eqn. 2.64 we obtain the time averaged value of $[x(t)]^2$ [108], provided that

we sample the motion for $T \gg 2\pi/\omega_{\rm m}$:

$$\langle x^2(t)\rangle = R(0) = \frac{1}{T}\int_0^T [x(t)]^2 dt. \tag{2.65}$$

This allows us to write

$$\langle x^2(t)\rangle = R(0) = \frac{1}{2\pi}\int_{-\infty}^{\infty} P_{xx}(\omega)e^{-i\omega 0}d\omega = \frac{1}{2\pi}\int_{-\infty}^{\infty} P_{xx}(\omega)d\omega, \tag{2.66}$$

which is an important relationship as it states that the area under the power spectral density curve is equal to the time averaged mean square amplitude of $x(t)$.

As only real valued signals are considered here $P_{xx}(\omega)$ is an even function and as such it is more convenient to define a one-sided power spectral density $S_{xx}(\omega) = 2P_{xx}(\omega)$ [108], whose frequency domain covers 0 to ∞, where the total power is found by integrating over positive frequency space. This result provides us with the relationship between the mean-square amplitude and the one-sided PSD for $x(t)$, $S_{xx}(\omega)$. The connection between $S_{xx}(\omega)$ and the spectrally flat thermal driving force, $S_{FF}^{\rm th}$ is

$$S_{xx}(\omega) = |\chi_{xx}(\omega)|^2 \, S_{FF}^{\rm th}, \tag{2.67}$$

where $\chi_{xx}(\omega)$ is the mechanical susceptibility given in Eqn. 2.35. Using Eqns. 2.67 and 2.66, along with the equipartition theorem, allows us to write the PSD of thermally driven harmonic oscillator as

$$S_{xx}^{\rm th} = \frac{4k_B T\omega_{\rm m}}{Q_{\rm m} m_{\rm eff}[(\omega^2-\omega_{\rm m}^2)^2 + (\omega\Gamma_{\rm m})^2]}, \tag{2.68}$$

where T is the temperature of the surrounding environment. This expression can be useful for calibrating the displacement sensitivity of optomechanical cavities, as discussed in Chapter 3.

In the lab, a real time spectrum analyzer (RSA) is used to measure the varying voltage output of a high speed photodetector, $V(t) = V_{\rm sig} + V_{\rm n}$ where $V_{\rm sig}$ is the fluctuating signal

due to the optomechanical coupling and V_{n} are technical fluctuations due to optical and detector measurement noise [88]. The power spectral density displayed by the RSA is given by $S_{VV} = |V(\omega)|^2/\mathrm{RBW}$ where $V(\omega)$ is the Fourier transformed $V(t)$ signal, and RBW is the resolution bandwidth of the RSA. S_{VV} can be related to the mechanical resonator's displacement noise spectral density, $S_{xx}(\omega)$, by

$$S_{VV}(\omega) = \alpha^2 S_{xx}(\omega) + S^n_{VV}(\omega) \tag{2.69}$$

Where α is a term which describes how efficiently the total experimental apparatus converts the mechanical motion to the varying $V(t)$ signal that is output by the photodetector. α has units of V/m to convert the m^2/Hz units of $S_{xx}(\omega)$ to the V^2/Hz of $S_{VV}(\omega)$. In general this will depend on the optomechanical properties of the device, laser detuning, and detection efficiency of the photodetector. In our measurements $S^n_{VV}(\omega)$ is comprised of optical shot noise and detector noise. Optical shot noise is intrinsically spectrally white, spanning all frequencies with equal amplitude, and the detector noise is also taken to be independent of frequency across its operating bandwidth, for fixed operating wavelength. $S_{xx}(\omega)$ can be broken into two terms, one due to thermomechanical noise $S^{\mathrm{th}}_{xx}(\omega)$ and one due to backaction noise, $S^{\mathrm{ba}}_{xx}(\omega)$. The backaction noise $S^{\mathrm{ba}}_{xx}(\omega)$ arises from the fluctuating radiation pressure force on the mechanical oscillator and scales as $\sqrt{N}$ compared to the optical shot noise which scales as $1/\sqrt{N}$. In practice, the interplay of these two noise terms limits the minimum achievable added noise in $S_{VV}(\omega)$ [18].

2.4.4 Optomechanically induced transparency & absorption

Optomechanically induced transparency (OMIT) and absorption (OMIA) is a signature of coherent coupling between optical and mechanical resonances, and has been demonstrated in numerous cavity optomechanical systems to date [110] such as microtoroids [63], optomechanical crystals (OMC's) [111], and microdisks [61]. OMIT, which is analogous to

electromagnetically induced transparency (EIT) results in a transparency window in the optical cavity transmission for a weak prove field, in the presence of a strong control field. This effect has applications in manipulating light propagation through the cavity, ground state cooling, and metrology [110].

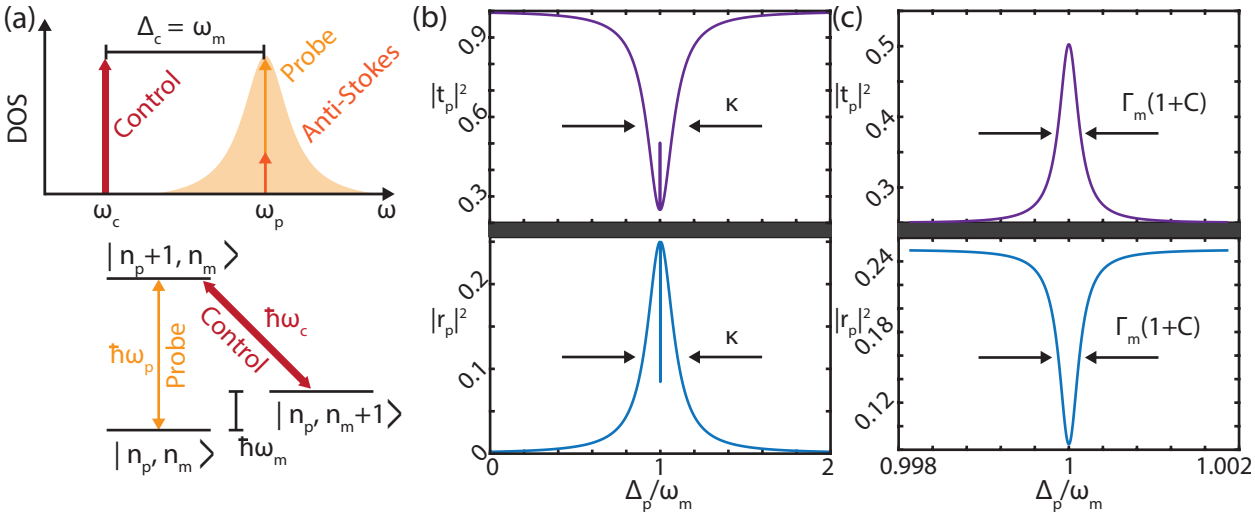

Figure 2.7: Optomechanically induced transparency. (a) Energy level scheme description where the control field with frequency ω_c may add a photon to the cavity photon number at ω_p (n_p) by annihilating a phonon of the mechanical mode (n_m). The probe field directly adds to n_p without affecting the mechanical mode. Wideband(b) and narrowband (c) probe field transmission (top) and reflection (bottom) as a function of normalized probe field detuning, Δ_p/ω_m.

OMIT occurs in the presence of a strong control field (ω_c) red-detuned from the cavity such that $\Delta_c = \omega_o - \omega_c = \omega_m$, and a weak probe field (ω_p), which is on resonance with the cavity, as shown in Fig. 2.7 (a-top). OMIT is commonly described in two ways, the first of which utilizes a scattering picture where the beat note produced by the control and probe fields induces a radiation-pressure force at ω_m. This resonantly drives the mechanics which oscillates coherently, scattering light from the control field preferentially into the anti-Stokes sideband, provided the system is sideband-resolved ($\omega_m > \kappa$). The anti-Stokes and probe field photons are at the same frequency, and destructive interference between them results in the cancellation of the intracavity field resulting in a transparency window as seen by the probe field. The second commonly used visualization of this phenomenon is by drawing analogies with electromagnetically induced transparency (EIT) to construct a

Λ-scheme energy level diagram as shown in Fig. 2.7 (a-bottom). Here n_{p} represents the number of photons or optical occupation of the cavity mode, where n_{m} is the number of phonons or mechanical occupation. In order to scatter a photon into the cavity mode when $\Delta_{\mathrm{c}} = \omega_{\mathrm{m}}$ a phonon must be annihilated ($n_{\mathrm{m}} + 1 \rightarrow n_{\mathrm{m}}$). As the probe field is on resonance with the cavity, the mechanical occupation is left un-perturbed while adding a photon to the cavity ($n_{\mathrm{p}} \rightarrow n_{\mathrm{p}} + 1$). There are two excitation pathways to reach the upper state, which under the resonant condition shown in Fig. 2.7 (a-top) results in destructive interference of the probability of absorbing a probe photon, resulting in the transparency window. This creates a transparency window (dip) in the probe transmission (reflection) spectrum when $\Delta_{\mathrm{p}} = \omega_{\mathrm{p}} - \omega_{\mathrm{c}} = \omega_{\mathrm{m}}$ (corresponding to $\omega_{\mathrm{p}} = \omega_{\mathrm{o}}$ if the control field detuning condition is ideally satisfied) as shown in Figs. 2.7 (b,c).

The detuning dependent probe field reflection $r_{\mathrm{p}}(\Delta_{\mathrm{p}})$, and transmission coefficients $t_{\mathrm{p}}(\Delta_{\mathrm{p}})$ for $\Delta_{\mathrm{c}} = \omega_{\mathrm{o}} - \omega_{\mathrm{c}} = \omega_{\mathrm{m}}$ are given by

$$t(\Delta_{\mathrm{p}}) = 1 - \frac{\kappa_{\mathrm{ex}}/2}{i(\omega_{\mathrm{m}} - \Delta_{\mathrm{p}}) + \kappa/2 + \dfrac{N g_0^2}{i(\omega_{\mathrm{m}} - \Delta_{\mathrm{p}}) + \Gamma_{\mathrm{m}}/2}}, \tag{2.70}$$

$$r(\Delta_{\mathrm{p}}) = -\frac{\kappa_{\mathrm{ex}}/2}{i(\omega_{\mathrm{m}} - \Delta_{\mathrm{p}}) + \kappa/2 + \dfrac{N g_0^2}{i(\omega_{\mathrm{m}} - \Delta_{\mathrm{p}}) + \Gamma_{\mathrm{m}}/2}}, \tag{2.71}$$

where the highlighted section of these equations describes the modification to the standard cavity Lorentzian for transmission and reflection. The derivation of these expressions is given in Appendix C. The bandwidth of the transparency window, Γ_{OMIT}, depends on the optomechanical cooperativity, C, as

$$\Gamma_{\mathrm{OMIT}} = \Gamma_{\mathrm{m}}(1 + C). \tag{2.72}$$

The depth of the OMIT dip on resonance ($\Delta_{\mathrm{c}} = \Delta_{\mathrm{p}} = \omega_{\mathrm{m}}$) is

$$t_{\rm p}|_{\Delta_{\rm c}=\Delta_{\rm p}=\omega_{\rm m}} = \frac{1-(\kappa_{\rm ex}/\kappa)+C}{1+C}, \tag{2.73}$$

which is maximized for $\kappa_{\rm ex} = \kappa$. OMIT has many applications, but will be primarily used in this work to provide an accurate measurement of the optomechanical cooperativity of the system. There some nuances in fitting the measured OMIT spectra, which are outlined in Appendix D.

Conversely, when placing the laser blue-detuned from the cavity, such that $\omega_{\rm o}-\omega_{\rm c} = -\omega_{\rm m}$ optomechanically induced absorption (OMIA) leads to amplification of light at the probe frequency. This can be thought of as constructive interference between light scattered from $\omega_{\rm c}$ to $\omega_{\rm o}$ with the on-resonance probe field. Here the maximum gain is limited by the maximum power that can be coupled into the cavity before $\Gamma_{\rm opt}+\Gamma_{\rm m} < 0$, resulting in optomechanically induced self-oscillations. The reflection and transmission coefficients for OMIA, $r_{\rm p}(\Delta_{\rm p})$, and $t_{\rm p}(\Delta_{\rm p})$ are given by

$$t(\Delta_{\rm p}) = 1 - \frac{\kappa_{\rm ex}/2}{i(-\omega_{\rm m}+\Delta_{\rm p})+\kappa/2+\dfrac{Ng_0^2}{i(\omega_{\rm m}-\Delta_{\rm p})-\Gamma_{\rm m}/2}}, \tag{2.74}$$

$$r(\Delta_{\rm p}) = -\frac{\kappa_{\rm ex}/2}{i(-\omega_{\rm m}+\Delta_{\rm p})+\kappa/2+\dfrac{Ng_0^2}{i(\omega_{\rm m}-\Delta_{\rm p})-\Gamma_{\rm m}/2}}. \tag{2.75}$$

2.4.5 Room temperature quantum optomechanics and the $Q_{\rm m}\cdot f_{\rm m}$ product

An extended goal of this research was to enable room temperature quantum optomechanics in these structures, which requires that the mechanical oscillation frequency be larger than the decoherence rate of the oscillator, $\omega_{\rm m} > \Gamma_{\rm m}\bar{n}_{\rm th}$ and that the timescale of the photon-phonon coupling, g, is greater than the timescale for one quantum of noise to enter from the environment. In general this requires that $g > \{\Gamma_{\rm m}\bar{n}_{\rm th}, \kappa\}$, although for the optical regime

studied here the temperature of the optical bath is effectively zero and the condition $g > \kappa$ can be disregarded.

The first condition ($\omega_{\mathrm{m}} > \Gamma_{\mathrm{m}}\bar{n}_{\mathrm{th}}$) can be formulated in terms of a $Q_{\mathrm{m}} \cdot f_{\mathrm{m}}$ product requirement as follows. As phonons are bosonic quasi-particles, the thermal occupation of the mechanical resonator in equilibrium is governed by the Bose-Einstein distribution with zero chemical potential [112]. This is also known as the Planck distribution, which was first described by Max Planck for black-body radiation, and gives the average phonon number in thermal equilibrium as

$$\bar{n}_{\mathrm{th}} = \frac{1}{e^{\hbar\omega_{\mathrm{m}}/k_B T} - 1}. \tag{2.76}$$

In the high temperature limit, where $k_B T \gg \hbar\omega_{\mathrm{m}}$, we can perform a Taylor series expansion of the exponential in the denominator to first order in T to find that

$$\bar{n}_{\mathrm{th}} \approx \frac{k_B T}{\hbar\omega}. \tag{2.77}$$

The quantum coherence condition is then

$$\omega_{\mathrm{m}} \gg \Gamma_{\mathrm{m}}\bar{n}_{\mathrm{th}} \approx \frac{k_B T}{\hbar Q_{\mathrm{m}}} \tag{2.78}$$

which gives the $Q_{\mathrm{m}} \cdot f_{\mathrm{m}}$ product requirement for neglecting thermal decoherence over one mechanical period as

$$Q_{\mathrm{m}} \cdot f_{\mathrm{m}} \gg \frac{k_B T}{h}. \tag{2.79}$$

As discussed in Chapter 5.4.1 the $Q_{\mathrm{m}} \cdot f_{\mathrm{m}}$ product $> 10^{13}$ Hz for the SCD microdisk structures fulfills the requirement of Equation 2.79. Unfortunately the strong coupling requirement is not met as the maximum $g/2\pi$ for these devices are on the order of tens of MHz, while at room temperature, $\Gamma_{\mathrm{m}}\bar{n}_{\mathrm{th}}/2\pi \sim 8$ GHz. However, if these devices were placed

in a dilution fridge (T = 15 mK) they could enter the quantum coherent regime.

2.5 Summary

This chapter presented an overview of the basics of cavity optomechanics in a microdisk cavity, which is the device geometry which will be studied in the remainder of this thesis. Using these tools the characteristics and performance of the devices can be studied and compared. The remainder of this thesis will focus on the fabrication, characterization and utilization of GaP and SCD microdisk optomechanical cavities for exploring coherent coupling between optical and mechanical degrees of freedom. Demonstrations of optomechanically mediated-self-oscillation, induced transparency, wavelength conversion will be presented.

Chapter 3

Gallium phosphide microdisks

3.1 Introduction

The optical revolution of the telecommunications industry was originally enabled by the development of III-V semiconductor light sources and photodetectors combined with low-loss optical fiber. III-V materials such as GaAs and InP have been instrumental in developing reliable photonic devices [113]. These innovations led to a dramatic increase in transmission throughput rates which have reached $\sim$ 10 Tb/s [114]. The development of high-quality growth techniques such as molecular beam epitaxy (MBE), and metalorganic vapour phase epitaxy [115] has enabled the fabrication and study of nanostructures in these materials. This had led to a second revolution in the photonics industry, giving rise to the field of nanophotonics which also utilizes advances in lithography techniques such as electron-beam lithography (EBL) to fabricate structures capable of confining light at to dimensions on the order its wavelength.

The field of cavity optomechanics has taken advantage of these innovations, enabling the fabrication of systems in semiconductors, such as Si [29, 116], SiN [58, 60, 61], SiO_2 [45, 62, 63, 64] and III-V semiconductors such as GaAs [117], InGaP [66], AlGaAs [66], GaP [1, 67, 118, 119, 120], and AlN [68], that allow tight optical confinement and large g_0 due to

the large refractive index contrast achievable. However, in some of these semiconductor-based large-g_0 devices, N is clamped by two-photon absorption [54, 55], which limits the maximum achievable optomechanical cooperativity, C. As discussed previously, the goal of this work was to develop optomechanical cavities capable of circumventing this problem by fabricating structures out of high refractive index materials which do not exhibit nonlinear optical loss at commonly used telecommunications wavelengths. This would enable increasing C (above, for example, the value of $C \sim 20$ demonstrated in optomechanical crystals [52]), and would enable improved bandwidth of coherent wavelength conversion [44], observation of normal mode splitting [53], and faster optomechanical cooling [29].

In this chapter, the fabrication and study of gallium phosphide (GaP) microdisk optomechanical cavities is presented. GaP is a semiconductor with a desirable combination of high refractive index ($n_{\mathrm{GaP}} \sim 3.05$ at 1550 nm) and large electronic bandgap (2.26 eV); it is therefore optically transparent from 550 nm to IR wavelengths and has low two-photon absorption at 1550 nm. Compared to other materials with similar transparency windows used in cavity optomechanics, such as SiO_2 ($n_{\mathrm{SiO_2}} = 1.45$) [45, 62, 63, 64], Si_3N_4 ($n_{\mathrm{Si_3N_4}} = 2.0$–$2.2$) [58, 60, 61] and AlN ($n_{\mathrm{AlN}} = 2.0$–$2.2$) [68], GaP has a larger refractive index, enabling the fabrication of optical nanocavities with ultra-small mode volumes [118, 119, 67, 120]. As such, GaP is a promising material for realizing cavity optomechanical systems with $g_0/2\pi$ approaching 1 MHz, as observed in Si and GaAs devices [52, 116, 117, 121, 122]. As GaP is a non-centrosymmetric crystal it can also display piezoelectricity which can be taken advantage of to directly drive mechanical motion in nanophotonic structures. This technique has been utilized in AlN structures to demonstrate coupling between microwave and optical photons [123, 124, 125] and deep phase modulation [126]. In this chapter, we show that GaP microcavities combine high optical quality factor $Q_{\mathrm{i}} \sim 2.8 \times 10^5$, large optomechanical coupling $g_0/2\pi > 30$ kHz, and no observed two-photon absorption at 1550 nm band wavelengths. These properties allow the devices to operate close to the resolved-sideband regime with sufficient C to allow observation of the optical spring effect.

3.2 GaP microdisk fabrication

The microdisks studied here were fabricated using the tools and equipment listed in Appendix F from an epitaxially grown wafer (supplied by IQE) consisting of a 250-nm-thick GaP device layer supported by a 750-nm-thick sacrificial aluminum gallium phosphide (AlGaP) layer and a GaP substrate, the process of which is outlined in Fig. 3.1. Before fabrication a $\sim 5 \times 5$ mm piece of the wafer was cleaved from a larger wafer and cleaned for 60 s in 30 mL of isopropyl alcohol (IPA) followed by a 3 $\times$ 30 s rinse in 30 mL of deionized (DI) water, and dried with N_2. Normally, more aggressive acid pre-cleaning steps such as piranha (3:1 mixture of H_2SO_4:H_2O_2) are used for silicon on insulator (SOI) or diamond materials, however, piranha etches GaP.

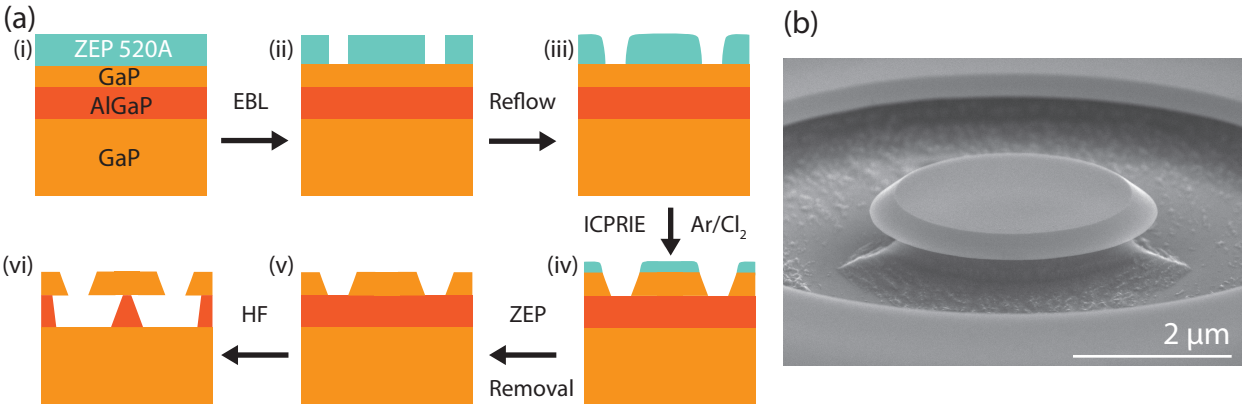

Figure 3.1: (a) Fabrication process for GaP microdisks as described in the text. (i) The sample is cleaned in IPA and dried with N_2 before spinning a $\sim$ 300 nm layer of ZEP EBL resist. (ii) The pattern is defined via EBL and developed in ZED-N50 at -15 ° C. (iii) Resist reflow is performed to reduce sidewall roughness. (iv) ICPRIE with Ar/Cl_2 chemistry is used to transfer the pattern to the GaP device layer. (v) The ZEP is removed before undercutting via UV exposure and heated Remover PG. (vi) Finally the microdisks are undercut using 49% HF, followed by an H_2O rinse and N_2 dry. (b) Example of reflowed microdisk with a sidewall angle of $\sim 54°$, as measured from the horizontal for the nominal reflow parameters of 165° C for 5 min in an oven.

The microdisk patterns were defined using electron-beam lithography (EBL), where the pattern to be written was coded using the Matlab toolbox developed by Aaron Hryciw [127]. A $\sim$ 300 nm layer of positive tone EBL resist (ZEP520A) was spun on the chip, followed by cleaning the back of the chip with acetone to remove any resist residue before baking it at 180 °C for 5 minutes on a covered hotplate (Fig. 3.1(a-i)). The purpose of the pre-bake step

is to minimize remaining solvent concentration in the resist. Exposure of the pattern was performed with an EBL accelerating voltage of 30 keV and beam aperture of 30 μm with a dose factor of 4×80 μC/cm^2 for the ring defining the disk. For a pattern consisting of 200 microdisks ranging in diameter from 6 μm – 8 μm the exposure time was $\sim$ 1 hour, with alignment, focusing and loading/unloading time ranging from 1 to 2 hours. Immediately after unloading the sample, the pattern was developed in 15 mL of ZED-N50 at -15 °C for 20 s followed by 15 mL of IPA at -15 °C for 20 s, and dried with N_2 (Fig. 3.1(a-ii)). The resist was then reflowed by baking the chip in an oven at 165 °C for 5 min, as illustrated in Fig. 3.1(a-iii) and Fig. 3.2. This step decreases imperfections in the circular electron-beam resist pattern, resulting in smoother sidewalls and an increased Q_o [128].

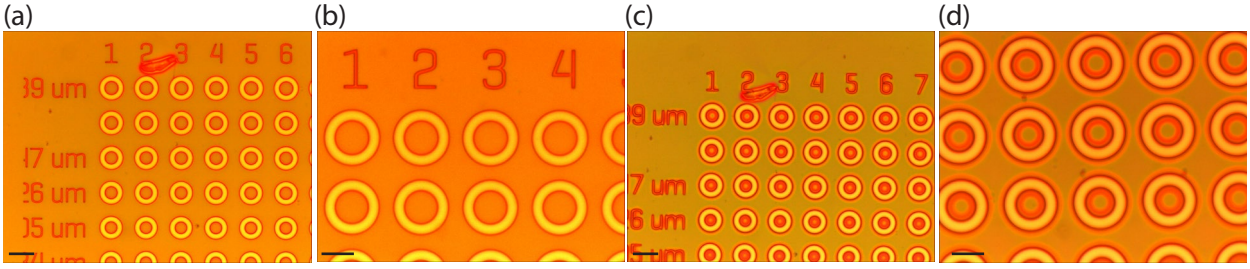

Figure 3.2: Optical micrographs comparing EBL resist post-development (a,b) and post-reflow(c,d). Scales bars are 16 μm (a,c) and 8 μm (c,d).

The resulting pattern was transferred into the GaP layer using inductively coupled reactive ion etching (ICP-RIE) with an Oxford PlasmaLab 100 system. ICP-RIE utilizes separate RF coils to control plasma density and ion acceleration which allows for low damage reactive ion etching of a wide variety of materials. Before carrying out the GaP etch the chamber was cleaned using an O_2/SF_6 etch for as long as the tool availability allowed (usually 1–2 hrs), where the etch parameters are given in Table 3.1. For etching the GaP layer, an Ar/Cl_2 etch chemistry was used with etch parameters given in Table 3.2, illustrated in Fig. 3.1(a-iv). A 10 min conditioning etch with a blank Si carrier wafer was first performed using the etch parameters in Table 3.2, followed by a 1 min 30 s etch of the sample. Here the sample is mounted to the Si carrier with a small spot of vacuum grease to ensure good

T [°C]	Pressure [mTorr]	RF [W]	Bias [V]	ICP [W]	O_2 [sccm]	SF_6 [sccm]
15	50	100	450	2000	100	10

Table 3.1: Nominal etch parameters used for cleaning the Oxford Plasma Lab Pro 100 ICP-RIE chamber prior to etching the GaP sample.

thermal contact to the carrier and so the chip does not move during the etch. The reflowed nature of the mask results in an angled GaP sidewall etch profile during this step, as seen in Fig. 3.1(b). In practice, for nominally identical reflow temperature and duration some variation in sidewall angle was observed. This could be due to variation in oven temperature and loading/unloading time and or remaining solvent in the EBL resist [94]. This angle is not expected to limit Q_i in these devices, as microdisks with similar profiles [128, 129] have been reported with $Q_\mathrm{i} > 10^6$ in other material systems. The resist was then removed with a 10 min deep-UV exposure (1.24 mW/cm^2 at 254 nm) to break up the polymer chains in the ZEP520A, followed by a 5 min soak in 30 mL of Remover PG, and subsequent rinsing in 30 mL of acetone, isopropyl alcohol, and 3 × de-ionized water for 30 s each. Finally, the microdisks were undercut by selectively removing the AlGaP layer using a hydrofluoric acid wet etch (H_2O: 49% HF = 3:1)[1]. As the size of microdisks being fabricated varied from sample to sample this was usually performed iteratively. Typically the microdisks were undercut for ∼ 30 s in the HF, followed by a 3 × 30 s rinse in DI water and drying with N_2 before examination under an optical microscope, as shown in Fig. 3.3. This process was repeated until the smallest disks were completely undercut, such that the remaining microdisk pedestals were as small as possible. In practice the N_2 drying step can cause the disks with the smallest pedestals to break, which could be avoided by using critical point drying to avoid the turbulence created by the N_2 gun used here.

After four iterations of fabrication, GaP microdisk cavities with sufficient optical and mechanical Q to observe optomechanical coupling were obtained. The main improvements made over these iterations were the resist reflow and deep-UV cleaning procedure steps,

[1]Disclaimer: Hydrofluoric acid (HF) should be treated with care as it is a corrosive acid that can cause extensive tissue damage and death. See Appendix G for handling precautions.

T [°C]	Pressure [mTorr]	RF [W]	Bias [V]	ICP [W]	Ar [sccm]	Cl_2 [sccm]
15	2.1	20	103	550	12	3

Table 3.2: Nominal etch parameters used for patterning the GaP microdisks with the Oxford Plasma Lab Pro 100. This results in an etch rate of ~ 3 nm/s for GaP material used here.

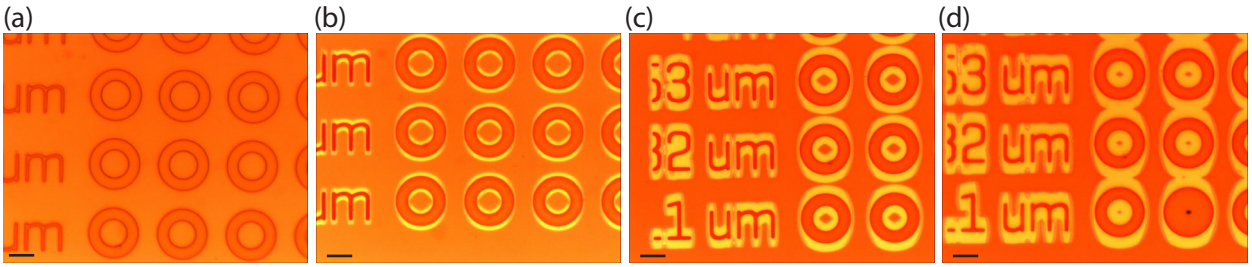

Figure 3.3: Optical micrographs comparing pedestal area as a function of undercut time. Microdisk pattern after (a) 0 s (b) 180 s, (c) 360 s, (d) 480 s where the scale bars are 8 μm.

which enabled high optical Q_o. Here we focused on microdisks with radius, R, as small as possible, that avoided radiation loss limitations to Q_i to increase the optomechanical coupling as much as possible, as $G \propto 1/R$.

3.3 Optical properties

The optomechanical properties of a microdisk similar to that shown in Fig. 3.4(a) were probed using a dimpled optical fiber taper [86] to evanescently couple light into and out of the cavity. The dimpled fiber taper was fabricated by modifying the process of Michael *et al.* [86] to use a ceramic edge as the dimple mold. The resulting dimple can be positioned within the optical near field of the microdisk, as shown in Fig. 3.5(b). Two tunable laser sources were used to measure the transmission of the fiber taper over the 1520–1625 nm wavelength range. A complete list of the equipment used in the following measurements is given in Appendix F. The transmitted signal was split using a 10:90 fiber coupler, detected using low- and high-speed photodetectors, and recorded using a data acquisition card and a real-time spectrum analyser (RSA).

The optical response of a typical microdisk as a function of input wavelength, as shown

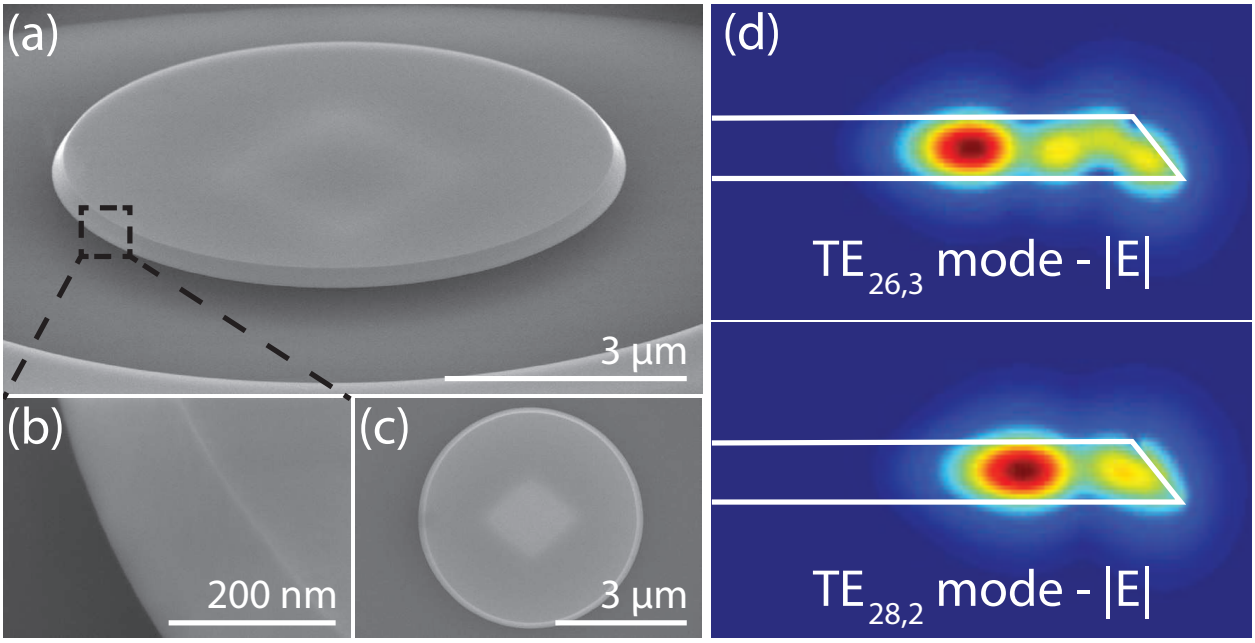

Figure 3.4: (a–c) Scanning electron micrographs of a GaP microdisk resonator with a close up of the disk sidewall. (d) Electric field distributions of the second ($n = 2$) and third ($n = 3$) radial order $\mathrm{TE}_{m,n}$ microdisk modes, where m represents the azimuthal mode index and is chosen such that the mode wavelength is near 1550 nm.

in Fig. 3.5(a-c), is observed when the fiber taper dimple is positioned in the microdisk near field (Fig. 3.5(b)), consists of numerous resonances corresponding to excitation of high-Q_i whispering-gallery modes (WGMs) of the microdisk. The modal indices of each resonance, describing their azimuthal (m) and radial (n) order, were determined from comparisons of the measured Q_i and mode spacing with the mode spectrum predicted by finite-difference time-domain (FDTD) simulations [81] of the device. Note that this identification of azimuthal mode number should be considered approximate as our simulations used the nominal refractive index of GaP, and do not take into account perturbations to the refractive index from material impurities. For the device geometry used here, only TE-like modes (electric field dominantly radially polarized) with fundamental vertical field profile have sufficiently high Q_i to be observed. Figure 3.5(c) displays the optical response of the highest-Q_i mode observed in the fabricated GaP microdisks, which has $Q_\mathrm{i}^\mathrm{s} \sim 2.8 \times 10^5$ with minimal fiber loading. These are the highest optical quality factors observed to date in GaP nanophotonic

devices. A mechanism limiting $Q_i < 10^6$ in these disks is the pedestal height (750 nm), which is determined by the thickness of the AlGaP layer. The choice of AlGaP layer thickness was determined by material availability, and should be further optimized in future devices. The doublet resonance structure is a result of scattering and modal coupling from imperfections in the microdisk, and indicates that the observed modes are standing waves [77]. Based on the comparisons with simulations, this mode is predicted to have modal indices $[m, n] = [28, 2]$, field profile shown in Fig. 3.4(d), and standing-wave mode volume $V = 9.7(\frac{\lambda}{n_{GaP}})^3$.

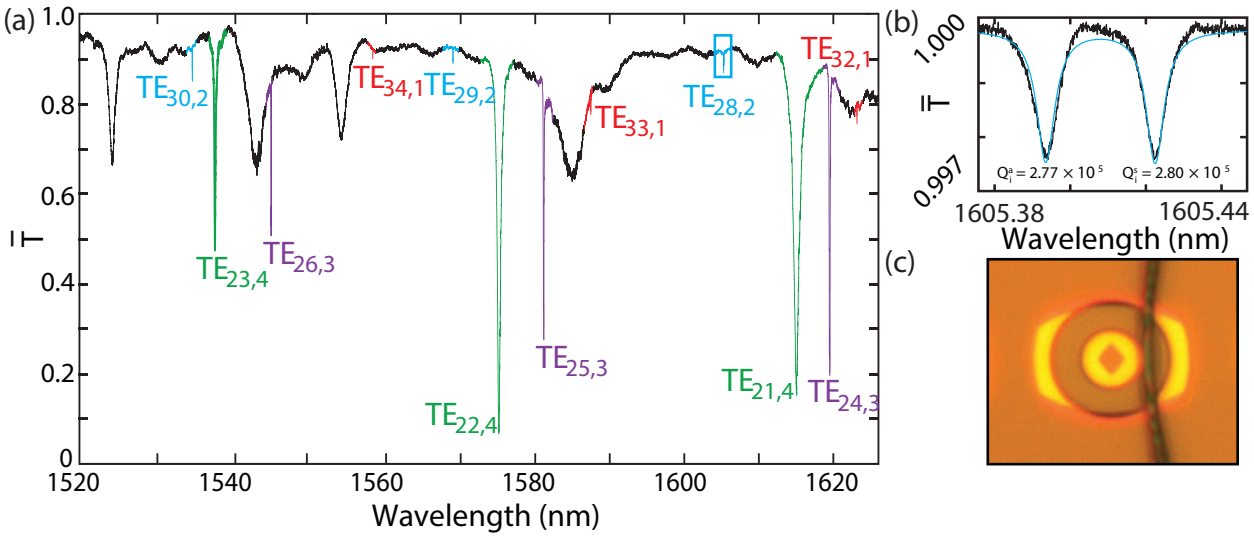

Figure 3.5: Fiber taper transmission spectrum of a GaP microdisk with a radius of 4 μm, normalized by the fiber taper transmission when it is positioned far from the microdisk. Modes with common free spectral range are color coded and labeled as $TE_{m,n}$, with azimuthal and radial mode indices m and n, respectively. Inset-left, microscope image of dimpled fiber taper side-coupled to microdisk. Inset-right, narrow-wavelength scan of a high-Q_i mode, associated with the $[m, n]$ = 28,2 mode indices.

3.4 Nonlinear absorption

To probe for nonlinear optical absorption in these microdisks, we measured their response as a function of fiber taper input power, P_{in}. Figure 3.6(a) shows the fiber taper transmission for varying P_{in} when the source laser is scanned with increasing wavelength across the $TE_{30,2}$ microdisk resonance. Although a power-dependent optical response is clearly observed, its behavior is indicative of a decrease in the internal optical loss of the microdisk, κ_i, with

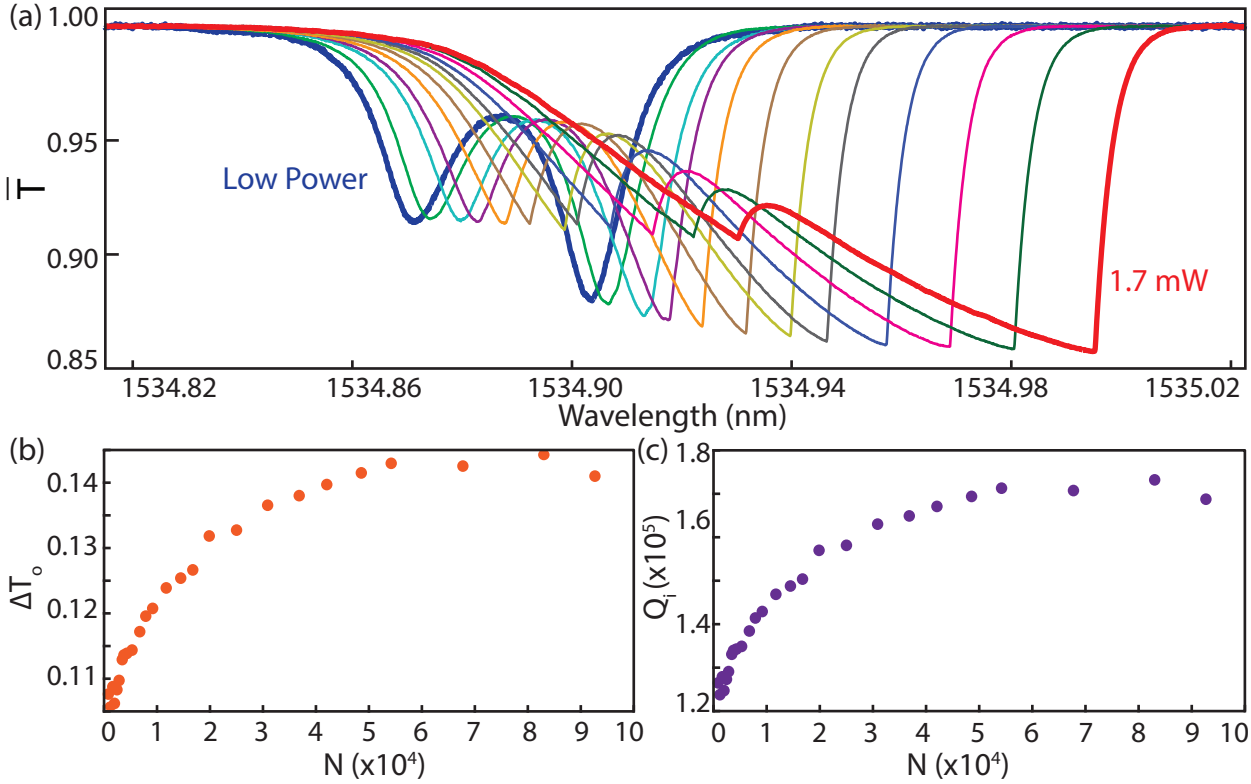

Figure 3.6: (a) Optical response of the $TE_{30,2}$ mode, measured for varying input power P_{in}. (b) Measured resonance contrast ΔT_o, and (c) increase of intrinsic optical quality factor Q_{i}, as a function of intracavity photon number N, for the $TE_{34,1}$ mode.

increasing P_{in}. This anomalous effect is illustrated in Fig. 3.6(b) for the $TE_{34,1}$ mode, which shows that the resonance contrast, $\Delta T_o = 4K/(1+K)^2$, increases with P_{in}, where $K = \kappa_{\text{ex}}/2/(\kappa_{\text{ex}}/2 + \kappa_{\text{i}}(P_{\text{in}}))$, and κ_{ex} is the total coupling rate between the microdisk standing wave mode and the fiber taper mode (i.e., $\kappa = \kappa_{\text{i}} + \kappa_{\text{ex}}$), which is measured at low input power. The increase of $\sim 40\%$ in Q_{i} observed is contrary to the behavior of cavities exhibiting multiphoton absorption, such as those fabricated from Si [54]. Note that this increase is higher than what was originally reported in Ref. [1] as an error in the analysis was detected. Figure 3.6(c) shows the corresponding increase of Q_{i} as a function of N, calculated according to:

$$\hbar\omega_{\text{cav}} N = \Delta T_o P_{\text{in}} \frac{Q_{\text{i}}}{\omega_{\text{cav}}}. \tag{3.1}$$

This effect may be the result of saturable absorbers in the microcavity, possibly in the form of O_2-related impurities [130, 131], and could be investigated in the future by probing the

transmission response at various wavelengths. A redshift in the cavity resonance wavelength λ_o, is also observed with increasing P_{in}. This dispersive effect is the result of heating of the microcavity due to optical absorption, and can be suppressed by operating at lower temperatures [61].

3.5 Cavity optomechanics

To study the optomechanical properties of the microdisks, the effect of the thermal motion of the microdisk mechanical modes on the noise spectrum of the optical power transmitted through the fiber taper was measured. The dimensions of the microdisks were chosen to maximize g_0 and ω_m, of the fundamental radial breathing mode (RBM), without compromising Q_i. The 4 μm radius of the microdisks studied here is small enough to enable a RBM with high frequency, $\omega_m/2\pi \sim 0.5$ GHz, and large enough to avoid optical radiation loss at a rate above other loss mechanisms of the microdisk. A typical spectrum, obtained in ambient conditions using the $TE_{26,3}$ mode, with input laser frequency ω_l blue detuned ($\omega_l \approx \omega_o + \kappa/2$), where ω_o is the cold cavity optical resonance frequency, is given in Fig. 3.7(a). Peaks associated with three mechanical resonances are visible; of particular interest is the fundamental RBM at $\omega_m/2\pi = 488$ MHz. The RBM was found to have a mechanical zero-point fluctuation amplitude, $x_{zpf} = 0.66$ fm using the COMSOL simulated effective mass (Equation 2.33) of $m_{eff} = 40$ pg (Actual disk mass is approximately 140 pg).

The displacement sensitivity s_{xx}^{min} or measurement resolution describes the minimum detectable mechanical motion and is extracted from the measured signal to noise ratio, α^2 (see Section 2.4.3), of the thermomechanically driven peak and is given by

$$s_{xx}^{min} = \sqrt{\frac{4k_B T Q_m/(m_{eff}\omega_m^3)}{\alpha^2}} \tag{3.2}$$

where $T = 300K$ is the device temperature. Note that for this estimation to be valid the measurement must be done at low enough power to avoid significant optomechanical

back action. For the RBM this gives $s_{xx}^{\min} = 4.43 \times 10^{-17}\mathrm{m}/\sqrt{\mathrm{Hz}}$ for P_{in} of $\sim$ 600 μW. The fundamental RBM was found to have a mechanical quality factor, measured at low P_{in} to avoid optical backaction effects, of $Q_{\mathrm{m}} \sim 640$, while the $\omega_{\mathrm{m}}/2\pi = 462$ MHz and $\omega_{\mathrm{m}}/2\pi = 498$ MHz modes have $Q_{\mathrm{m}} \sim 360$ and 450, respectively. Q_{m} can be improved by engineering the device geometry and testing environment. While the RBM should not be limited by squeeze film damping, operation in vacuum could increase Q_{m} by eliminating air damping [132, 133, 134, 135]. Mechanical clamping and phonon radiation loss can be reduced by further undercutting the microdisks to create ultra-small pedestals [61, 136, 137]. Phononic Bragg mirror inspired pedestal structures as demonstrated in Ref. [137, 138] could also be used to reduce clamping losses. This would require the growth of hetero-structured wafers, which would also allow control over pedestal height, as well as provide an opportunity to reduce impurities present in the current device layer. Through a combination of these techniques a 10^2 increase in Q_{m} is reasonable.

The optomechanical coupling coefficient G and rate g_0 [18, 116] between the fundamental RBM and the various optical WGMs of the microdisk were calculated using COMSOL finite element method simulations and are given in Table 3.3. For the devices under study, $g_0/2\pi \sim$ 30 kHz and $G/2\pi \sim 50$ GHz/nm are comparable to record values for microdisks [117]. The realizable cooperativity parameter for this device can be predicted from g_0 and the measured dissipation rates, $\Gamma_{\mathrm{m}}/2\pi \sim 7.63 \times 10^5$ Hz and $\kappa/2\pi \sim 6.68 \times 10^8$ Hz, of the high-Q_{i} $\mathrm{TE}_{28,2}$ mode. These rates correspond to a single-photon cooperativity of $\sim 1.3 \times 10^{-6}$, which is on the same order of magnitude as similar WGM microcavity devices [18, 62, 64]. It is predicted that $C > 1$ for $N > 7.53 \times 10^5$ intracavity photons for the $\mathrm{TE}_{28,2}$ mode. The largest experimental C inferred was $C \sim 0.53$ for the $\mathrm{TE}_{30,2}$ mode, with $N \sim 4.15 \times 10^5$ (corresponding to ~ 700 μW of dropped power). Note that this C is not a fundamental limit of our system, as C can be enhanced in future by improving the fiber-microdisk coupling efficiency or increasing P_{in}.

The measurement noise background in Fig. 3.7 was dominated by detector noise ($\sqrt{S_{xx}^{DET}} \sim 2\times$

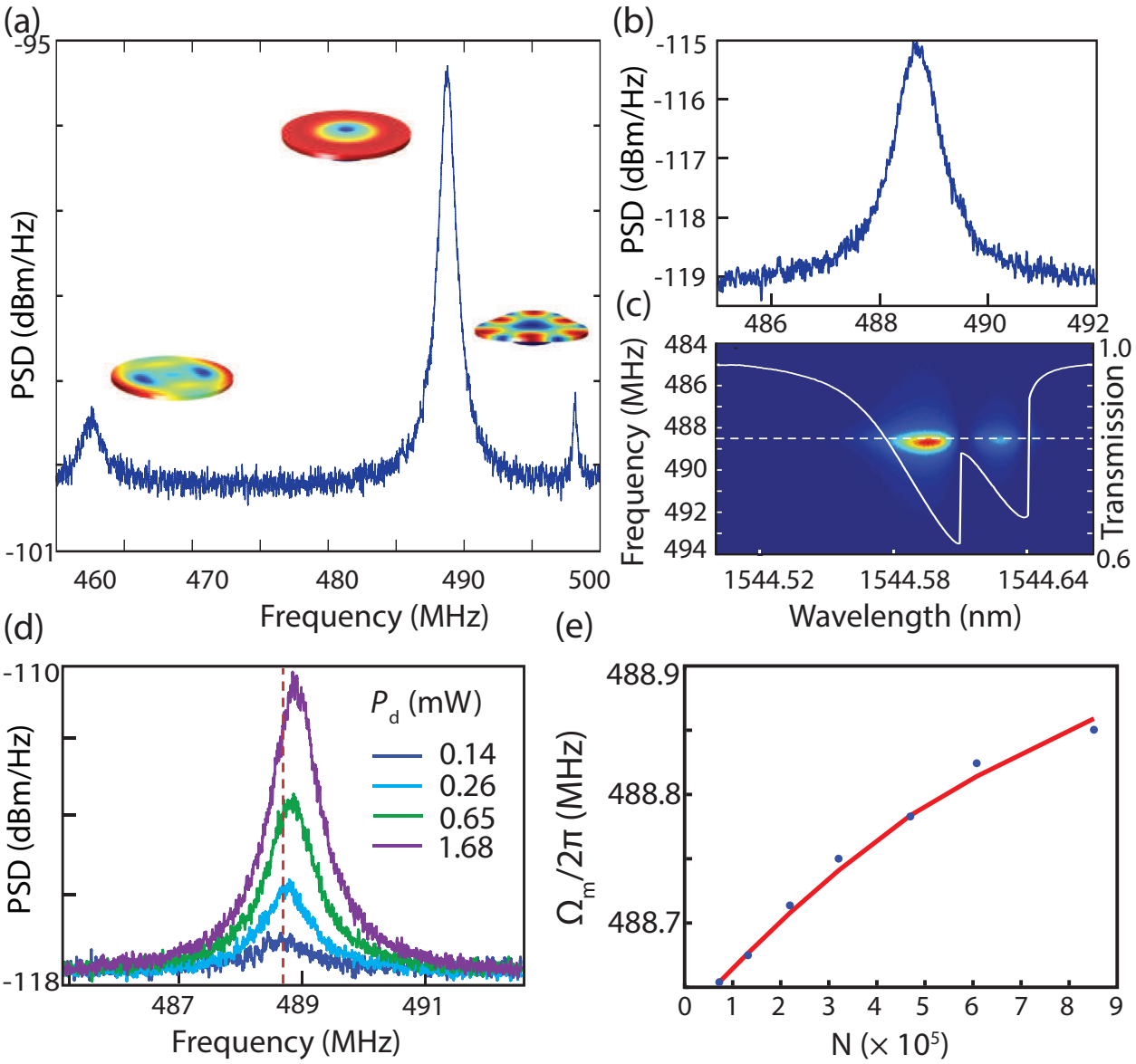

Figure 3.7: Optomechanical data for a 4 μm radius GaP microdisk. (a) Electronic power spectral density (PSD) of photodetected taper transmission when ω_l is blue detuned by $\sim \kappa/2$ from the $TE_{26,3}$ optical resonance. Simulated displacement amplitude profiles of the mechanical modes corresponding to the observed resonances in the PSD are also shown. (b) PSD of the fundamental RBM, measured for $P_{in} \sim 100$ μW. (c) Mechanical response of the RBM for varying laser wavelength for $P_{in} \sim 2.1$ mW. The corresponding transmission spectrum of the fiber taper evanescently coupled to the microdisk (white line), and low power RBM frequency (white dashed line), are also shown. (d) PSD of the fundamental RBM at four optical dropped powers when the laser was blue detuned by $\sim \kappa/2$ from ω_o. (e) Resonance frequency of the RBM as a function of intracavity photon number, when the laser was blue detuned by $\sim \kappa/2$ from ω_o. The solid red line represents predicted values from a theoretical model (see text).

10^{-17} m/$\sqrt{\text{Hz}}$), and shot noise ($\sqrt{S_{xx}^{SN}} \sim 5 \times 10^{-18}$ m/$\sqrt{\text{Hz}}$). This noise level is roughly a factor of 100 times the standard quantum limited displacement noise ($\sqrt{S_{xx}^{SQL}} = 6 \times 10^{-19}$ m/$\sqrt{\text{Hz}}$). For the current device, at higher operating P_{in}, where optomechanical backaction

Table 3.3: Simulated (FDTD) radiation-loss-limited optical quality factor for substrate-free and substrate-limited cases ($Q_{\rm rad}^{\rm free}$ and $Q_{\rm rad}^{\rm sub}$, respectively), measured intrinsic optical quality factors ($Q_{\rm i}$), and simulated optomechanical coupling parameters for fundamental RBM ($\omega_{\rm m}/2\pi = 488$ MHz), for select measured optical modes.

Mode	$Q_{\rm rad}^{\rm free}$	$Q_{\rm rad}^{\rm sub}$	$Q_{\rm i}$	$G/2\pi$ ($\frac{\rm GHz}{\rm nm}$)	$g_0/2\pi$ (kHz)
$TE_{33,1}$	$> 10^8$	1.1×10^6	2.6×10^5	48	31
$TE_{28,2}$	$> 10^8$	3.9×10^5	2.8×10^5	40	26
$TE_{25,3}$	6.0×10^7	1.4×10^5	0.9×10^5	35	23
$TE_{22,4}$	1.8×10^5	2.1×10^4	0.5×10^4	32	21

noise is equal to shot noise ($S_{xx}^{BA} = S_{xx}^{SN}$), detector noise will remain dominant. As such, detection of the RBM with SQL precision using the $TE_{26,3}$ optical mode, would require lower noise photodetection. Alternatively, using higher $Q_{\rm i}$ modes such as the $TE_{28,2}$ mode in Fig. 3.5(c), would further increase the measurement precision. However, reaching the SQL using these high-$Q_{\rm i}$ modes will not be possible without significantly improved fiber coupling efficiency, as critical coupling is a requirement for SQL measurements [18].

We further explored the optomechanical coupling by measuring the dependence of the lineshape of the fundamental RBM on N. Figure 3.7(c) illustrates the dependence of the mechanical spectrum on laser wavelength as it is swept across the $TE_{26,3}$ optical cavity resonance, at a fixed $P_{\rm in} = 2.1$ mW. As the laser approaches the cavity resonance and N increases, $\Omega_{\rm m}$ is observed to increase by up to 250 kHz. This is the result of the optical spring effect, and is further illustrated in Figs. 3.7(d) and (e), which show the effect of varying $P_{\rm in}$ for fixed $\omega_{\rm l} = \omega_{\rm o} + \kappa/2$. Note that for $P_{\rm in} \gg 200$ μW, $\omega_{\rm o}$ red-shifts due to the heating of the microdisk by the intracavity saturable absorption described above. The fit in Fig. 3.7(e) was obtained using Eqn. 2.60, taking into account the measured dependence of $\Delta\omega = \omega_{\rm l} - \omega_{\rm c}$, and ΔT_o on N. The observed power dependent shift in $\Omega_{\rm m}$ of up to 218 kHz is in good agreement with this model. We also observe mechanical damping while blue detuned from the cavity resonance, as can be observed from Fig. 3.7(d). This effect is a result of thermo-optic damping [58, 139]. For small N, the $TE_{26,3}$ mode used in these spring effect measurements had an intrinsic $Q_i \sim 6.3\times10^4$ and a resonance contrast of $\Delta T_o \sim 0.63$. From FDTD simulations, this mode is predicted to have a standing-wave mode volume of

$V = 11.1(\frac{\lambda}{n_{\mathrm{GaP}}})^3$ and the field profile shown in Fig. 3.4(d).

For optomechanical cooling of a mechanical resonator, it is desirable to be in the sideband-resolved regime [64, 136]. In our case, the optical linewidth of the highest-Q_i mode is $\kappa/2\pi \sim 668$ MHz. As shown in Table 3.3, our measured Q_i values are significantly lower than the radiation-loss-limited quality factor, $Q_\mathrm{rad}^\mathrm{sub}$, which includes leakage into the substrate. We also observe that the $\mathrm{TE}_{33,1}$ and $\mathrm{TE}_{28,2}$ modes have similar Q_i, despite the lower predicted radiation loss of the $\mathrm{TE}_{33,1}$ mode. This suggests that either material absorption or surface scattering is placing the upper limit on Q_i for these devices. The sideband-resolved regime may be attainable through further optimization of Q_i by fabricating devices from wafers with a thicker sacrificial AlGaP layer and lower GaP linear absorption, and with reduced surface roughness.

3.6 Optomechanically induced transparency & absorption

As discussed in Section 2.4.4, OMIT and OMIA is a signature of coherent coupling between optical and mechanical resonances, and has been demonstrated in cavity optomechanical systems such as microtoroids [63], optomechanical crystals (OMC's) [111], and microdisks [61]. OMIT occurs when a strong control field (ω_c) is red–detuned from the microdisk such that $\Delta_\mathrm{c} = \omega_\mathrm{o} - \omega_\mathrm{c} = \omega_\mathrm{m}$, resulting in destructive interference between anti-Stokes photons scattered from the control field and a weak probe field (ω_p). This creates a transparency window (dip) in the probe transmission (reflection) spectrum when $\Delta_\mathrm{p} = \omega_\mathrm{p} - \omega_\mathrm{c} = \omega_\mathrm{m}$ (corresponding to $\omega_\mathrm{p} = \omega_\mathrm{o}$ if the control field detuning condition is ideally satisfied) whose amplitude and width depends on the cooperativity [18, 63, 111].

By traveling to Kartik Srinivasan's lab at NIST-Gaithersburg, we were able to measure both OMIT and OMIA in GaP microdisks similar to those studied above. Marcelo Davanço was an invaluable source of knowledge there, and guided me through this measurement using

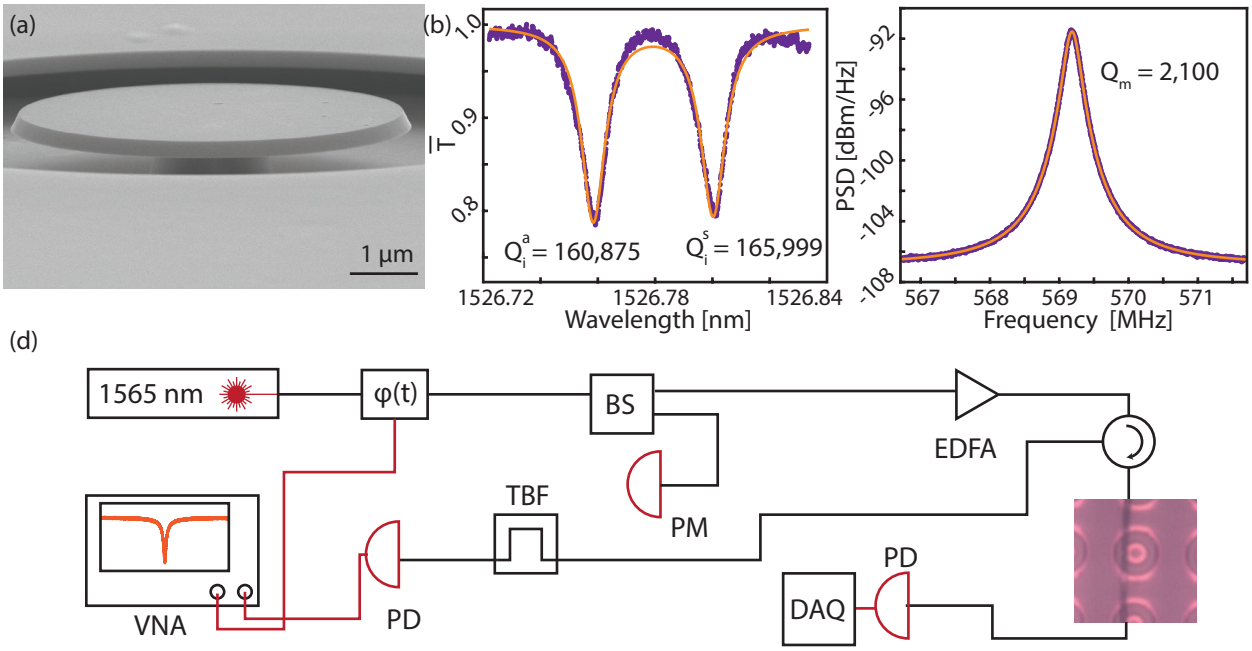

Figure 3.8: (a) SEM of GaP microdisk similar to that used in the OMIT/OMIA experiment, with diameter ~ 6.5 μm. The actual microdisk used would have a smaller pedestal diameter, but was not imaged to prevent damage of the microdisk. (b) Optical WGM used in the experiment, with optical Q_o's as extracted from the shown fits. (c) PSD of RBM measured in ambient conditions after optimization of the pedestal width.(d) Apparatus used to measure OMIT and OMIA in the GaP microdisks. A EOM driven by the vector network analyzer (VNA: Rhode & Schwarz) are used to generate the probe field from the control field. A 50%/50% waveguide coupler (BS) splits off part of the signal for measuring $P_{\rm in}$ on an optical power meter (PM), where the other output was sent through an erbium doped fiber amplifier (EDFA: Pritel). The output of the EDFA was then sent to a circulator whose output was connected to the fiber taper which was coupled to the microdisk of interest. A tunable band pass filter (TBF: Optoplex) is used to filter the reflected light from the cavity to avoid noise due to amplified spontaneous emission from the EDFA. The filtered light was then photodetected with a high-speed detector (PD: Lab Buddy) and analyzed by the VNA. Lastly, the transmission past the microdisk was used to obtain the optical scan shown in (b) using a low speed photodetector and data acquisition card (DAQ: National Instruments PCIe-6221).

the apparatus at NIST. This demonstration utilized a 6.5 μm diameter GaP microdisk, similar to the one shown in Fig. 3.8(a), with intrinsic optical quality factors of $Q_{\rm i}^{\rm a} = 160,875$, and $Q_{\rm i}^{\rm s} = 165,999$ as shown in Fig. 3.8(b), measured at $P_{\rm in} \sim 40$ μW, for the anti-symmetric and symmetric doublet modes, respectively. After initial characterization of this microdisk, additional undercutting was performed at NIST to etch the pedestal of this disk as small as possible, according to the procedure outlined in Section 3.2, to achieve $Q_{\rm m} \sim 2,100$ (Fig. 3.8(c)) in ambient conditions for the 569 MHz RBM. These microdisks operate sufficiently near the sideband resolved regime ($\kappa/\omega_{\rm m} \sim 2$) to observe OMIT and OMIA with $C \sim 1$ as discussed below.

To characterize OMIT in the GaP microdisks, the apparatus shown in Fig. 3.8(d) was used. The control field was generated by a tunable diode laser (New Focus TLB-6700) which was amplified with an erbium doped fiber amplifier (EFDA: Pritel) and detuned from the cavity by $\Delta_c \sim \omega_m$ while P_{in} was varied to study the dependence of the response on N. An electro–optic modulator (EOM) weakly driven by a vector network analyzer (VNA:Rhode & Schwarz ZVL13) was used to create a sideband on the control field that serves as the probe, and whose frequency can be swept across the cavity resonance, varying Δ_p [63, 111]. The probe field reflected by the microdisk back into the fiber taper was measured using a high–bandwidth photoreceiver connected to an optical circulator, and analyzed by the VNA. The symmetric mode of the microdisk doublet ($\omega_o - \frac{\gamma_\beta}{2}$) was used for all of the measurements described below. Figure 3.9(b) shows the results of these measurements for several P_{in}, with each exhibiting a sharp OMIT feature when $\Delta_p = \omega_m$. Here $\overline{S_{21}}$ is the cavity reflection amplitude normalized by its maximum value in absence of OMIT. The cooperativity was extracted by fitting the response to the model described in Appendix D and Section 2.4.4. From this a maximum cooperativity $C \sim 1.27$ was extracted for $N \sim 1 \times 10^5$. As a full measurement of the saturable absorption properties of the disk used in this measurement was not performed, the same Q_i enhancement observed in Fig. 3.6 was applied. Here $g = g_0\sqrt{N}$ was used as a fitting parameter as an independent measurement of g_0 was not available for this microdisk. The measured P_{in}, along with equation 3.1 was then used to compute N, and estimate g_0 using the extracted value of C, i.e. $g_0 = \sqrt{C\kappa\Gamma_m/4N}$. While this is not ideal, it gives $g_0/2\pi \sim 34$ kHz, which is consistent with the results shown in Section 3.5. When combined with an independent measure of g_0, fitting the OMIT spectra to extract C is attractive as it avoids relying on precise knowledge of N, which has many sources of potential error.

The measurement of OMIA was carried out identically as for OMIT, save for blue-detuning the control laser from the cavity, $\Delta_c \sim -\omega_m$. Here we were able to push P_{in} to slightly higher values before the system became thermally unstable. As mentioned in

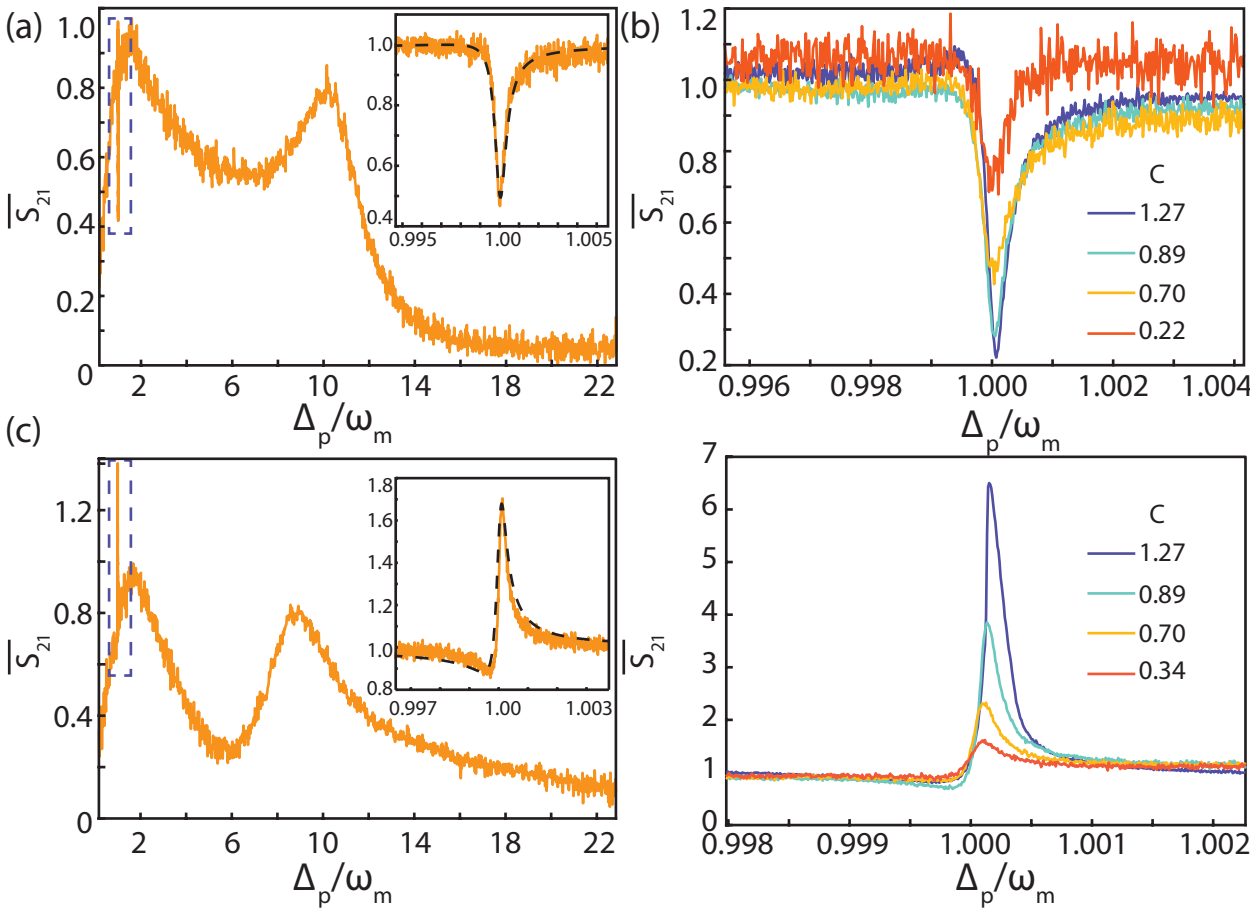

Figure 3.9: Measurement of OMIT (a,b) and OMIA (c,d) in a 6.5μ m diameter GaP microdisk. Measurements are performed by sweeping the RF drive frequency of the EOM using the VNA. The output of the high-speed photodetector is sent to the VNA, which demodulates the signal, where the amplitude of the detected beat note is shown here ($\overline{S}_{21}$). This reveals the broad optical cavity response and narrow OMIT and OMIA features, (a) and (b), respectively. By varying $P_{\rm in}$ we see the amplitude of the OMIT/OMIA features grow, reflecting the larger optomechanical cooperativity C. By fitting the response we can extract C, where $g = g_0\sqrt{N}$ was used as the sole fitting parameter (a- and c-inset).

Section 2.4.4 as $\Gamma_{\rm opt} > \Gamma_{\rm m}$ when blue-detuned, optomechanically induced self-oscillations will occur, which marks the end of the OMIA regime. This limit was not reached for the GaP microdisks studied here.

3.7 Summary & outlook

In summary, this work was the first demonstration of cavity optomechanics in GaP, which also exhibits the highest intrinsic optical quality factors observed to date ($Q_{\rm i} > 2.8 \times 10^5$).

This was also the first demonstration of cavity optomechanics in GaP devices, where we measured a single photon optomechanical coupling rate of $g_0 \sim 30$ kHz, which agreed with COMSOL simulations. The observed increase in Q_i with input power, paired with the absence of nonlinear absorption for $N > 10^5$, illustrates the potential that GaP holds for experiments in quantum optomechanics which requires the ability to handle large N while remaining thermally stable. This was reflected in the demonstration of OMIT and OMIA with $C > 1$. Since this demonstration researchers have also fabricated one dimensional optomechanical crystals in GaP [67, 120].

These devices are also promising for implementing high-frequency cavity optomechanics at visible wavelengths and for applications in nonlinear optics. In fact, these structures were also used by my colleague David Lake to demonstrate efficient second harmonic generation, converting light from 1550 nm to 775 nm [2]. GaP optomechanical cavities could also incorporate piezoelectric elements, as it has a modest piezoelectric response of $\epsilon_{14} = -0.1$ C/m^2 [120], to add electromechanical coupling to the system, enabling transduction of photons between microwave and optical frequencies, in an on-chip platform as has been demonstrated in AlN [123, 140], GaAs [125, 141], and $LiNbO_3$ [142, 143].

Chapter 4

SCD microdisks: fabrication and optical characterization

4.1 Introduction

As far as wide-bandgap materials go, single-crystal diamond is one of the best in terms of its optical and mechanical properties, making it highly desirable for applications in quantum and nonlinear nanophotonics and cavity optomechanics. Optically, some of diamond's advantages include its large electronic bandgap (5.45 eV) and correspondingly broad optical transparency window (225 nm to far-IR), and its relatively high refractive index (2.4 @ λ =1550 nm). Diamond's low multi-photon absorption and thermal stability amid high optical intensities can be harnessed for nonlinear effects, including Raman lasing [144] and parametric down-conversion [145]. Diamond also possesses exceptional mechanical properties, such as a high Young's modulus (1220 GPa) and low intrinsic mechanical dissipation [146, 147], which in combination with its ability to support high optical field intensities, make diamond a promising platform for cavity-optomechanics experiments [18]. SCD can also host optically active color center spins [148] with excellent coherence properties of the electronic and nuclear spins associated with diamond color centers. These are relevant to a wide range of quantum

optics and quantum information processing applications, including storing and manipulating quantum information [149, 150, 151, 152, 153, 154], generating single photons [155, 156] and creating entanglement [157, 158].

High Q_i, small mode-volume, V, optical microcavities, which increase the rate of light-matter interactions via a local density of state $\propto Q_\mathrm{i}$ and per-photon intensity $\propto 1/V$, enhance many physical processes underlying these applications [159, 160, 161, 162]. Microdisk based microcavities have proven to be particularly effective, enabling experiments such as single photon generation [163], strong coupling between photons and quantum emitters [164, 165], and sideband resolved optomechanics [61]. In this chapter we demonstrate the first generation of microdisks fabricated from SCD which supported optical modes with $Q_\mathrm{i} > 1.1 \times 10^5$ and $V < 11\,(\lambda/n)^3$. In particular we will discuss the modification of the SCD fabrication process developed by Behzad Khanaliloo, and Aaron Hryciw for fabricating nanobeam structures [69] to microdisks, which was carried out by myself and Behzad, and the optical characterization of the resulting microdisks [69].

Microdisk fabrication typically involves patterning devices from thin films supported by a substrate which can be undercut, leaving a microdisk supported by a pedestal, as was demonstrated in Chapter 3. Unfortunately, SCD is not currently commercially available in hetero-epitaxially grown thin film form, and although efforts to grow high quality diamond films on substrates such as Ir/MgO [166], Ir/YSZ/Si [167, 168], and SiC/Si [169] are underway, this material is not yet readily available. Integrated optical and optomechanical devices have been demonstrated in polycrystalline diamond (PCD) [170, 171, 71], which is commercially available in thin film form but is not an ideal host for highly coherent quantum emitters. Most state-of-the-state studies of highly coherent SiV and NV colour centres [172, 173, 174] are performed using "bulk" SCD chips grown using chemical vapour deposition. As such, several alternative approaches to fabrication of SCD nanophotonic devices from this material have been investigated.

Efforts to create nanophotonic devices from SCD include wafer bonding and polishing

[145, 160, 175, 176, 177], liftoff [175, 178], and use of hybrid materials [119, 162]. An arguably simpler approach is to fabricate devices directly from bulk diamond chips. This offers the possibility of creating devices from the highest quality material without requiring any manual processing steps such as bonding or polishing. To this end, ion-beam milling [179, 180, 181], angled plasma etching [70, 182, 183], and plasma undercutting [3] approaches have been successful in fabricating nanophotonic structures from SCD. Of these, the quasi-isotropic plasma undercutting technique developed by Behzad Khanaliloo and Aaron Hryciw [69] for fabricating structures from bulk diamond is unique in its ability to harness etching along diamond crystal planes in both vertical and lateral directions.

4.2 Fabrication: first generation SCD microdisks

The approach demonstrated here, outlined in Fig. 4.1(a) and inspired by the SCREAM technique for creating structures from single-crystal silicon [184], defines monolithic microdisks such as those shown in Figs. 4.1(b) and 4.1(c) from bulk diamond. This scalable technique relies upon undercutting of diamond with inductively coupled plasma reactive-ion etching (ICP-RIE) along diamond crystal planes using a zero bias oxygen plasma [69]. This approach, which was also used to create diamond nanobeams [69], shares the low material damage characteristics of the Faraday cage ICP-RIE process of Burek et al. [182], while providing an undercut profile intrinsic to the device geometry and etching parameters. It is fully compatible with standard nanofabrication tools, and does not require modification to the etching tool setup.

The high-Q_i/V single crystal diamond microdisks studied in this chapter were fabricated as follows, where a complete list of the equipment used is given in Appendix F. A $\langle 100 \rangle$-oriented optical-grade single crystal diamond chip (3 mm $\times$ 3 mm $\times$ 0.3 mm) grown using chemical vapor deposition and purchased from Element Six [185, 186] was first mechanically polished (Delaware Diamond Knives) to surface roughness $<$ 5 nm RMS and cleaned in

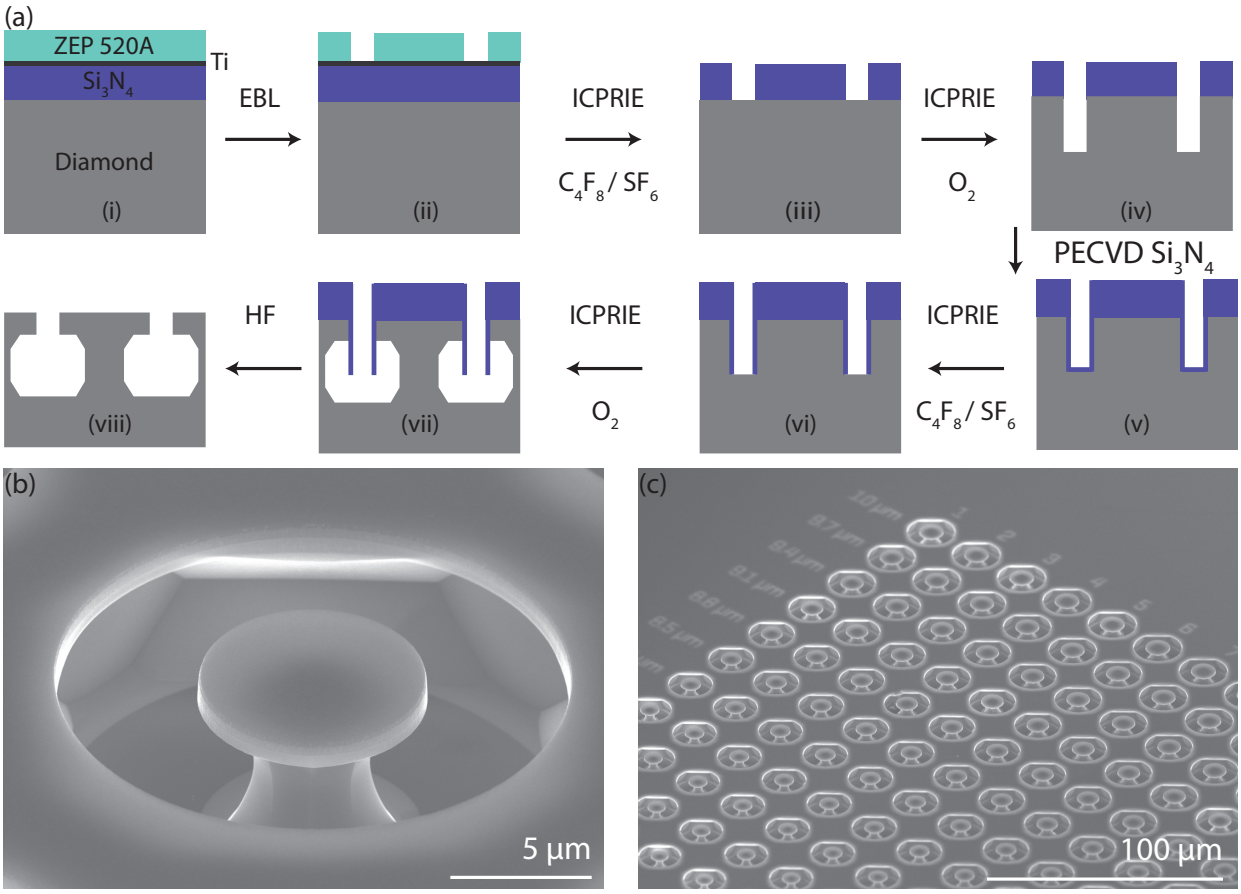

Figure 4.1: (a) Schematic of the microdisk fabrication process steps: (i) Polished bulk single crystal diamond chips are cleaned in boiling piranha and coated with a 400 nm thick PECVD Si_3N_4 layer, coated with a thin ($\sim$ 5 nm) Ti anti-charging layer, and EBL resist (ZEP 520A). (ii) Microdisks are patterned in ZEP using EBL and developed in ZED-N50. (iii) Patterns are transferred to the Si_3N_4 hard mask using an ICP-RIE etch. ZEP is removed using a deep-UV exposure and Remover PG. (iv) Patterns are transferred to the diamond using an anisotropic O_2 plasma ICP-RIE etch. (v) The diamond sidewalls are protected with a conformal coating of PECVD Si_3N_4. (vi) A short ICP-RIE etch removes Si_3N_4 from the bottom of the etch windows. (vii) A zero bias O_2 ICP-RIE plasma undercuts the microdisks by etching along crystal planes. (viii) The sample is soaked in HF to remove the remaining Si_3N_4 layer, followed by a piranha clean. (b) A 45 ° rotated scanning electron microscope (SEM) image of a 7.9 μm diameter microdisk in a diamond chip with $\langle 100 \rangle$-oriented surface and edge crystal planes. (c) Overview of an array of fabricated microdisks.

boiling piranha (150 mL H_2SO_4:50 mL H_2O_2)[1] followed by a 3 $\times$ 30 s rinse in H_2O, and drying with N_2. As an O_2 ICP-RIE etch is used for all of the diamond etching steps, it is necessary to use a hard mask for patterning which can withstand the O_2 plasma. We have chosen silicon nitride (Si_3N_4) in order to take advantage of highly optimized Si etching recipes

[1]Disclaimer: Piranha should be treated with care as it is highly corrosive and a very strong oxidizer. Improper mixing, or introduction of large amounts of organic material may cause an explosion. See Appendix G for handling precautions.

during later steps. A 400-nm-thick layer of PECVD Si_3N_4 was deposited, where the SCD chip was taped to a Si carrier wafer with double sided Kapton tape (see Appendix G), which was then placed in the PECVD chamber and surrounded by Si wafer pieces to encourage deposition uniformity (Fig. 4.1(a-i)). The Si_3N_4 was then coated with a thin Ti layer (5 - 10 nm), deposited via electron-beam physical vapor deposition (EBPVD), which reduces charging that can be problematic during subsequent EBL steps due to diamond's insulating properties. Alternatively, coating the EBL resist with a water-soluble conductive polymer (aquaSAVE) can be effective, however we experienced some difficulty in film uniformity when spinning the polymer on the SCD chip. Finally, a 400 nm layer of ZEP 520A is spin coated on the surface of the chip (4000 RPM, 60 s, 180° C bake for 5 min while semi-covered by reflective lid). Patterning of the ZEP was performed using EBL, with beam energy of 30 keV, aperture of 10 μm, and dose factor of 4×80 $\mu C/cm^2$, followed by development for 20 s in a bath of ZED-N50, followed by IPA, both cooled to $-15°C$.

Table 4.1: Nominal etch parameters used for patterning the Si_3N_4 hard mask with the Oxford Plasma Lab Pro 100. This results in an etch rate of $\sim$ 7.5 nm/s for Si_3N_4 and 5.4 nm/s for ZEP, resulting in an etch selectivity of 7:5 for Si_3N_4:ZEP.

T [°C]	Pressure [mTorr]	RF [W]	Bias [V]	ICP [W]	C_4F_8 [sccm]	SF_6 [sccm]
15	10	25	110	3500	12	16

The resist pattern was transferred to the Si_3N_4 hard mask using an ICP-RIE etch with C_4F_8/SF_6 chemistry (Fig. 4.1(a-iii)) whose etch parameters are given in Table 4.1. All ICP-RIE steps were performed using an Oxford Instruments PlasmaLab 100 etcher. Before performing the Si_3N_4 etch the chamber was first cleaned with the same chamber clean recipe given in Table 3.1 and conditioned for 10 min with a Si carrier wafer and the same etch recipe given in Table 4.1. The exposed Ti layer was also removed by the Si_3N_4 etch. Following the etch, the remaining resist was stripped off using a 10 minute deep-UV exposure (1.24 mW/cm^2, 254 nm wavelength) and a 5 minute soak in Remover PG at 70° C followed by a 3×30 second rinse in H_2O and drying with N_2.

Table 4.2: Nominal etch parameters used for diamond anisotropic etch with the Oxford Plasma Lab Pro 100. This results in an etch rate of $\sim$ 60 nm/min for the diamond and 1.5 nm/min for Si_3N_4, resulting in an etch selectivity of 40:1 for SCD:Si_3N_4.

T [°C]	Pressure [mTorr]	RF [W]	Bias [V]	ICP [W]	O_2 [sccm]
15	10	80	345	850	30

The pattern was transferred to the diamond using an anisotropic O_2 ICP-RIE etch with high diamond-to-Si_3N_4 etch selectivity of 40:1 (Fig. 4.1(a-iv)), whose etch parameters are given in Table 4.2. Again, before performing the etch the chamber was cleaned and then conditioned for 10 min with the same etch recipe given in Table 4.2. This etch is characterized by a high diamond etch rate (60 nm/min), smooth and vertical diamond sidewalls, and no observed micromasking. The etch time was determined by the desired final device thickness. Next, the vertical sidewalls were protected using a conformal coating of $\sim$ 200 nm PECVD Si_3N_4 (Fig. 4.1(a-v)) in preparation for the quasi-isotropic diamond undercut etch. This deposition was followed by a slower anisotropic C_4F_8/SF_6 ICP-RIE etch to remove the Si_3N_4 from patterned non-sidewall surfaces such as the bottoms of the windows surrounding the microdisks (Fig. 4.1(a-vi)), where the etch parameters are given in Table 4.3.

Table 4.3: Nominal etch parameters used for the second Si_3N_4 etch with the Oxford Plasma Lab Pro 100. This results in an etch rate of $\sim$ 3.5 nm/s for Si_3N_4.

T [°C]	Pressure [mTorr]	RF [W]	Bias [V]	ICP [W]	C_4F_8 [sccm]	SF_6 [sccm]
15	10	20	125	2400	30	18

During this step it is crucial not to over-etch the Si_3N_4 protection layer, to ensure that the top corners of the vertical sidewalls remain coated with Si_3N_4. If the top corners are over-etched then breakthrough of the protection layer ensues, which results in unwanted etching of the diamond device in the next step. This severely reduced the yield of successful devices, and the optimization of this step is discussed in further detail in Chapter 6. The patterned structures were then undercut using a quasi-isotropic O_2 ICP-RIE etch with zero preferential ion directionality (Fig. 4.1(a-vii)). This etch employs no vertical ion plasma

acceleration (zero forward RF power), a dense plasma, and an elevated sample temperature, as listed in Table 4.4. Finally, as shown in Fig. 4.1(a-viii), the Si_3N_4 and Ti layers were removed by wet-etching in 49% HF solution (20 mL)[2], and cleaned in boiling piranha, where each acid step is followed by a 3 × 30 second rinse in H_2O and drying with N_2.

Table 4.4: Nominal etch parameters used for the diamond quasi-isotropic etch with the Oxford Plasma Lab Pro 100.

T [°C]	Pressure [mTorr]	RF [W]	Bias [V]	ICP [W]	O_2 [sccm]
250	15	0	0	3000	90

The quasi-isotropic undercut etch step is critical for creating microdisk devices, and prior to this work had not been reported for microcavity fabrication. Of particular importance for creating high-Q_i whispering-gallery mode cavities is that the fabrication process creates a pedestal sufficiently isolated from the whispering gallery modes to prevent radiation loss into the substrate, and a microdisk bottom surface free of features which break the azimuthal symmetry. As illustrated schematically in Fig. 4.2(a), and visible in the SEM images of fabricated devices in Figs. 4.1(b) and 4.1(c), the quasi-isotropic undercut was observed to etch in directions defined by clearly visible diamond crystal planes. This behavior is consistent with the etch being dominantly chemical in nature, and is commonly observed in wet etching of crystalline materials such as silicon. Figure 4.1(b) identifies the {100} and {111} families of crystal planes along which the undercut of the unpatterned region surrounding the microdisk is observed to proceed. Etching along the {100} planes is horizontal or vertical, while etching along the {111} planes is at a 35.26° angle with respect to the diamond surface. The microdisk pillar is etched along similar families of crystal planes, which intersect as the pillar diameter is reduced. As indicated in Fig. 4.2(d), purely vertical and horizontal etching along the {100} planes will result in a square microdisk pedestal and reduced microdisk thickness, respectively. Etching along the {111} planes defines surfaces at a 35.26° angle with respect to the sample surface. The resulting quasi-isotropic undercut etch creates an

[2]Disclaimer: Hydrofluoric acid (HF) should be treated with care as it is a corrosive acid that can cause extensive tissue damage and death. See Appendix G for handling precautions.

hourglass-shaped pedestal supporting a microdisk, whose bottom surface can be seen in Fig. 4.2(e).

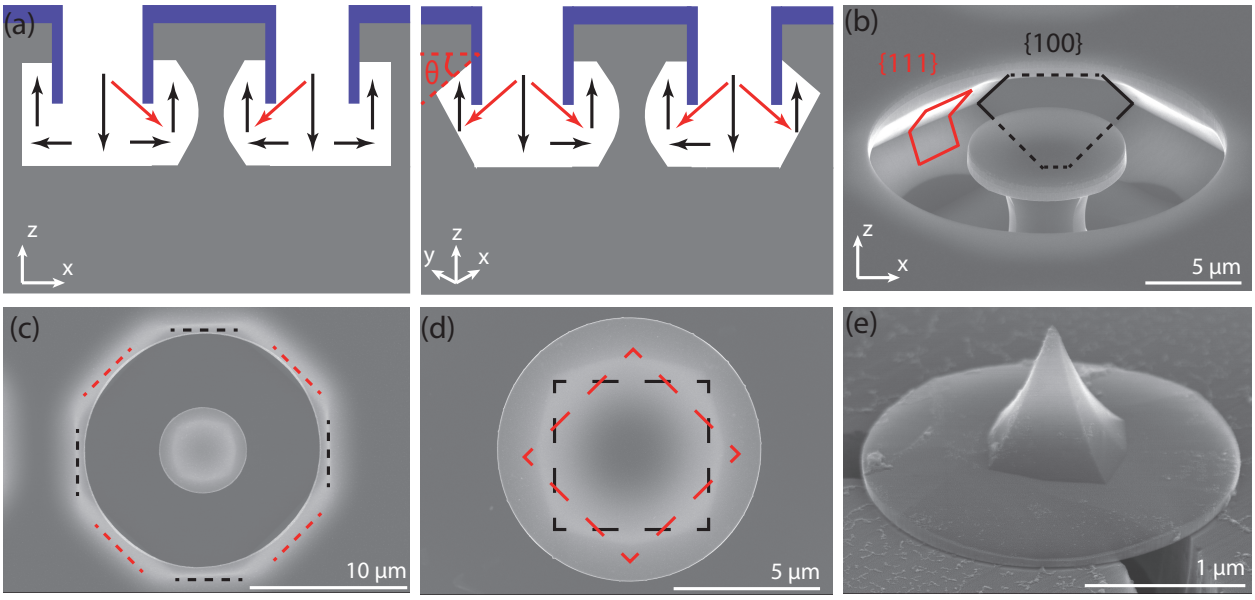

Figure 4.2: (a) Illustration of the observed undercut etching processes. Etching along the {100} and {111} families of crystal planes is shown by black and red arrows, respectively. The left (right) image shows a right angle (45 degree rotated) view of the microdisk cross-section. (b) Tilted (60°) SEM image shows the (010) and {111} planes, marked in black and red, respectively. The {111} planes have an angle of $\theta = 35.26°$ with respect to the diamond surface. (c) Top-down SEM image of the microdisk and windows showing the amount of undercut along the crystal directions. (d) SEM image illustrating how the octagon shaped pedestal results from etching along {100} and {111} crystal planes. (e) A 60° tilted image of a broken and flipped microdisk.

Figure 4.3(a) shows the effect of microdisk diameter on the observed upward, minor inward, and major inward undercut etch distances, as defined in the Fig. 4.3(a) inset, for two sets of microdisks with different anisotropic and quasi-isotropic etch times. Etch distances were measured directly from SEM images. A small variation ($< 100\,\text{nm}$) in microdisk thickness was observed as a function of increasing microdisk diameter, resulting from smaller diamond microdisks requiring less undercut time before etching along the {100} and {111} families of crystal planes intersect.

The nonlinear nature of the undercut etch rates is shown in Fig. 4.3(b), which gives etch distance as a function of etch time. The upward etch rate, which together with the initial anisotropic etch depth defines the microdisk thickness, is observed to vary quadratically with the undercut etch time. The minor inward etch distance, which defines the pedestal base

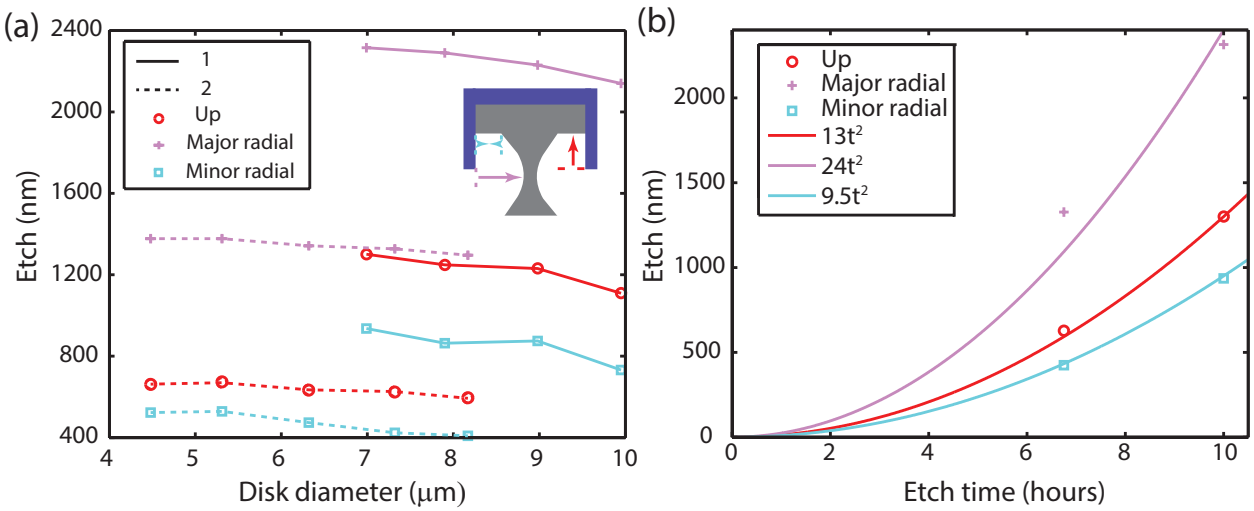

Figure 4.3: (a) Undercut etch distance as a function of microdisk diameter. The upward, major inward, and minor inward etch distances, as defined in the inset, are shown for chip 1 (2) with $\sim$ 24 (15) minutes of anisotropic and $\sim$ 10 (7) hours of isotropic etch times with solid (dashed) lines as a guide for eye. Inset: Schematic showing definition of upward, major inward, and minor inward etch distances. (b) Etch distance as a function of undercut etch time for a 7 μm microdisk, extracted by comparing chip 1 and 2. Solid lines are t^2 (t: time) fits to the data.

size, has a similar etch time dependence. This is consistent with the minor inward etch distance and thickness being defined by the ((100), ($\bar{1}$00), (010), (0$\bar{1}$0)) and (001) planes, respectively. The major inward etch distance increases approximately twice as fast as the upward and minor inward etch rates, which can be explained by the fact that the pedestal waist is etched simultaneously along both the {100} and {111} families of crystal planes. It is expected that the inward etch rates can be increased by introducing a second diamond anisotropic etch step after (vi) in Fig. 4.1(a), as in the SCREAM process [184]. The surface area of the exposed region surrounding the disk was also observed to affect undercut time, where a larger surrounding window resulted in a faster undercut, however, a systematic study to quantify this speedup was not performed here.

4.3 Optical characterization

Microdisk optical cavities require small pedestal size and wavelength scale thickness to support high-Q_i optical modes. Here, microdisk cavities were fabricated using a 35 minute

($\sim 2\ \mu$m deep) anisotropic etch followed by an 11 hour quasi-isotropic etch to undercut the devices. The optical properties of the microdisks were measured by monitoring the wavelength dependent transmission of a tunable diode laser (Santec TSL-510, wavelength range of 1500–1630 nm) through a dimpled optical fiber taper [86] evanescently coupled to the microdisk. A typical normalized transmission spectra for a $\sim 7.0\,\mu$m diameter microdisk with a thickness of $\sim 1.0\,\mu$m and pillar base diameter of $\sim 4.6\,\mu$m is shown in Fig. 4.4(a). This spectra contains many resonances corresponding to high-$Q_{\rm i}$ whispering-gallery modes of the microdisk, including high-$Q_{\rm i}$ TE and TM-like modes, and modes which are higher-order in the radial and vertical directions. The highest-$Q_{\rm i}$ resonance observed in this microdisk is shown in Fig. 4.4(b), with intrinsic $Q_{\rm i} \sim 1.15 \times 10^5$. At the time of this demonstration this was comparable to the highest reported $Q_{\rm i}$ measured in single crystal microcavities to date [145, 183], however significant improvements to this value are discussed in Chapter 6.

By comparing measured $Q_{\rm i}$ and mode wavelength spacing values with the mode spectrum predicted from finite-difference-time-domain (FDTD) simulations [81], and measuring the polarization dependence of the resonance contrast, this resonance is identified as the fundamental TM-like mode. The predicted modal indices are $\{m, n, q\} = \{28, 1, 1\}$, which describe the mode's azimuthal (m), radial (n), and vertical (q) order. The resonance corresponding to the fundamental TE-like mode is shown in Fig. 4.4(c), with $Q_{\rm i} \sim 1.02 \times 10^5$, and modal indices of $\{27, 1, 1\}$. The doublet structure of the resonances in Figs. 4.4(b,c) is the result of backscattering, and indicates that the resonances correspond to standing wave modes as discussed in Section 2.2.3 and Ref. [77]. The FDTD calculated field profiles of these modes are shown in Fig. 4.4(a), and are found to have standing-wave mode volume $V_{\rm TM} = 10.7\ (\lambda/n_{\rm d})^3$ and $V_{\rm TE} \sim 12.6\ (\lambda/n_{\rm d})^3$, as defined by the maximum electric field strength. These mode volumes are approximately an order of magnitude smaller than those of comparable high-$Q_{\rm i}$ whispering gallery mode microcavities [183].

Insight into the mechanism limiting $Q_{\rm i}$ of these devices is provided by the FDTD simulations and the observed $Q_{\rm i}$ dependence on microdisk diameter. Simulations of the ideal-

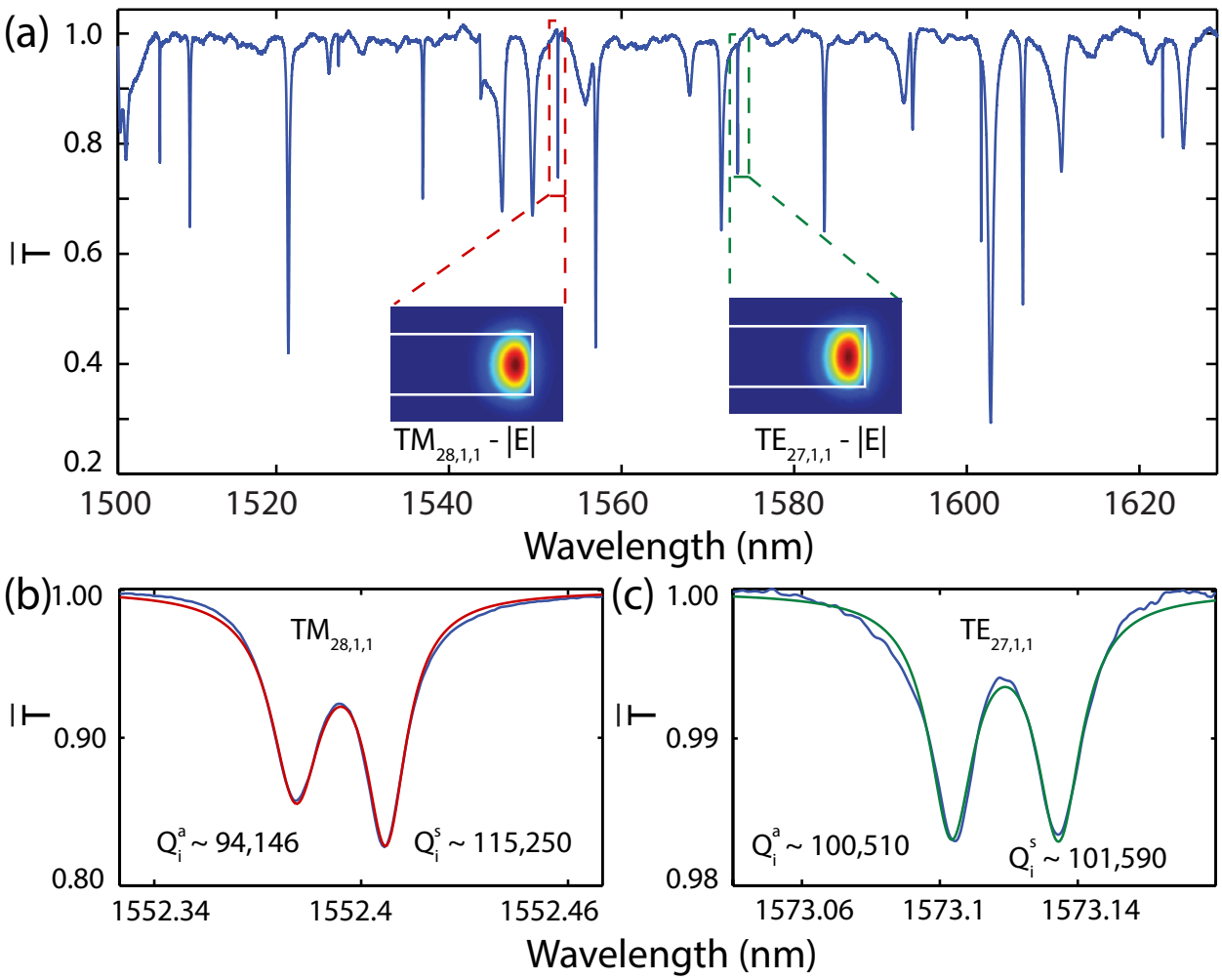

Figure 4.4: (a) Normalized transmission spectra of an optical fiber taper evanescently coupled to a single crystal diamond microdisk with diameter $\sim 7.0\,\mu$m and thickness $\sim 1.0\,\mu$m. Fundamental TE-like and TM-like modes and the associated electric field profiles are highlighted. (b,c) Narrow-range wavelength scan of a high-Q_i TM-like (TE-like) mode with $\{m, n, q\} = \{28, 1, 1\}$ ($\{27, 1, 1\}$) mode indices, respectively.

ized microdisk geometry studied here, which assumes perfect azimuthal symmetry for the pedestal, predict $Q_\mathrm{i} > 10^7$ for both the fundamental TE and TM-like modes, indicating that radiation loss and leakage into the substrate via the pedestal does not limit the Q_i of these devices. However, the non-cylindrical pedestal shape created by the undercut etch can significantly affect optical loss in the microdisk by breaking the azimuthal microdisk symmetry and creating scattering not accounted for in the FDTD simulations performed here. The microdisk studied in Fig. 4.4 is both the smallest diameter device on the chip, and the device with the highest-Q_i modes. For the chip studied here, Q_i was observed to decrease

with increasing microdisk diameter. This behavior contradicts expectations that Q_i should increase in larger disks due to stronger optical confinement [77, 128]. However, this behavior is consistent with interactions between the whispering gallery modes and the non-cylindrical pedestal limiting Q_i: as the microdisk diameter increases, the non-cylindrical pedestal extends closer to the microdisk perimeter, as shown in Fig. 4.3(a), and its influence on Q_i increases. This effect can be reduced by increasing the relative undercut, either through fabrication of smaller diameter microdisks or using a longer undercut etch. It is expected that the addition of the previously mentioned second anisotropic diamond etch will reduce this effect by increasing the horizontal undercut rate [184]. Finally, surface roughness also affects the Q_i of these devices and may be reduced through improved cleaning and use of reflow techniques [128], which is investigated further in Chapter 6.

4.4 Summary & outlook

In summary, the first generation of SCD microdisks demonstrated in this chapter realized high Q_i/V devices using our novel fabrication technique. However, the pedestal diameter was too large to observe optomechanical coupling due to the significant mechanical clamping loss to the substrate. While this did not make these devices viable for cavity optomechanics they did have the ability to handle $N > 10^6$ remaining thermally stable, due to the large pedestal diameter; in fact, as discussed in Chapter 5, as the pedestal diameter is reduced the thermal handling of the structure suffers. Following this demonstration my focus turned to fabricating SCD optomechanical cavities primarily by reducing the pedestal diameter. Reducing the microdisk diameter and thickness, and as a result V, is also desirable in order to enhance processes involving light matter coupling, and is possible without reducing Q_i for sufficiently small pedestals. An ongoing effort was also made to improve the optical and mechanical properties of these devices, which culminated in the results discussed in Chapter 6.

Chapter 5

SCD microdisks: first demonstration of cavity optomechanics

5.1 Introduction

As mentioned earlier, diamond cavity optomechanical devices are an attractive platform for controlling interactions between light, vibrations, and electrons that underly future hybrid quantum technologies [187]. Their potential arises from diamond's exceptional mechanical and optical properties [148] combined with its ability to host color centers such as the nitrogen-vacancy (NV) whose electron spins are excellent qubits that can be manipulated by local mechanical strain fields [188, 189, 190, 191, 192]. Recently, piezoelectric actuation of bulk [188, 193] and nanomechanical [194, 189, 190, 191, 192, 195, 196] diamond resonators has been used to demonstrate phononic spin control. Cavity optomechanics [18] harnesses optical forces in place of piezoelectric actuation, allowing coherent phonon state manipulation [61, 63, 111] of GHz frequency mechanical resonators with quantum limited sensitivity [29]. These phonons can be made resonant with NV center electron spin transitions that are central to proposals for spin-spin entanglement [197], spin-phonon state transfer [198, 199, 200], spin mediated mechanical normal mode cooling [197, 201, 202], and photon-phonon-spin coupling

[203]. Additionally, the relatively small thermal occupancy and mechanical dissipation of GHz diamond devices, combined with diamond's ability to support strong optical fields due its large electronic bandgap, make them an ideal system for the cavity optomechanical backaction cooling and study of mechanical resonators in their quantum ground state [29]. In this chapter we demonstrate a SCD cavity optomechanical system for the first time. This system is based on the same microdisk device geometry studied in the previous chapter, but possesses a pedestal diameter small enough to reduce the mechanical damping to a suitable level to observe optomechanical coupling.

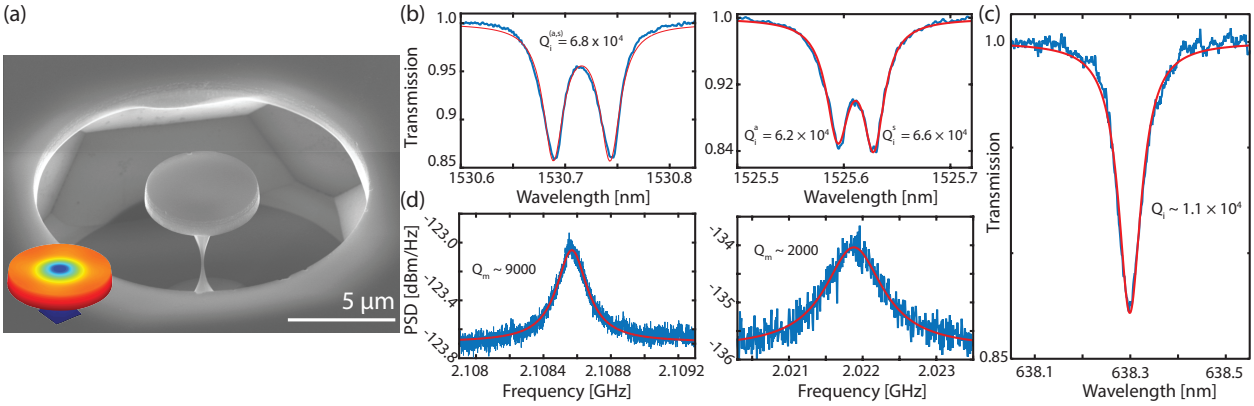

Figure 5.1: Characterization of diamond microdisk optical and mechanical modes at low optical input power. (a) SEM image of a 5 μm diameter microdisk, with minimum pedestal width of 100 nm. Inset: Simulated displacement distribution of the RBM mechanical resonance of this device. (b) Highest Q_o TM-like optical modes of a 5 μm (left) and 5.5 μm (right) diameter microdisk, with intrinsic quality factors for each doublet resonances as labeled, extracted via the shown fits. (c) High-Q_o visible mode, with intrinsic quality factor as shown for a 6.2 μm diameter microdisk, extracted via the shown fit. (d) $S_P(f)$ produced by the thermal motion of the RBM of the microdisks in (b), showing that the larger diameter, larger pedestal waist microdisk has a lower Q_m, extracted via the shown fits.

5.2 Fabrication modifications

These devices were fabricated using the same process described in Section 4.2 from an optical grade, chemical vapor deposition (CVD) grown ⟨100⟩-oriented SCD substrate supplied by Element Six. Some steps that differed were a 6 minute deep-UV exposure (5 mW/cm^2 at 254 nm) followed by a 2 minute soak in room temperature Remover PG for stripping the ZEP resist before the anisotropic diamond etch. The devices studied in this chapter also have

smaller diameters of 5.0 μm to 6.0 μm and average thickness $\sim$ 940 nm. As evident from the image in Fig. 5.1(a), devices are fabricated with a process modified to minimize the waist of the pedestal supporting the microdisk, reducing it to $<$ 100 nm, where the waist is defined as the smallest point of the pedestal. This consisted of choosing smaller disk radii (R) to reduce the required quasi-isotropic undercut time to avoid unwanted diamond etching and to increase the optomechanical coupling rate, as $g_0 \sim \omega/R$. Further fabrication optimization steps that followed this work are discussed in Chapter 6.

In order to make the pedestal waists of the $\sim$ 5 μm diameter disks studied here as small as possible, the quasi-isotropic etch was performed for a total of 12 hours. As the exact length of time required to undercut the target diameter device to the point where the pedestal diameter was as small as possible was unknown, a stepwise approach was taken. Here the device is etched for an appropriate amount of time, and then examined under an optical microscope. It was then possible to determine by eye if the smallest diameter microdisks on the SCD chip had been fully released or not, as shown in Appendix G. This process was repeated until the target microdisks were the smallest remaining in the written array. Once this occurred, the rest of the process was carried out as described in Section 4.2. It was also observed that the N_2 drying step post cleaning could destroy the devices with the smallest microdisk pedestal widths. If the smallest possible pedestal width is desired, a less turbulent Si_3N_4 removal and drying approach should be taken, such as the use of critical point drying [204] or HF vapor etching [205].

5.3 Device overview

The microdisk system studied here, an example of which is shown in Fig. 5.1(a), supports optical modes at visible and telecommunication wavelengths ($\omega_o/2\pi \sim 200 - 470$ THz) that interact via radiation pressure with GHz frequency mesoscopic mechanical resonances of the structure. We find that these resonances have a record combination of high ω_m and

low mechanical dissipation ($\Gamma_{\rm m} \sim 2\pi \times 0.2\,{\rm MHz}$) compared to other mechanical resonators operating in ambient temperature and pressure, and that their $Q_{\rm m} \cdot f_{\rm m} = 1.9 \times 10^{13}$ Hz product is sufficiently high to satisfy the minimum criteria for single phonon coherent behaviour described in Section 2.4.5. The microdisk optical modes have low dissipation ($\kappa \sim 2\pi \times 3\,{\rm GHz}$, limited by surface roughness), and owing to the negligible nonlinear absorption in diamond at telecom optical frequencies, they can support intracavity photon number $N > 10^6$ without degrading $Q_{\rm i}$. In combination, this allows realization of optomechanical cooperativity, $C \sim 3$, large enough (> 1) for coherent photon-phonon coupling [63, 111], with $g_0 \sim 2\pi \times 26\,{\rm kHz}$. These devices operate on the border of the sideband resolved regime ($\kappa \sim \omega_{\rm m}$), enabling radiation pressure backaction excitation of mechanical self-oscillations with $\sim 31\,{\rm pm}$ amplitude. The accompanying stress fields are strong enough to drive diamond color center spin transitions with a single phonon-spin coupling rate that is predicted to exceed that of previously studied MHz frequency nanomechanical structures [190, 191, 192], despite having orders of magnitude higher $\omega_{\rm m}$ and smaller phonon amplitude, owing to the localized nature of the microdisk mechanical resonances. In addition, the ability of the microdisks to support optical modes at visible wavelengths is compatible with resonant coupling to NV center optical transitions [160], as well as operation in fluid environments of interest for sensing applications [206].

The devices were characterized by monitoring the transmission of a dimpled optical fiber taper [1, 86] evanescently coupled to the microdisk and input with light from tunable diode lasers with wavelengths near 1530 nm or 637 nm. For the 1530 nm measurements, the output of the fiber taper was monitored by both low- and high-bandwidth photoreceivers, and a calibrated optical power meter (see Appendix F for the list of equipment used). Figure 5.1(b) shows typical $\overline{T}(\lambda_{\rm l})$ when the fiber taper is evanescently coupled to devices with diameters of $5.0\,\mu{\rm m}$ and $5.5\,\mu{\rm m}$ and the wavelength $\lambda_{\rm l}$ of the 1530 nm tunable laser is scanned across microdisk modes at $\lambda_{\rm o}$. Here $\overline{T}$ is the average transmission measured by the low-bandwidth photodetector over a timescale long compared to $1/f_{\rm m}$. These measurements

reveal resonant coupling to modes with loaded $Q_o \sim 5.8 \times 10^4 - 6.0 \times 10^4$ (intrinsic $Q_i = 6.1 \times 10^4 - 6.8 \times 10^4$), and a degree of doublet structure that depends on the internal backscattering of a given device. Maximizing Q_o, and thereby minimizing κ, is important for achieving the aforementioned regime allowing coherent photon-phonon coupling ($C > 1$).

The ability of these devices to support modes over a wide wavelength range is demonstrated in Fig. 5.1(c), where the 637 nm tunable laser was used to probe a mode with high-$Q_i > 1 \times 10^4$. This is promising for applications involving NV center optical transitions in this wavelength range [195]. These devices have a predicted radiation loss limited $Q_i > 10^7$ at both 1550 nm and 637 nm wavelengths; κ is currently limited by surface roughness and linear absorption, as discussed in Chapter 6. In previous work the microdisk pedestal size was observed to limit Q_i for insufficient relative undercut. In the devices studied here scattering due to the non-cylindrical pedestal shape is predicted to dominate the contribution to κ from the pedestal [3]. The lower Q_o observed at 637 nm can be attributed in part to sub-optimal fiber taper positioning [77] and an increased sensitivity to surface scattering [183].

5.4 First demonstration of cavity optomechanics in SCD

To probe optomechanical coupling within the microdisks, time (t) dependent transmission fluctuations $\delta T(t, \lambda_l)$ of 1550 nm light were monitored using the RSA. Excitations of the microdisk mechanical resonances modulate λ_o, resulting in a dispersive optomechanical transduction of mechanical motion to an optical signal $P_o \delta T(t; \lambda_l)$ that can then be observed in the measured electronic power spectrum $S_P(f)$. Here P_o is the average power transmitted to the photoreceiver. Figure 5.1(d) shows typical spectra when λ_l is tuned near the point of maximum transduction of the modes in Fig. 5.1(b). Resonances near $f_m \sim 2.0 - 2.1$ GHz are observed, corresponding to optomechanical transduction of the thermomechanical motion of the fundamental RBM of the microdisks. The predicted displacement of the RBM

calculated using finite element simulations (COMSOL) is shown in the inset to Fig. 5.1(a). The simulated $f_{\rm m}$ of the RBM for varying microdisk diameter was found to be within 10% of observed values. These measurements were conducted at low input power $P_{\rm in} \sim 50$ μW to avoid optomechanical backaction effects discussed below. Here an erbium doped fiber amplifier (EDFA) was used on the output side of the fiber taper to boost the optical signal prior to photodetection to a level just below the detector saturation power ($P_{\rm o} \approx 0.7$ mW).

5.4.1 Mechanical properties and $Q_{\rm m} \cdot f_{\rm m}$ product

The microdisk pedestal can significantly affect the RBM properties, and minimizing its waist size is important in order to maximize $Q_{\rm m}$ and reach $C > 1$. For the diamond microdisks studied in Chapter 4 which had $> 1\mu$m pedestal waists [3], transduction of mechanical modes was not observed. As shown in Fig. 5.1(a), the devices used here for cavity optomechanics have significantly smaller waists, e.g., the 5.0 μm diameter microdisks have a pedestal waist < 100 nm. Figure 5.1(d) shows that when microdisk diameter, and as a result, pedestal waist are increased to 5.5 μm and 400 nm, respectively, $Q_{\rm m}$ is found to decrease from ~ 9000 to ~ 2000. Mechanical resonances are not observed in devices with pedestal diameter > 500 nm. This indicates that $Q_{\rm m}$ for these devices is limited by clamping loss [137, 207]. The hourglass shape of the pedestals obtained for the $\langle 100 \rangle$ optical grade diamond samples used here limits the minimum size of the pedestal where it connects to the microdisk, and may result in increased dissipation. Given the crystal plane selective nature of the diamond undercut [3], fabricating microdisks from samples with alternate crystal orientation such as $\langle 111 \rangle$ may alleviate this limitation. Additionally, operation in vacuum, where viscous air damping can be avoided [132, 133], and at low temperature [69, 176] would allow a decrease in dissipation, as the total $Q_{\rm m}$ is given by $Q_{\rm m} = (\sum_j 1/Q_m^j)^{-1}$, where the Q_m^j represent the quality factor due to each damping mechanism. Despite present limitations, the demonstrated devices have $Q_{\rm m} \cdot f_{\rm m} = 1.9 \times 10^{13}$ Hz, that is larger than all previously studied cavity optomechanical systems operating in ambient conditions [116, 137, 207]. A

comparison of some of the highest $Q_{\mathrm{m}} \cdot f_{\mathrm{m}}$ products for optomechanical systems observed in ambient, cryogenic, and low pressure environments is shown in Figure 5.2. Note that higher $Q_{\mathrm{m}} \cdot f_{\mathrm{m}}$ products have been demonstrated compared to this work, but required either vacuum or low-temperature environments.

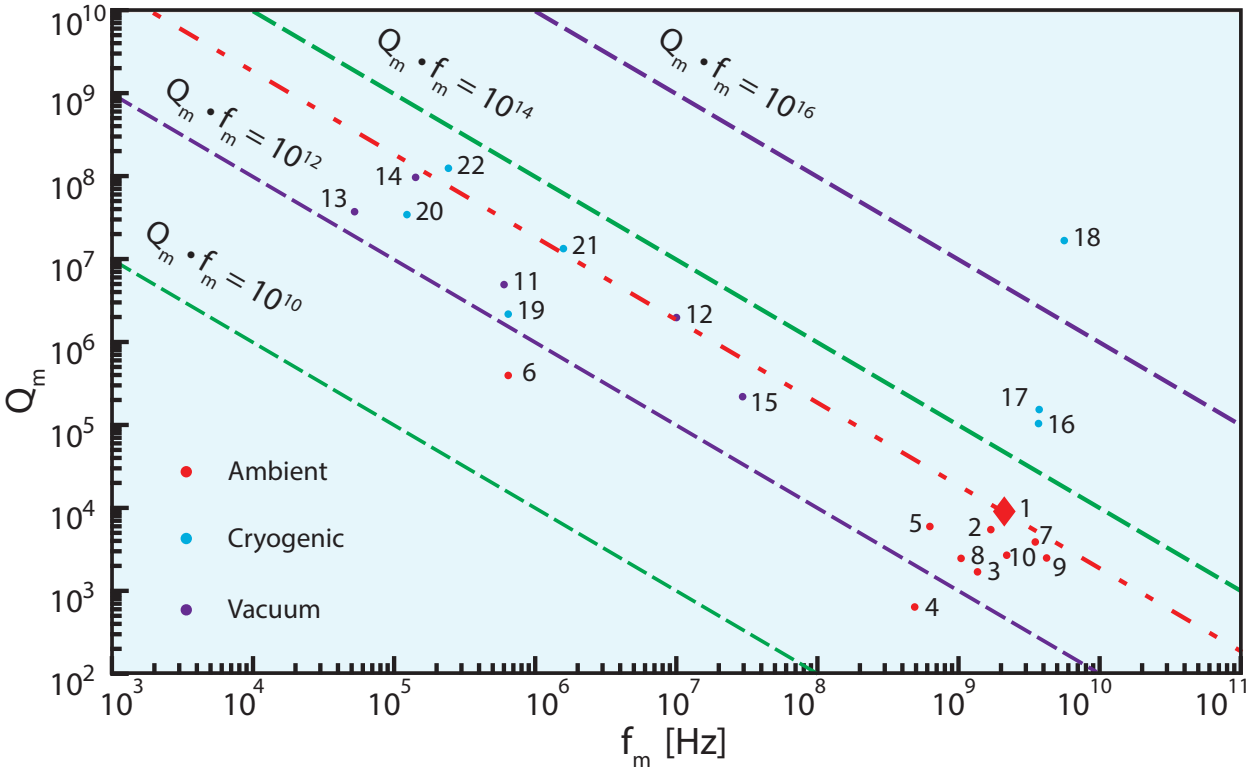

Figure 5.2: Comparison of high $Q_{\mathrm{m}} \cdot f_{\mathrm{m}}$ product products for a variety of optomechanical systems, as listed in Table 5.1.

This figure of merit is critical for cavity optomechanical mass spectroscopy [40, 206, 219] and low phase noise oscillators [220]. Within the context of quantum optomechanics, this product satisfies a key minimum requirement for room temperature studies of single phonon coherence by over an order of magnitude: $\omega_{\mathrm{m}}/\Gamma_{\mathrm{m}} \gg n_{\mathrm{th}}$, where n_{th} is the room temperature phonon population of the RBM, ensuring that thermal decoherence is slow compared to a mechanical oscillation [18]. By satisfying this condition, cooling to the quantum ground state from room temperature should also be possible [213].

Table 5.1: Survey of highest $Q_{\mathrm{m}} \cdot f_{\mathrm{m}}$ products observed in cavity optomechanical systems to date, corresponding to those shown in Fig. 5.2.

No.	Author/Reference	Material	Structure
1	Mitchell et al. (This Work)	Diamond	Microdisk
2	Lu et al. [207]	SiC	Microdisk
3	Nguyen et al. [137]	GaAs	Microdisk
4	Mitchell et al. [1]	GaP	Microdisk
5	Liu et al. [61]	Si_3N_4	Microdisk
6	Fong et al. [208]	Si_3N_4	Beam & Waveguide
7	Grutter et al. [209]	Si_3N_4	Optomechanical Crystal
8	Xiong et al. [68]	AlN	Suspended Ring Resonator
9	Bochmann et al. [123]	AlN	Optomechanical Crystal
10	Eichenfield et al. [116]	Si	Optomechanical Crystal
11	Bui et al. [210]	Si_3N_4	Membrane Photonic Crystal + Fabry Pérot Cavity
12	Wilson et al. [211]	Si_3N_4	Membrane + Fabry Pérot Cavity
13	Reinhardt et al. [212]	Si_3N_4	Membrane + Fabry Pérot Cavity
14	Norte et al. [213]	Si_3N_4	Membrane Photonic Crystal + Fabry Pérot Cavity
15	Zhang et al. [214]	Si_3N_4	Tuning Fork + Microdisk
16	Chan et al.[29]	Si	Optomechanical Crystal + Phononic Shield
17	Krause et al. [215]	Si	Optomechanical Crystal + Phononic Shield
18	Meenehan et al. [216]	Si	Optomechanical Crystal + Phononic Shield
19	Fong et al. [208]	Si_3N_4	Beam + On-chip Interferometer
20	Yuan et al. [217]	Si_3N_4	Membrane + Superconducting Microwave Cavity
21	Purdy et al. [59]	Si_3N_4	Membrane + Fabry Pérot Cavity
22	Yuan et al. [218]	Si_3N_4	Membrane + Superconducting Microwave Cavity

5.4.2 Optomechanical transduction and thermal bistablility

To investigate the response of the cavity optomechanical transduction, S_P was monitored while λ_{l} was scanned across λ_{o}. Figure 5.4(a) shows the resulting measurement of $S_P(f, \lambda_{\mathrm{l}})$ for the microdisk in Fig. 5.1(a), clearly illustrating that optomechanical transduction is only observable when λ_{l} is tuned in the vicinity of λ_{o}. In this measurement the EDFA was connected to the input side of the fiber taper, resulting in maximum $N \sim 6.5 \times 10^5$ and $P_{\mathrm{d}} \sim 1.5$ mW, where P_{d} is the optical power dropped into the microdisk mode. From the thermo-optic coefficient of diamond we estimate that the shift of 400 pm from the cold cavity λ_{o}, as seen in Figure 5.4(a), corresponds to a change in device temperature $\Delta\mathrm{T} \sim 50$ K. COMSOL simulations that take into account the reduced thermal conductivity coefficient of the ~ 100 nm diameter pedestal compared to bulk [221] confirm that an absorbed power of $\sim 10\%$ of P_{d} reproduces the temperature shift observed here, as shown in Fig. 5.3.

When analyzing the mechanical response of a function of laser wavelength it is essential

that we know the detuning from the optical cavity for all $\lambda_{\rm l}$, which is complicated by the thermal shift of $\lambda_{\rm o}$ due to linear absorption of light in the microdisk. The process for extracting the power dependent detuning, Δ used here follows Carmon et al. [56], beginning with the expression for the shifted cavity resonance wavelength as a function of temperature, in thermal equilibrium

$$\lambda'_{\rm o}(\Delta{\rm T}) = \lambda_{\rm o} + \Delta\lambda_{\rm o}\,, \tag{5.1}$$

$$= \lambda_{\rm o}\left[1 + \left(\eta_\epsilon\epsilon + \eta_T\frac{1}{n}\frac{dn}{d{\rm T}}\right)\Delta{\rm T}\right]\,, \tag{5.2}$$

$$= \lambda_{\rm o}\left[1 + a\Delta{\rm T}\right]. \tag{5.3}$$

This expression is obtained by considering thermal expansion of the cavity, determined by the thermal expansion coefficient ϵ, and the thermo-optic effect, which shifts the refractive index n with temperature T. Here $\eta_{\rm T}$ and η_ϵ are geometric factors accounting for the optical mode overlap with the changing n and volume, respectively. Lumped constant a describes the net thermo-optic dispersion of the cavity mode. Using the room temperature SCD values of $\epsilon \sim 1\times10^{-6}$ and $dn/d{\rm T} \sim 1\times10^{-5}$ we can estimate the change in temperature of the cavity as

$$\Delta{\rm T} = \left[\frac{\lambda'_{\rm o}(\Delta{\rm T})}{\lambda_{\rm o}} - 1\right]\cdot\frac{1}{a}. \tag{5.4}$$

The shift of $\Delta\lambda_{\rm o} \sim 400$ pm, as seen in Fig. 5.4, corresponds to a change in device temperature $\Delta{\rm T} \sim 50$ K. In this device the diamond forming the ~ 100 nm diameter pedestal has a significantly smaller thermal conductivity than that of bulk diamond (${\rm K} \sim 1500\,{\rm Wm^{-1}K^{-1}}$), reaching values $< 100\,{\rm Wm^{-1}K^{-1}}$ for nanowires < 100 nm in diameter [221]. In order to confirm that the cavity temperature shift predicted by Equation (5.4) was reasonable for our system we performed finite element COMSOL simulations to estimate $\Delta{\rm T}$, including the modified thermal conductivity for the pedestal, as shown in Fig. 5.3 for varying pedestal

widths. Fig. 5.3 indicates that for a pedestal width of $\sim$ 100 nm, and corresponding diamond thermal conductivity of $\sim 300\,\mathrm{Wm^{-1}K^{-1}}$ a shift of 50 K is expected when $P_{\mathrm{abs}} \sim 170\,\mu\mathrm{W}$, where P_{abs} is the total power absorbed by the cavity. This corresponds to an optical absorption rate, $\kappa_{\mathrm{abs}} \times 2\pi \sim 312$ MHz, which is $\sim 10\%$ of the total cavity decay rate, κ. A linear relationship between ΔT and P_{abs} is observed for the pedestal thicknesses studied here.

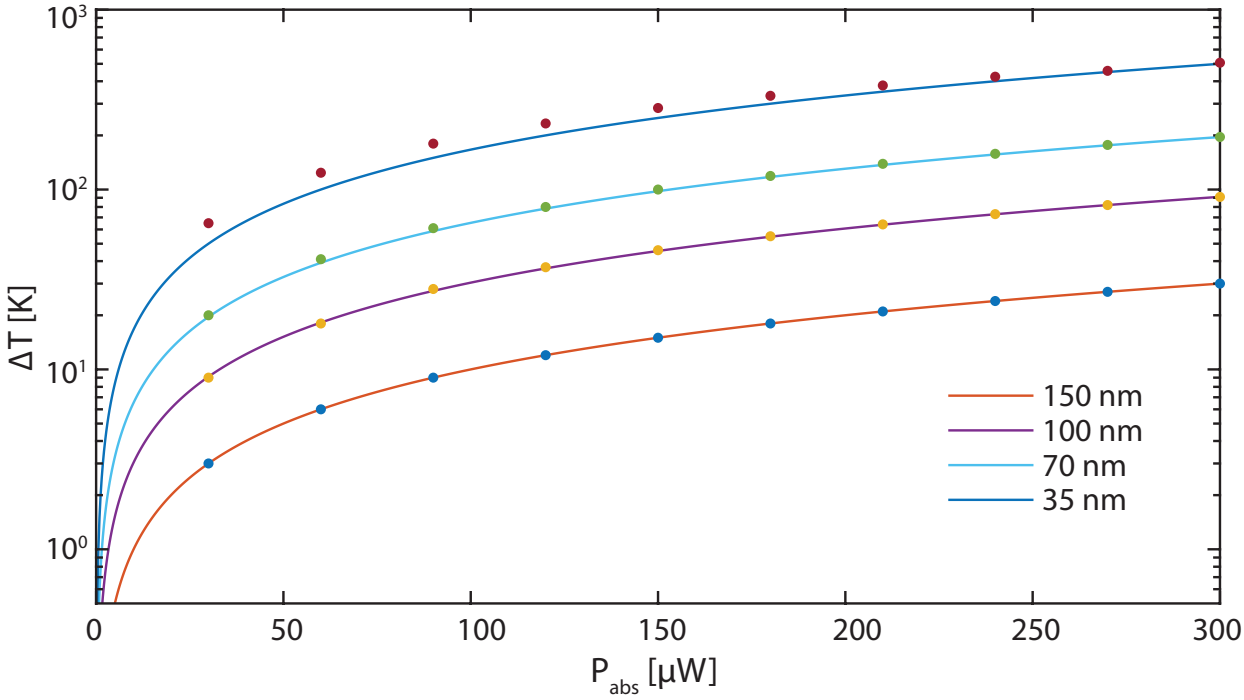

Figure 5.3: Simulated change in temperature, ΔT of a $\sim 5\,\mu$m diameter microdisk as a function of absorbed power, P_{abs} for varying pedestal widths. Here the total heat flow to the device is given by P_{abs}/V, where V is the volume defined by the outer edge of the microdisk, with $V \sim 2\,\mu\mathrm{m}^3$. Each line represents a linear line of best fit to ΔT as a function of P_{abs}

.

To convert Equation (5.3) to a form that depends on the experimentally measured, normalized cavity transmission $\overline{T}$, we treat the microdisk as being in thermal equilibrium with its environment such that

$$\dot{q}_{\mathrm{in}} = \frac{\kappa_{\mathrm{abs}}}{\kappa} P_{\mathrm{d}}\,, \tag{5.5}$$

where $\dot{q}_{\mathrm{in}}$, and P_{d} are the heat flow and power dropped into the cavity, respectively. Furthermore, we assume that

$$\dot{q}_{\mathrm{out}} = K\Delta\mathrm{T}\,, \tag{5.6}$$

where K is the thermal conductivity between the cavity mode volume and the surrounding [56]. In thermal equilibrium the heat flow into the cavity will be equal to the heat flow out of the cavity, which allows us to write the equilibrium temperature as

$$\Delta \mathrm{T} = \frac{\kappa_{\mathrm{abs}}}{\kappa}\frac{P_{\mathrm{d}}}{K}. \tag{5.7}$$

Next we observe that since $P_{\mathrm{d}} = (1-\overline{T})P_{\mathrm{in}}$ where P_{in} is the fiber taper waveguide input power, we can write

$$\Delta \mathrm{T} = \frac{\kappa_{\mathrm{abs}}}{\kappa}\frac{(1-\overline{T})P_{\mathrm{in}}}{K}\,, \tag{5.8}$$

and the expected cavity mode shift in terms of the resonance contrast

$$\lambda_{\mathrm{o}}'(\Delta \mathrm{T}) = \lambda_{\mathrm{o}}\left[1 + a\Delta \mathrm{T}\right]\,, \tag{5.9}$$

$$= \lambda_{\mathrm{o}}\left[1 + \left(\frac{a}{K}\frac{\kappa_{\mathrm{abs}}}{\kappa}P_{\mathrm{in}}\right)(1-\overline{T})\right]\,, \tag{5.10}$$

$$= \lambda_{\mathrm{o}}\left[1 + d(1-\overline{T})\right]. \tag{5.11}$$

This gives the laser-cavity wavelength detuning, Δ_λ as

$$\Delta_\lambda = \lambda_{\mathrm{l}} - \lambda_{\mathrm{o}}'\,, \tag{5.12}$$

$$= \lambda_{\mathrm{l}} - \lambda_{\mathrm{o}} - d(1-\overline{T}). \tag{5.13}$$

where $d = \frac{a}{K}\frac{\kappa_{\mathrm{abs}}}{\kappa}P_{\mathrm{in}}$ is used as a free parameter in fitting our cavity transmission profile. The laser detuning Δ can then be calculated for any bistable lineshape.

Although the temperature increase observed here is not desirable for quantum optomechanics applications, it is considerably smaller than the expected increase for a similar Si device. Assuming a similar absorption rate and identical device geometry, a Si device with a Si or SiO_2 pedestal would result in $\Delta \mathrm{T} \sim 200$ K or 450 K, respectively, where a modified thermal conductivity also applies for the silicon in the pedestal [222]. It is expected that

the rate of linear absorption observed here, which corresponds to $Q_{\rm abs} = 6.2 \times 10^5$, can be reduced through improvements to processing, as diamond devices with $Q_{\rm o} > 10^6$ have been reported elsewhere [145].

5.4.3 Optomechanical backaction

The influence of cavity optomechanical backaction [18] on the dynamics of the mechanical resonator is analyzed in Figs. 5.4. The optomechanical damping/anti-damping, $\Gamma_{\rm opt}$, and spring effect, $\delta\omega_{\rm m}$, were measured as a function of laser-cavity detuning $\Delta = \omega_{\rm l} - \omega_{\rm o}$. Their strong dependence on Δ clearly indicates that the mechanical dynamics are affected by the intracavity field. We were prevented from measuring significant $\Gamma_{\rm opt}$ and $\delta\omega_{\rm m}$ for red-detuned wavelengths ($\Delta < 0$) due to the thermal bistability (see discussion in Section 6.6) present in our system for large $P_{\rm d}$, as shown in Fig. 5.4(a), and described further in Section 6.6. As such, this study concentrated on blue-detuned wavelengths ($\Delta > 0$) only. Determining Δ for each data point in this analysis required accounting for the dependence of $\omega_{\rm o}$ on N due to the thermo-optic effect, as discussed in Section 5.4.2. For a given operating $\omega_{\rm l}$, $\omega_{\rm o}$ was predicted from N, where $N(\omega_{\rm l})$ was determined from $\overline{T}(\omega_{\rm l})$, $P_{\rm in}$, $Q_{\rm i}$ and measurements of loss through the fiber taper and other elements of the apparatus.

To quantitatively investigate the role of radiation pressure on the mechanical resonance dynamics, the observed $\Gamma_{\rm opt}(\Delta)$ was fit to Equation 2.61, with the single photon optomechanical coupling rate g_0 as the only free parameter. Using this method, the fit shown in Fig. 5.4(b) was obtained for $g_0/2\pi \sim 26\,{\rm kHz}$, with an associated 95% confidence interval of ± 2 kHz. Errors bars for each $\Gamma_{\rm opt}$ data point in Fig. 5.4(b) represent the 95% confidence interval of fits used to extract $\Gamma_{\rm m}$ from S_P. The large uncertainty as well as the discrepancy between the measured and predicted values when $\Delta \sim 0$ or $\gg \kappa$ are due to the low signal to noise of S_P in these regions. This low signal to noise of S_P also prohibited measuring the optomechanical response for $\Delta \gg \kappa$. The fit value for g_0 has good agreement with g_0 predicted from COMSOL calculations that include both moving boundary (MB) and pho-

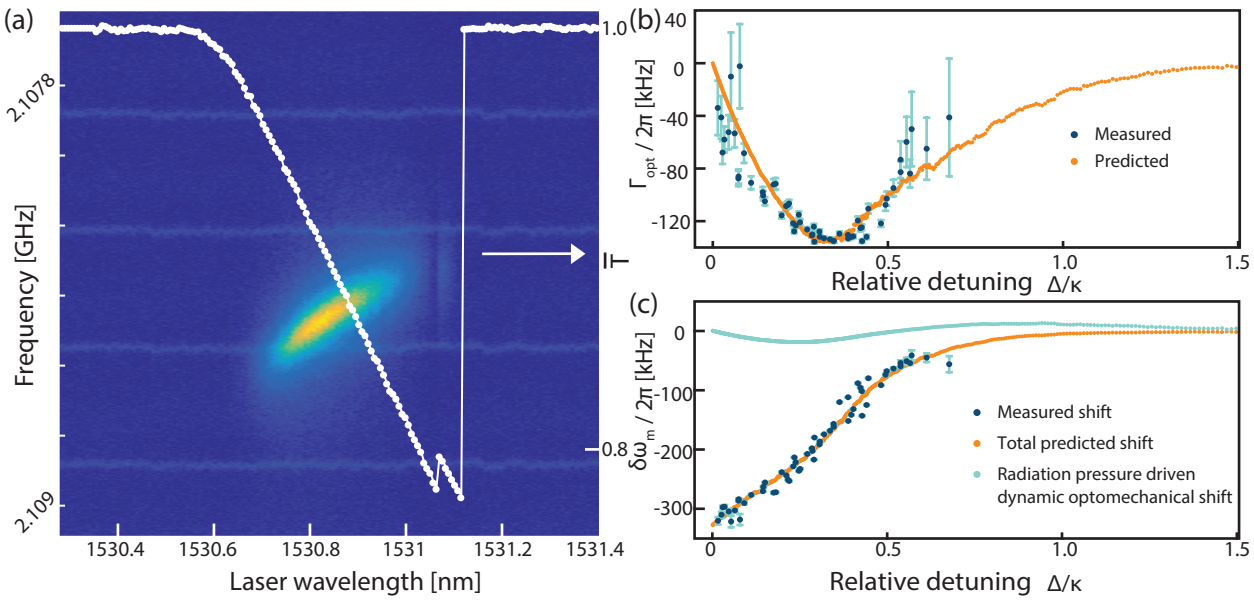

Figure 5.4: Optomechanical backaction measurements. (a) $S_P(f, \lambda_l)$ and corresponding fiber transmission $T(\lambda)$ for $P_{\rm in}$ corresponding to maximum $N \sim 6.5 \times 10^5$ and $P_{\rm d} \sim 1.5$ mW. The regularly spaced horizontal features are electronic noise from the apparatus. (b) Observed and predicted optomechanical linewidth narrowing of the RBM. The predicted $\Gamma_{\rm opt}$ depends on measured N and Δ for each point, as well as fitting parameter $g_0/2\pi = 26 \pm 2$ kHz. Error bars indicate 95% confidence interval for $\Gamma_{\rm m}$ extracted from $S_P(f)$ at each data point. (c) Observed and predicted $\delta\omega_m$. Both the predicted shift due to optomechanical backaction for g_0 found from the fits in (b), and the predicted shift including an additional static thermal softening determined by a free fitting parameter, are shown.

toelastic (PE) contributions [52]. The predicted g_0 is dependent on the spatial overlap of the optical field and mechanical displacement profile, which varies for each optical mode. We find that the fit value of g_0 most closely agrees with the predicted coupling rate to the second order radial TM-like mode, with $g_{0_{PE}}/2\pi = 18$ to 24 kHz and $g_{0_{MB}}/2\pi = 16$ kHz. In comparison, $g_{0_{MB}}/2\pi = 17$ kHz (19 kHz) and $g_{0_{PE}}/2\pi = 29$ to 36 kHz (-24 to -26 kHz) for the fundamental TM (TE) mode of the microdisk. This is consistent with measurements of the mode polarization in the fiber taper that indicated that the microdisk mode studied here is TM polarized. Note that the stated uncertainty in the predicted $g_{0_{PE}}$ is due to variations in reported PE coefficients of single-crystal diamond [223].

Figure 5.4(c) shows a similar analysis of $\delta\omega_{\rm m}(\Delta)$, indicating that $\omega_{\rm m}$ is softened by over 300 kHz by the intracavity field. This shift is due to both optomechanical dynamical backaction and static thermal effects. For the operating regime and devices used here, dynamic

thermal effects are expected to be below 5% of the optomechanical radiation pressure dynamical backaction effects, and can be neglected [116]. However, static thermal effects are significant. Heating of the microdisk for large $P_{\rm d}$ results in both thermal expansion and a change in Young's modulus, resulting in a shift to $\omega_{\rm m}$ [100, 138, 224]. This effect is linear in $P_{\rm d}$, assuming that $Q_{\rm o}$ is independent of power, i.e., nonlinear absorption is small. To compare the measured $\delta\omega_{\rm m}(\Delta)$ with theory, we used a model that includes radiation pressure induced optomechanical dynamic backaction (Equation 2.60) and a static heating term linearly proportional to $P_{\rm d}$:

$$\begin{aligned}\delta\omega_{\rm m}(\Delta) =& g_0^2 N \left[\frac{\Delta-\omega_{\rm m}}{\kappa^2/4+(\Delta-\omega_{\rm m})^2}+\frac{\Delta+\omega_{\rm m}}{\kappa^2/4+(\Delta+\omega_{\rm m})^2}\right] \\ &+\alpha P_{\rm d}. \end{aligned} \tag{5.14}$$

The resulting fit of Equation 5.14 to the measured $\delta\omega_{\rm m}$ is shown in Fig. 5.4(c) to have close agreement. Notably, this model reproduces the kink in $\delta\omega_{\rm m}(\Delta)$ where the amplitude of the optomechanical contribution reaches a maximum and changes sign. This fit was obtained with g_0 fixed to the value extracted from the analysis of $\Gamma_{\rm opt}$ in Fig. 5.4(b), and with α as a fitting parameter.

5.5 Optomechanically induced self-oscillation

At higher power the microdisk optomechanical dynamics can be dramatically modified. Figure 5.5 shows the behavior of the microdisk RBM when the input power to the fiber taper is increased sufficiently for $P_{\rm d}$ to reach 13 mW. This elevated power level corresponds to an intracavity photon number $N \sim 2.8\times10^6$, and an optomechanical cooperativity $C = 2.7$ for the device shown in Fig. 5.1(a). This C exceeds all previously reported values for devices operating in ambient conditions [61, 111]. For such large $P_{\rm d}$, if the input $\lambda_{\rm l}$ is appropriately blue detuned from $\lambda_{\rm o}$, it is possible for $\Gamma_{\rm opt}+\Gamma_{\rm m}\rightarrow 0$, resulting in self-oscillation of

the microdisk RBM. Operation in this regime results in large dynamical strain within the microdisk, offering a potential path for achieving for large NV spin-phonon coupling.

We predict the strain achievable in our devices from measurements as follows. The microdisk mechanical response in the transition from thermal motion to self-oscillation is shown in Fig. 5.5(a), which displays $S_P(f;\lambda_{\rm opt})$ for varying $P_{\rm d}$, with $\lambda_{\rm l}$ tuned to the value $\lambda_{\rm opt}$ where $S_P(f_{\rm m})$ is maximum.

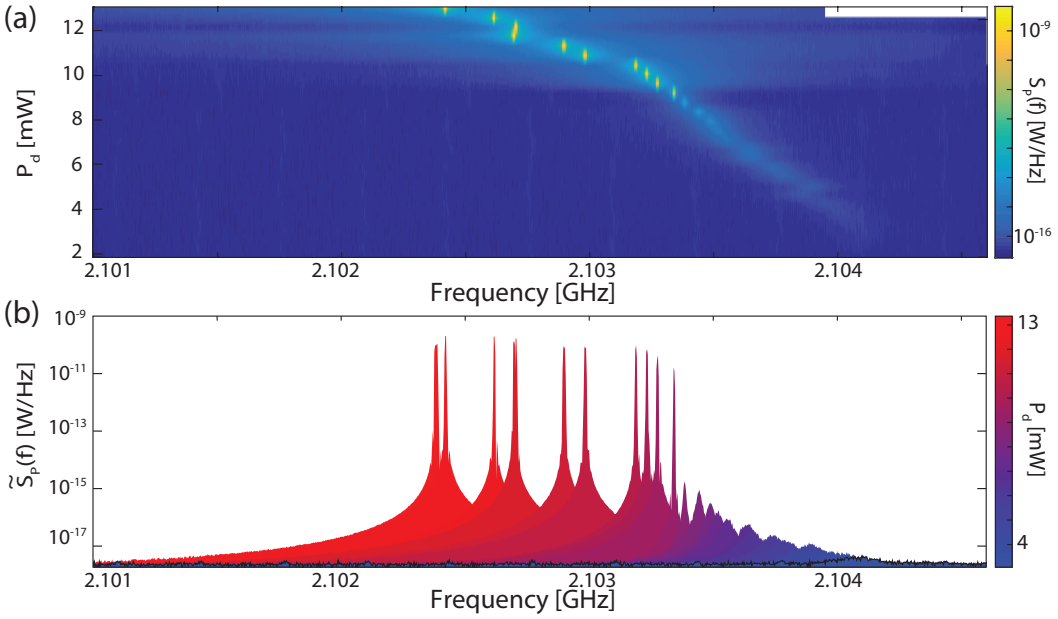

Figure 5.5: Observation of microdisk self-oscillation. (a) $S_P(f;\lambda_{\rm opt})$ as a function of dropped power. (b) Normalized cross-sections of (a), where $\tilde{S}_P(f)$ is given by $S_P(f;\lambda_{\rm opt})$ normalized by the transduction gain so that the area under the curve represents the mechanical energy of the RBM. The black data is the thermal displacement spectra, and the jumps in mechanical frequency are a result of thermal instability due to linear absorption based heating of the device.

As $P_{\rm d}$ is increased the mechanical resonance is observed to narrow and increase in amplitude, suggestive of the onset of self-oscillations. This is more clearly illustrated in Fig. 5.5(b), which shows the normalized spectrum $\tilde{S}_P(f)$ for varying $P_{\rm d}$. Here $\tilde{S}_P(f)$ has been obtained by normalizing $S_P(f;\lambda_{\rm opt})$ with the power dependent transduction gain, such that the area under $\tilde{S}_P(f)$ represents the mechanical energy of the RBM, i.e. $\tilde{S}_P$ is constant with respect to $P_{\rm in}$ in absence of optomechanical backaction. In the weak damping regime ($\Gamma_{\rm m} \ll \omega_{\rm m}$) the oscillation amplitude of a thermally driven harmonic oscillator is given by the equipartition

theorem [18] as

$$x_{\mathrm{th}} = \sqrt{\frac{k_B \mathrm{T}}{m_{\mathrm{eff}}\omega_{\mathrm{m}}^2}}\,, \tag{5.15}$$

where k_B is the Boltzmann constant, T = 295 K is the bath temperature, and $m_{\mathrm{eff}} = 40$ pg and $\omega_{\mathrm{m}}/2\pi \sim 2$ GHz are the effective mass and mechanical frequency of the radial breathing mode studied here, respectively. This results in $x_{\mathrm{th}} = 24$ fm and a zero point fluctuation amplitude, $x_{\mathrm{zpf}} = 0.32$ fm.

While $S_P(f) \propto \langle x^2 \rangle$, where $\langle x^2 \rangle$ is the variance of the mechanical displacement, one must be more careful when calculating the mechanical energy. Strictly speaking $\langle x^2 \rangle$ is related to the single sided displacement spectral density $S_{xx}(\omega)$ by

$$\langle x^2 \rangle = \int_0^\infty S_{xx}(\omega) \frac{d\omega}{2\pi}. \tag{5.16}$$

This can be connected to the measured cavity transmission noise spectrum $S_P(\omega)$ through a cavity transfer function $H(\omega, \Delta)$, P_{in}, and G [225]

$$S_P(\omega) = G^2 P_{\mathrm{in}}^2 S_{xx}(\omega) H(\omega, \Delta). \tag{5.17}$$

In this experiment we measure $S_P(\omega)$, and can compute the area under the curve, A, given by $A = \int_0^\infty S_P(\omega)\frac{d\omega}{2\pi}$. If we change P_{in} from P_{in_1} to P_{in_2}, keep Δ constant,and ignore the small ($\sim 0.02\%$) changes in ω_{m}, such that $H(\omega, \Delta; P_{\mathrm{in}_1}) = H(\omega, \Delta; P_{\mathrm{in}_2})$, we can show that the ratio of the area under the curve corresponding to P_{in_1} and P_{in_2} given by A_1 and A_2, respectively, is

$$\frac{A_1}{A_2} = \frac{P_{\mathrm{in}_1}^2 \langle x_1^2 \rangle}{P_{\mathrm{in}_2}^2 \langle x_2^2 \rangle}. \tag{5.18}$$

We can then calibrate high P_{in} measurements to the thermal case, where P_{in} is small enough for optomechanical backaction effects to be ignored. The displacement amplitude, x_{om}, of

the RBM in the self-oscillation regime can then be calculated as

$$x_{\rm om} = x_{\rm th}\sqrt{\frac{A_{\rm om}}{A_{\rm th}}\frac{P_{\rm T}^2}{P_{\rm om}^2}}\,, \tag{5.19}$$

where $\rm A_{om}$ and $\rm A_{th}$ are the area under the curve in the driven ($P_{\rm in} = P_{\rm om}$) and thermal ($P_{\rm in} = P_{\rm T}$) states, respectively. Similarly, for the purpose of comparing mechanical spectra it is useful to calculate the normalized cavity transmission noise spectrum $\tilde{S}_P$, given by

$$\tilde{S}_P(\omega; P_{\rm in}, \Delta) = S_P(\omega; P_{\rm in})\frac{P_{\rm in}^2}{P_{\rm T}^2}\bigg|_{\Delta}\,. \tag{5.20}$$

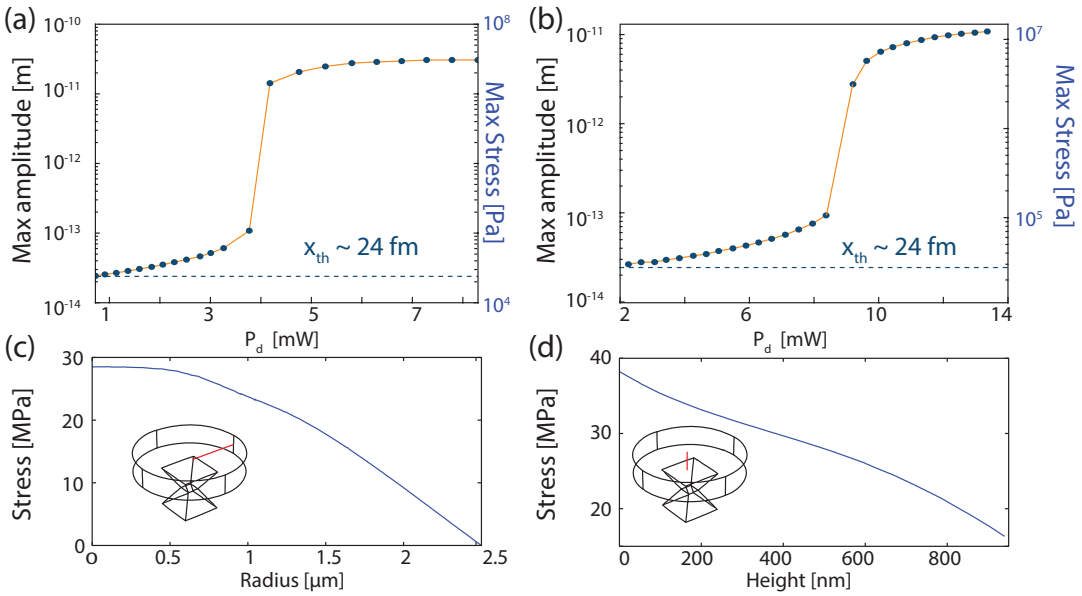

Figure 5.6: (a, b) Maximum displacement amplitude and stress for 5 μm diameter devices with (a) $Q_{\rm m} \sim 9000$, $Q_{\rm o} \sim 6 \times 10^4$, and (b) $Q_{\rm m} \sim 8000$, $Q_{\rm o} \sim 4 \times 10^4$. (c,d) Simulated stress along (c) radial and (d) vertical cuts in the microdisk, as indicated by the red lines in the insets, for the self-oscillating amplitude in (a,b).

At low power, this mechanical energy is dominantly from the thermal bath, and is predicted from the equipartition theorem to correspond to oscillation amplitude $x_{\rm th} \sim 24\,$fm. Figures 5.6(a,b) show that for large $P_{\rm d}$ a maximum $x_{\rm om} = 31\,$pm is reached, likely limited by nonlinearity of the material. The corresponding predicted stress maximum associated with the self-oscillations, also shown in Figs. 5.6(c) and (d), is $> 30\,$MPa. Stress values were

determined from $x_{\rm om}$ and finite element simulations of the RBM displacement field shown in Fig. 5.1(a), assuming that diamond behaves as a linear elastic material. This predicts that the maximum stress is predicted to occur at the center of the microdisk top surface, as shown by the plots in Figs. 5.6(c,d). The corresponding maximum strain is $\approx 30 \times 10^{-6}$.

The self-oscillation threshold behaviour can be quantitatively analyzed by extracting the mechanical displacement amplitude $x_{\rm om}$ as a function of $P_{\rm d}$ from $\tilde{S}_P$. This is shown Figs. 5.6(a,b) for two similarly sized microdisks. In each case, a clear threshold is observed. Since these microdisks have different $Q_{\rm m}$ and $Q_{\rm o}$ (see Fig. 5.6 caption), their threshold power $P_{\rm T}$ differ. For devices close to the sideband resolved regime, the optimal detuning for self-oscillation to occur is $\Delta \sim \omega_{\rm m}$, and $P_{\rm T}$ is given by [226]

$$P_{\rm T} = \frac{m_{\rm eff}\omega_{\rm o}}{2G^2}\frac{\Gamma_{\rm m}\kappa_{\rm i}}{\omega_{\rm m}\kappa}(\kappa/2)^2[(2\omega_{\rm m})^2 + (\kappa/2)^2]. \tag{5.21}$$

The observed $P_{\rm T} = 3.5\,{\rm mW}$ and $8.5\,{\rm mW}$, for the devices in Figs. 5.6(a) and 5.6(b) respectively, are above the predicted values of $760\,\mu{\rm W}$ and $3.0\,{\rm mW}$ obtained from 5.21 assuming g_0 is given by the fits in Fig. 5.4. This disagreement could be related to uncertainty in κ given that $P_{\rm T}$ scales to the fourth power of this quantity, interplay between doublets that is ignored by 5.21, and uncertainty in Δ inferred from the cavity response in the presence of thermo-optic dispersion.

5.6 Potential for hybrid spin-optomechanics

The potential of these devices for hybrid spin-optomechanics applications can be measured by the predicted strain coupling rate g_{e^-} between a single phonon of the microdisk RBM and a single diamond NV center electron spin. The maximum zero point amplitude strain of the RBM is $\epsilon_{\rm zpf} \approx 3 \times 10^{-10}$, and we estimate $g_{e^-}/2\pi = d\,\epsilon_{\rm zpf} \approx 6\,{\rm Hz}$ for a negatively charged NV^- center electron spin optimally located 50 nm below the top surface of the device in Fig. 5.5(c), exceeding the highest rate demonstrated to date [192]. Here $d \approx 10 - 20$ GHz is

the strain susceptibility of the ground state spin [190, 191]. When the RBM is self-oscillating as in Fig. 5.5(c), the predicted coupling rate is $G_{e^-}/2\pi \approx 0.6\,\mathrm{MHz}$ [190]. This is comparable to coupling rates achieved in piezoelectric actuated nanomechanical [190, 191, 192] and bulk devices [188, 193]. The longest room-temperature ground state spin decoherence time (T_2) observed to date in isotopically engineered single-crystal diamond is 1.8 ms [172], while typical T_2 values in nanostructures are on the order of 100 μs [190, 227]. Additionally, dynamical decoupling schemes can be utilized to extend this time, as $T_2 \sim 600$ ms has been observed at low temperature [228]. Photon-spin control should be possible provided $(G_{e^-}/2\pi)^{-1} > T_2$, which is the case for these devices.

The GHz frequency of the RBM enables low room temperature phonon occupation, relevant for cooling to the quantum ground state from room temperature [29]. This also enables access to larger energy spin transitions [188, 193] than possible using previously demonstrated diamond nanomechanical resonators. This may be particularly important for future studies of phonon coupling to the NV^- center excited state manifold, which could achieve single phonon coupling rates close to a MHz due to the $\sim 10^5$ times larger strain susceptibility of the excited states [195, 202, 229, 230]. This is promising for implementing fully quantum photon-phonon-spin interfaces, and for proposals of spin-mediated cooling of nanomechanical resonators [197, 201, 202].

In the samples under study, we expect to find NVs optimally coupled to the RBM since the nitrogen concentration for this diamond sample ($\sim$ ppm, corresponding to a number density of $1.76 \times 10^5 \mu\mathrm{m}^{-3}$) results in high-concentration NV ensembles. However, future studies with higher purity samples may require NV implantation to optimally locate NVs $\sim$ 50 nm below the device surface. Additionally, due to minimal coupling of fluorescence from an NV centre located at the centre of the disk to the optical modes, free space collection would most likely be required. However, use of higher order radial breathing modes could allow for greater spatial overlap of the strain and electromagnetic field maxima [104], allowing for more efficient fiber based excitation and collection.

5.7 Summary & outlook

In summary, we have shown that cavity optomechanical devices can be realized from single-crystal diamond, with record high ambient condition optomecanical cooperativity, $C \sim 3$, and $Q_\mathrm{m} \cdot f_\mathrm{m}$ product of 1.9×10^{13} Hz. These devices are a promising testbed for ambient condition coherent optomechanics experiments, e.g. ground state cooling [29], optomechanically induced transparency [61, 63, 111] and phonon mediated wavelength conversion [44, 45, 61], as well as studies in quantum information science [231], and hybrid quantum systems involving light, phonons, and diamond NV center spins [188, 190, 191, 192, 197, 201, 203]. We have also shown that the microdisks demonstrated here support high-Q_i optical modes at wavelengths near-resonant with the 637 nm optical transition of NV centers, further enhancing their potential for photon-phonon-spin coupling experiments. We note that, in parallel to this work, Burek et al. demonstrated cavity optomechanics in single-crystal diamond optomechanical crystals fabricated by a Faraday cage angled-etching technique. We coordinated with Burek et al. such that our articles were published concurrently [70].

While this work was a successful demonstration of cavity optomechanics in SCD, the mechanical and optical properties of the microdisks left much room for improvement. Improvements to Q_o to values above 10^5 and approaching 10^6 should be possible in microdisks [3, 183], enabling ultralow self-oscillation threshold [226] and operation deep in the sideband resolved regime required for optomechanical ground state cooling [29], optomechanically induced transparency [63, 111], and wavelength conversion [44, 45]. Operating in vacuum, at low temperature, and using devices fabricated from high-purity electronic grade diamond may allow further increases in Q_m [176], boosting the achievable photon-phonon cooperativity C and $Q_\mathrm{m} \cdot f_\mathrm{m}$ product. Similarly, reducing the microdisk diameter may increase C through enhanced g_0, while also increasing ω_m. Simulations predict that diameters close to 3.5 μm are possible before radiation loss limits $Q_\mathrm{i} < 10^5$; such devices would have $g_0/2\pi > 95$ kHz and $f_\mathrm{m} \sim 3.4\,\mathrm{GHz}$. Finally, using electronic grade diamond material and investigating processing techniques to reduce surface state absorption may decrease optical absorption and allow

larger N before device heating becomes significant. Chapter 6 will discuss the optimization work that was carried out to enhance the performance of these devices. This optimization ultimately resulted in microdisk structures that operate in the sideband resolved regime and were utilized to demonstrate coherent cavity optomechanics at room temperature.

Chapter 6

SCD microdisks: optimization for room-temperature cavity optomechanics

6.1 Introduction

The fabrication process outlined in Chapter 4 has since become the standard technique for researchers fabricating a wide variety of nanoscale structures from bulk SCD [232, 233, 234]. The properties of the quasi-isotropic etch and its interaction with the diamond crystal planes have also been investigated in detail by Xie et al. [235]. This was encouraging for us as it was a sign that we were doing good work, but also meant more competition. In this chapter, we provide a detailed description of the modifications and optimization that was performed on this process to enable coherent cavity optomechaincs at room temperature and pressure. These changes resulted in an increase of optical Q_{i} by $\sim 4\times$ compared to our results reported in Ref. [5]. This places the devices in the resolved sideband regime, which is a requirement for observing efficient radiation-pressure dynamical back-action effects [18, 236], such as ground state cooling [29], and efficient optomechanical wavelength conversion

[44, 45, 61], which we have recently demonstrated [7]. By tailoring the pedestal profile that supports the microdisk we were also able to reduce linear absorption based heating, enabling stable operation with a laser red-detuned from the optical cavity at high N, enabling the demonstration of optomechanically induced transparency [5], and wavelength conversion [7], which will be discussed in Chapter 7.

6.2 Optimized process overview

The modified process used in Ref. [5] for fabricating improved microdisk optomechanical cavities is shown in Fig. 6.1, where the optimized steps that are the focus of this chapter have been highlighted in green. We start, as before, with 3 mm $\times$ 3 mm optical grade, CVD grown, SCD chips purchased from Element Six [185, 186]. These are mechanically polished further by Delaware Diamond Knives to surface roughness < 5 nm RMS, and are cleaned in boiling piranha (150 mL H_2SO_4:50 mL H_2O_2)[1] followed by a 3 $\times$ 30s rinse in H_2O, and drying with N_2. A 300 nm thick PECVD Si_3N_4 layer is deposited as the hard mask. The Si_3N_4 is then coated with a thin anti-charging Ti layer (5 - 10 nm), deposited via EBPVD, followed by a 400 nm spin-coated layer of ZEP 520A (4000 RPM, 60 s, 180°C bake for 5 min while semi-covered by reflective lid). Patterning of the ZEP was performed with beam energy of 30 keV, aperture of 10 μm, and dose factor of 4×80 μC/cm^2, followed by development for 20 s in a bath of ZED-N50, followed by IPA, both cooled to -15°C. The ZEP pattern is then transferred to the Si_3N_4 hard mask layer via ICP-RIE with C_4F_8/SF_6 chemistry using an Oxford PlasmaPro 100 Estrelas Deep Silicon Etching system, instead of the Oxford PlasmaLab Pro 100 used in Chapter 4. This etch step is vital for ensuring smooth sidewalls of the diamond structures and is discussed in Section 6.3. The pattern is then transferred to the diamond layer via a nearly vertical anisotropic O_2 ICP-RIE etch, the optimization of which is discussed in Section 6.4.

[1]Disclaimer: Piranha should be treated with care as it is highly corrosive and a very strong oxidizer. Improper mixing, or introduction of large amounts of organic material may cause an explosion. See Appendix

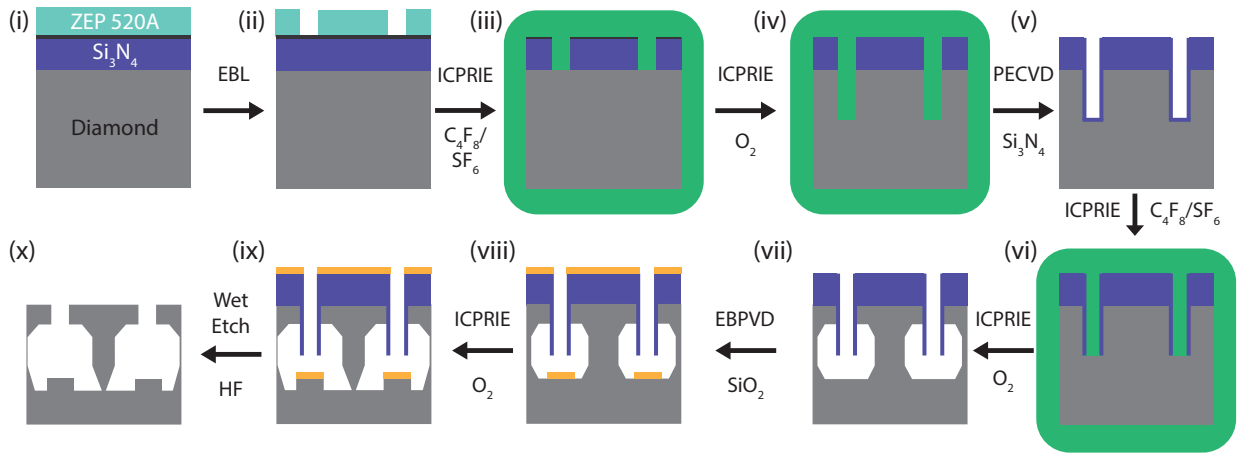

Figure 6.1: Single-crystal diamond fabrication process, where the steps optimized in this work are highlighted in green. (i) 300 nm thick PECVD Si_3N_4 layer, $\sim$ 5 nm of Ti as an anti-charging layer, and EBL resist (ZEP 520A) is deposited. (ii) EBL is performed and chip is developed in ZED N50 followed by IPA at $-15°$C. (iii) Patterns are transferred to the Si_3N_4 hard mask using the optimized ICP-RIE etch discussed in the text. (iv) ZEP is removed using a deep-UV exposure followed by Remover PG, and the pattern is transferred to the diamond using an anisotropic O2 plasma ICP-RIE etch. (v) Sidewall protection layer via a conformal coating of PECVD Si_3N_4. (vi) A short ICP-RIE etch removes Si_3N_4 from the bottom of the etch windows. (vii) An initial zero bias O_2 ICP-RIE plasma partially undercuts the microdisks. (viii) A $\sim$ 100 nm layer of SiO_2 is deposited via electron—beam physical vapor deposition (EBPVD). (ix) A second zero bias O_2 plasma etch is performed, finishing the plasma undercutting process. (x) The sample is soaked in HF to remove the remaining Si_3N_4 layer, followed by a piranha clean.

Before the undercut step, a sidewall protection layer is required to prevent unwanted etching of the patterned device. Here a 150 nm thick conformal layer of PECVD Si_3N_4 was used, however, atomic layer deposited Al_2O_3 has also been successfully employed by Mouradian et al.[232]. This layer is then removed only from the top surface and bottom of the etch wells using the same hard mask etch chemistry and conditions as in the patterning step, which preferentially etches horizontal surfaces. The devices are then undercut via a zero bias O_2 quasi-isotropic etch performed at an elevated temperature (250°C) to reduce the etching time required for sufficient undercutting [4]. An additional SiO_2 electron beam evaporation step was added to alter microdisk pedestal profiles, as depicted in Fig. 6.1(viii-ix) which led to improved thermal handling, and is discussed in Section 6.4. Finally, after sufficient undercutting the hard mask is stripped in 49% HF solution (20 mL)[2], and cleaned

G for handling precautions.

[2]Disclaimer: Hydrofluoric acid (HF) should be treated with care as it is a corrosive acid that can cause extensive tissue damage and death. See Appendix G for handling precautions.

in boiling piranha, where each acid step is followed by a 3 × 30 second rinse in H_2O and drying with N_2. Further post-processing surface treatments are discussed in Section 6.5.

6.3 Hard mask & sidewall protection layer etch optimization

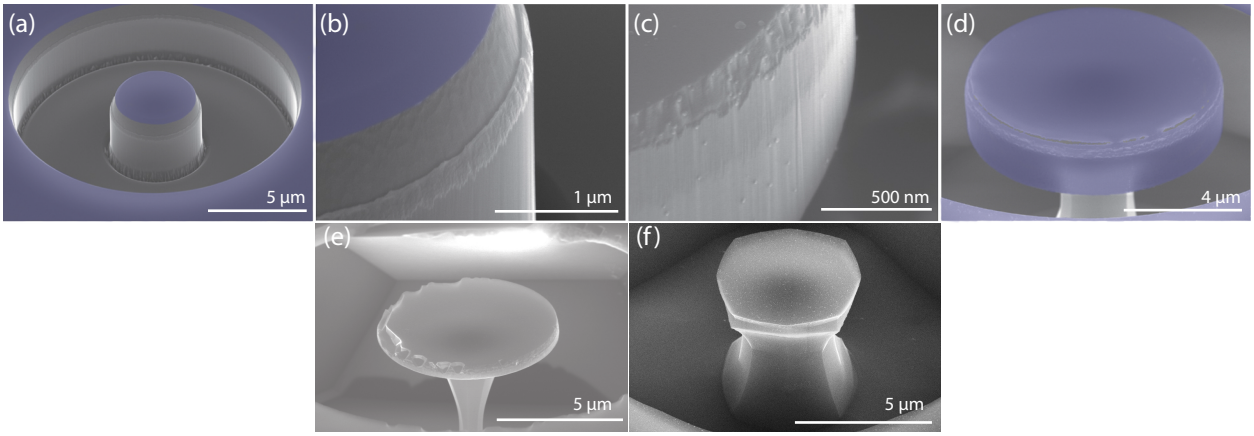

Figure 6.2: Consequences of poor hard mask etch where the Si_3N_4 layer has been colorized; non-colorized surfaces are SCD. (a,b) The highly angled sidewalls of the Si_3N_4 hard mask is a consequence of over-passivation during the etch. (c) This leads to breakthrough of the hard mask layer during the anisotropic diamond etch resulting in "ledge" in the diamond layer. (d) More severe breakthrough, resulting in holes in the hard mask, can also result in complete etching of the device. Result of partial (e) and complete (f) breakthrough of the hardmask layer.

While EBL offers ultra-high resolution nano-lithography, it is vital to make the initial hard mask etch as smooth as possible to reap these benefits. Major limiting factors to Q_i of the previously studied diamond microdisk structures were sidewall roughness and a "ledge" on the top edge of the microdisk [4, 5]. Both of these imperfections were caused by a non-ideal hard mask etch that impacted the quality of the etched vertical surfaces of the SCD. Fig. 6.2(a-c) illustrates the importance of the hard mask etch on the diamond sidewall roughness. The ledge seen in Fig. 6.2(c) was a result of breakthrough of the Si_3N_4 hard mask's angled sidewalls during the anisotropic diamond etch, as seen in Fig. 6.2(d). It was also found that this ledge caused breakthrough of the sidewall protection layer during the quasi-isotropic plasma undercutting step (Fig. 6.1(vii)). Prior to the etch optimization

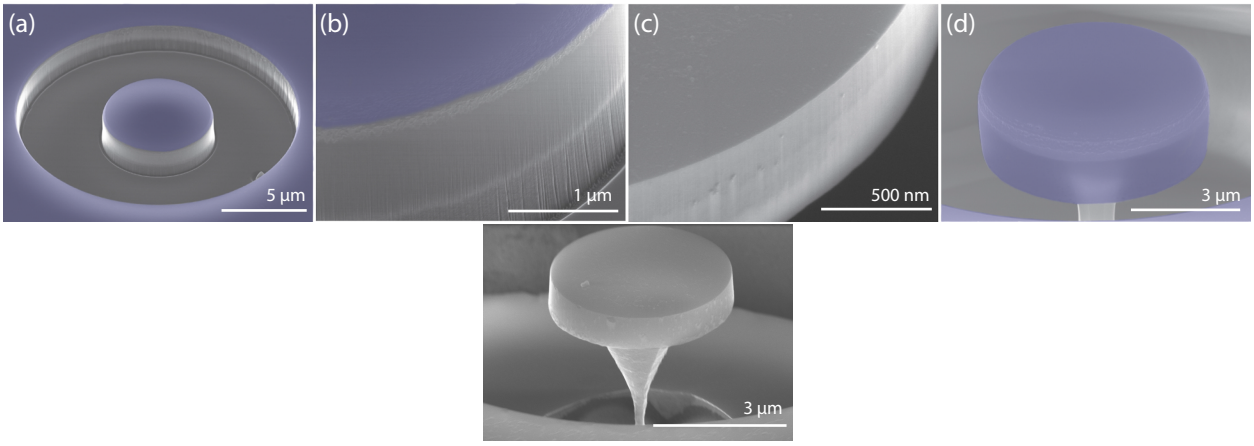

Figure 6.3: Result of optimized hard mask etch where the Si_3N_4 layer has been colorized; non-colorized surfaces are SCD. (a,b) The optimized hard mask etch resulted in less angled, smooth sidewalls that do not exhibit breakthrough during the anisotropic diamond etch. (c,d) Smooth diamond sidewalls resulting from optimized hard mask etch, with no holes in the hardmask layer. (e) Example microdisk structure after subsequent processing described in Section 6.2.

described below, this breakthrough severely limited the yield of the process. In extreme cases it resulted in complete delamination of the sidewall protection layer, and subsequent unwanted etching of the device surfaces, as shown in Fig. 6.2(e,f).

The hard mask etch was optimized following a procedure similar to Hill [237], by performing the identical EBL process described above on $\sim$ 300 nm thick Si_3N_4 deposited on Si substrates. This was stopped when the Si_3N_4 sidewalls were smooth and close to vertical, ensuring that there was no breakthrough during the anisotropic diamond etch as shown in Fig. 6.3(a-c). The optimized ICP-RIE etch parameters are given in Table 6.2. Note that before performing these etch tests the chamber was cleaned for 1 hour with the recipe shown in Table 6.1. Here the ICP column refers to the power applied to the coil responsible for generating the plasma, hence controlling the ion density, while the RF column refers to the power applied to the coil responsible for accelerating the ions towards the substrate, controlling ion energy. In optimizing this etch the temperature (15°C) and pressure (10 mTorr) were held constant. Initially tests were performed to find a bounding region for the bias voltage, which is a measure of the potential difference between the plasma and substrate electrode, achieved by varying the ICP and RF power and C_4F_8:SF_6 gas ratio. Several it-

T [°C]	Pressure [mTorr]	RF [W]	Bias [V]	ICP [W]	O_2 [sccm]
0	20	150	230	2000	100

Table 6.1: Nominal etch parameters used for the chamber cleaning process with the Oxford PlasmaPro 100 Estrelas.

T [°C]	Pressure [mTorr]	RF [W]	Bias [V]	ICP [W]	C_4F_8 [sccm]	SF_6 [sccm]
15	10	20	50	1200	14	14

Table 6.2: Nominal etch parameters used for patterning the Si_3N_4 hard mask with the Oxford PlasmaPro 100 Estrelas. This results in an etch rate of ~ 3.0 nm/s for PECVD Si_3N_4.

erations were performed holding either the gas ratio or RF and ICP powers constant, while varying the other. The etch quality was analyzed for varying bias voltage and gas ratio until an acceptable etch was achieved, where etch quality was determined by analyzing SEM images post-etching. Overall ratios of C_4F_8:SF_6 from 3.75 to 0.56, ICP powers from 650 – 1800 W, and RF powers from 10–25 W were explored.

6.4 Anisotropic diamond etch optimization

A smooth vertical diamond etch is also critical for realizing devices with low optical loss. To this end, following the Si_3N_4 hard mask etch optimization, the anisotropic diamond etching process was optimized to reduce micromasking effects that can lead to rough device sidewalls [238]. This optimization is also important for future devices such as photonic crystals, whose sensitivity to roughness is enhanced owing to their large surface area to volume ratio, and whose optical design is simplified if vertical sidewalls are achievable.

The anisotropic SCD etches were performed using an Oxford PlasmaPro 100 Cobra ICP system (step (iv) in Fig. 6.1), where the goal of this optimization was to create as smooth of diamond sidewalls as possible to reduce optical loss due to surface roughness [128]. During this optimization the temperature (15°C), chamber pressure (10 mTorr), and O_2 flow rate (30 sccm) of the etches were held constant, and a 1 hour chamber clean was performed before

T [°C]	Pressure [mTorr]	RF [W]	Bias [V]	ICP [W]	O_2 [sccm]	SF_6 [sccm]
15	10	100	220	2000	50	5

Table 6.3: Nominal etch parameters used for the chamber cleaning process with the Oxford PlasmaPro 100 Cobra.

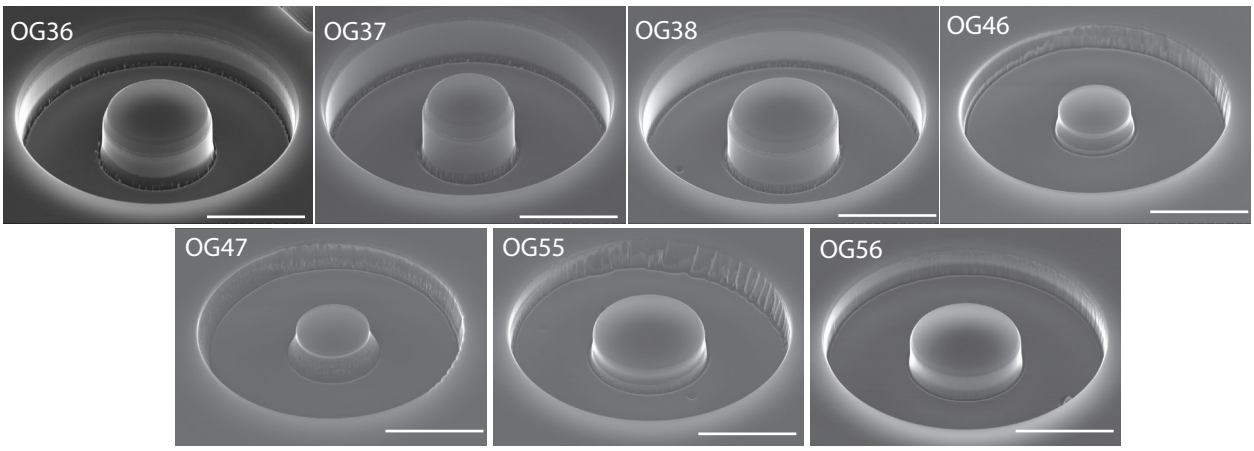

Figure 6.4: Scanning electron micrographs of microdisk structures after the anisotropic etch step for varying RF power. Etch setting at each point in the parameter sweeps RF-α (top two rows of images) and RF-β (bottom row of images) are detailed in Table 6.4. Scale bars are 5 μm.

starting the etches with the parameters listed in Table 6.3. Initially a sweep of the etcher RF power from 20 – 100 W was performed, with the ICP power held constant at 850 W. These etch conditions are labeled RF-α in Table 6.4, and SEM images of the resulting etched devices are shown in Fig. 6.4. From this sweep it is apparent that low RF power results in highly angled sidewalls and slower etch rates, while the high forward RF power induces some roughness at the bases of the sidewalls. The sidewall angle as a function of DC-bias is shown in Fig. 6.6(a), where a maximum angle of $\sim$16° was observed. The etch rate was found to vary less dramatically throughout this sweep, as shown in Fig. 6.6(b). Note that roughness in the surrounding etch window walls present in some of these etches is a result of non-ideal EBL and is not a consequence of the individual diamond etch conditions.

The smoothest etch, identified to be the OG36 conditions as determined by SEM images, was then used as a starting point for an ICP power sweep. During this sweep the DC-bias was kept roughly constant by adjusting the RF power to compensate for variations caused by the changing ICP power. This sweep is labeled "ICP" in Table 6.4, and SEM images

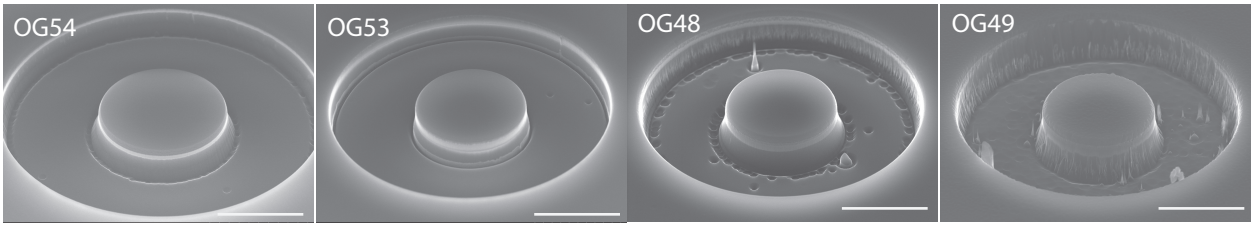

Figure 6.5: Scanning electron micrographs of microdisk structures after the anisotropic etch step for varying ICP power. Etch setting at each point in the parameter sweep are detailed in Table 6.4. Scale bars are 5 μm.

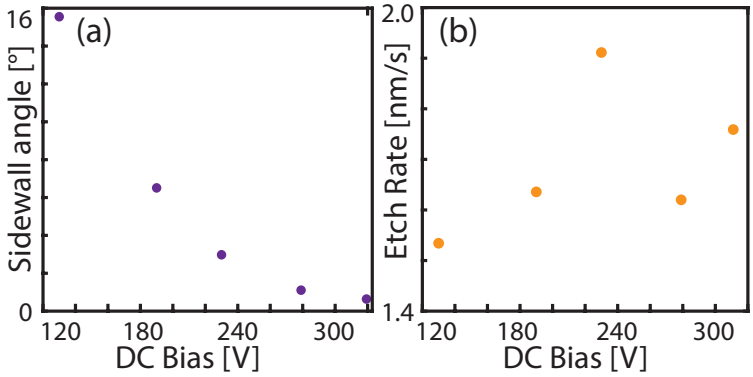

Figure 6.6: Etch rates and sidewall angles for RF sweep points (RF-α) with constant 850 W ICP power. (a) Sidewall etch angle as a function of DC bias, measured from the horizontal. (b) Etch rate as a function of DC bias.

of its results are shown in Fig. 6.5. Based on this sweep, an ICP power of 1000 W was determined to provide the best combination of sidewall smoothness and verticality. This ICP value was used for a final RF sweep, labeled "RF-β'' in Table 6.4. Its results are shown in Fig. 6.4, from which the parameters used for sample OG56 were identified as the optimized combination of etch verticality and sidewall smoothness, and were used in the fabrication of the devices whose optical properties are characterized in Section 6.5, and those studied in Chapter 7.

6.5 Optical characterization and surface treatments

Although the evaluation of the various etch conditions presented above is somewhat qualitative, a more quantitative evaluation is possible by measuring the optical properties of a fully fabricated microdisk. This requires further processing steps (vii) - (x) in Fig. 6.1 in order to

Sample	ICP [W]	RF [W]	Bias [V]	Etch Rate [nm/s]	Sidewall Angle [°]	Sweep
OG47	850	20	130	1.534	15.55	RF-α
OG46	850	40	190	1.636	6.509	
OG38	850	60	230	1.911	2.976	
OG36	850	80	279	1.620	1.107	
OG37	850	100	311	1.759	0.636	
OG54	850	80	281	2.206	13.27	ICP
OG53	1000	90	286	2.454	4.063	
OG48	1150	100	291	3.225	6.952	
OG49	1300	110	293	4.062	8.994	
OG55	1000	100	304	2.685	3.242	RF-β
OG56	1000	110	319	2.378	2.634	

Table 6.4: Parameters used in the anisotropic SCD etch optimization with the Oxford PlasmaPro 100 Cobra. The parameters used for OG56 were found to give the best results, as discussed in the main text. The selectivity of diamond to Si_3N_4 for this etch is 30:1, as the Si_3N_4 etch rate was measured as 0.08 nm/s.

undercut the device, as described in Section 6.2. Step (vii) has already been characterized in Chapter 4, and provides a smooth bottom surface for the undercut microdisk structure, vital to observe high-Q_i optical resonances. The pedestal shaping steps (viii) and (ix) are optional, and are described in Section 6.6 below. In step (x), after stripping the mask layers the sample was cleaned in heated piranha. During this step the sample was placed in H_2SO_4 (6 mL), heated to 70°C before adding H_2O_2 (2 mL), which raised the temperature of the resulting piranha solution to ~ 100°C. After 1 hour the sample was removed and rinsed in H_2O (3×30 s) and dried with N_2.

The optimized devices were evaluated by measuring Q_i of their optical modes and comparing with Q_i of un-optimized devices. Measurements were carried out as before by coupling light from a tunable diode laser to the device via a dimpled optical fiber taper. All measurements were performed in a N_2 purged environment. Fig. 6.7 compares the fiber taper transmission spectrum for the highest-Q_o optical mode observed in a optimized fabrication process microdisk (Fig. 6.7(a)), with that of the highest-Q_o device from earlier work [5] (Fig. 6.7(b)), demonstrating a $\sim 4\times$ improvement in intrinsic quality factor, Q_i, to $Q_i \sim 335,000$. The confidence interval obtained when fitting the optical lineshape to extract Q_i is typically $\ll 1\%$ of Q_i and is omitted in the following analysis and figures as it would not be resolved.

In this work 67 of 154 pre- and 88 of 161 post-optimization devices were initially studied as only a subset of the patterned devices are had a sufficiently small pedestal after the undercut to support high-Q_o modes, as described in Ref. [3]. From this set only devices possessing a doublet structure, as shown in Fig. 6.7, were used in our analysis, which corresponds to 62 pre- and 68 post-optimization devices. This corresponded to the highest-Q_i modes ($Q_i > 1.4 \times 10^4$) of each device, the measurements of which are presented in Figs. 6.9-6.10. Note that the vast majority of singlet modes observed did not exceed this doublet-Q_o cutoff. A small handful of singlet modes with Q_i's up to 5×10^4 were observed, but are omitted from this study. The doublet nature of these modes is created by backscattering that couples the microdisk's nominally degenerate clockwise and counterclockwise traveling wave whispering gallery modes to create standing waves [239, 128]. Each standing wave mode is a symmetric or anti-symmetric superposition of the traveling wave modes, and they can have different Q_i^s and Q_i^a respectively, as their intensity profiles sense different volumes of the microdisk.

As discussed in Section 2.1.1, multiple mechanisms contribute to the total optical loss rate of the microdisks, which scales as $1/Q_o$. Since loss rates are additive, we can write $1/Q_o = 1/Q_i + 1/Q_{ex}$. The intrinsic Q_i can be decomposed as $1/Q_i = 1/Q_{rad} + 1/Q_b + 1/Q_{ss} + 1/Q_{sa}$, where Q_{rad}, Q_b, Q_{ss}, and Q_{sa} relate to radiation loss via leakage into unbound modes, bulk absorption, surface scattering, and surface absorption, respectively. Etch smoothness impacts Q_{ss}, while etch chemistry and other processing that influences the diamond surface can impact Q_{sa}. Q_b is determined by the bulk optical properties of the material, and Q_{rad} is defined by solutions to Maxwell's equations for modes of a device fabricated without any imperfections. Loss related to coupling with the fiber taper is accounted for in the "external" Q_{ex}.

The dominant source of loss can be identified through theoretical calculations or experimental measurements. For typical fiber taper coupling in these devices, $Q_{ex} > 10^6$ is extracted from the fit to the optical resonance. Note that "parasitic" loss introduced by the fiber into modes not involved in input or output coupling can also be accounted for

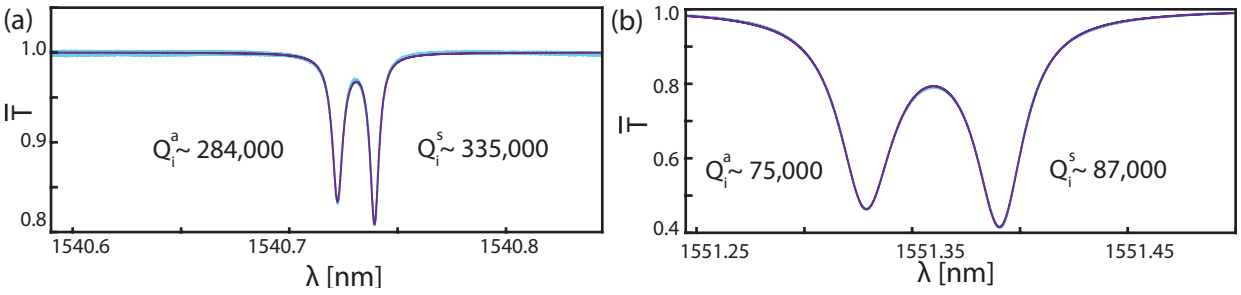

Figure 6.7: (a,b) Normalized fiber transmission as a function of laser wavelength for an optical mode fabricated using the described optimized process (a) compared to previous work (b), for fixed span in λ. The intrinsic quality factor Q_i for the symmetric and antisymmetric modes is extracted by fitting (purple) the transmission profile (blue).

as in Spillane et al.[240], and was found to be small compared to $1/Q_\mathrm{o}$. Bulk loss for a weakly absorbing media can be approximated by $1/Q_\mathrm{b} = \alpha/k$, where the wavenumber $k = 2\pi n_r/\lambda = n_r\omega_\mathrm{o}/v_p$ where ω_o and v_p are the frequency and phase velocity of the light, respectively. Here $\alpha = 4\pi n_i/\lambda$ is the absorption coefficient of the bulk, where n_r and n_i are the real and imaginary parts of the refractive index [241, 242, 243]. Using $\alpha \sim 1 \times 10^{-3}$ cm^{-1} for the absorption coefficient of CVD-SCD at IR wavelengths [244], results in an estimated $Q_\mathrm{b} > 10^7$. The radiation loss limited contribution was estimated via finite-difference time-domain simulations [81] and found to be $Q_\mathrm{rad} > 10^6$ for the disk geometry (thickness, radius and pedestal size) studied here.

To investigate loss due to surface absorption, the pre-optimized devices were subjected to tri-acid cleaning. This 1:1:1 sulfuric, perchloric, nitric acid bath[3] is typically used to remove graphitic surfaces detrimental to spin coherence properties of diamond nitrogen vacancy (NV) and silicon vacancy (SiV) centers [173, 174]. It was performed using 10 mL of the acid mixture heated with a hotplate that was set to 250°C for 1 hr using the reflux system shown in Fig. 6.8 to capture the acid vapor. This reflux system was built by JP Hadden and I, and originally used a 100 mm long condenser coil and a filter flask instead of the 300 mm condenser coil and horizontal bubbler shown in Fig. 6.8(a). The system was changed to

[3]Disclaimer: Sulfuric, perchloric, and nitric acid are all corrosive acids and strong oxidizers when heated, which should be handled with care. Perchlorate crystals are highly explosive, and can form if perchloric acid is allowed to dry. It is necessary to thoroughly rinse the apparatus after use, and complete the fume hood wash down procedure to reduce the risk of this occurring.

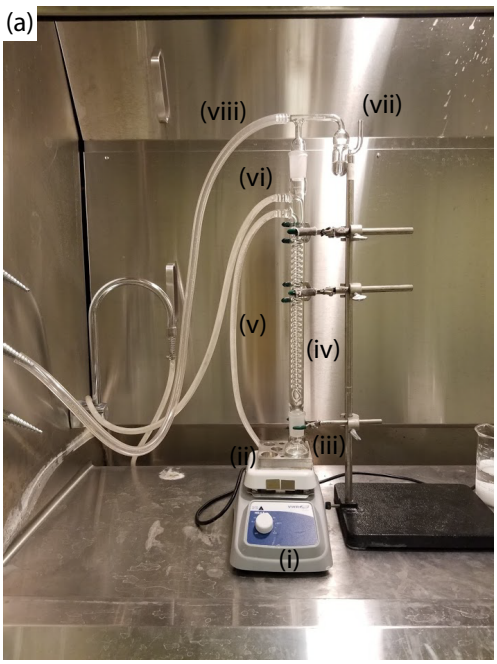

(b)

Parts list - pictured

(i) Hotplate

(ii) Heat transfer block

(iii) Round bottom flask - 25 mL, ST 24/40

(iv) Condenser coil - 300 mm, ST 24/40

(v) Condenser water supply

(vi) Condenser water output

(vii) Horizontal bubbler, ST 24/40

(viii) Bubbler air supply

Parts list - not pictured

Acrylic blast sheild

Figure 6.8: Tri-acid cleaning apparatus (a) and parts list (b). Not pictured is the acrylic blast shield placed in front of the apparatus, and the beakers and personal protective equipment (PPE) used for handling the acid mixture and diamond sample.

the current configuration after noticing corrosion of the tubing connecting the filter flask to the 100 mm condenser coil, indicating the condenser length was insufficient for condensing the vapor produced by boiling the tri-acid mixture. When performing the acid clean we also placed a small piece of aluminum foil between the round bottom (RB) flask and heat transfer block, and ensured that the level of acid mixture in the RB flask was above the level of the top of the heat transfer block. This was done to mitigate risk of breaking the RB flask due to thermal expansion and contraction during the heating and cooling stages of the procedure. Following the acid boil, the diamond sample was rinsed in H_2O (3×30 s) and dried with N_2. This procedure was carried out in a dedicated wash down fume hood to mitigate risk of perchlorate crystals forming, which are highly explosive.

To assess the impact of this cleaning, microdisk modes of the devices were measured before and after cleaning. These results are summarized in Fig. 6.9, which shows the change in measured doublet Q_{av}, defined as the average of $Q_{\mathrm{i}}^{\mathrm{s}}$ and $Q_{\mathrm{i}}^{\mathrm{a}}$, for a range devices with varying diameter. This is quantified as "Q% difference", defined as $(Q_{\mathrm{after}} - Q_{\mathrm{before}})/Q_{\mathrm{before}}$

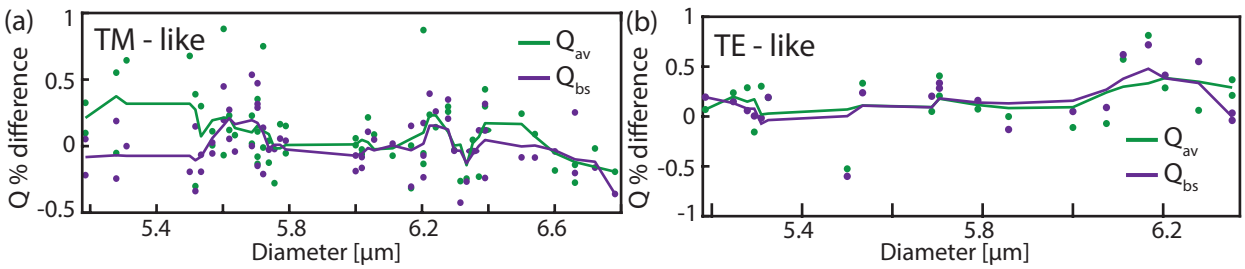

Figure 6.9: Comparison of Q_{av}, and Q_{bs} before and after cleaning in tri-acid as described in the text for TM-like (a) and TE-like (b) modes.

for both Q_{av} and Q_{bs}, for before and after cleaning. No change in Q_{av} consistent across many devices or with a clear trend as a function of microdisk diameter is observed. This holds for both TE and TM like mode, whose fields are most strongly concentrated near the vertical and horizontal microdisk surfaces, respectively [128]. Additionally, no significant change in the thermal capacity of the devices was observed, as determined by measuring the shift in doublet center wavelength, λ_{o}, as a function of dropped optical power, P_{d}. This suggests that loss due to surface absorption is not limiting Q_{i}, provided the surface is not contaminated by material impervious to the tri-acid clean, or to the hydrofluoric acid and piranha cleaning carried out post-fabrication (see Fig. 6.1). Also shown in Fig. 6.9 is a measure of the backscattering rate, $Q_{\mathrm{bs}} \sim \lambda_o/\Delta\lambda$, where $\Delta\lambda$ is the doublet splitting [128]. This was also found to be unaffected by the tri-acid, suggesting that any surface roughness responsible for the mode coupling is likely related to etched diamond surface morphology, which is expected to be unaffected by the cleaning steps used here.

To gain additional insight into the mechanism limiting Q_{i}, the dependence of Q_{av} and Q_{bs} on diameter for the optimized devices is plotted in Figs. 6.10(a) and 6.10(b). Although variations in Q_{av} and Q_{bs} of an order of magnitude are observed, no clear dependence on diameter is noted, and we attribute the variability to imperfections unique to each microdisk, and to differences in modal radial and vertical quantum number of the modes used in the data set. However, as shown qualitatively in Figs. 6.10(a) and 6.10(b), we observe that Q_{bs} tracks changes in Q_{av} as a function of diameter. This is shown more quantitatively in Figs. 6.10(c) and 6.10(d), which show scatter plots of $1/Q_{\mathrm{av}}$ as a function $1/Q_{\mathrm{bs}}$ for the TE and TM

modes, respectively. We find that $1/Q_{\mathrm{av}}$ and $1/Q_{\mathrm{bs}}$ have a correlation coefficient, r = 0.83 and r = 0.75 for the TM- and TE-like modes, respectively. This correlation suggests that surface roughness is limiting Q_{o}. Additionally, as shown by the $1/Q_{\mathrm{o}}$ histogram in Figs. 6.10(e,f), the density (ρ) of high-Q_{av} TE-like modes (Fig. 6.10(e)) in these microdisks is larger than that of the TM-like modes (6.10(f)). This suggests that there is a greater degree of surface roughness and scattering for the TM-like modes. The probability densities of $1/Q_{\mathrm{o}}$ for the TE- and TM- like modes in Fig. 6.10(e) and 6.10(f) were well fit to a half-normal or folded normal distribution expected for Q_{o} limited by surface roughness that varies randomly along the perimeter of the microdisk, with different random distribution for each disk. Finally, no large asymmetry between $Q_{\mathrm{i}}^{\mathrm{s}}$ and $Q_{\mathrm{i}}^{\mathrm{a}}$ of the standing wave modes was observed for any of the devices measured in this study, further supporting the conclusion that the dominant form of surface roughness limiting Q_{o} is distributed along the perimeter of the microdisk. This is in contrast to the effect of large discrete local perturbations along the microdisk perimeter, which can couple differently to the phase shifted spatial intensity profiles of the standing wave modes [128].

Based on the evaluation of each loss mechanism described above we conclude that Q_{ss} is limiting Q_{i}, most likely due to remaining etch roughness in the anisotropic diamond etch and roughness on the top or bottom surfaces. This suggests that further improvements to Q_{i} could be achieved by developing a smoother anisotropic diamond etch.

6.6 Thermal engineering via pedestal shape

When confining light to a small mode volume in a structure both linear and nonlinear absorption of light in the material can cause significant heating of the cavity [54, 56]. This heating can cause instability in the cavity resonance frequency due to the thermo-optic effect and make it practically difficult to maintain a constant-cavity detuning, which is vital in many optomechanical processes. In previous work it was found that the $\sim$ 100 nm diameter

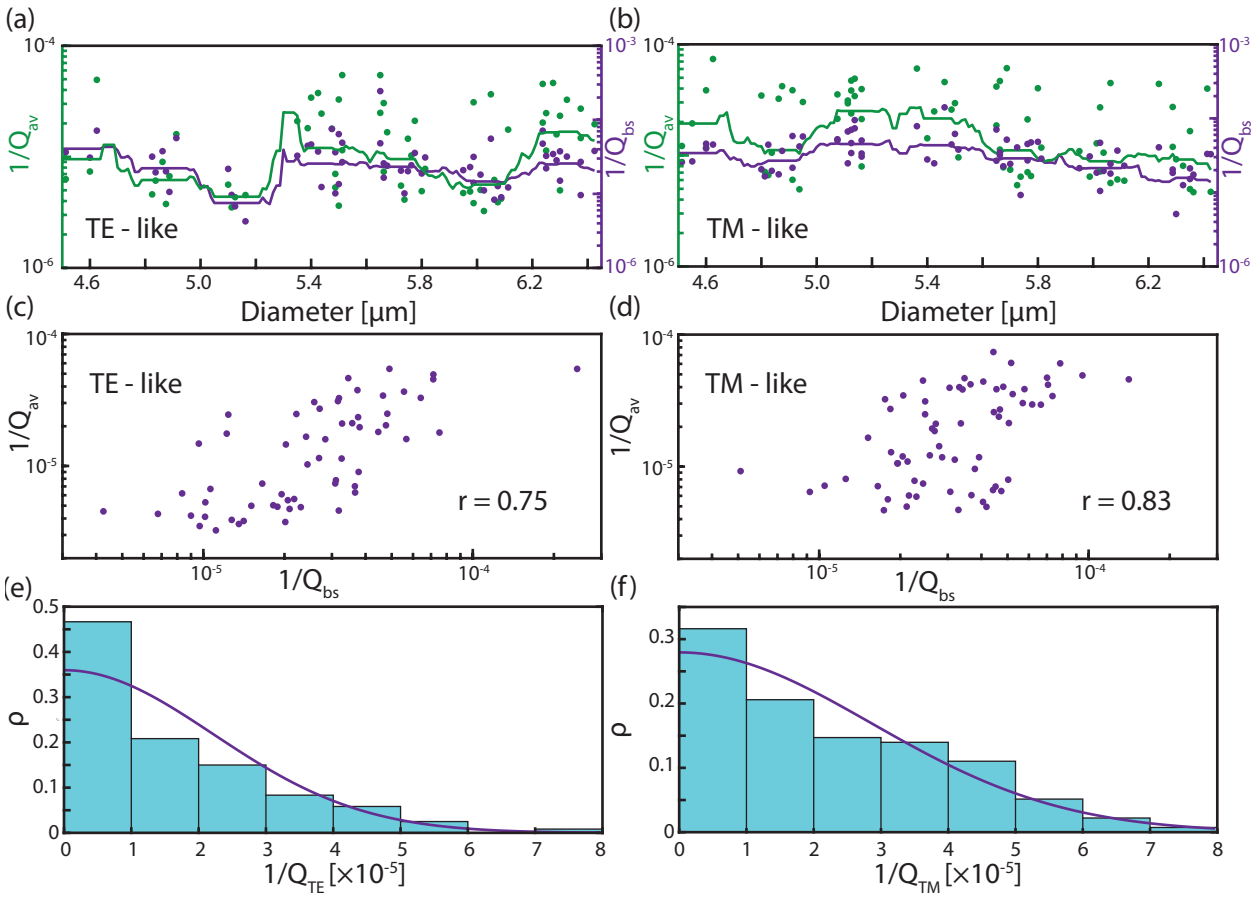

Figure 6.10: (a,b) $1/Q_{\mathrm{av}}$ and $1/Q_{\mathrm{bs}}$ vs. disk diameter for the TE- and TM-like modes, where an average value of Q_{a} and Q_{s} is taken. Solid lines are a boxcar average of the data, potted as a guide to the eye. (c,d) $1/Q_{\mathrm{av}}$ vs. $1/Q_{\mathrm{bs}}$ for the TE- and TM-like modes with calculated correlation coefficient, r, suggesting positive correlation between $1/Q_{\mathrm{av}}$ and $1/Q_{\mathrm{bs}}$. (e,f) Probability distribution of measured values for (c) $1/Q_{\mathrm{TE}}$ and (d) $1/Q_{\mathrm{TM}}$ for microdisks of varying diameter where each histogram has been fit to a half-normal distribution.

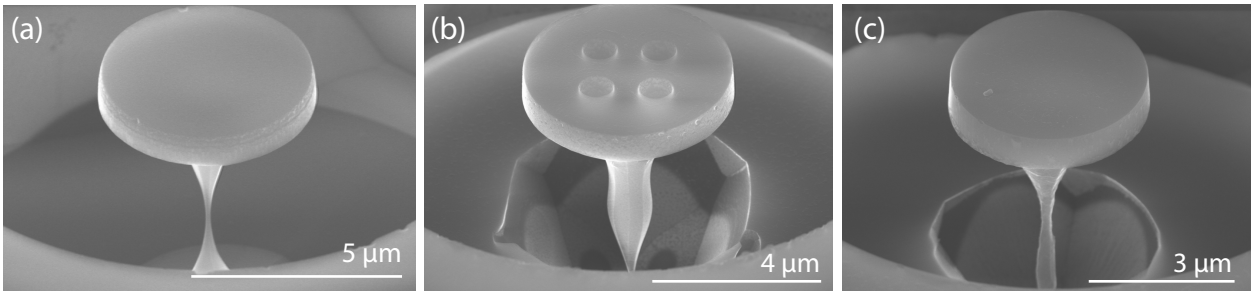

Figure 6.11: Effect of additional masking step during the quasi-isotropic undercut on microdisk pedestal geometry. (a) Hourglass pedestal shape resulting from no additional masking step. (b) Flared shape resulting from masking after undercutting by $\sim$ 45%. The circular holes observed in the microdisk were part of a separate study, and did not affect the flared pedestal shape. (c) Pedestal shape resulting from masking after undercutting by $\sim$ 40%.

pedestal size of the microdisk structure pictured in Fig. 6.11(a) was limiting the thermal time constant of the device due to the reduced thermal conductivity in the pedestal [4].

To attempt to alleviate this issue a method for altering the pedestal shape was investigated. Namely by depositing an additional masking layer it is possible to tailor the pedestal shape of the microdisk during the undercut stage. It is important to use a non-conformal layer such that the undercutting process may continue horizontally as shown in Fig. 6.1(viii). Here EBPVD was used to deposit a 100 nm layer of SiO_2, in a line of sight fashion, allowing undercutting to continue immediately after. Here a Johnson Ultravac load-locked electron beam evaporation system was used with a deposition pressure of $\sim 1 \times 10^{-6}$ Torr, and a deposition rate of 0.5 Å/s. By varying the point at which this deposition occurs during the undercut the pedestal shape can be altered differently as shown in Figs. 6.11(a–c). Here the SiO_2 was deposited after 4 hours of undercutting for the structures in Figs. 6.11(b,c), where an additional 4 and 5 hours were required to undercut each device respectively. This corresponds to 45% and 40% of the total undercut time, where the discrepancy in time is due to different etch depths during the anisotropic etch [3]. This process can be repeated to customize the pedestal shape and could potentially be used to engineer the phononic properties of the structure, similar to the work of Nguyen et al.[138]. By altering the pedestal geometry, the device in Fig. 6.11(b) demonstrated an order of magnitude decrease in the thermal time constant of the microdisk structures, measured by fitting the response of the optical transmission for an input optical step function. This alteration resulted in the ability to support roughly an order of magnitude larger intracavity photon number before the onset of thermal instability [5]. The ability to operate at large N while avoiding thermal instability is practically important in cavity optomechanics applications due to the linear dependance of the optomechanical cooperativity $C = 4g_0^2 N/\kappa\Gamma_{\mathrm{m}}$ on N [18]. This enabled the observation of optomechanically induced transparency and optomechanically mediated wavelength conversion with $C > 1$ [5, 7].

Following the analysis of Carmon et al [56], we can quantitatively analyze the improve-

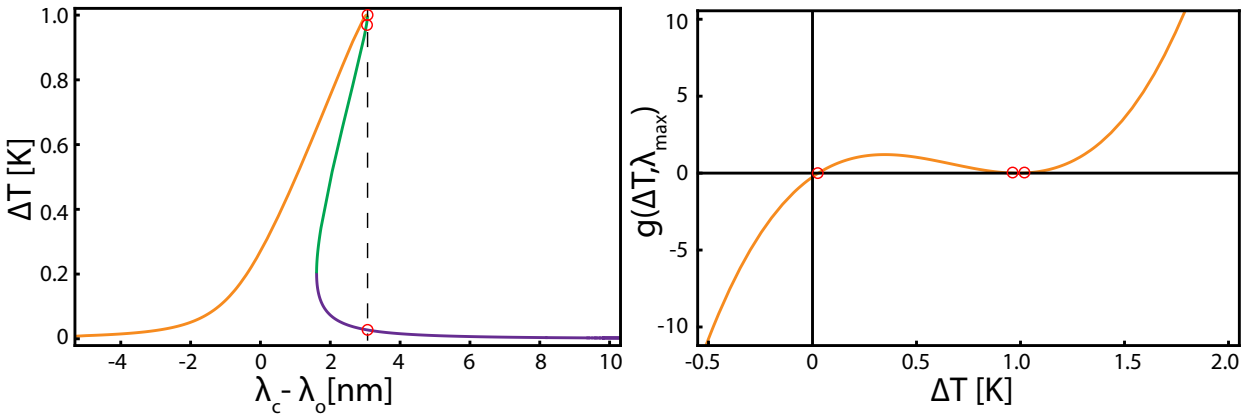

Figure 6.12: (a)Cavity temperature at equilibrium as a function of laser-cavity detuning found by numerically solving Eqn. 6.1, with $\frac{d}{dt}\Delta T = 0$. (b) Equilibrium temperature solutions at maximum shift in resonance wavelength, $\lambda_{\max}$.

ment in the thermal conductivity achieved with this alteration. We start by writing an equation governing the time evolution of the cavity temperature in response to an input field with power $P_{\text{in}}(t)$,

$$\frac{d}{dt}\Delta T = P_{\text{in}}(t) f\left(\lambda_p, \Delta T\right) - \frac{\Delta T}{\tau_{\text{th}}}, \tag{6.1}$$

where for a singlet mode,

$$f\left(\lambda, \Delta T\right) = \frac{\eta Q_{\text{i}}}{C_p Q_{\text{abs}}} \frac{\left[\Delta\lambda/2\right]^2}{\left[\lambda_p - \lambda_o(1+\beta\Delta T)\right]^2 + \left[\Delta\lambda/2\right]^2}. \tag{6.2}$$

In the above ΔT is the difference between the cavity temperature and environment temperature, τ_{th} is the thermal time constant, C_p is the heat capacity of the cavity, and β is defined as a temperature coefficient of resonance-wavelength accounting for thermal expansion and refractive index perturbations, $\beta = \epsilon + \frac{dn}{dT}/n_0$. The fraction of light coupled into the cavity is defined as η, λ_p is the input field wavelength, $\lambda_o(\Delta T)$ is the cavity resonance wavelength, and Q_{abs} is the quality factor due to absorption only.

For a constant input signal, the equilibrium temperature ΔT_{eq} of the cavity can be found by setting $\frac{d}{dt}\Delta T = 0$, and solving the cubic equation $a(\Delta T_{\text{eq}})^3 + b(\Delta T_{\text{eq}})^2 + c(\Delta T_{\text{eq}}) + d = 0$. As only real solutions to this equation are physical, we can deduce the number of valid solutions at equilibrium by determining the number of real roots associated with the cubic

equation. To do so one can evaluate the discriminant, Δ, as,

$$\Delta = \frac{q^2}{4} + \frac{p^3}{27}, \tag{6.3}$$

$$p = \frac{3ac - b^2}{3a^2}, \tag{6.4}$$

$$q = \frac{2b^3 - 9abc + 27a^2d}{27a^3}. \tag{6.5}$$

This can be divided into three distinct cases,

$$\Delta < 0 : \text{Three real, distinct roots.} \tag{6.6}$$

$$\Delta = 0 : \text{Three real, degenerate roots.}$$

$$\Delta > 0 : \text{One real root, and two complex roots.}$$

The case where $\Delta < 0$ is shown in Fig. 6.12, where 3 real distinct roots exist resulting in a thermal bistability.

Reaching the regime of coherent optomechanical coupling can in principle always be achieved by operating with high enough P_{in} to increase N so that $C > 1$. In practice, even in absence of nonlinear absorption, N is limited by linear absorption and thermo-optic dispersion, particularly in small optical mode volume devices such as microdisks. The microdisk pedestal shape plays a critical role in determining whether $C > 1$ can be reached, as it influences Q_{m} ($\propto C$) [4] as well as the device's ability to conduct thermal energy away from the microdisk and mitigate optical heating. The importance of the pedestal's thermal conductance can be seen by considering the threshold for N above which the microdisk becomes bistable due to the thermo-optic effect [245, 246], for λ_{p} red-detuned from λ_{o} as required for optomechanically induced transparency [61, 63, 111] and cooling [29]. To determine if the red-detuned side of the cavity is accessible for a given input pump power, we evaluate Δ at zero detuning, e.g. $\lambda_p = \lambda_o(1 + \beta\Delta T)$. This leads to the requirement for access to red-detunings:

$$\frac{1}{\tau_{\rm th} Q_{\rm i}} > |\beta| \left(\frac{\eta Q_{\rm i}}{Q_{\rm abs}}\right) \left(\frac{P_{\rm in}}{C_p}\right), \tag{6.7}$$

or,

$$\left(\frac{\eta P_{\rm in} Q_{\rm i}}{\hbar \omega_{\rm o}^2}\right) \equiv N < \frac{C_p}{|\beta| \tau_{\rm th} \hbar \omega_{\rm o}^2} \left(\frac{Q_{\rm abs}}{Q_{\rm i}}\right). \tag{6.8}$$

Equation (6.8) illustrates the inverse relationship between $\tau_{\rm th}$ and maximum N. Note that in the anomalous case of $\beta < 0$, the cavity becomes bistable for blue instead of red-detuning.

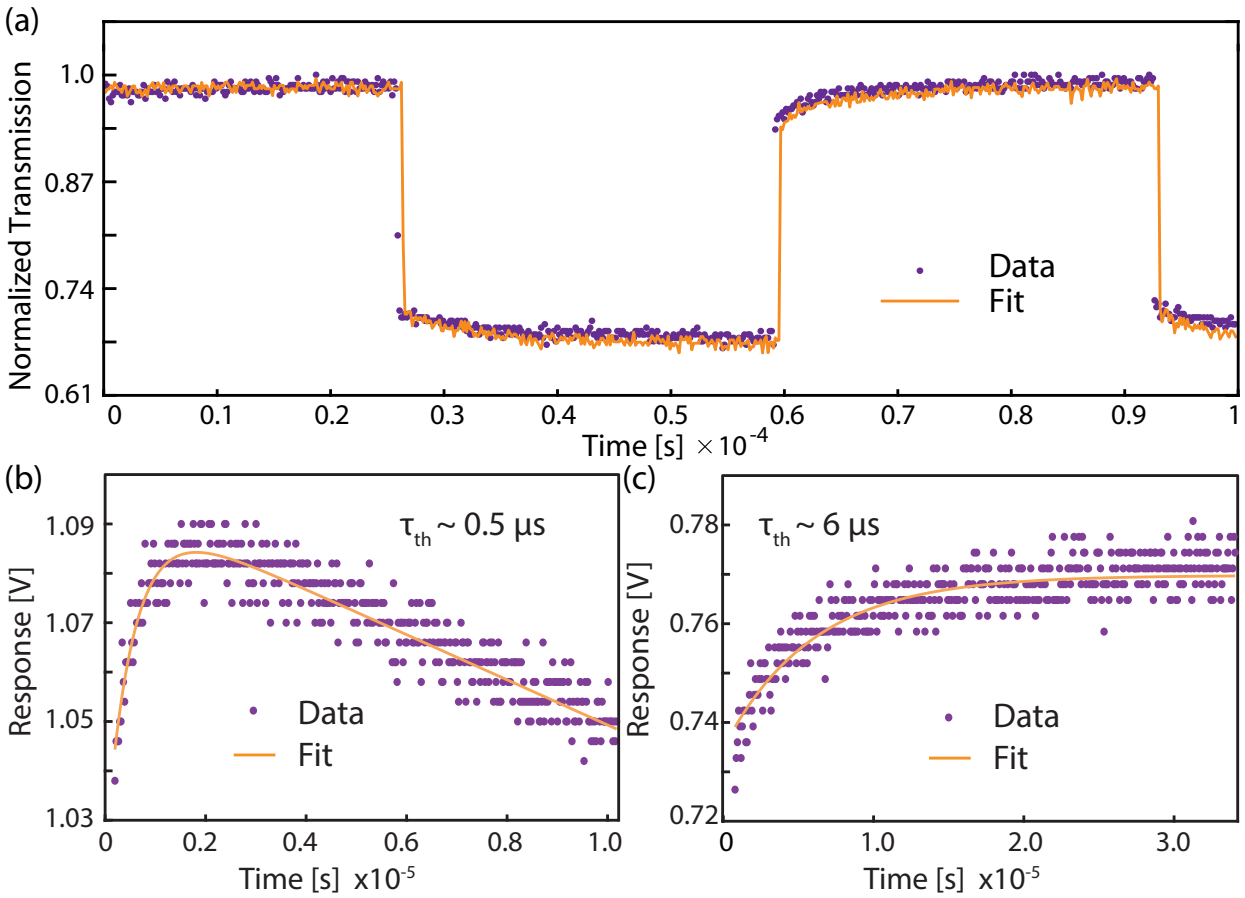

Figure 6.13: (a) Transmission of an optical cavity in response to a square wave driving function. (b,c) Response of the optical transmission for an input step function for microdisks with similar sized flared and hourglass shaped pedestals, respectively. The exponential rise is fit to extract the thermal time constant. The negatively sloped feature in (b) is an EDFA artifact, resultant from the large input powers required to achieve thermal bistability.

To measure the thermal time constant, the input field is modulated between two distinct

powers, as shown in Fig. 6.13(a). For relatively small modulations, the time evolution of the cavity temperature will resemble the input field, low pass filtered by the finite response time of the thermal cavity shift. This can then be read out by choosing a laser drive wavelength where changes in the cavity resonance frequency result in a change in optical transmission, namely,

$$P_{\text{out}}(t) \approx T\left[1 + \frac{\partial T}{\partial \lambda_o}\frac{\partial \lambda_o}{\partial \Delta T}\Delta T\right] P_{\text{in}}(t), \tag{6.9}$$

where P_{out} is the power output into the taper and T is the transmission through the cavity. Together Eqns. 6.1-6.9 were used to fit experimental data to find τ_{th}.

To determine the impact of the pedestal shape on the properties of the microdisks, we compare the flared pedestal microdisks (Fig. 6.11(b)) with hourglass pedestal microdisks ((Fig. 6.11(a))). In Ref. [4] it was found that increasing pedestal width degraded Q_{m}. However, the Q_{m} of the flared pedestal device measured here is similar to the best valued reported for the hourglass microdisks, despite the larger width of the flared pedestals. However, as shown by measurements of τ_{th} in Fig. 6.13(b,c), the highest Q_{m} flared and hourglass pedestal microdisks have $\tau_{\text{th}} \sim 0.5$ μs and 6 μs, respectively, indicating that the flared pedestal devices studied here can support over an order of magnitude larger N in the red-detuned regime compared to previous hourglass pedestal devices. Here τ_{th} was measured by monitoring the response of the microdisk to an optical pulse that causes λ_{o} to shift via the photothermal effect, as described above. The improved thermal handling of the optimized microdisks is illustrated in Fig. 6.14 which shows the absence of thermal bistability, and much smaller thermo-optic shift in λ_{o} for similar N for the optimized structures. As shown in Fig. 6.14(b) the optimized microdisks can be display self oscillation while avoiding thermal bistability, which was not the case for the microdisks studied in Chapter 5.

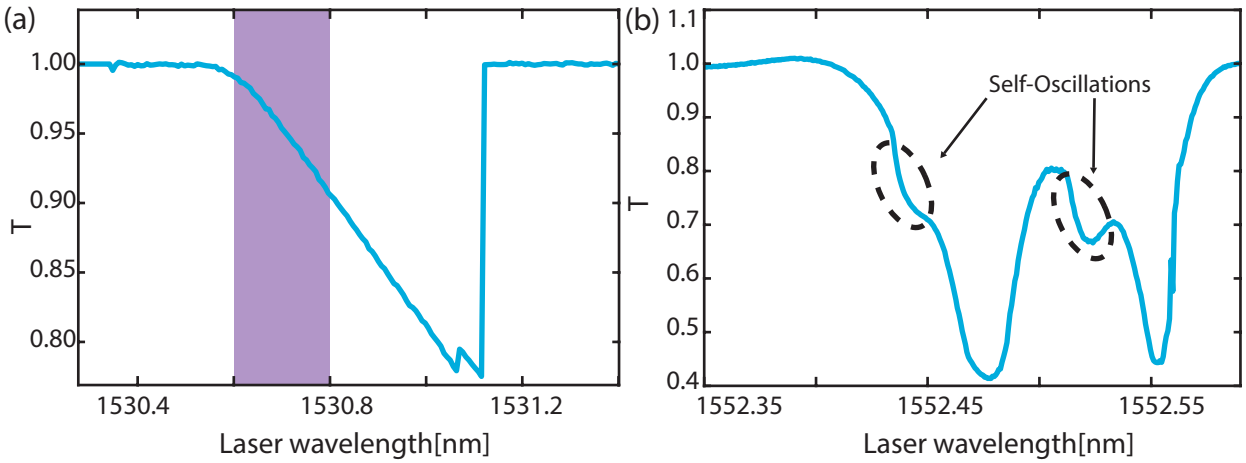

Figure 6.14: (a) Normalized fiber taper transmission for a microdisk with an hourglass shaped pedestal and max $N \sim 6.5 \times 10^5$. The wavelength span in (b) is indicated by the shaded region. (b) Normalized fiber taper transmission for a microdisk with a flared pedestal and max $N \sim 1 \times 10^6$. The circled dips are signatures of large amplitude mechanical oscillations [32].

6.7 Summary & outlook

The optimization presented in this chapter resulted in a $\sim 4\times$ increase in average Q_i for TE-like modes and an order of magnitude improvement in the thermal time constant compared to the previous cavity optomechanical devices studied in Chapter 5. As etch parameters vary from tool to tool, we hope that the optimization results presented here could be utilized by others to identify similar issues or devices characteristics and use our procedure to improve overall etch quality. For reference, Table 6.5 compares this result with the current state of the art for SCD cavities at telecommunications wavelengths. Further enhancement in optical Q_o could be achieved by improving the etch quality, and reducing surface roughness that is still present, as we conclude from the analysis above that the optical Q_o remains limited by surface imperfections. For example, incorporation of Cl_2 based etching may enable smoother diamond surfaces [247]. Additional cleaning steps such as post-fabrication oxygen annealing, as utilized by Burek et al. [70], or investigating appropriate surface termination techniques such as those developed for silicon [248] could also be investigated for improving optical Q_o. Finally, while current SCD microdisks mechanical quality factors, Q_m, are limited by clamping loss [4, 5], the pedestal shaping step described in Section 6.6 could be utilized to

reduce mechanical dissipation and increase $C \gg 1$, by incorporating a phononic shield into the pedestal as demonstrated by Nguyen et al. in GaAs microdisks [138].

Table 6.5: Comparison of SCD cavities supporting modes at telecommunications wavelengths. Indicates which works have also demonstrated optomechanical coupling in the structure.

Author/Reference	Structure	$Q_{\mathrm{i}}(\times 10^5)$	Optomechanics
This work	Microdisk	3.35	Yes
Lake et al. [5]	Microdisk	0.87	Yes
Mitchell et al. [4]	Microdisk	0.68	Yes
Khanaliloo et al. [3]	Microdisk	1.02	No
Burek et al. [183]	Racetrack	2.70	No
Burek et al. [70]	OMC	3.02	Yes
Teodoro et al. [249]	Microdisk	0.057	No

While SCD optomechanical crystals, demonstrated by Burek et al. [70] provide superior g_0, microdisks have an advantage in that they naturally support optical modes across the entire transparency window of the material, enabling multimode optomechanical experiments such as optomechanical wavelength conversion [7, 44, 61], and for larger microdisk diameter can have much greater radiation loss limited optical Q_{o}. The improvement demonstrated here is particularly meaningful for applications in cavity optomechanics, as it places the optimized devices in the resolved sideband regime where the mechanical resonance frequency, $\omega_{\mathrm{m}}/2\pi \sim 2-3$ GHz for the microdisks studied here, exceeds the cavity optical energy decay rate, $\kappa/2\pi \sim 0.6$ GHz for the high-Q_{o} device [18]. This regime is a requirement for observing efficient radiation-pressure dynamical back-action effects [18, 236], such as ground state cooling [29], optomechanically mediated wavelength conversion [7, 44, 61], optomechanically induced transparency [5, 63, 111] and low-noise amplification [250]; some of which will be discussed in Chapter 7.

Chapter 7

SCD microdisks: coherent multimode cavity optomechanics

7.1 Introduction

Multimode cavity optomechanical devices have great potential to connect disparate quantum technologies in a quantum network or quantum internet [251], namely as a coherent, phonon mediated way of transducing quantum information from visible or microwave photons to telecommunication wavelength photons [46, 252, 253]. As such, the field of optical to microwave transduction [47, 123, 140, 254, 255, 256] is currently a highly active area of research. Optomechanical systems are one of the most promising of these technologies, as coupling any two optical/microwave cavity modes to a single mechanical mode of the structure can be utilized to efficiently convert photons between the two.

The fabrication optimization described in Chapter 6 enabled the study of coherent photon-phonon interactions in SCD microdisks in ambient conditions, with $C > 1$. This allowed the demonstration of optomechanical cooling [5], optomechanically induced transparency [5], and optomechanically mediated and amplified wavelength conversion [7] between two telecom wavelength optical modes via the RBM. These experiments highlight how SCD

microdisks can be utilized to form a multimode optomechanical cavity capable of handling large N while remaining thermally stable, enabling the demonstration of optomechanical phenomena previously not observed in the optical regime such as optomechanically amplified wavelength conversion [7], double optomechanically induced transparency [8], and all-optically tunable optomechanical pulse storage [257].

7.2 Optomechanical damping and spring effect

The thermal handling improvements discussed in Section 6.6 enabled operation with large N for both red- and blue- laser detuning. As mentioned above, operation red-detuned from the cavity with large N allowed the study of coherent photon-phonon coupling with $C > 1$. This also enabled high quality fits of the optical spring effect, and optomechanical damping/anti-damping as a function of detuning, as shown in Fig. 7.1, which are greatly improved compared to the fits in Fig. 5.4, where only blue-detunings were accessible for large N. For this measurement, $P_{\rm in}$ was increased via an EDFA connected to the tunable laser output. The laser wavelength was then discretely stepped across the optical cavity resonances, and the PSD of the transmitted signal was acquired at each step. By fitting a Lorentzian lineshape to the PSD, both $\omega_{\rm m}(\Delta; P_{\rm in}) = \omega_m^0 + \delta\omega_{\rm m}(\Delta; P_{\rm in})$ and $\Gamma_{\rm m}(\Delta; P_{\rm in}) = \Gamma_{\rm m}^0 + \Gamma_{\rm opt}(\Delta; P_{\rm in})$ as a function of laser-cavity detuning, $\Delta = \omega_{\rm l} - \omega_{\rm o}$, were extracted. The results of this measurement for intermediate input power ($P_{\rm in} \sim 4.7$ mW) are shown in Figs. 7.1(a) and 7.1(b). Here the data is fit to the analytic expressions for the predicted values of the optomechanical spring effect $\delta\omega_{\rm m}$ and optomechanical damping $\Gamma_{\rm opt}$, taking into account the doublet nature of the optical mode as given by Eqns. 7.1 and 7.2.

The microdisk modes used in this measurement have a central wavelength of $\lambda_{\rm o} \equiv 2\pi{\rm c}/\omega_{\rm o} \sim 1550$ nm, splitting of $\frac{\lambda_{\rm o}^2}{2\pi c}\gamma_\beta \sim 70$ pm, and intrinsic (unloaded) $Q_{\rm i}^{\rm (s,a)} = \omega_{\rm o}/\kappa_{\rm i}^{\rm (s,a)} = 8.7 \times 10^4$ and 7.4×10^4, where $\kappa_{\rm i}^{\rm (s,a)}$ are the optical energy decay rates of the symmetric and antisymmetric (red and blue shifted) modes of the doublet, respectively. This places the

system near the resolved sideband regime, with $\omega_{\rm m}/\kappa_{\rm i}^{\rm (s,a)} \sim 1.0$ and 0.84. Typically these devices are operated in the under–coupled regime with $\kappa_{\rm ex}/\kappa_{\rm i} \sim 0.58$. Using the fact that the symmetric and antisymmetric modes are orthogonal ($\langle\alpha_{\rm a}|\alpha_{\rm s}\rangle = 0$), we can write the optomechanical spring effect (Eqn. 2.60) as [18],

$$\begin{aligned}\delta\omega_{\rm m} =& g^2\left[\frac{\Delta-\omega_{\rm m}}{\kappa_{\rm s}^2/4+(\Delta-\gamma_\beta/2-\omega_{\rm m})^2}\right]+g^2\left[\frac{\Delta+\omega_{\rm m}}{\kappa_{\rm s}^2/4+(\Delta-\gamma_\beta/2+\omega_{\rm m})^2}\right]\\ &+g^2\left[\frac{\Delta-\omega_{\rm m}}{\kappa_{\rm a}^2/4+(\Delta+\gamma_\beta/2-\omega_{\rm m})^2}\right]+g^2\left[\frac{\Delta+\omega_{\rm m}}{\kappa_{\rm a}^2/4+(\Delta+\gamma_\beta/2+\omega_{\rm m})^2}\right],\end{aligned} \tag{7.1}$$

Similarly, the optomechanical damping rate (Eqn. 2.61) for doublets is,

$$\begin{aligned}\Gamma_{\rm opt} =& g^2\left[\frac{\kappa_{\rm s}}{\kappa_{\rm s}^2/4+(\Delta-\gamma_\beta/2+\omega_{\rm m})^2}\right]-g^2\left[\frac{\kappa_{\rm s}}{\kappa_{\rm s}^2/4+(\Delta-\gamma_\beta/2-\omega_{\rm m})^2}\right]\\ &+g^2\left[\frac{\kappa_{\rm a}}{\kappa_{\rm a}^2/4+(\Delta+\gamma_\beta/2+\omega_{\rm m})^2}\right]-g^2\left[\frac{\kappa_{\rm a}}{\kappa_{\rm a}^2/4+(\Delta+\gamma_\beta/2-\omega_{\rm m})^2}\right].\end{aligned} \tag{7.2}$$

Using measurements of $N(\Delta) = N^{\rm s}(\Delta)+N^{\rm a}(\Delta)$ shown in Fig. 7.1(c) determined from the power dropped into the microdisk and $\kappa^{\rm s,a}$ we are able to extract the sole fitting parameter, $g_0/2\pi \sim 17$ kHz. The optomechanical coupling rate is not expected to vary for each mode of the doublet, which was confirmed in our analysis by allowing g_0 to vary for the symmetric and antisymmetric modes, which gave the same result as a single g_0 value. In general, as the coupling rates to each of the modes will depend on the phase of fields compared to the point of fiber taper coupling, $\kappa_{\rm ex}$ can differ for each mode [94]. However, for the modes considered in this work $\kappa_{\rm ex}$ was approximately equal for each mode, and a single value was used. Unlike previous measurements of the optical spring effect in diamond microdisks [4], $\delta\omega_{\rm m}$ here was dominated by optomechanical back-action owing to the device's reduced $\tau_{\rm th}$.

The cavity optomechanical damping, $\Gamma_{\rm opt}$, modifies the mechanical normal-mode temperature, $T_{\rm eff}$, as in experiments of ground state cooling [29], or generation of self–oscillations

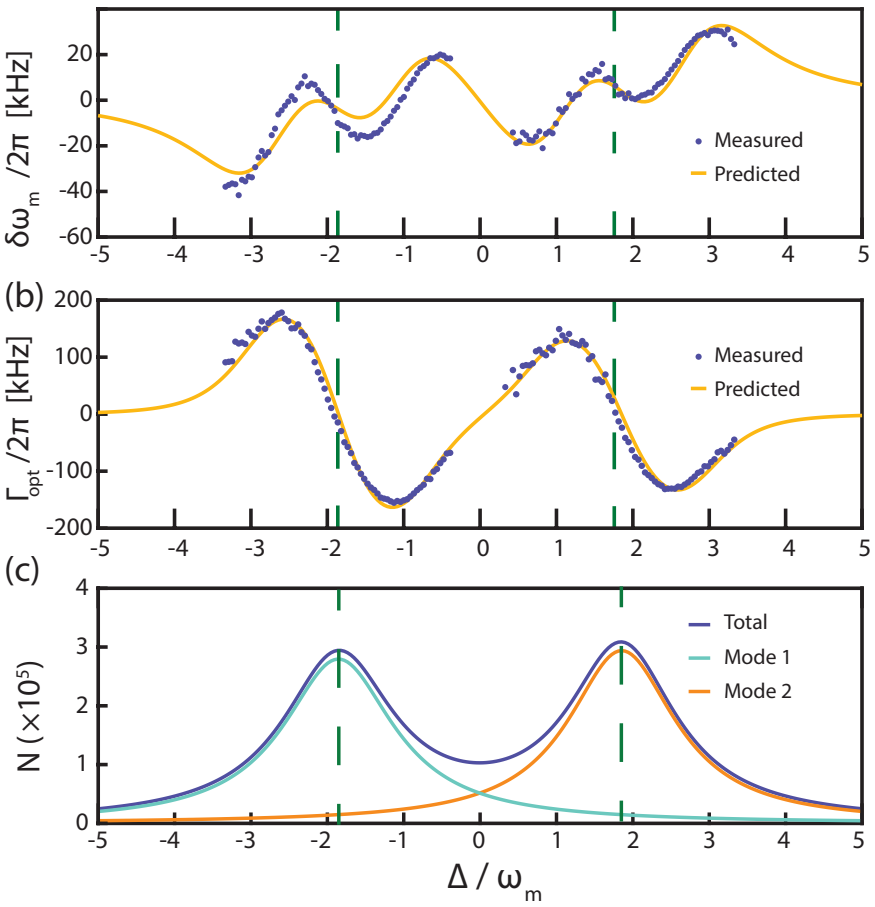

Figure 7.1: Characterization of optomechanical coupling via the spring effect for a $\sim 5\mu$m diameter microdisk, for $P_{\rm in} \sim 4.7$ mW. Shift in (a) mechanical resonance frequency $\delta\omega_{\rm m}$ and (b) optomechanical damping/anti-damping $\Gamma_{\rm opt}$ as a function of laser detuning. The fits are from the optomechanical spring effect calculation with a single–photon optomechanical coupling rate of $g_0/2\pi \sim 17$ kHz as the sole free parameter, and the measured N shown in (c). Dashed lines indicate $\Delta \pm \gamma_\beta/2 = 0$ (corresponding to the resonance frequency of each doublet mode), and illustrate that $\delta\omega_{\rm m}$ and $\Gamma_{\rm opt} = 0$ when the laser is on-resonance with the cavity mode.

that drive stress fields for coupling to diamond colour center spins [4]. The normal-mode temperature can be measured as a function of Δ from the area under the PSD normalized by the wavelength dependent optomechanical transduction (see Appendix E) and assuming that for large $|\Delta|$ the cavity is in thermal equilibrium with the room-temperature environment. Figure 7.2(a) shows the normal mode temperature $T_{\rm eff}$ and corresponding phonon occupation $n_{\rm m}$ measured using this technique. Also shown is a prediction of $T_{\rm eff}$ obtained by inputting

the fit of $\Gamma_{\rm opt}(\Delta)$ from Fig. 7.1(b) to the optomechanical back-action cooling expression,

$$n_{\rm m} = n_{\rm th} \times \frac{\Gamma_{\rm m}^0}{\Gamma_{\rm m}^0 + \Gamma_{\rm opt}(\Delta)}, \tag{7.3}$$

where $n_{\rm m}$ is the final phonon number, $n_{\rm th} = k_B T/\hbar\omega_{\rm m}$ is the equilibrium thermal phonon occupation [18]. This expression is valid in the high–T limit $n_{\rm th} \gg n_{\rm min}$ applicable here, where $n_{\rm min} = 0.088$ is the minimum backaction limited phonon number achievable through optomechanical damping, which in the resolved sideband regime is given by $n_{\rm min} = (\kappa/4\omega_{\rm m})^2$, which holds for the device studied here [18]. The good agreement indicates that the Δ dependent normalization of the PSD is accurate, and that optical absorption and heating is small compared with changes to $n_{\rm m}$ from optomechanical backaction.

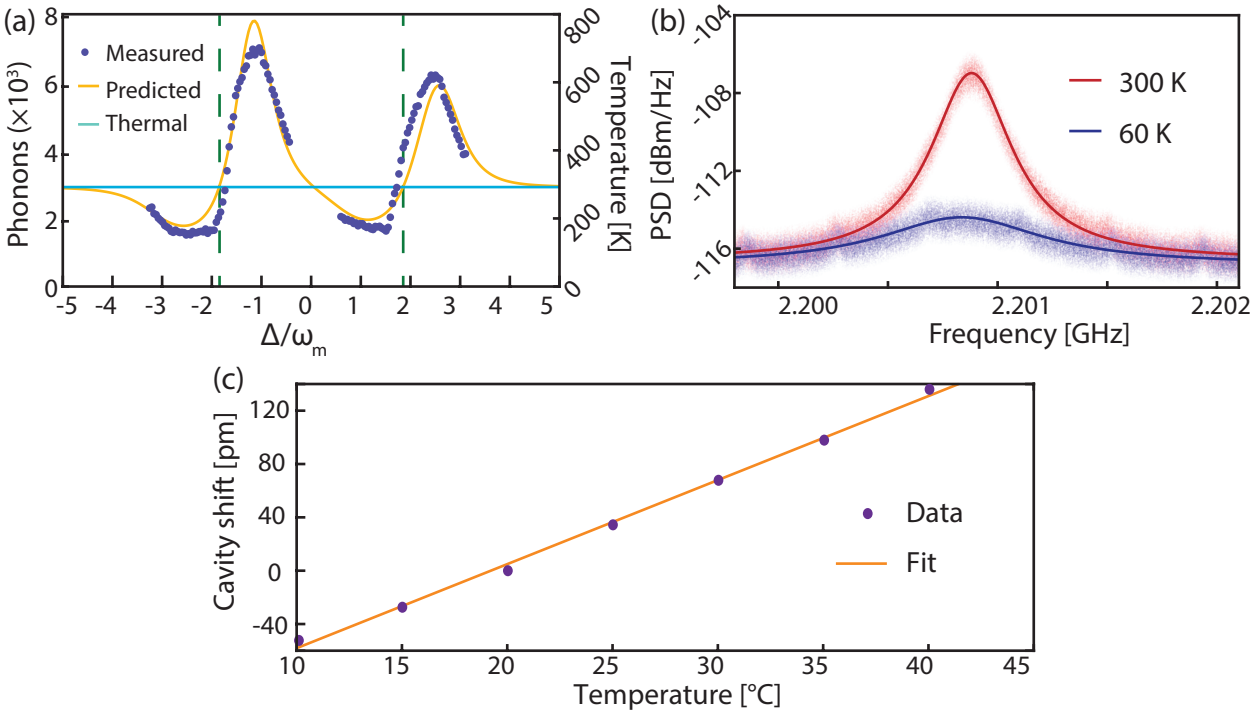

Figure 7.2: Optomechanical heating and cooling. (a) Measured phonon occupation and temperature of the RBM, and the corresponding values predicted from the fit to $\Gamma_{\rm opt}$ in Fig. 7.1(b). (b) PSD at the operating point $\Delta \sim -\gamma_\beta/2 - \omega_{\rm m}$ of maxiumum cooling (blue), and at Δ tuned to the point of zero damping (red). Small peaks at intervals of 500 kHz are from technical noise.(c) Cavity wavelength shift, relative to ambient conditions, as a function of temperature for the device and optical mode described in Section 7.2. The cavity temperature was varied using a thermoelectric heater/cooler (see Appendix F for parts). The linear line of best fit shown was used to calculate the laser absorption induced heating present in the cooling experiment.

At higher $P_{\rm in}$, microdisk heating and modal thermo-optic dispersion become significant, and the transduction calibration could not be readily applied to measurements of PSD area for varying Δ. However, measurement of optomechanical cooling using Eq. (7.3) with Δ optimized to maximize $\Gamma_{\rm opt}$ was possible: for $N \sim 1 \times 10^6$ ($P_{\rm in} \sim 20$ mW), $T_{\rm eff} = 60$ K ($n_{\rm m} = 588$ phonons) was measured for the symmetric mode, as shown in Fig. 7.2(b). Here $T_{\rm eff}$ includes an increase in bath temperature (i.e. $n_{\rm th}$) of 4 K due to optical heating, inferred from the shift in $\lambda_{\rm o}$ calibrated by its independently measured temperature dependence shown in Fig. 7.2(c). This optimized cooling was obtained when red-detuned by $\omega_{\rm m}$ from the higher-$Q_{\rm o}$ doublet mode, as expected for a sideband-resolved cavity optomechanical device. This detuning was not achievable in previous work with hourglass pedestal microdisks due to an inability to operate at red-detuning with $P_{\rm in}$ large enough to significantly reduce $n_{\rm m}$ because of thermal instability [4].

7.3 Optomechanically induced transparency

A natural measurement to perform now that large N could be achieved while red-detuned from the cavity was to characterize OMIT in the SCD microdisks. Compared to the results for GaP given in Section 3.6 here we hoped to achieve even larger C, due to the optimized structures ability to handle an order of magnitude larger N and $Q_{\rm m}$. To characterize OMIT the laser output was amplified to $P_{\rm in} \sim 40$ mW, and its wavelength was slowly stepped across the cavity resonance, creating a control field with varying $\Delta_{\rm c}$. At each $\Delta_{\rm c}$, a phase EOM driven by a vector network analyzer (see Appendix F for equipment list) was used to create a sideband on the control field that serves as the probe, and whose frequency can be swept across the cavity resonance, varying $\Delta_{\rm p}$. The probe field reflected by the microdisk back into the fiber taper was measured using a high–bandwidth photoreceiver connected to an optical circulator, and analyzed by the VNA. The symmetric mode of the microdisk doublet ($\omega_{\rm o} - \frac{\gamma_\beta}{2}$) was used for all of the measurements described below. Figure 7.3(a) shows the

results of these measurements for several Δ_c, with each exhibiting a sharp OMIT feature when $\Delta_p = \omega_m$. Here $\overline{R}$ is the reflectivity normalized by its maximum value in absence of OMIT. This can be approximated by taking the maximum to be at a point slightly detuned from $\Delta_p = \omega_m$, which is valid as long as $\kappa \gg \omega_m$. When Δ_c is tuned away from ω_m the OMIT feature exhibits a Fano shape due to the phase difference between the scattered control field and the probe field. At the OMIT condition $\Delta_c = \omega_m$ the dip amplitude reaches a maximum, as shown in detail in Fig. 7.3(b). From the dip amplitude $\sim 0.8 = 1 - 1/(1+C)^2$ [61], cooperativity $C \sim 1.2$ was extracted. This C was achieved with an intracavity photon number of $N \sim 2.7 \times 10^6$, and corresponds to $g_0/2\pi = 18$ kHz, in excellent agreement with the value predicted from the optomechanical spring effect fits in Figs. 7.1(a) and (b).

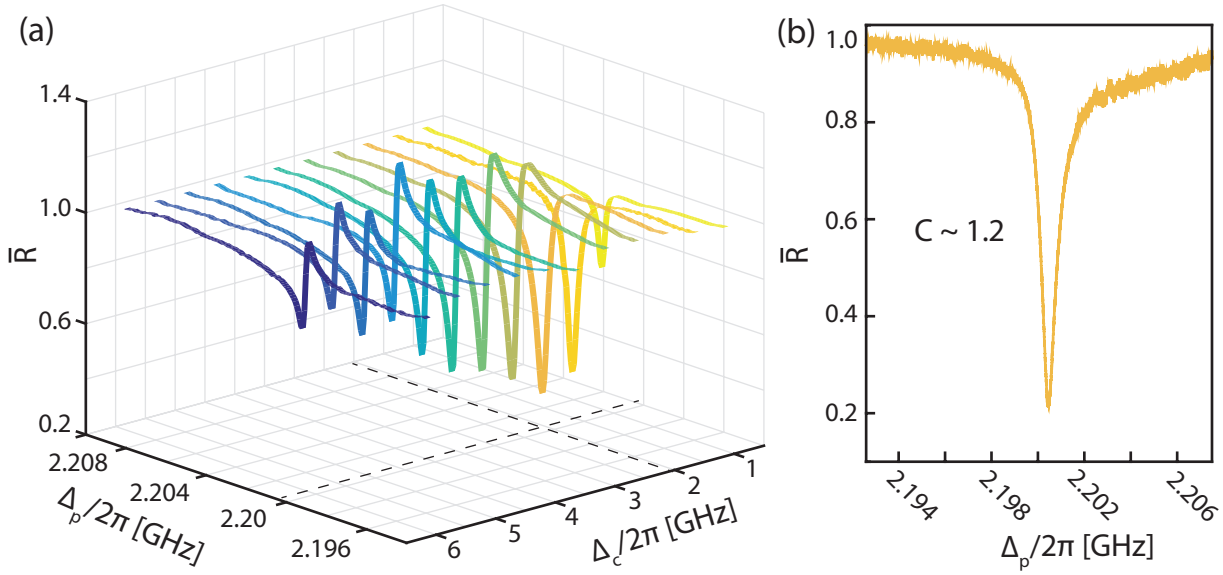

Figure 7.3: Optomechanically induced transparency in SCD microdisks. (a) Probe reflection, $\bar{R}$, as a function of Δ_c and Δ_p shown for OMIT using the symmetric mode of the doublet. (b) OMIT response corresponding to $C \sim 1.2$ for $N \sim 2.7 \times 10^6$, with $\Delta_p = \Delta_c = \omega_m$.

Compared with previous demonstrations of OMIT in Si_3N_4 microdisks [61], the diamond devices demonstrated here support nearly two orders of magnitude higher N and 2.6 times higher C, despite their lower Q_i. Furthermore, this performance is realized without thermal stabilization or cryogenic cooling. This enables optomechanical cooling with large N in the red-detuned regime not accessible in previous studies [4]. Additionally, the microdisk

geometry combined with the broadband transparency of diamond allows these devices to simultaneously support high-Q_i optical modes spanning a broad wavelength range, for example at both the 637 nm range of diamond NV centre emission and in the 1550 nm telecommunications wavelength band [4]. The $C > 1$ OMIT shown here will allows these multi-wavelength cavities to be used for optomechanical wavelength conversion [44, 61], as will be shown in the next section, and the broad microdisk mode spectrum will allow conversion over a larger range than a diamond optomechanical crystal [70]. Finally, any improvement to Q_m, either through low-temperature operation [69] or engineering of the microdisk connection to the pedestal [137, 138, 258] would greatly increase the maximum achievable cooperativity. This could potentially be achieved using the pedestal shaping technique described in Section 6.6 for the SCD microdisks.

7.4 Optomechanically mediated wavelength conversion

As mentioned previously, a bonus of working with diamond is that it also hosts highly coherent artificial atoms such as the nitrogen vacancy (NV) and silicon vacancy (SiV) color centers [259], which have been used in demonstrations of quantum memory [260, 261], quantum entanglement [157, 158], quantum teleportation [262], loophole-free Bell's inequality violation [263], and the transfer of phase information from microwave to optical fields [264]. Diamond cavity optomechanics can in principle interface these color centers with light and other quantum systems in new ways [252, 253]. One such application is conversion of color center emission to telecommunication wavelengths. A purely optomechanical approach allows high efficiency wavelength conversion between any two wavelengths of a cavity's mode spectrum [44, 45, 61, 265] for relatively low input power, negating the need for material dependent nonlinear optical processes [266, 267, 268, 269, 270, 271, 272, 273]. Here we demonstrate optomechanical wavelength conversion in a diamond cavity for the first time, and show that this scheme can be operated in a regime where the converted signal is op-

tomechanically amplified. We also probe the bandwidth and noise properties of this process using a novel broadband coherent spectroscopy technique.

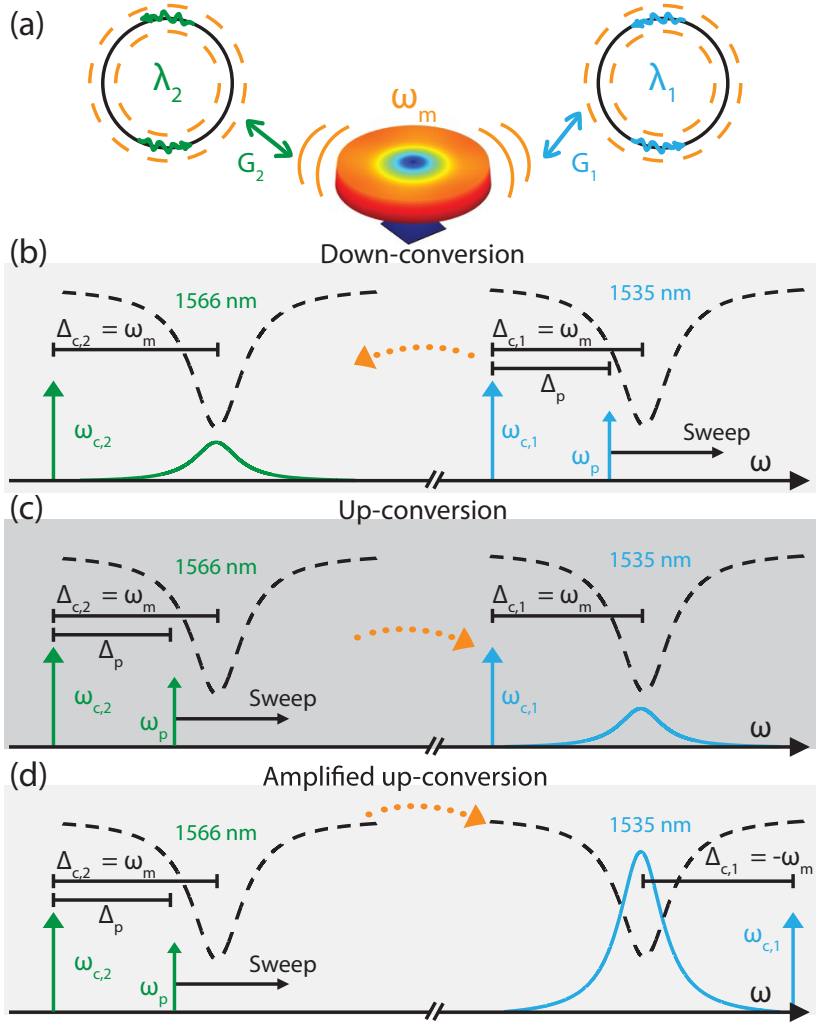

Figure 7.4: (a) Illustration of the system under study. Two microdisk optical whispering gallery mode resonances at λ_1 and λ_2 are coupled to the microdisk's mechanical radial breathing mode whose frequency is ω_{m}. Schematics illustrating the cavity density of states, control and probe field detunings for the case of frequency up- and down-conversion with no amplification (b,c), and (d) frequency up-conversion with amplification.

Cavity optomechanical wavelength conversion coherently couples two optical cavity modes at frequencies $\omega_{\mathrm{o},1}$ and $\omega_{\mathrm{o},2}$ via their independent optomechanical coupling to a common cavity mechanical resonance at frequency ω_{m}. In microdisk cavities, such as the diamond cavity studied here and illustrated in Fig. 7.4(a), the optomechanical coupling is created by the radiation pressure force exerted by optical whispering gallery modes on the microdisk. This

interaction can coherently exchange energy between optical and mechanical domains when a strong control laser is input to the cavity at a frequency ω_c red-detuned $\Delta_c = \omega_o - \omega_c = \omega_m$ from the cavity mode by the mechanical resonance frequency. The resulting system can be represented by a photon-phonon beamsplitter Hamiltonian [18], and has been used to demonstrate optomechanically induced transparency (OMIT) and slow light [63, 111] in a variety of devices, including in diamond microdisks [5].

In multimode cavity optomechanical systems, coherent photon-phonon coupling is harnessed to convert probe photons input on resonance with a mode at $\omega_{o,1}$ to a mechanical excitation that is in turn converted to signal photons resonant with the second cavity mode $\omega_{o,2}$. This process requires inputting two control lasers, referred to as write and read fields, to the cavity. Typically both control lasers are red-detuned by $\Delta_c = \omega_m$ from their respective cavity modes as illustrated in Figs. 7.4(b,c). This setup, which has been used in previous optical domain wavelength conversion demonstrations [44, 45, 61], can in principle be amplified by blue-detuning the read laser from the cavity ($\Delta_c = -\omega_m$), as shown in Fig. 7.4(d). This enables low-noise amplification of the converted photons, as recently demonstrated by Ockeloen-Korppi et al. in the microwave regime [250] and reported below for the first time in the optical domain. Such two-port amplification avoids optomechanical self oscillation by balancing optomechanical amplification with damping for the blue- and red-detuned optical modes, respectively, and unlike traditional optomechanical amplification [274, 275, 276] has a fundamentally unlimited gain-bandwidth product.

The diamond microdisks used here for wavelength conversion, an example of which is shown in the scanning electron micrograph image in Fig. 7.5(a), support whispering gallery modes with optical quality factor Q_o sufficiently high for operation in the resolved sideband regime of cavity optomechanics. These devices were fabricated using an optimized reactive ion undercutting process described in Chapter 6 that results in a smooth diamond microdisk supported by a thin diamond pillar, and have higher Q_o than those previously used for single-mode diamond optomechanics studies [5].

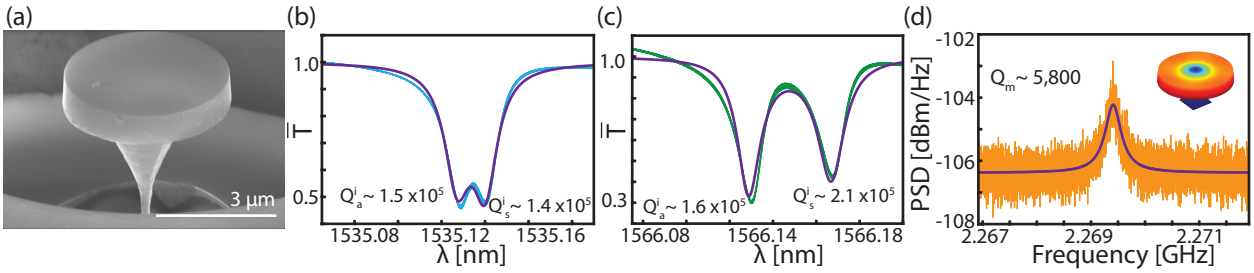

Figure 7.5: (a) Scanning electron micrograph of a diamond microdisk similar to the device under study here (~ 5 μm diameter). (b,c) Optical whispering gallery mode resonances used in the frequency conversion process. Intrinsic optical quality factors of the symmetric ($Q^i_{\rm s}$) and anti-symmetric ($Q^i_{\rm a}$) doublet modes extracted from fit lineshapes are indicated. (d) Photodetected power spectral density of the optomechanically transduced thermally driven microdisk RBM motion in ambient pressure and temperature (Inset: COMSOL simulated mode profile). Measured at input power sufficiently low to not affect the mechanical resonance dynamics. Mechanical quality factor $Q_{\rm m} \sim 5,800$ is extracted from the fit lineshape.

All of the measurements presented below involve two sets of microdisk optical modes widely separated in wavelength and mutually coupled to the same mechanical RBM of the microdisk, whose mechanical displacement profile is illustrated in Fig. 7.4(a). Their optomechanical properties were probed using coherent fiber taper optical mode spectroscopy as in previous work [4, 6, 5] using the apparatus described in more detail below. Fiber taper transmission spectra for the two modes are shown in Figs. 7.5(b,c), revealing resonances with frequencies $\omega_{\rm o,1}/2\pi = 195$ THz ($\lambda_1 = 1535$ nm) and $\omega_{\rm o,2}/2\pi = 191$ THz ($\lambda_2 = 1566$ nm), and unloaded $Q^{\rm i}_{\rm o} \sim 1.4 \times 10^5$ and 2.1×10^5, respectively. The doublet nature of the resonances indicates that they are standing wave modes [128]; the red mode of each doublet was used for all of the measurements described below. The λ_1 mode was found to be TM-like, while the λ_2 mode was TE-like, which is reflected in the different splitting of each doublet, but is not an essential ingredient for the results presented here. These modes are used to optomechanically transduce the motion of the microdisk mechanical resonances, with a typical photodetected power spectral density of the thermomechanical motion of the microdisk's RBM shown in Fig. 7.5(d), revealing a resonance frequency $\omega_{\rm m}/2\pi = 2.27$ GHz and mechanical quality factor $Q_{\rm m} = 5,800$ in the ambient conditions used for all of the reported measurements. The device's combination of high mechanical frequency and high $Q_{\rm o}$ places it in the resolved sideband regime $\kappa/\omega_{\rm m} \leq 1$. The device studied here was the 'best' that

I fabricated during my graduate studies, partly because it was the first to firmly lie in the sideband resolved regime.

The experimental setup used to coherently couple light at multiple wavelengths to the microdisk's mechanical motion is shown in Fig. 7.6(a), and a complete equipment list is given in Appendix F. Two independent tunable diode lasers generate the control fields. An amplitude or phase EOM driven by a VNA at a swept frequency Δ_{p} generates the probe field by adding sidebands to the $\omega_{\mathrm{c},1}$ or $\omega_{\mathrm{c},2}$ control field, respectively. An RF switch selects which control laser will be modulated, determining whether to carry out frequency down- or up-conversion, respectively. The control field intensities are amplified via an EDFA before being coupled to the microdisk via the optical fiber taper. The transmitted signal is used for the optical mode spectroscopy described above, while the reflected signal is routed via an optical circulator through a tunable band pass filter (TBF) that separates the converted signal and the read control field from the write control and the input probe fields. The beat note from the converted signal field interfering with the read control field is then demodulated from the photodetector output by the VNA.

To demonstrate wavelength conversion the lasers were first setup in the up-conversion configuration illustrated in Fig. 7.4(c): both read and write control fields red-detuned from their respective cavity modes by $\Delta_{\mathrm{c},1} = \Delta_{\mathrm{c},2} = \omega_{\mathrm{m}}$, and the write control field weakly modulated at Δ_{p} to generate the probe sideband (wavelength λ_2). The resulting measured beatnote, $S_{\mathrm{C}}(\Delta_{\mathrm{p}})$, between the up-converted field at λ_1 and the read control field, is shown in Fig. 7.6(b). Efficient conversion is observed when $\Delta_{\mathrm{p}} = \omega_{\mathrm{m}}$, i.e. when the probe field is on-resonance with the cavity mode, and is observed over a bandwidth defined by the optomechanically broadened mechanical linewidth.

Calibrating S_{C} and writing it as a wavelength conversion efficiency requires careful characterization of the detectors and electronics used in the experiment. Instead, following previous reports [44, 61], we infer an external conversion efficiency $\eta_{\mathrm{ex}} = \eta_1\eta_2\eta_{\mathrm{int}}$ between λ_2 and λ_1 from the optomechanical properties of our device. Here $\eta_1 = 13\%$ and $\eta_2 = 21\%$

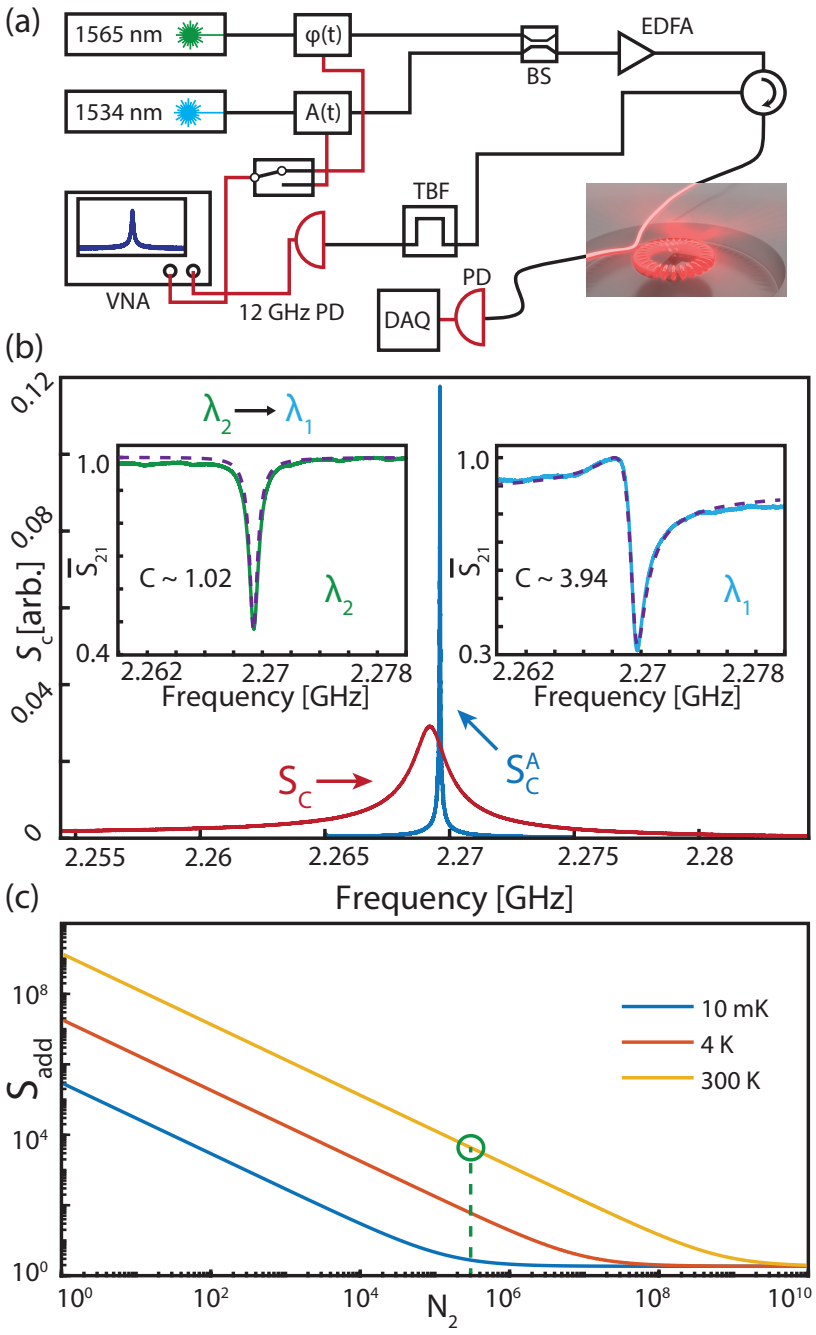

Figure 7.6: (a) Experimental setup used for wavelength conversion and amplification. Phase, $\phi(t)$ and amplitude ($A(t)$) EOM's driven by the vector network analyzer (VNA) are used to generate the probe fields from the control fields where an RF switch controls which laser to modulate. A 50%/50% waveguide coupler combines the input fields which are coupled to the microdisk via a dimpled tapered fiber. A tunable band pass filter (TBF) is used to filter the output of the cavity and the photodetected signal is analyzed by the VNA. (b) Beat note between converted photons and control field of the same color measured on the VNA for frequency up-conversion with and without amplification. OMIT spectra for the λ_2 and λ_1 optical modes are shown as insets, where the cooperativity is extracted from the depth of the OMIT feature. (c) Predicted added noise to amplified signal based on Eq. 7.8, and system parameters, with operating regime circled.

are the experimentally measured waveguide-cavity coupling efficiencies at wavelengths λ_1 and λ_2 respectively, extracted by determining the coupling rate $\kappa_{\rm ex}$ between the microdisk standing wave modes and the forward propagating fiber mode from fits to the doublet resonances, taking into account the standing wave modes' equal coupling to the backwards propagating fiber mode. The internal conversion efficiency, $\eta_{\rm int} = 4C_1C_2/(1+C_1+C_2)^2$, is determined solely by the optomechanical cooperativity, C_j, of each mode λ_j [44]. Here $C_j = 4N_j g_{0,j}^2/\kappa_j\Gamma_{\rm m}$ was measured from the modes' OMIT dips shown in the insets to Fig. 7.6(b), where N_j and $g_{0,j}$ are the respective control field intracavity photon number and the vacuum optomechanical coupling rate of mode j. These single color OMIT measurements record the beatnote between control field j in the red detuned configuration ($\Delta\omega_{{\rm oc},j} = \omega_{\rm m}$) and its modulator generated sideband at $\omega_{{\rm c},j} + \Delta_{\rm p}$. Note that while both control lasers were kept on during this measurement, only one OMIT process was carried out at a time, by placing the other laser off resonance. By fitting the OMIT spectra in Fig. 7.6(b) to the model described in Appendix D we extract $C_1 \sim 3.94$ and $C_2 \sim 1.02$, for $N_1 \sim 3.1\times10^6$ and $N_2 \sim 2.2\times10^5$, respectively, corresponding to $\eta_{\rm int} \sim 45\%$. Here N_j and $\Delta_{{\rm oc},j}$ were used as the only fitting parameters where all other required parameters were measured independently. Measurements of g_0 were performed using the phase tone calibration method [277], giving $g_0/2\pi \sim$15 kHz and 27 kHz for the λ_1 and λ_2 modes, respectively, as described in Supplement 1. Note that the Fano-shape of the λ_1 OMIT dip is related to a non-zero phase imparted by the amplitude modulator, and the demodulation process of the VNA, as described in detail in Appendix D. These measured values for C_j are consistent with the estimated fiber taper input power for each control field of $P_{\rm in} \sim 16$ mW and ~ 3.8 mW.

Increasing $\eta_{\rm int}$ could be achieved by operating in the $C_j \gg 1$ regime and by matching $C_1 = C_2$. For the diamond cavities studied here, in practice N_j can be increased above 10^6 until becoming limited by thermal instabilities within the cavity. In this experiment we were unable to balance C_1 and C_2 while maintaining $C_j > 1$ as the input laser used to drive λ_2 mode was less efficiently amplified in the EDFA. Combined with greater loss in the system at

λ_2, this resulted in $N_2 < N_1$. The use of a second EDFA with a gain maximum near λ_2 would allow independent control of N for each mode. Assuming each mode could reach $C \sim 2$, $\eta_{\rm int} \sim 64\%$ would be achievable. Finally, the relatively small $\eta_{\rm ex} = 1.23\%$ demonstrated here could be improved by operating in the over-coupled regime, which requires either higher $Q_{\rm i}$ or improved coupling via, for example, an external on-chip waveguide. Unfortunately the $\omega_{\rm o,2}$ mode was outside the range of the TBF, prohibiting measurement of down-conversion for this device. However, down-conversion was measured using a different device, with lower conversion efficiency, as described below.

For completeness, a demonstration of wavelength up– and down– conversion in the same device is presented here with an alternative microdisk on the same SCD substrate as presented above. This device exhibited two high-$Q_{\rm o}$ optical modes that were within the operating range of a 1510/1550 nm wavelength division multiplexer (WDM) which allowed the filtering of each mode from the fiber taper transmission, which we were unable to do with the device studied above. Contrary to the measurement presented in the main text this device was measured in transmission instead of reflection, as outlined in Fig. 7.7(a). Here two optical modes at $\lambda_1 = 1520$ nm and $\lambda_2 = 1560$ nm, as shown in Fig. 7.7(b,c), were coupled to the fundamental radial breathing mode (RBM) at $\omega_{\rm m}/2\pi = 2.135$ GHz, with $Q_{\rm m} \sim 7,500$, for a similarly sized microdisk as studied in the main text. The measurement of both the up– and down–converted signal with the VNA is shown in Fig. 7.7(d,e).

During this measurement the symmetric mode ($\omega_{\rm o} - \frac{\gamma_\beta}{2}$) of the λ_1 doublet was used such that the blue sideband of the EOM was off-resonance. However, the anti–symmetric ($\omega_{\rm o} + \frac{\gamma_\beta}{2}$) mode of the λ_2 doublet was used in the conversion process due it's the higher optical-$Q_{\rm o}$. When setting up the experiment, balancing C for each mode was performed by maximizing the contrast of each OMIT window, while attempting to reach $C_1 = C_2 > 1$. However, the relatively small splitting of this doublet led to a modification to the OMIT window spectral profile, due to participation of the red mode of the doublet, resulting in lower C than expected based on the depth of the OMIT feature alone, and an overall low

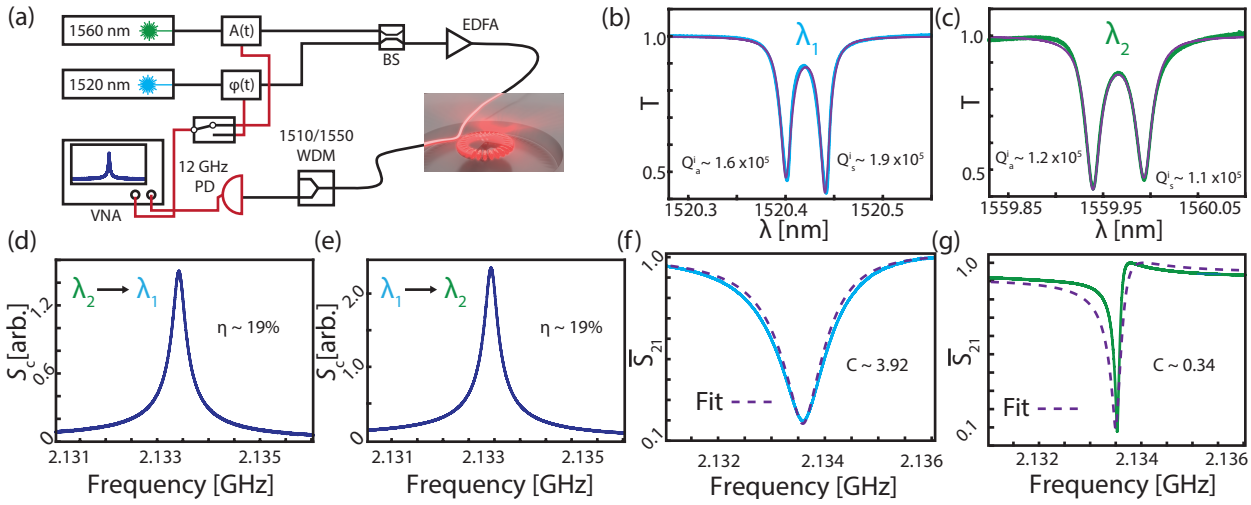

Figure 7.7: (a) Experimental setup used for frequency up– and down–conversion. Phase ($\phi(t)$)and amplitude ($A(t)$) EOM's driven by the vector network analyzer (VNA) are used to generate the probe fields from the control fields where an RF switch controls which laser to modulate. A 50%/50% waveguide coupler combines the input fields which are coupled to the microdisk via a dimpled tapered fiber. A 1510/1550 WDM is used to filter the output of the cavity and the photodetected signal is analyzed by the VNA. (b,c) Optical whispering gallery mode resonances used in frequency conversion process. Intrinsic optical quality factors for the symmetric and anti–symmetric doublet modes labelled. (d,e) Beat note between converted photons and control field of the same color measured on the VNA for frequency up– and down– conversion respectively. (f,g) OMIT spectra for the λ_1 and λ_2 optical modes, respectively, where the cooperativity is extracted from fitting the OMIT lineshape.

conversion efficiency due to the mismatch of C_1 and C_2. To account for this contribution the transmission amplitude for the blue sideband, $t^-(-\Delta_\mathrm{p})$, for an optical doublet was included (see Section 2.2.3) as

$$t^-(-\Delta_\mathrm{p}) = 1 - \sqrt{\kappa_\mathrm{ex}/2}(a_\mathrm{s}(-\Delta_\mathrm{p}) + a_\mathrm{a}(-\Delta_\mathrm{p})), \tag{7.4}$$

where

$$a_\mathrm{s,a}(-\Delta_\mathrm{p}) = \frac{-\sqrt{\kappa_\mathrm{ex}/2}}{-\kappa_\mathrm{s,a}/2 + i((\Delta_\mathrm{c} - (-\Delta_\mathrm{p})) \pm \kappa_\mathrm{bs}/2)} \tag{7.5}$$

are the symmetric (a_s) and anti-symmetric (a_a) combinations of the degenerate clockwise and counter–clockwise propagating travelling wave modes of the microdisk [128]. Here κ_bs is the backscattering rate between each mode, and κ_ex is taken to be equal for each doublet.

The OMIT spectrum obtained with the phase EOM shown in Fig. 7.7(f) was fit by includ-

ing both side bands ($t^{\pm}(\pm\Delta_{\mathrm{p}})$ where a small phase delay ($< 5^{\circ}$) in sidebands was included to obtain good agreement with the spectra. In order to fit the OMIT spectrum obtained with the amplitude EOM shown in Fig. 7.7(g) both the inclusion of the chirp induced sideband phase difference ($2\theta \sim 70^{\circ}$) and the doublet transmission profile for ($t^{-}(-\Delta_{\mathrm{p}})$ were included. While the quality of this fit is inferior compared to the other OMIT fits, the inclusion of the doublet transmission profile reproduces the sharp, large contrast OMIT feature that in reality has $C < 1$. This results in $C_1 \sim 3.92$, $C_2 \sim 0.34$, and $\eta_{\mathrm{int}} \sim 15\%$, for $\eta_{1,2} \sim 19\%$, resulting in $\eta_{\mathrm{ext}} = 0.55\%$ for the device studied here. The fiber taper input power, P_{in}, was ~ 17 mW and ~ 4.2 mW, respectively, corresponding to $N_1 \sim 7.0 \times 10^5$ and $N_2 \sim 9.0 \times 10^4$ for λ_1 and λ_2.

7.5 Optomechanically amplified wavelength conversion

These devices are also promising for quantum limited amplification of the wavelength converted signal field, as previously demonstrated in the microwave domain [250]. As described above and shown in Fig. 7.4(d), signal amplification is achieved by placing the λ_1 read control laser blue-detuned from the cavity, $\Delta_{\mathrm{c},1} = -\omega_{\mathrm{m}}$, while keeping the λ_2 write control laser red-detuned as before, $\Delta_{\mathrm{c},2} = \omega_{\mathrm{m}}$. This results in what can be thought of as a two step process involving a beam-splitter interaction between the λ_2 mode and the mechanical mode, and parametric amplification between the mechanical mode and the λ_1 mode [250]. The converted-amplified signal is detected in the same fashion as above, where the beat note $S_{\mathrm{C}}^{\mathrm{A}}$ produced by the amplified converted light and the read control field is shown in Fig. 7.6(b). The frequency and linewidth of the amplified, $S_{\mathrm{C}}^{\mathrm{A}}$, and unamplified, S_{C}, spectra is governed by the optomechanical damping (Γ_{opt}) and optical spring effect ($\delta\omega_{\mathrm{m}}$) induced on the mechanical resonance dynamics by each control laser. As both control lasers are red-detuned for S_{C}, its effective mechanical linewidth is broader and the center frequency is red-shifted compared to its intrinsic value shown in Fig. 7.5(d). In contrast, as described above, for $S_{\mathrm{C}}^{\mathrm{A}}$ the λ_1 laser

is blue-detuned while λ_2 is red-detuned. As the photon assisted optomechanical coupling rates, $G_j = g_{0,j}\sqrt{N_j}$, are such that $G_1 > G_2$ ($G_1 = 2\pi \times 26.4$ MHz, $G_2 = 2\pi \times 12.5$ MHz), this initially resulted in the microdisk being in the self-oscillation regime. To obtain the amplified spectra in Fig. 7.6(b) $\Delta_{c,1}$ was adjusted such that the device was no longer in the self-oscillation regime, although a narrowed linewidth and blue-shift of the center frequency is still observed. Ideally, in the low-noise amplification scheme described in Ref. [250] the system should be operated in the $G_2 \gtrsim G_1$ regime to avoid instabilities associated with optomechanical self oscillation.

To characterize the noise properties of the $S_{\mathrm{C}}^{\mathrm{A}}$ spectrum we follow the analysis of Ockeloen-Korppi et al. [250], starting with expected frequency-converted gain, given by

$$A_{\mathrm{x}} = 2\left(\frac{\kappa_{\mathrm{ex}}}{\kappa}\frac{4G_1G_2/\kappa}{\Gamma_{\mathrm{m}} - 4\overline{G}^2/\kappa}\right), \tag{7.6}$$

where the optical cavity dissipation constants have been taken to be equal and $\overline{G}^2 = G_1^2 - G_2^2$. The adjusted G_1 value was determined from the linewidth of $S_{\mathrm{C}}^{\mathrm{A}}$ where G_2 was held constant, giving $G_1 \sim 2\pi \times 14.1$ MHz. For the operating conditions here, and taking $\kappa = \kappa_2$ we find $A_{\mathrm{x}} \sim 1.2$. For these operating conditions the amplifier is not in a low-noise regime as the added noise to $S_{\mathrm{C}}^{\mathrm{A}}$ is dominated by the contribution from the mechanical bath, whose equivalent added noise on resonance is given by $S_{\mathrm{add,m}}/|A_{\mathrm{x}}|^2$:

$$S_{\mathrm{add,m}} = \frac{\Gamma_{\mathrm{m}}\kappa_{\mathrm{ex}}G_1^2}{\left|\Gamma_{\mathrm{m}}\kappa/4 - \overline{G}^2\right|^2}\left(n_{\mathrm{th}} + \frac{1}{2}\right), \tag{7.7}$$

where $n_{\mathrm{th}} \sim k_{\mathrm{B}}T/\hbar\omega_{\mathrm{m}}$ is the thermal occupation of the RBM. For this experiment this results in $\sim 6.52 \times 10^3$ added quanta to the $S_{\mathrm{C}}^{\mathrm{A}}$ spectra. To predict future performance of this system within the context of low-noise single photon wavelength conversion, we calculate the added noise to the amplified optical signal in the ideal high gain ($G_2 \gtrsim G_1$) and large Γ_{opt} regime, given by

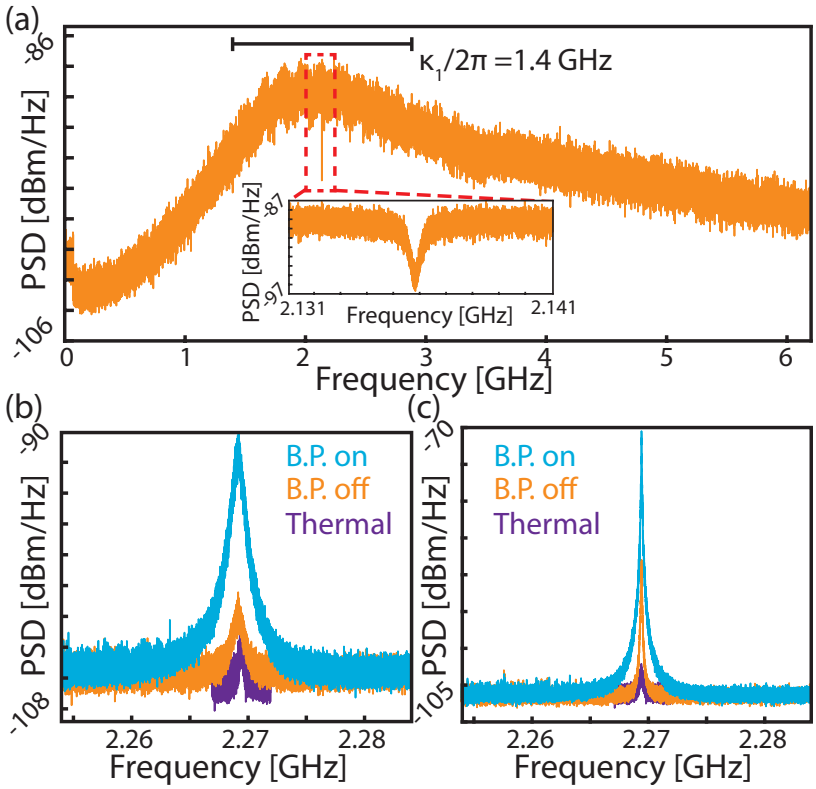

Figure 7.8: Measurement of OMIT and wavelength conversion via the RSA. (a) Broadband and narrowband (inset) spectrum showing the cavity response and the OMIT feature at $\omega_{\mathrm{m}}/2\pi$ when a phase EOM is driven with a broadband RF noise source for the device shown in Supplement 1. (b,c) Wavelength conversion for the same device in Fig. 7.6 without (b) and with (c) amplification as measured on the RSA, with the noisy broadband probe (B.P.) field. The thermal motion of the RBM is also shown, which was measured at low power with a single laser to avoid optomechanical back action.

$$S_{\mathrm{add}} = \frac{\Gamma_{\mathrm{m}}\kappa}{4G_2^2}\frac{\kappa}{\kappa_{\mathrm{ex}}}\left(n_{\mathrm{th}} + \frac{1}{2}\right) + \frac{\kappa_{\mathrm{i}}}{\kappa_{\mathrm{ex}}} + \frac{1}{2}. \tag{7.8}$$

Here $\kappa_{\mathrm{i}} = \kappa - 2\kappa_{\mathrm{ex}}$ is the intrinsic cavity photon decay rate, where the optical decay rates have been taken to be similar for each cavity. The predicted added noise as a function of N_2 is shown in Fig. 7.6(c) for the parameters of the device under study and for various temperatures. We predict that the minimum added noise of ~ 2 quanta, limited by the coupling efficiency achieved here, can be approached for $N_2 \sim 1 \times 10^6$ at 10 mK and $N_2 \sim 1 \times 10^8$ at 4 K for this device, provided that operation in the ($G_2 \gtrsim G_1$) regime is enabled by overcoming technical limitations in our experiment. Furthermore, amplification at the SQL of 1/2 quanta could be possible by improving the coupling to the device such that $\kappa_{\mathrm{ex}} \gg \kappa_{\mathrm{i}}$.

To further characterize the converted amplified signal we used a broadband (compared to κ) RF noise source to drive the phase modulator generating the OMIT probe field, similar to the approach described in Ref. [278]. Here an arbitrary waveform generator (AWG) outputting a pseudo Gaussian white noise signal with a sampling rate and length of 25 GS/s and 2 GS, respectively, drove the RF input of the phase EOM (20 GHz bandwidth) to create a broadband optical probe field from the write field control laser. When the control laser is tuned to $\Delta_{c,2} = \omega_m$, observation of both OMIT and wavelength conversion on a RSA is possible. Figure 7.8(a) shows the measured probe field's power spectral density, revealing the cavity response for frequency components of the probe that do not coherently drive the mechanics, which in these measurements is the broad peak in the demodulator signal with a line width of $\kappa/2\pi = 1.4$ GHz, and an OMIT dip at $\Delta_p = \omega_m$, i.e. where the OMIT condition is satisfied. This demonstrates a straightforward method for measuring OMIT and the cavity response simultaneously in frequency space.

Wavelength conversion of the λ_2 broadband probe generated by the RF noise source, in both the unamplified and amplified configurations, measured in reflection, is shown in Figs. 7.8(b) and 7.8(c) respectively. The plots in Figs. 7.8(b) and 7.8(c) show the detected power spectral density of the converted signal at λ_1 (blue trace) compared for reference with the corresponding measurement when the λ_2 probe is off (orange trace) so that the detected spectrum is derived entirely from the optomechanically modified motion of the microdisk due to the λ_1 and λ_2 control fields. As above, when both control lasers are red-detuned in Fig. 7.8(b) , the effective mechanical linewidth is broader and the center frequency is red-shifted compared to its intrinsic value (purple trace), which was measured at low power with a single optical mode to avoid optomechanical back action. In the amplified conversion case shown in Fig. 7.8(c) the linewidth is slightly narrowed and shifted to higher frequency due to the fact that $G_1 > G_2$. In principle this technique could be utilized in balancing G_j by adjusting N_j such that the linewidth of the observed spectra with the broadband probe off is equal to the intrinsic linewidth observed in the absence of the strong control fields.

The converted signal power in both amplified and unamplified cases can be computed directly from the area under the spectrum. When the probe is off we see the added noise from the thermally driven signal level that would have to be overcome by increasing C_j to allow operation at the single-photon level. To compare the signal to noise ratio (SNR) for each case, we have defined the SNR as the difference in integrated power with the broadband probe field on and off, divided by the off-resonant noise floor. We find that the amplified conversion SNR is 1.62 $\times$ larger than without amplification, for the same input broadband probe. With calibration of the probe spectrum, this broadband probe technique could also be used to determine the conversion efficiency, similar to what has been suggested by Liu et al. [61] where a coherent drive and RSA were used to characterize the converted signal.

7.6 Summary & Outlook

In summary, we have demonstrated a diamond cavity optomechanical system capable of coherent photon-phonon interactions such as optomechanically induced transparency, and phonon-mediated wavelength conversion with $C > 1$ and an internal conversion efficiency of $\sim 45\%$. While we were limited by an imbalance of G_1 and G_2, and $\kappa_{\mathrm{ex}} < \kappa$ in this experiment, operation in the stable, high-gain regime $G_2 \gtrsim G_1$ should be possible by utilizing a second EDFA to allow separate control of G_1 and G_2, and improving waveguide-cavity coupling would enable $A_{\mathrm{x}} \gg 1$. To the best of our knowledge, this is also the first demonstration of optomechanical amplification, albeit not operating in the low-noise regime, of the converted light in the optical domain. In this configuration this system has promise for reaching a minimum added noise of ~ 2 quanta during the amplification process by operating at larger photon number and with $G_2 \gtrsim G_1$. This device can in principle operate at the standard quantum limit (SQL) where a minimum of half an energy quanta of noise is added to the signal by improving the waveguide-cavity coupling efficiency, and has immediate practical use in increasing signal to noise when measuring quantum optomechanical effects [279]. In

addition, use of a broadband noisy optical probe field was introduced for both OMIT and wavelength conversion. Finally, as previous studies in these structures [4] have demonstrated the existence of high-Q_o optical modes at $\sim$ 738 nm and $\sim$ 637 nm, near the zero phonon lines of SiV and NV color centers respectively, these devices have potential as a converter of diamond color center emission to telecommunications wavelengths for application in quantum networks.

Chapter 8

Conclusion

8.1 Summary

In this work optomechanical cavities in gallium phosphide and single-crystal diamond were demonstrated for the first time, avoiding the detrimental nonlinear absorption present for large N in non wide-band gap materials such as silicon at telecommunications wavelengths. These demonstrations entailed the design, simulation, fabrication, characterization, and modelling of microdisk cavities in these materials, all of which I had the opportunity to carry out during my graduate studies. For the SCD microdisk fabrication in particular, great effort was required to optimize the fabrication process due to the difficulty with working with bulk SCD substrates. The optomechanical properties of these devices were sufficient for exploring coherent cavity optomechanical phenomena in ambient conditions. By reaching optomechanical cooperativity, $C > 1$, the devices realized in this work are able to exchange energy between photons and phonons in the system at a rate faster than the rate at which energy leaks out of the system. This enabled the study of coherent photon-phonon interactions such as optomechanically induced transparency and optomechanically mediated wavelength conversion with an internal conversion efficiency of 45%, all at room temperature and pressure.

8.2 Outlook

Here I will briefly discuss some of our current work using SCD microdisks for investigating multimode optomechanical phenomena and outline potential routes forward for further optimization of SCD microdisks and other potential routes to explore quantum cavity optomechanics in SCD.

8.2.1 Multimode optomechanics

Microdisk optomechanical cavities are well suited towards multimode operation, where multiple optical modes can be coupled simultaneously to the radial breathing mode. Multimode devices have enabled studies of fundamental science involving interaction between light at widely separated optical wavelengths inaccessible to single-mode optomechanical systems. In addition to the optomechanically mediated wavelength conversion demonstrated in this work, we have been investigating other multimode phenomena such as double-optomechanically induced transparency (DOMIT), which enabled all optical two-color switching [8], and optomechanically tunable pulse storage [257], the later of which I will briefly discuss here to highlight the potential of these devices.

Optomechanical pulse storage typically utilizes coupling between a single optical and mechanical mode, where an optical pulse is stored as a mechanical excitation, which has an intrinsic damping rate Γ_{m} due its coupling to the environment [43, 280]. Here we extend this protocol to multimode operation, where one optical mode is used to manipulate both the phase and amplitude of the stored optical pulse during the optomechanical storage protocol. By adjusting the control laser (frequency ω_l) detuning relative to the supplementary optical mode ($\Delta_{\mathrm{s}} = \omega_{\mathrm{l}} - \omega_{\mathrm{s}}$, the phase lag between the resonator and coupling dynamics can be modified, while adjusting the power of the control laser, P_{s}, modifies the coupling strength. In particular, coupling to the optical mode induces mechanical dissipation $\Gamma_{\mathrm{s}}^{\mathrm{opt}}$, and shifts the mechanical resonator frequency by $\omega_{\mathrm{s}}^{\mathrm{opt}}$ via optomechanical damping/heating and the

optical spring effect.

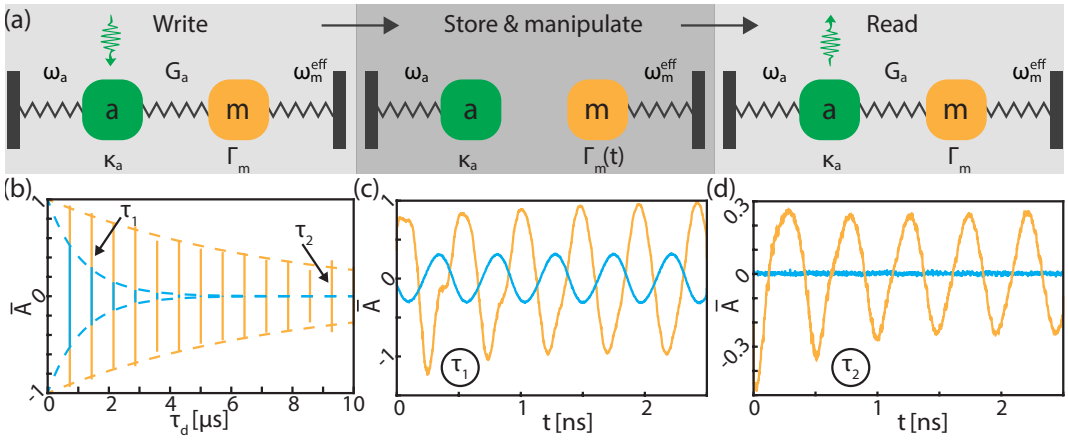

Figure 8.1: (a) Outline of pulse storage protocol where the optomechanical coupling between optical mode a and the mechanical mode facilitates storage of an optical pulse as a mechanical excitation. Mode s is used to manipulate the mechanical damping rate, $\Gamma_{\rm m}^{\rm eff}(t)$, and frequency, $\omega_{\rm m}^{\rm eff}(t)$ which can be carried out concurrently with the storage process. (b) Normalized read pulse amplitude, $\bar{A}$ for the off-resonant, $\Delta_{\rm s} \gg \omega_{\rm m}$, case (cyan) and for $\Delta_{\rm s} \sim \omega_{\rm m}$ (orange) as a function of $\tau_{\rm d}$. Here the control field for s was operated in continuous wave mode such there is no time dependence in $\Gamma_{\rm m}^{\rm eff}(t)$, and $\omega_{\rm m}^{\rm eff}(t)$. (c,d) Example measurements for points α and β illustrating the enhancement in $\bar{A}$ when $\Delta_{\rm s} \sim \omega_{\rm m}$.

The steps of our pulse storage protocol are illustrated in Fig. 8.1(a), where the optical mode, a, and mechanical mode, m, are represented as a damped mass-spring system. During the write stage, a strong control laser is red detuned from the cavity by the mechanical frequency ($\Delta_{\rm a} = \omega_{\rm l} - \omega_{\rm a} = -\omega_{\rm m}$). This couples mode a to mode m with the photon enhanced optomechanical coupling rate, $g_{\rm a}$, permitting the coherent exchange of photons and phonons [18]. As a consequence, when a probe photon enters the optical cavity, it is converted into a mechanical excitation. Following the write stage, the control laser is removed, which decouples modes a and m, and ensures that the signal pulse remains as a mechanical excitation of the RBM. At this point, coupling to the supplementary mode is turned on, permitting dynamic control of the damping rate and resonant frequency of the mechanical mode. Finally, during the read stage, the initial control laser is turned on, once again coupling a and m. This coupling converts the signal from the mechanical mode into the optical mode, which then exits the cavity via the fiber taper waveguide.

Through continuous amplification of the stored mechanical pulse by the supplementary mode, we drastically extend the lifetime of a stored pulse. To measure the storage time,

we varied the delay between the write and read pulses by an amount τ_{d}. The measured amplitude encodes the decay envelope of the mechanical pulse, and decays exponentially at a rate $\Gamma_{\mathrm{m}}^{\mathrm{eff}}$. An example of this decay is plotted on Fig. 8.1(b) for the case that the reservoir laser is optimally detuned for storage ($\Delta_{\mathrm{s}} \approx \omega_{\mathrm{m}}$), and for comparison the far detuned case ($\Delta_{\mathrm{s}} \gg \omega_{\mathrm{m}}$), where the effective damping rate is simply $\Gamma_{\mathrm{m}}^{\mathrm{eff}} = \Gamma_{\mathrm{m}}$. The ratio of the decay envelopes $\Gamma_{\mathrm{m}}^{\mathrm{eff}}/\Gamma_{\mathrm{m}}$ indicates a 7× enhancement. Examples of the signal extracted at two values of τ_{d} are shown on Fig. 8.1(c,d) and demonstrate a dramatic difference in the amplitude of the enhanced versus the unenhanced signal at longer timescales.

Finally, we demonstrate that the phase of the stored pulse can also be controlled via the supplementary mode. By changing $\omega_{\mathrm{b}}^{\mathrm{eff}}$ adiabatically and hence the frequency of the stored pulse, we can complete a trajectory which moves away from and then returns to the original frequency. Over the course of this trajectory, the mechanical oscillator acquires a dynamical phase $\varphi(t_2) = \varphi(t_1) + \int_{t_1}^{t_2} \delta\omega(t)dt$, assuming that we return to the original mechanical frequency. This is analogous to a pendulum whose length is adjusted in time [281]. In our experiment, we varied the amplitude of the reservoir mode in time using an amplitude electro-optic modulator driven by a symmetric RF ramp pulse for various Δ_{s} as shown in Fig. 8.2(a). Here the ramp pulse was 3.5 μs long and was situated 1.5 μs after the write, and before the read pulse. By fitting the beat note detected at the fiber output for each of the write, ramp, and read pulse segments we can plot the phase as referenced to the well-defined write pulse, as shown in shown in Fig. 8.2(b). Here we have removed the phase shift associated with the spring effect induced by the write pulse, which added a linear slope to the ramp and read pulse segments. This allows us to isolate the shift due to the spring effect associated with the reservoir mode ramp pulse. From the read pulse segments we extract the phase relative to the write pulse, demonstrating a reservoir controlled phase shift, $\Delta\varphi > 2\pi$ as shown in Fig. 8.2(c).

Here we have demonstrated that the in-situ control offered by this multimode optomechanical system is a powerful tool for enhancement of storage times, bypassing the usual

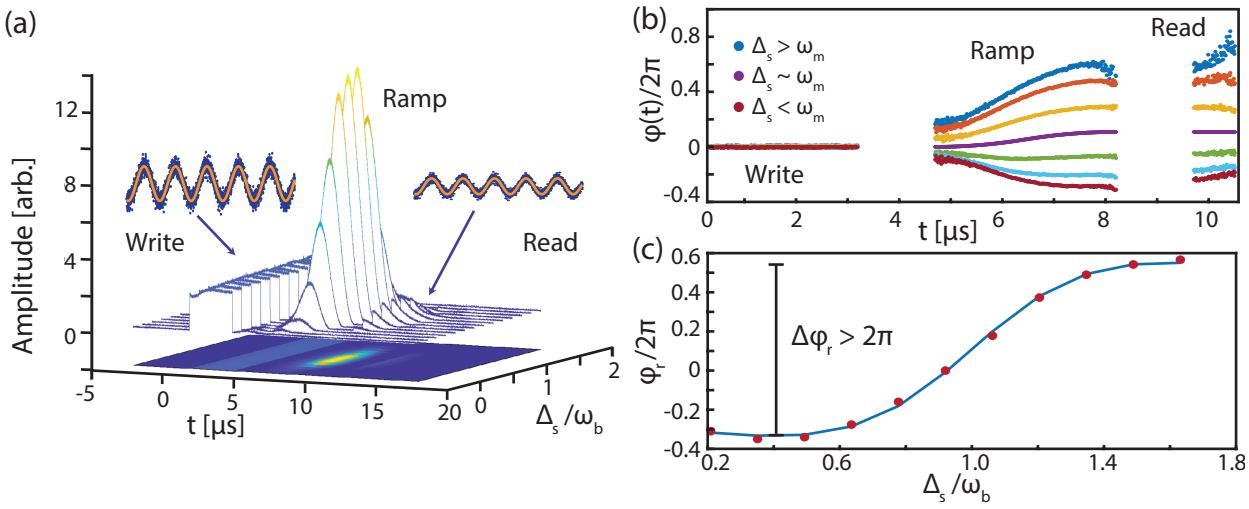

Figure 8.2: (a) Amplitude of the acquired signals vs. time and supplementary mode detuning for the phase supplementary experiment. In this experiment no optical filtering was used, so that the write, ramp, and read pulses may all be detected. (b) Phase of the mechanical oscillator vs. time as inferred from the optical output of the device. (c) Final phase as a function of Δ_s along with a fit to the data based on the optical spring effect associated with the ramp pulse.

limitations imposed by the intrinsic damping rate, and can be used to generate controllable phase shifts in the stored pulse. For optomechanical devices in the sideband resolved regime ($\omega_m > \kappa$), Γ_m^{eff} and ω_m^{eff} are linearly independent in g_s and Δ_s [282]. The ability to control the damping rate dynamically would enable pulse compression by the realization of a time lens [283]. Furthermore, multiple pulses could be used in succession to realize very large phase shifts and pulse compression. As a mechanical mode is being used here, long storage times in excess of 90 μS [43, 280] are possible, however, there is an associated inherent bandwidth limitation on the length of pulses that can be effectively stored, in contrast to Brillouin scattering devices [284, 285]. The long storage times enabled by this protocol will enable longer interaction times for interfacing the stored mechanical pulse with other systems, such as spins, or mechanical or electric fields.

8.2.2 Towards operation in the quantum regime

While the SCD microdisks studied in this work were a successful demonstration of a high-C, multimode optomechanical system, there is still much room for improvement. While the

$Q_{\mathrm{m}} \cdot f_{\mathrm{m}}$ product is sufficient for room temperature quantum optomechanics, the operation of these devices in the quantum regime was not explored as the requirement that $g > \Gamma_{\mathrm{m}}\bar{n}_{\mathrm{th}}$ is not met. For the SCD microdisks studied here, the photon assisted optomechanical coupling rate, g, is approximately three orders of magnitude smaller than the mechanical decoherence rate, $\Gamma_{\mathrm{m}}\bar{n}_{\mathrm{th}}$. To improve the optomechanical properties of these microdisk structures there are several possible improvements to make. The parameters most likely to be improved are the intrinsic optical quality factor, Q_{i}, and mechanical quality factor, Q_{m}; the potential ways to achieve this are listed below, along with the affect each optimization would have on the system. Unfortunately, for microdisk geometries g_0 can not be appreciably improved before radiation loss would limit Q_{i}.

1. $\mathbf{Q}_{\mathrm{i}}$

   (a) Microdisk sidewall roughness

   Further improvements to the diamond anisotropic etch should improve the optical quality factor, by eliminating remaining surface roughness, as FDTD simulations suggest that the radiation loss limited quality factor, $Q_{\mathrm{rad}} > 10^7$ for the > 5 μm diameter microdisks studied here. Improvements to Q_{i} would allow for larger N at lower P_{in}, and result in larger C for fixed N.

   (b) Higher quality SCD material

   Using higher purity SCD material, i.e. material that has less defects in it could also improve Q_{i} by reducing linear absorption. This would also allow for larger N while remaining thermally stable, which would allow operation red-detuned from the cavity for larger N, and as a result, C.

2. $\mathbf{Q}_{\mathrm{m}}$

   (a) Different SCD crystal orientation

   Using a SCD chip with a different crystal orientation should also be investigated to determine the effects on the pedestal geometry, which is determined by the

etch rates along the various crystal planes and their orientation relative to the surface of the chip. If the inverse of the current pedestal geometry was possible, the clamping losses could be significantly reduced [61, 136, 137], which should allow us to take full advantage of SCD's mechanical properties, as $Q_{\mathrm{m}} > 10^6$ has been demonstrated in SCD nanobeams [176]. This would reduce the mechanical decay and decoherence rate, which would lead to larger C for fixed N, and move the system closer to the strong coupling regime in ambient conditions.

(b) Pedestal engineering

The pedestal shaping technique discussed in Section 6.6 could in principle be used to reduce clamping loss by introducing structure to the pedestal that is engineered to act as a phononic shield, preventing phonons from leaking into the substrate via the pedestal, as first demonstrated in Refs. [137, 138, 258].

Depending on the application there are two routes forward to placing a SCD optomechanical device in the quantum regime. First, the existing devices could be placed in a dilution fridge ($T = 15$ mK) such that the mechanical oscillator is in its ground state ($n_{\mathrm{th}} < 1$). However, if working at room temperature and pressure is desired, a different type of structure should be investigated to achieve larger g_0. The fabrication process optimized in this work is the only potential method for fabricating two dimensional optomechanical crystal cavities from bulk SCD. For example, consider the design of Amir Safavi-Naeini et al.[286], which exhibits $g_0 \sim 220$ kHz and $f_{\mathrm{m}} \sim 10$ GHz in silicon. Naively, if we scale f_{m} by the ratio of silicon to diamond's-$\sqrt{E/\rho}$, then the confined mechanical mode would exhibit $f_{\mathrm{m}} \sim 20$ GHz, resulting in a thermal phonon occupation, $\bar{n}_{\mathrm{th}} \sim 50$, placing it very close to the quantum ground state at room temperature. A design such as this would surpass the performance of one dimensional photonic crystals that have been demonstrated in SCD to date [70], and to the best of our knowledge can only be fabricated from bulk SCD using our process.

Bibliography

[1] M. Mitchell, A. C. Hryciw, and P. E. Barclay, "Cavity optomechanics in gallium phosphide microdisks," Appl. Phys. Lett. **104**, 141104 (2014).

[2] D. P. Lake, M. Mitchell, H. Jayakumar, L. F. dos Santos, D. Curic, and P. E. Barclay, "Efficient telecom to visible wavelength conversion in doubly resonant gallium phosphide microdisks," Appl. Phys. Lett. **108**, 031,109 (2016).

[3] B. Khanaliloo, M. Mitchell, A. C. Hryciw, and P. E. Barclay, "High-Q/V monolithic diamond microdisks fabricated with quasi-isotropic etching," Nano Lett. **15**, 5131–5136 (2015).

[4] M. Mitchell, B. Khanaliloo, D. P. Lake, T. Masuda, J. P. Hadden, and P. E. Barclay, "Single-crystal diamond low-dissipation cavity optomechanics," Optica **3**, 963–970 (2016).

[5] D. P. Lake, M. Mitchell, Y. Kamaliddin, and P. E. Barclay, "Optomechanically induced transparency and cooling in thermally stable diamond microcavities," ACS Photonics **5**, 782–787 (2018).

[6] M. Mitchell, D. P. Lake, and P. E. Barclay, "Realizing $Q > 300\ 000$ in diamond microdisks for optomechanics via etch optimization," APL Photonics **4**, 016,101 (2019).

[7] M. Mitchell, D. P. Lake, and P. E. Barclay, "Optomechanically amplified wavelength conversion in diamond microcavities," Optica **6**, 832–838 (2019).

[8] D. P. Lake, M. Mitchell, B. C. Sanders, and P. E. Barclay, "Two-color interferometry and switching through optomechanical dark mode excitation," arXiv:1906.10754 (2019).

[9] J. Kepler, *De Cometis Libelli Tres* (Augsburg, 1619).

[10] A. Bartoli, "Il calorico raggiante e il secondo principio di termodinamica," Il Nuovo Cimento (1877-1894) **15**, 193–202 (1884).

[11] P. Lebedew, "Untersuchungen über die druckkräfte des lichtes," Ann. Phys. **311**, 433–458 (1901).

[12] E. Nichols and G. Hull, "The pressure due to radiation," The Astrophysical Journal (1903).

[13] Y. K. Bae, "Photonic laser propulsion: Proof-of-concept demonstration," Journal of Spacecraft and Rockets **45**, 153–155 (2008).

[14] J. A. E. Agency, "Confirmation of photon acceleration of small solar power sail demonstrator IKAROS (ikaros)," (2010).

[15] P. Lubin, "A roadmap to interstellar flight," arXiv:1604.01356 (2016).

[16] A. Ashkin, J. M. Dziedzic, J. E. Bjorkholm, and S. Chu, "Observation of a single-beam gradient force optical trap for dielectric particles," Opt. Lett. **11**, 288–290 (1986).

[17] B. Abbott *et al.*, "Observation of gravitational waves from a binary black hole merger," Phys. Rev. Lett. **116**, 061,102 (2016).

[18] M. Aspelmeyer, T. J. Kippenberg, and F. Marquardt, "Cavity optomechanics," Rev. Mod. Phys. **86**, 1391–1452 (2014).

[19] T. Pozar, J. Lalos, A. Babnik, R. Petkovsek, M. Bethune-Waddell, K. J. Chau, G. V. B. Lukasievicz, and N. G. C. Astrath, "Isolated detection of elastic waves driven by the momentum of light," Nat. Commun. **9**, 3340 (2018).

[20] V. Braginsky and A. Manukin, "Ponderomotive effects of electromagnetic radiation," JETP **25**, 653 (1967).

[21] V. Braginsky, A. Manukin, and M. Tikhonov, "Investigation of dissipative ponderomotive effects of electromagnetic radiation," JETP **31**, 829 (1970).

[22] V. B. Braginskiĭ and Y. I. Vorontsov, "Quantum-mechanical limitations in macroscopic experiments and modern experimental technique," Soviet Physics Uspekhi **17**, 644–650 (1975).

[23] A. Dorsel, J. D. McCullen, P. Meystre, E. Vignes, and H. Walther, "Optical bistability and mirror confinement induced by radiation pressure," Phys. Rev. Lett. **51**, 1550–1553 (1983).

[24] C. J. Sarabalis, J. T. Hill, and A. H. Safavi-Naeini, "Guided acoustic and optical waves in silicon-on-insulator for Brillouin scattering and optomechanics," APL Photonics **1**, 071,301 (2016).

[25] C. J. Sarabalis, Y. D. Dahmani, R. N. Patel, J. T. Hill, and A. H. Safavi-Naeini, "Release-free silicon-on-insulator cavity optomechanics," Optica **4**, 1147–1150 (2017).

[26] A. H. Safavi-Naeini, D. V. Thourhout, R. Baets, and R. V. Laer, "Controlling phonons and photons at the wavelength scale: integrated photonics meets integrated phononics," Optica **6**, 213–232 (2019).

[27] T. Carmon, H. Rokhsari, L. Yang, T. J. Kippenberg, and K. J. Vahala, "Temporal behavior of radiation-pressure-induced vibrations of an optical microcavity phonon mode," Phys. Rev. Lett. **94**, 223,902 (2005).

[28] J. Teufel, T. Donner, D. Li, J. Harlow, M. Allman, K. Cicak, A. Sirois, J. D. Whittaker, K. Lehnert, and R. W. Simmonds, "Sideband cooling of micromechanical motion to the quantum ground state," Nature **475**, 359–363 (2011).

[29] J. Chan, T. P. M. Alegre, A. H. Safavi-Naeini, J. T. Hill, A. Krause, S. Groblacher, M. Aspelmeyer, and O. Painter, "Laser cooling of a nanomechanical oscillator into its quantum ground state," Nature **478**, 89–92 (2011).

[30] H. Rokhsari, T. J. Kippenberg, T. Carmon, and K. J. Vahala, "Radiation-pressure-driven micro-mechanical oscillator," Opt. Express **13**, 5293–5301 (2005).

[31] F. Marquardt, J. G. E. Harris, and S. M. Girvin, "Dynamical multistability induced by radiation pressure in high-finesse micromechanical optical cavities," Phys. Rev. Lett. **96**, 103,901 (2006).

[32] M. Poot, K. Fong, M. Bagheri, W. Pernice, and H. Tang, "Backaction limits on self-sustained optomechanical oscillations," Phys. Rev. A **86**, 053,826 (2012).

[33] M. Bagheri, M. Poot, M. Li, W. Pernice, and H. Tang, "Dynamic manipulation of nanomechanical resonators in the high-amplitude regime and non-volatile mechanical memory operation," Nat. Nanotechnol. **6**, 726–732 (2011).

[34] A. G. Krause, M. Winger, T. D. Blasius, W. Lin, and O. Painter, "A high-resolution microchip optomechanical accelerometer," Nat. Photon. **6**, 768–772 (2012).

[35] S. Forstner, S. Prams, J. Knittel, E. van Ooijen, J. Swaim, G. Harris, A. Szorkovszky, W. Bowen, and H. Rubinsztein-Dunlop, "Cavity optomechanical magnetometer," Phys. Rev. Lett. **108**, 120,801 (2012).

[36] S. Forstner, E. Sheridan, J. Knittel, C. L. Humphreys, G. A. Brawley, H. Rubinsztein-Dunlop, and W. P. Bowen, "Ultrasensitive optomechanical magnetometry," Adv. Mater. **26**, 6348–6353 (2014).

[37] J. Davis, D. Vick, D. Fortin, J. Burgess, W. Hiebert, and M. Freeman, "Nanotorsional resonator torque magnetometry," Appl. Phys. Lett. **96**, 072,513 (2010).

[38] P. Kim, C. Doolin, B. Hauer, A. MacDonald, M. Freeman, P. Barclay, and J. Davis, "Nanoscale torsional optomechanics," Appl. Phys. Lett. **102**, 053,102 (2013).

[39] M. Wu, N. L. Y. Wu, T. Firdous, F. Fani Sani, J. E. Losby, M. R. Freeman, and P. E. Barclay, "Nanocavity optomechanical torque magnetometry and radiofrequency susceptometry," Nat. Nanotechnol. **12**, 127–131 (2016).

[40] W. Yu, W. C. Jiang, Q. Lin, and T. Lu, "Cavity optomechanical spring sensing of single molecules," Nat. Commun. **7**, 12,311 (2016).

[41] M. C. Kuzyk and H. Wang, "Controlling multimode optomechanical interactions via interference," Phys. Rev. A **96**, 023,860 (2017).

[42] W. H. P. Nielsen, Y. Tsaturyan, C. B. Møller, E. S. Polzik, and A. Schliesser, "Multimode optomechanical system in the quantum regime," Proc. Natl. Acad. Sci. **114**, 62–66 (2017).

[43] T. Palomaki, J. Harlow, J. Teufel, R. Simmonds, and K. Lehnert, "Coherent state transfer between itinerant microwave fields and a mechanical oscillator," Nature **495**, 210–214 (2013).

[44] J. T. Hill, A. H. Safavi-Naeini, J. Chan, and O. Painter, "Coherent optical wavelength conversion via cavity optomechanics," Nat. Commun. **3**, 1196 (2012).

[45] C. Dong, V. Fiore, M. C. Kuzyk, and H. Wang, "Optomechanical dark mode," Science **338**, 1609–1613 (2012).

[46] R. W. Andrews, R. W. Peterson, T. P. Purdy, K. Cicak, R. W. Simmonds, C. A. Regal, and K. W. Lehnert, "Bidirectional and efficient conversion between microwave and optical light," Nat. Phys. **10**, 321–326 (2014).

[47] A. Rueda, F. Sedlmeir, M. C. Collodo, U. Vogl, B. Stiller, G. Schunk, D. V. Strekalov, C. Marquardt, J. M. Fink, O. Painter, G. Leuchs, and H. G. L. Schwefel, "Efficient microwave to optical photon conversion: an electro-optical realization," Optica **3**, 597–604 (2016).

[48] M. J. Weaver, F. Buters, F. Luna, H. Eerkens, K. Heeck, S. de Man, and D. Bouwmeester, "Coherent optomechanical state transfer between disparate mechanical resonators," Nat. Commun. **8**, 824 (2017).

[49] K. Fang, J. Luo, A. Metelmann, M. H. Matheny, F. Marquardt, A. A. Clerk, and O. Painter, "Generalized non-reciprocity in an optomechanical circuit via synthetic magnetism and reservoir engineering," Nat. Phys. **13**, 465–471 (2017).

[50] Z. Shen, Y.-L. Zhang, Y. Chen, F.-W. Sun, X.-B. Zou, G.-C. Guo, C.-L. Zou, and C.-H. Dong, "Reconfigurable optomechanical circulator and directional amplifier," Nat. Commun. **9**, 1797 (2018).

[51] F. Ruesink, J. P. Mathew, M.-A. Miri, A. Alù, and E. Verhagen, "Optical circulation in a multimode optomechanical resonator," Nat. Commun. **9**, 1798 (2018).

[52] J. Chan, A. Safavi-Naeini, J. Hill, S. Meenehan, and O. Painter, "Optimized optomechanical crystal cavity with acoustic radiation shield," Appl. Phys. Lett. **101**, 081,115 (2012).

[53] S. Gröblacher, K. Hammerer, M. R. Vanner, and M. Aspelmeyer, "Observation of strong coupling between a micromechanical resonator and an optical cavity field," Nature **460**, 724–727 (2009).

[54] P. E. Barclay, K. Srinivasan, and O. Painter, "Nonlinear response of silicon photonic crystal microresonators excited via an integrated waveguide and a fiber taper," Opt. Express **13**, 801–820 (2005).

[55] X. Sun, X. Zhang, C. Schuck, and H. X. Tang, "Nonlinear optical effects of ultrahigh-Q silicon photonic nanocavities immersed in superfluid helium," Sci. Rep. **3**, 1436 (2013).

[56] T. Carmon, L. Yang, and K. J. Vahala, "Dynamical thermal behavior and thermal self-stability of microcavities," Opt. Express **12**, 4742–4750 (2004).

[57] J. L. Cheng, J. Rioux, and J. E. Sipe, "Full band structure calculation of two-photon indirect absorption in bulk silicon," Appl. Phys. Lett. **98**, 131101 (2011).

[58] M. Eichenfield, R. Camacho, J. Chan, K. J. Vahala, and O. Painter, "A picogram and nanometer scale photonic crystal opto-mechanical cavity," Nature **459**, 550–555 (2009).

[59] T. P. Purdy, R. W. Peterson, P.-L. Yu, and C. A. Regal, "Cavity optomechanics with Si_3N_4 membranes at cryogenic temperatures," New J. Phys. **14**, 115,021 (2012).

[60] C. Baker, S. Stapfner, D. Parrain, S. Ducci, G. Leo, E. M. Weig, and I. Favero, "Optical instability and self-pulsing in silicon nitride whispering gallery resonators," Opt. Express **20**, 29,076–29,089 (2012).

[61] Y. Liu, M. Davanço, V. Aksyuk, and K. Srinivasan, "Electromagnetically induced transparency and wideband wavelength conversion in silicon nitride microdisk optomechanical resonators," Phys. Rev. Lett. **110**, 223,603 (2013).

[62] A. Schliesser, O. Arcizet, R. Rivière, G. Anetsberger, and T. Kippenberg, "Resolved-sideband cooling and position measurement of a micromechanical oscillator close to the Heisenberg uncertainty limit," Nat. Phys. **5**, 509–514 (2009).

[63] S. Weis, R. Rivière, S. Deléglise, E. Gavartin, O. Arcizet, A. Schliesser, and T. J. Kippenberg, "Optomechanically induced transparency," Science **330**, 1520–1523 (2010).

[64] Y.-S. Park and H. Wang, "Resolved-sideband and cryogenic cooling of an optomechanical resonator," Nat. Phys. **5**, 489–493 (2009).

[65] X. Lu, J. Y. Lee, P. X.-L. Feng, and Q. Lin, "Silicon carbide microdisk resonator," Opt. Lett. **38**, 1304–1306 (2013).

[66] B. Guha, S. Mariani, A. Lemaître, S. Combrié, G. Leo, and I. Favero, "High frequency optomechanical disk resonators in III–V ternary semiconductors," Opt. Express **25**, 24,639–24,649 (2017).

[67] K. Schneider, Y. Baumgartner, S. Hönl, P. Welter, H. Hahn, D. J. Wilson, L. Czornomaz, and P. Seidler, "Optomechanics with one-dimensional gallium phosphide photonic crystal cavities," Optica **6**, 577–584 (2019).

[68] C. Xiong, X. Sun, K. Y. Fong, and H. X. Tang, "Integrated high frequency aluminum nitride optomechanical resonators," Appl. Phys. Lett. **100**, 171,111 (2012).

[69] B. Khanaliloo, H. Jayakumar, A. C. Hryciw, D. P. Lake, H. Kaviani, and P. E. Barclay, "Single-crystal diamond nanobeam waveguide optomechanics," Phys. Rev. X **5**, 041,051 (2015).

[70] M. J. Burek, J. D. Cohen, S. M. Meenehan, N. El-Sawah, C. Chia, T. Ruelle, S. Meesala, J. Rochman, H. A. Atikian, M. Markham, D. J. Twitchen, M. D. Lukin, O. Painter, and M. Lončar, "Diamond optomechanical crystals," Optica **3**, 1404–1411 (2016).

[71] P. Rath, S. Khasminskaya, C. Nebel, C. Wild, and W. H. Pernice, "Diamond-integrated optomechanical circuits," Nat. Commun. **4**, 1690 (2013).

[72] L. Rayleigh, "The problem of the whispering gallery," Philos. Mag. **20**, 1001–1004 (1910).

[73] M. R. Foreman, J. D. Swaim, and F. Vollmer, "Whispering gallery mode sensors," Adv. Opt. Photon. **7**, 168–240 (2015).

[74] J. Knight, N. Dubreuil, V. Sandoghdar, J. Hare, V. Lefèvre-Seguin, J. M. Raimond, and S. Haroche, "Characterizing whispering-gallery modes in microspheres by direct observation of the optical standing-wave pattern in the near field," Opt. Lett. **21**, 698–700 (1996).

[75] D. W. Vernooy, V. S. Ilchenko, H. Mabuchi, E. W. Streed, and H. J. Kimble, "High-Q measurements of fused-silica microspheres in the near infrared," Opt. Lett. **23**, 247–249 (1998).

[76] B. Gayral, J. M. Gérard, A. Lemaître, C. Dupuis, L. Manin, and J. L. Pelouard, "High-Q wet-etched GaAs microdisks containing InAs quantum boxes," Appl. Phys. Lett. **75**, 1908–1910 (1999).

[77] M. Borselli, K. Srinivasan, P. E. Barclay, and O. Painter, "Rayleigh scattering, mode coupling, and optical loss in silicon microdisks," Appl. Phys. Lett. **85**, 3693–3695 (2004).

[78] P. Rabiei, W. H. Steier, , and L. R. Dalton, "Polymer micro-ring filters and modulators," Journal of Lightwave Technology **20**, 1968–1975 (2002).

[79] J. Heebner, R. Grover, and T. A. Ibrahim, *Optical Microresonators Theory, Fabrication, and Applications* (Springer-Verlag London Limited, 2008).

[80] T. J. Kippenberg, "Nonlinear Optics in Ultra-high-Q Whispering-Gallery Optical Microcavities," Ph.D. thesis, Caltech (2004).

[81] A. F. Oskooi, D. Roundy, M. Ibanescu, P. Bermel, J. Joannopoulos, and S. G. Johnson, "Meep: A flexible free-software package for electromagnetic simulations by the FDTD method," Comp. Phys. Comm. **181**, 687–702 (2010).

[82] M. L. Gorodetsky, A. A. Savchenkov, and V. S. Ilchenko, "Ultimate Q of optical microsphere resonators," Opt. Lett. **21**, 453–455 (1996).

[83] J. Sarathy, R. A. Mayer, K. Jung, S. Unnikrishnan, D.-L. Kwong, and J. C. Campbell, "Normal-incidence grating couplers in Ge-Si," Opt. Lett. **19**, 798–800 (1994).

[84] W. Kuang, C. Kim, A. Stapleton, and J. O'Brien, "Grating-assisted coupling of optical fibers and photonic crystal waveguides," Opt. Lett. **27**, 1604–1606 (2002).

[85] H. Subbaraman, X. Xu, J. Covey, and R. T. Chen, "Efficient light coupling into in-plane semiconductor nanomembrane photonic devices utilizing a sub-wavelength grating coupler," Opt. Express **20**, 20,659–20,665 (2012).

[86] C. P. Michael, M. Borselli, T. J. Johnson, C. Chrystala, and O. Painter, "An optical fiber-taper probe for wafer-scale microphotonic device characterization," Opt. Express **15**, 4745–4752 (2007).

[87] C. Healey, "Nanophotonic Devices for Nonlinear Optomechanics," Ph.D. thesis, University of Calgary (2019).

[88] M. Wu, "Nanophotonic Optomechanical Devices for Torque Magnetometry," Ph.D. thesis, University of Calgary (2016).

[89] C. W. Gardiner and P. Zoller, *Quantum Noise* (Springer, Berlin, 1991).

[90] A. A. Clerk, M. H. Devoret, S. M. Girvin, F. Marquardt, and R. J. Schoelkopf, "Introduction to quantum noise, measurement, and amplification," Rev. Mod. Phys. **82**, 1155–1208 (2010).

[91] D. F. Walls and G. J. Milburn, *Quantum Optics* (Springer-Verlag, Berlin, 2008).

[92] K. Srinivasan, "Semiconductor Optical Microcavities for Chip-Based Cavity QED," Ph.D. thesis, California Institute of Technology (2006).

[93] M. L. Gorodetsky, A. D. Pryamikov, and V. S. Ilchenko, "Rayleigh scattering in high-Q microspheres," J. Opt. Soc. Am. B **17**, 1051–1057 (2000).

[94] M. Borselli, "High-Q Microresonators as Lasing Elements for Silicon Photonics," Ph.D. thesis, California Institute of Technology (2006).

[95] N. W. Ashcroft and N. D. Mermin, *Solid State Physics* (Saunders College Publishing, New York, NY, 1976).

[96] A. N. Cleland, *Foundations of nanomechanics: from solid-state theory to device applications* (Springer-Verlag Berlin Heidelberg, 2010).

[97] A. E. H. Love, *Mathematical Theory of Elasticity* (Cambridge University Press, 1927), 4th ed.

[98] M. Onoe, "Contour vibrations of isotropic circular plates," J. Acoust. Soc. Am. **28**, 1158–1162 (1956).

[99] S. S. H. Chen and T. M. Liu, "Extensional vibration of thin plates of various shapes," J. Acoust. Soc. Am. **58**, 828–831 (1975).

[100] J. R. Clark, W.-T. Hsu, M. A. Abdelmoneum, and C. T.-C. Nguyen, "High-Q UHF micromechanical radial-contour mode disk resonators," Jour. of Micro. Sys. **14**, 1298–1310 (2005).

[101] M. Eichenfield, J. Chan, A. Safavi-Naeini, K. Vahala, and O. Painter, "Modeling dispersive coupling and losses of localized optical and mechanical modes in optomechanical crystals," Opt. Express **17**, 20,078–20,098 (2009).

[102] S. G. Johnson, M. Ibanescu, M. A. Skorobogatiy, O. Weisberg, J. D. Joannopoulos, and Y. Fink, "Perturbation theory for Maxwell's equations with shifting material boundaries," Phys. Rev. E **65**, 066,611 (2002).

[103] A. Yariv and P. Yeh, *Photonics: Optical Electronics in Modern Communications* (Oxford, 2006).

[104] C. Baker, W. Hease, D.-T. Nguyen, A. Andronico, S. Ducci, G. Leo, and I. Favero, "Photoelastic coupling in gallium arsenide optomechanical disk resonators," Opt. Express **22**, 14,072–14,086 (2014).

[105] K. C. Balram, M. Davanço, J. Y. Lim, J. D. Song, and K. Srinivasan, "Moving boundary and photoelastic coupling in GaAs optomechanical resonators," Optica **1**, 414–420 (2014).

[106] T. J. Kippenberg, H. Rokhsari, T. Carmon, A. Scherer, and K. J. Vahala, "Analysis of radiation-pressure induced mechanical oscillation of an optical microcavity," Phys. Rev. Lett. **95**, 033901 (2005).

[107] R. Leijssen, G. R. La Gala, L. Freisem, J. T. Muhonen, and E. Verhagen, "Nonlinear cavity optomechanics with nanomechanical thermal fluctuations," Nat. Commun. **8**, 16,024 (2017).

[108] M. Norton and D. Karczub, *Fundamentals of Noise and Vibration Analysis for Engineers* (Cambridge University Press, 2003), 2nd ed.

[109] B. D. Hauer, C. Doolin, K. S. D. Beach, and J. P. Davis, "A general procedure for thermomechanical calibration of nano/micro-mechanical resonators," Ann. Phys. **339**, 181–207 (2013).

[110] H. Xiong and Y. Wu, "Fundamentals and applications of optomechanically induced transparency," Appl. Phys. Rev **5**, 031,305 (2018).

[111] A. H. Safavi-Naeini, T. M. Alegre, J. Chan, M. Eichenfield, M. Winger, Q. Lin, J. T. Hill, D. Chang, and O. Painter, "Electromagnetically induced transparency and slow light with optomechanics," Nature **472**, 69–73 (2011).

[112] D. V. Schroeder, *Introduction to Thermal Physics* (Addison Wesley Longman, 2000).

[113] O. Wadu and H. Hasegawa, eds., *InP-Based Materials and Devices:Physics and Technology* (Wiley-Interscience, 1999), 1st ed.

[114] R. Maher, A. Alvarado, D. Lavery, and P. Bayvel, "Increasing the information rates of optical communications via coded modulation: a study of transceiver performance," Sci. Rep. **6**, 21,278 (2016).

[115] A. Rockett, *The Materials Science of Semiconductors* (Springer, Boston, MA, 2008).

[116] M. Eichenfield, J. Chan, R. Camacho, K. Vahala, and O. Painter, "Optomechanical crystals," Nature **462**, 78–82 (2009).

[117] L. Ding, C. Baker, P. Senellart, A. Lemaitre, S. Ducci, G. Leo, and I. Favero, "High frequency GaAs nano-optomechanical disk resonator," Phys. Rev. Lett. **105**, 263,903 (2010).

[118] K. Rivoire, A. Faraon, and J. Vučković, "Gallium phosphide photonic crystal nanocavities in the visible," Appl. Phys. Lett. **93**, 063,103 (2008).

[119] P. E. Barclay, K. M. C. Fu, C. Santori, A. Faraon, and R. G. Beausoleil, "Hybrid nanocavities for resonant enhancement of color center emission in diamond," Phys. Rev. X **1**, 011,007 (2011).

[120] R. Stockill, M. Forsch, G. Beaudoin, K. Pantzas, I. Sagnes, R. Braive, and S. Gröblacher, "Gallium phosphide as a piezoelectric platfrom for quantum optomechanics," Phys. Rev. Lett. **123**, 163,602 (2019).

[121] L. Ding, C. Baker, P. Senellart, A. Lemaitre, S. Ducci, G. Leo, and I. Favero, "Wavelength-sized GaAs optomechanical resonators with gigahertz frequency," Appl. Phys. Lett. **98**, 113108 (2011).

[122] X. Sun, J. Zhang, M. Poot, C. Wong, and H. Tang, "Femtogram doubly clamped nanomechanical resonators embedded in a high-Q two-dimensional photonic crystal nanocavity," Nano Lett. **12**, 2299–2305 (2012).

[123] J. Bochmann, A. Vainsencher, D. D. Awschalom, and A. N. Cleland, "Nanomechanical coupling between microwave and optical photons," Nat. Phys. **9**, 712–716 (2013).

[124] K. Y. Fong, L. Fan, L. Jiang, X. Han, and H. X. Tang, "Microwave-assisted coherent and nonlinear control in cavity piezo-optomechanical systems," Phys. Rev. A **90**, 051,801 (2014).

[125] K. C. Balram, M. I. Davanço, J. D. Song, and K. Srinivasan, "Coherent coupling between radiofrequency, optical and acoustic waves in piezo-optomechanical circuits," Nat. Photon. **10**, 346–352 (2016).

[126] L. Fan, C.-L. Zou, N. Zhu, and H. X. Tang, "Spectrotemporal shaping of itinerant photons via distributed nanomechanics," Nat. Photon. **13**, 323–327 (2019).

[127] A. C. Hryciw, "Raith_GDSII MATLAB toolbox," `https://github.com/nrc-cnrc/Raith_GDSII`. Accessed: 2019-07-05.

[128] M. Borselli, T. J. Johnson, and O. Painter, "Beyond the Rayleigh scattering limit in high-Q silicon microdisks: theory and experiment," Opt. Express **13**, 1515–1530 (2005).

[129] P. E. Barclay, B. Lev, K. Srinivasan, H. Mabuchi, and O. Painter, "Integration of fiber coupled high-Q SiN_x microdisks with atom chips," Appl. Phys. Lett. **89**, 131,108 (2006).

[130] P. J. Dean and C. H. Henry, "Electron-capture ("internal") luminescence from the oxygen donor in gallium phosphide," Phys. Rev. **176**, 928–937 (1968).

[131] P. Dean, C. Henry, and C. Frosch, "Infrared donor-acceptor pair spectra involving the deep oxygen donor in gallium phosphide," Phys. Rev. **168**, 812 (1968).

[132] R. Rivière, "Cavity optomechanics with silica toroidal microresonators down to low phonon occupancy," Ph.D. thesis, Ludwig-Maximilians-Universität München (2011).

[133] X. Sun, X. Zhang, and H. X. Tang, "High-Q silicon optomechanical microdisk resonators at gigahertz frequencies," Appl. Phys. Lett. **100**, 173116 (2012).

[134] O. Svitelskiy, V. Sauer, D. Vick, K.-M. Cheng, N. Liu, M. R. Freeman, and W. K. Hiebert, "Nanoelectromechanical devices in a fluidic environment," Phys. Rev. E **85**, 056,313 (2012).

[135] D. Parrain, C. Baker, T. Verdier, P. Senellart, A. Lemaitre, S. Ducci, G. Leo, and I. Favero, "Damping of optomechanical disks resonators vibrating in air," Appl. Phys. Lett. **100**, 242105 (2012).

[136] A. Schliesser, R. Rivière, G. Anetsberger, O. Arcizet, and T. J. Kippenberg, "Resolved-sideband cooling of a micromechanical oscillator," Nat. Phys. **4**, 415–419 (2008).

[137] D. T. Nguyen, C. Baker, W. Hease, S. Sejil, P. Senellart, A. Lemaître, S. Ducci, G. Leo, and I. Favero, "Ultrahigh Q-frequency product for optomechanical disk resonators with a mechanical shield," Appl. Phys. Lett. **103**, 241112 (2013).

[138] D. T. Nguyen, W. Hease, C. Baker, E. Gil-Santos, P. Senellart, A. Lemaître, S. Ducci, G. Leo, and I. Favero, "Improved optomechanical disk resonator sitting on a pedestal mechanical shield," New J. Phys. **17**, 023,016 (2015).

[139] K. Srinivasan, H. Miao, M. Rakher, M. Davanço, and V. Aksyuk, "Optomechanical transduction of an integrated silicon cantilever probe using a microdisk resonator," Nano Lett. **11**, 791 (2011).

[140] L. Fan, C.-L. Zou, R. Cheng, X. Guo, X. Han, Z. Gong, S. Wang, and H. X. Tang, "Superconducting cavity electro-optics: A platform for coherent photon conversion between superconducting and photonic circuits," Sci. Adv. **4**, eaar4994 (2018).

[141] M. Forsch, R. Stockill, A. Wallucks, I. Marinković, C. Gärtner, R. A. Norte, F. van Otten, A. Fiore, K. Srinivasan, and S. Gröblacher, "Microwave-to-optics conversion using a mechanical oscillator in its quantum groundstate," arXiv:1812.07588 (2018).

[142] W. Jiang, C. J. Sarabalis, Y. D. Dahmani, R. N. Patel, F. M. Mayor, T. P. McKenna, R. V. Laer, and A. H. Safavi-Naeini, "Efficient bidirectional piezo-optomechanical transduction between microwave and optical frequency," arXiv:1909.04627 (2019).

[143] L. Shao, M. Yu, S. Maity, N. Sinclair, L. Zheng, C. Chia, A. Shams-Ansari, C. Wang, M. Zhang, K. Lai, and M. Lončar, "Microwave-to-optical conversion using lithium niobate thin-film acoustic resonators," arXiv:1907.08593 (2019).

[144] D. J. Spence, E. Granados, and R. P. Mildren, "Mode-locked picosecond diamond raman laser," Optics **35**, 556–558 (2010).

[145] B. J. Hausmann, I. Bulu, V. Venkataraman, P. Deotare, and M. Lončar, "Diamond nonlinear photonics," Nat. Photon. **8**, 369–374 (2014).

[146] M. J. Burek, D. Ramos, P. Patel, I. W. Frank, and M. Lončar, "Nanomechanical resonant structures in single-crystal diamond," Appl. Phys. Lett. **103**, 131904 (2013).

[147] I. Aharonovich and E. Neu, "Diamond nanophotonics," Adv. Opt. Mater **2**, 911–928 (2014).

[148] I. Aharonovich, A. D. Greentree, and S. Prawer, "Diamond photonics," Nat. Photon. **5**, 397–405 (2011).

[149] J. Wrachtrup and F. Jelezko, "Processing quantum information in diamond," J. Phys.: Condens. Matter **18**, S807–S824 (2006).

[150] P. C. Maurer, G. Kucsko, C. Latta, L. Jiang, N. Y. Yao, S. D. Bennett, F. Pastawski, D. Hunger, N. Chisholm, M. Markham, D. J. Twitchen, J. I. Cirac, and M. D. Lukin, "Room-temperature quantum bit memory exceeding one second," Science **336**, 1283–1286 (2012).

[151] F. Jelezko, T. Gaebel, I. Popa, M. Domhan, A. Gruber, and J. Wrachtrup, "Observation of coherent oscillation of a single nuclear spin and realization of a two-qubit conditional quantum gate," Phys. Rev. Lett. **93**, 130,501 (2004).

[152] F. Jelezko, T. Gaebel, I. Popa, A. Gruber, and J. Wrachtrup, "Observation of coherent oscillations in a single electron spin," Phys. Rev. Lett. **92**, 076,401 (2004).

[153] M. V. Gurudev Dutt, L. Childress, L. Jiang, E. Togan, J. Maze, F. Jelezko, A. S. Zibrov, P. R. Hemmer, and M. D. Lukin, "Quantum register based on individual electronic and nuclear spin qubits in diamond," Science **316**, 1312–1316 (2007).

[154] K. Heshami, C. Santori, B. Khanaliloo, C. Healey, V. M. Acosta, P. E. Barclay, and C. Simon, "Raman quantum memory based on an ensemble of nitrogen-vacancy centers coupled to a microcavity," Phys. Rev. A **89**, 040,301(R) (2014).

[155] A. Sipahigil, K. Jahnke, L. Rogers, T. Teraji, J. Isoya, A. Zibrov, F. Jelezko, and M. Lukin, "Indistinguishable photons from separated silicon-vacancy centers in diamond," Phys. Rev. Lett. **113**, 113,602 (2014).

[156] C. Kurtsiefer, S. Mayer, P. Zarda, and H. Weinfurter, "Stable solid-state source of single photons," Phys. Rev. Lett. **85**, 290 (2000).

[157] H. Bernien, B. Hensen, W. Pfaff, G. Koolstra, M. S. Blok, L. Robledo, T. H. Taminiau, M. Markham, D. J. Twitchen, L. Childress, and R. Hanson, "Heralded entanglement between solid-state qubits separated by three meters," Nature **497**, 86–90 (2013).

[158] E. Togan, Y. Chu, A. S. Trifonov, L. Jiang, J. Maze, M. V. G. D. L. Childress and, A. S. Sørensen, P. R. Hemmer, A. S. Zibrov, and M. D. Lukin, "Quantum entanglement between an optical photon and a solid-state spin qubit," Nature **466**, 730–735 (2010).

[159] C. Santori, P. Barclay, K. Fu, R. Beausoleil, S. Spillane, and M. Fisch, "Nanophotonics for quantum optics using nitrogen-vacancy centers in diamond," Nanotechnology **21**, 274,008 (2010).

[160] A. Faraon, P. E. Barclay, C. Santori, K.-M. C. Fu, and R. G. Beausoleil, "Resonant enhancement of the zero-phonon emission from a color center in a diamond cavity," Nat. Photon. **5**, 301 (2011).

[161] X. Gan, K. F. Mak, Y. Gao, Y. You, F. Hatami, J. Hone, T. F. Heinz, and D. Englund, "Strong enhancement of light–matter interaction in graphene coupled to a photonic crystal nanocavity," Nano Lett. **12**, 5626–5631 (2012).

[162] J. Riedrich-Moller, L. Kipfstuhl, C. Hepp, E. Neu, C. Pauly, F. Mucklich, A. Baur, M. Wandt, S. Wolff, M. Fischer, S. Gsell, M. Schreck, and C. Becher, "One-and two-dimensional photonic crystal microcavities in single crystal diamond," Nat. Nanotechnol. **7**, 69–74 (2012).

[163] P. Michler, A. Kiraz, C. Becher, W. V. Schoenfeld, P. M. Petroff, L. Zhang, E. Hu, and A. Imamoğlu, "A quantum dot single-photon turnstile device," Science **290**, 2282–2285 (2000).

[164] K. Srinivasan and O. Painter, "Linear and nonlinear optical spectroscopy of a strongly coupled microdisk quantum dot system," Nature **450**, 862–865 (2007).

[165] E. Peter, P. Senellart, D. Martrou, A. Lemaître, J. Hours, J. Gérard, and J. Bloch, "Exciton-photon strong-coupling regime for a single quantum dot embedded in a microcavity," Phys. Rev. Lett. **95**, 067,401 (2005).

[166] S. Washiyama, S. Mita, K. Suzuki, and A. Sawabe, "Coalescence of epitaxial lateral overgrowth-diamond on stripe-patterned nucleation on Ir/MgO(001)," Appl. Phys. Express **4**, 095,502 (2011).

[167] S. Gsell, T. Bauer, J. Goldfuß, M. Schreck, and B. Stritzker, "A route to diamond wafers by epitaxial deposition on silicon via iridium/yttria-stabilized zirconia buffer layers," Appl. Phys. Lett. **84**, 4541–4543 (2004).

[168] M. Fischer, S. Gsell, M. Schreck, R. Brescia, and B. Stritzker, "Preparation of 4-inch Ir/YSZ/Si(001) substrates for the large-area deposition of single-crystal diamond," Diamond Relat. Mater. **17**, 1035 – 1038 (2008). Proceedings of Diamond 2007, the 18th European Conference on Diamond, Diamond-Like Materials, Carbon Nanotubes, Nitrides and Silicon Carbide.

[169] J. Yaita, T. Iwasaki, M. Natal, S. E. Saddow, and M. Hatano, "Heteroepitaxial growth of diamond films on 3C-SiC/Si substrates with utilization of antenna-edge microwave plasma CVD for nucleation," Jpn. J. Appl. Phys. **54**, 04DH13 (2015).

[170] C. F. Wang, R. Hanson, D. D. Awschalom, E. L. Hu, T. Feygelson, J. Yang, and J. E. Butler, "Fabrication and characterization of two-dimenstional photonic crystal microcavities in nanocrystalline diamond," Appl. Phys. Lett. **91**, 201,112 (2007).

[171] P. Rath, N. Gruhler, S. Khasminskaya, C. Nebel, C. Wild, and W. H. P. Pernice, "Waferscale nanophotonic circuits made from diamond-on-insulator substrates," Opt. Express **21**, 11,031–11,036 (2013).

[172] G. Balasubramanian, P. Neumann, D. Twitchen, M. Markham, R. Kolesov, N. Mizuochi, J. Isoya, J. Achard, J. Beck, J. Tissler, V. Jacques, P. Hemmer, F. Jelezko, and F. Wrachtrup, "Ultralong spin coherence time in isotopically engineered diamond," Nat. Mater. **8**, 383–387 (2009).

[173] Y. Chu, N. de Leon, B. Shields, B. Hausmann, R. Evans, E. Togan, M. J. Burek, M. Markham, A. Stacey, A. Zibrov, A. Yacoby, D. Twitchen, M. Loncar, H. Park, P. Maletinsky, and M. Lukin, "Coherent optical transitions in implanted nitrogen vacancy centers," Nano Lett. **14**, 1982–1986 (2014).

[174] R. E. Evans, A. Sipahigil, D. D. Sukachev, A. S. Zibrov, and M. D. Lukin, "Narrow-linewidth homogeneous optical emitters in diamond nanostructures via silicon ion implantation," Phys. Rev. Applied **5**, 044,010 (2016).

[175] J. C. Lee, I. Aharonovich, A. P. Magyar, F. Rol, and E. L. Hu, "Coupling of silicon-vacancy centers to a single crystal diamond cavity," Opt. Express **20**, 8891–8897 (2012).

[176] Y. Tao, J. M. Boss, B. A. Moores, and C. L. Degen, "Single-crystal diamond nanomechanical resonators with quality factors exceeding one million," Nat. Commun. **5**, 3638 (2013).

[177] I. Bayn, S. Mouradian, L. Li, J. A. Goldstein, T. Schroder, J. Zheng, E. H. Chen, O. Gaathon, M. Lu, A. Stein, C. A. Ruggiero, J. Salzman, R. Kalish, and D. Englund, "Fabrication of triangular nanobeam waveguide networks in bulk diamond using single-crystal silicon hard masks," Appl. Phys. Lett. **105**, 211,101 (2014).

[178] A. H. Piracha, P. Rath, K. Ganesan, S. Kühn, W. H. P. Pernice, and S. Prawer, "Scalable fabrication of integrated nanophotonic circuits on arrays of thin single crystal diamond membrane windows," Nano Lett. **16**, 3341–3347 (2016).

[179] T. M. Babinec, J. T. Choy, K. J. M. Smith, M. Khan, and M. Loncar, "Design and focused ion beam fabrication of single crystal diamond nanobeam cavities," J. Vac. Sci. Technol. B **29**, 010,601 (2011).

[180] M. Hiscocks, K. Ganesan, B. Gibson, S. Huntington, F. Ladouceur, and S. Prawer, "Diamond waveguides fabricated by reactive ion etching," Opt. Express **16**, 19,512–19,519 (2008).

[181] H. A. Atikian, P. Latawiec, M. J. Burek, Y.-I. Sohn, S. Meesala, N. Gravel, A. B. Kouki, and M. Loncar, "Freestanding nanostructures via reactive ion beam angled etching," APL Photonics **2**, 051,301 (2017).

[182] M. J. Burek, N. P. de Leon, B. J. Shields, B. J. Hausmann, Y. Chu, Q. Quan, A. S. Zibrov, H. Park, M. D. Lukin, and M. Lončar, "Free-standing mechanical and photonic nanostructures in single-crystal diamond," Nano Lett. **12**, 6084–6089 (2012).

[183] M. J. Burek, Y. Chu, M. S. Z. Liddy, P. Patel, J. Rochman, S. Meesala, W. Hong, Q. Quan, M. D. Lukin, and M. Lončar, "High quality-factor optical nanocavities in bulk single-crystal diamond," Nat. Commun. **5**, 5718 (2014).

[184] K. A. Shaw, Z. Zhang, and N. C. MacDonald, "{SCREAM} i: A single mask, single-crystal silicon, reactive ion etching process for microelectromechanical structures," Sens. Actuators, A **40**, 63 – 70 (1994).

[185] J. Isberg, J. Hammersberg, E. Johansson, T. Wikström, D. J. Twitchen, A. J. Whitehead, S. E. Coe, and G. A. Scarsbrook, "High carrier mobility in single-crystal plasma-deposited diamond," Science **297**, 1670–1672 (2002).

[186] R. S. Balmer, J. R. Brandon, S. L. Clewes, H. K. Dhillon, J. M. Dodson, I. Friel, P. N. Inglis, T. D. Madgwick, M. L. Markham, T. P. Mollart, N. Perkins, G. A. Scarsbrook, D. J. Twitchen, A. J. Whitehead, J. J. Wilman, and S. M. Woollard, "Chemical vapour deposition synthetic diamond: materials, technology and applications," J. Phys.: Condens. Matter **21**, 364,221 (2009).

[187] P. Treutlein, C. Genes, K. Hammerer, M. Poggio, and P. Rabl, "Hybrid mechanical systems," in "Cavity Optomechanics," (Springer, 2014), pp. 327–351.

[188] E. R. MacQuarrie, T. A. Gosavi, N. R. Jungwirth, S. A. Bhave, and G. D. Fuchs, "Mechanical spin control of nitrogen-vacancy centers in diamond," Phys. Rev. Lett. **111**, 227,602 (2013).

[189] J. Teissier, A. Barfuss, P. Appel, E. Neu, and P. Maletinsky, "Strain coupling of a nitrogen-vacancy center spin to a diamond mechanical oscillator," Phys. Rev. Lett. **113**, 020,503 (2014).

[190] P. Ovartchaiyapong, K. W. Lee, B. A. Myers, and A. C. B. Jayich, "Dynamic strain-mediated coupling of a single diamond spin to a mechanical resonator," Nat. Commun. **5**, 4429 (2014).

[191] A. Barfuss, J. Teissier, E. Neu, A. Nunnenkamp, and P. Maletinsky, "Strong mechanical driving of a single electron spin," Nat. Phys. **11**, 820–824 (2015).

[192] S. Meesala, Y.-I. Sohn, H. A. Atikian, S. Kim, M. J. Burek, J. T. Choy, and M. Lončar, "Enhanced strain coupling of nitrogen-vacancy spins to nanoscale diamond cantilevers," Phys. Rev. Applied **5**, 034,010 (2016).

[193] E. R. MacQuarrie, T. A. Gosavi, A. M. Moehle, N. R. Jungwirth, S. A. Bhave, and G. D. Fuchs, "Coherent control of a nitrogen-vacancy center spin ensemble with a diamond mechanical resonator," Optica **2**, 233–238 (2015).

[194] O. Arcizet, V. Jacques, A. Siria, P. Poncharal, P. Vincent, and S. Seidelin, "A single nitrogen-vacancy defect coupled to a nanomechanical oscillator," Nat. Phys. **7**, 879–883 (2011).

[195] D. A. Golter, T. Oo, M. Amezcua, K. A. Stewart, and H. Wang, "Optomechanical quantum control of a nitrogen-vacancy center in diamond," Phys. Rev. Lett. **116**, 143,602 (2016).

[196] K. W. Lee, D. Lee, P. Ovartchaiyapong, J. Minguzzi, J. R. Maze, and A. C. Bleszynski Jayich, "Strain coupling of a mechanical resonator to a single quantum emitter in diamond," Phys. Rev. Applied **6**, 034,005 (2016).

[197] K. V. Kepesidis, S. D. Bennett, S. Portolan, M. D. Lukin, and P. Rabl, "Phonon cooling and lasing with nitrogen-vacancy centers in diamond," Phys. Rev. B **88**, 064,105 (2013).

[198] P. Rabl, S. Kolkowitz, F. Koppens, J. Harris, P. Zoller, and M. Lukin, "A quantum spin transducer based on nanoelectromechanical resonator arrays," Nat. Phys. **6**, 602–608 (2010).

[199] K. Stannigel, P. Rabl, A. S. Sørensen, P. Zoller, and M. D. Lukin, "Optomechanical transducers for long-distance quantum communication," Phys. Rev. Lett. **105**, 220,501 (2010).

[200] M. J. A. Schuetz, E. M. Kessler, G. Giedke, L. M. K. Vandersypen, M. D. Lukin, and J. I. Cirac, "Universal quantum transducers based on surface acoustic waves," Phys. Rev. X **5**, 031,031 (2015).

[201] I. Wilson-Rae, P. Zoller, and A. Imamoğlu, "Laser cooling of a nanomechanical resonator mode to its quantum ground state," Phys. Rev. Lett. **92**, 075,507 (2004).

[202] E. R. Macquarrie, M. Otten, S. K. Gray, and G. D. Fuchs, "Cooling a mechanical resonator with nitrogen-vacancy centres using a room temperature excited state spin-strain interaction," Nat. Commun. **8**, 14358 (2017).

[203] T. Ramos, V. Sudhir, K. Stannigel, P. Zoller, and T. J. Kippenberg, "Nonlinear quantum optomechanics via individual intrinsic two-level defects," Phys. Rev. Lett. **110**, 193,602 (2013).

[204] I. H. Jafri, H. Busta, and S. T. Walsh, "Critical point drying and cleaning for MEMS technology," in "Proc.SPIE vol. 3880," (1999).

[205] A. Witvrouw, B. D. Bois, P. D. Moor, A. Verbist, C. A. V. Hoof, H. Bender, and C. Baert, "Comparison between wet HF etching and vapor HF etching for sacrificial oxide removal," in "Proc. SPIE vol. 4174," (2000).

[206] E. Gil-Santos, C. Baker, D. Nguyen, W. Hease, A. Lemaître, S. Ducci, G. Leo, and I. Favero, "High frequency nano-optomechanical disk resonators in liquids," Nat. Nanotechnol. **10**, 810–816 (2015).

[207] X. Lu, J. Y. Lee, and Q. Lin, "High-frequency and high-quality silicon carbide optomechanical microresonators," Sci. Rep. **5**, 17,005 (2015).

[208] K. Y. Fong, W. H. P. Pernice, and H. X. Tang, "Frequency and phase noise of ultrahigh Q silicon nitride nanomechanical resonators," Phys. Rev. B **85**, 161,410 (2012).

[209] K. E. Grutter, M. I. Davanço, and K. Srinivasan, "Slot-mode optomechanical crystals: a versatile platform for multimode optomechanics," Optica **2**, 994–1001 (2015).

[210] C. H. Bui, J. Zheng, S. W. Hoch, L. Y. T. Lee, J. G. E. Harris, and C. Wei Wong, "High-reflectivity, high-Q micromechanical membranes via guided resonances for enhanced optomechanical coupling," Appl. Phys. Lett. **100**, 021110 (2012).

[211] D. J. Wilson, C. A. Regal, S. B. Papp, and H. J. Kimble, "Cavity optomechanics with stoichiometric SiN films," Phys. Rev. Lett. **103**, 207,204 (2009).

[212] C. Reinhardt, T. Müller, A. Bourassa, and J. C. Sankey, "Ultralow-noise SiN trampoline resonators for sensing and optomechanics," Phys. Rev. X **6**, 021,001 (2016).

[213] R. A. Norte, J. P. Moura, and S. Gröblacher, "Mechanical resonators for quantum optomechanics experiments at room temperature," Phys. Rev. Lett. **116**, 147,202 (2016).

[214] R. Zhang, C. Ti, M. I. Davanço, Y. Ren, V. Aksyuk, Y. Liu, and K. Srinivasan, "Integrated tuning fork nanocavity optomechanical transducers with high $f_M Q_M$ product and stress-engineered frequency tuning," Appl. Phys. Lett. **107**, 131110 (2015).

[215] A. G. Krause, J. T. Hill, M. Ludwig, A. H. Safavi-Naeini, J. Chan, F. Marquardt, and O. Painter, "Nonlinear radiation pressure dynamics in an optomechanical crystal," Phys. Rev. Lett. **115**, 233,601 (2015).

[216] S. M. Meenehan, J. D. Cohen, G. S. MacCabe, F. Marsili, M. D. Shaw, and O. Painter, "Pulsed excitation dynamics of an optomechanical crystal resonator near its quantum ground state of motion," Phys. Rev. X **5**, 041,002 (2015).

[217] M. Yuan, V. Singh, Y. M. Blanter, and G. A. Steele, "Large cooperativity and microkelvin cooling with a three-dimensional optomechanical cavity," Nat. Commun. **6** (2015).

[218] M. Yuan, M. A. Cohen, and G. A. Steele, "Silicon nitride membrane resonators at millikelvin temperatures with quality factors exceeding 10^8," Appl. Phys. Lett. **107**, 263501 (2015).

[219] K. Ekinci, Y. Yang, and M. Roukes, "Ultimate limits to inertial mass sensing based upon nanoelectromechanical systems," J. Appl. Phys. **95**, 2682–2689 (2004).

[220] C. T.-C. Nguyen, "MEMS technology for timing and frequency control," IEEE Transactions on Ultrasonics, Ferroelectrics and Frequency Control **54**, 251–270 (2007).

[221] W. Li, N. Mingo, L. Lindsay, D. A. Broido, D. A. Stewart, and N. A. Katcho, "Thermal conductivity of diamond nanowires from first principles," Phys. Rev. B **85**, 195,436 (2012).

[222] D. Li, Y. Wu, P. Kim, L. Shi, P. Yang, and A. Majumdar, "Thermal conductivity of individual silicon nanowires," Appl. Phys. Lett. **83**, 2934–2936 (2003).

[223] L. S. Hounsome, R. Jones, M. J. Shaw, and P. R. Briddon, "Photoelastic constants in diamond and silicon," Phys. Status Solidi A **203**, 3088–3093 (2006).

[224] R. Yang, Z. Wang, J. Lee, K. Ladhane, D. J. Young, and P. X. L. Feng, "Temperature dependence of torsional and flexural modes in 6H-SiC microdisk resonators," in "Frequency Control Symposium (FCS), 2014 IEEE International," (2014), pp. 1–3.

[225] Q. Lin, J. Rosenberg, D. Chang, R. Camacho, M. Eichenfield, K. J. Vahala, and O. Painter, "Coherent mixing of mechanical excitations in nano-optomechanical structures," Nat. Photon. **4**, 236–242 (2010).

[226] W. C. Jiang, X. Lu, J. Zhang, and Q. Lin, "High-frequency silicon optomechanical oscillator with an ultralow threshold," Opt. Express **20**, 15,991–15,996 (2012).

[227] J. Hodges, L. Li, M. Lu, E. H. Chen, M. Trusheim, S. Allegri, X. Yao, O. Gaathon., H. Bakhru, and D. Englund, "Long-lived NV- spin coherence in high-purity diamond membranes," New J. Phys. **14**, 093,004 (2012).

[228] N. Bar-Gill, L. Pham, A. Jarmola, D. Budker, and R. Walsworth, "Solid-state electronic spin coherence time approaching one second," Nat. Commun. **4**, 1743 (2013).

[229] G. Davies and M. F. Hamer, "Optical studies of the 1.945 eV vibronic band in diamond," Proc. R. Soc. Lond. A **348**, 285–298 (1976).

[230] A. Batalov, V. Jacques, F. Kaiser, P. Siyushev, P. Neumann, L. J. Rogers, R. L. McMurtrie, N. B. Manson, F. Jelezko, and J. Wrachtrup, "Low temperature studies of the excited-state structure of negatively charged nitrogen-vacancy color centers in diamond," Phys. Rev. Lett. **102**, 195,506 (2009).

[231] K. Stannigel, P. Komar, S. J. M. Habraken, S. D. Bennett, M. D. Lukin, P. Zoller, and P. Rabl, "Optomechanical quantum information processing with photons and phonons," Phys. Rev. Lett. **109**, 013,603 (2012).

[232] S. Mouradian, N. H. Wan, T. Schröder, and D. Englund, "Rectangular photonic crystal nanobeam cavities in bulk diamond," Appl. Phys. Lett. **111**, 021,103 (2017).

[233] N. H. Wan, S. Mouradian, and D. Englund, "Two-dimensional photonic crystal slab nanocavities on bulk single-crystal diamond," Appl. Phys. Lett. **112**, 141,102 (2018).

[234] M. Kiss, T. Graziosi, and N. Quack, "Trapezoidal diffraction grating beam splitters in single crystal diamond," in "Proc. SPIE vol. 10513," (2018).

[235] L. Xie, T. X. Zhou, R. J. Stöhr, and A. Yacoby, "Crystallographic orientation dependent reactive ion etching in single crystal diamond," Adv. Mater. **30**, 1705,501 (2018).

[236] T. Kippenberg and K. Vahala, "Cavity optomechanics: Back-action at the mesoscale," Science **321**, 1172–1176 (2008).

[237] J. T. Hill, "Nonlinear Optics and Wavelength Translation Via Cavity-Optomechanics," Ph.D. thesis, Caltech (2013).

[238] M. J. Madou, *Fundamentals of Microfabrication and Nanotechnology*, vol. 2 (CRC Press, 2011), 3rd ed.

[239] T. J. Kippenberg, S. M. Spillane, and K. J. Vahala, "Modal coupling in traveling-wave resonators," Opt. Lett. **27**, 1669–1671 (2002).

[240] S. M. Spillane, T. J. Kippenberg, O. J. Painter, and K. J. Vahala, "Ideality in a fiber-taper-coupled microresonator system for application to cavity quantum electrodynamics," Phys. Rev. Lett. **91**, 043,902 (2003).

[241] T. Asano, B.-S. Song, and S. Noda, "Analysis of the experimental Q factors (1 million) of photonic crystal nanocavities," Opt. Express **14**, 1996–2002 (2006).

[242] T. Xu, S. Yang, S. V. Nair, and H. E. Ruda, "Nanowire-array-based photonic crystal cavity by finite-difference time-domain calculations," Phys. Rev. B **75**, 125,104 (2007).

[243] C. Kreuzer, J. Riedrich-Möller, E. Neu, and C. Becher, "Design of photonic crystal microcavities in diamond films," Opt. Express **16**, 1632–1644 (2008).

[244] R. P. Mildren and J. R. Rabeau, eds., *Optical Engineering of Diamond* (Wiley-VCH Verlag & Co. KGaA, 2013).

[245] H. M. Gibbs, *Optical bistability: controlling light with light* (Academic Press, Orlando, FL, 1985).

[246] V. R. Almeida and M. Lipson, "Optical bistability on a silicon chip," Opt. Lett. **29**, 2387–2389 (2004).

[247] C. Lee, E. Gu, M. Dawson, I. Friel, and G. Scarsbrook, "Etching and micro-optics fabrication in diamond using chlorine-based inductively-coupled plasma," Diamond Relat. Mater. **17**, 1292 – 1296 (2008). Proceedings of Diamond 2007, the 18th European Conference on Diamond, Diamond-Like Materials, Carbon Nanotubes, Nitrides and Silicon Carbide.

[248] M. Borselli, T. J. Johnson, and O. Painter, "Measuring the role of surface chemistry in silicon microphotonics," Appl. Phys. Lett. **88**, 131114 (2006).

[249] T. Graziosi, S. Mi, M. Kiss, and N. Quack, "Single crystal diamond micro-disk resonators by focused ion beam milling," APL Photonics **3**, 126,101 (2018).

[250] C. F. Ockeloen-Korppi, E. Damskägg, J.-M. Pirkkalainen, T. T. Heikkilä, F. Massel, and M. A. Sillanpää, "Low-noise amplification and frequency conversion with a multiport microwave optomechanical device," Phys. Rev. X **6**, 041,024 (2016).

[251] H. Kimble, "The quantum internet," Nature **453**, 1023–1030 (2008).

[252] S. J. M. Habraken, K. Stannigel, M. D. Lukin, P. Zoller, and P. Rabl, "Continuous mode cooling and phonon routers for phononic quantum networks," New J. Phys. **14**, 115,004 (2012).

[253] C. Simon, "Towards a global quantum network," Nat. Photon. **11**, 678–680 (2017).

[254] A. Vainsencher, K. J. Satzinger, G. A. Peairs, and A. N. Cleland, "Bi-directional conversion between microwave and optical frequencies in a piezoelectric optomechanical device," Appl. Phys. Lett. **109**, 033,107 (2016).

[255] A. P. Reed, K. H. Mayer, J. D. Teufel, L. D. Burkhart, W. Pfaff, M. Reagor, L. Sletten, X. Ma, R. J. Schoelkopf, E. Knill, and K. W. Lehnert, "Faithful conversion of propagating quantum information to mechanical motion," Nat. Phys. **13**, 1163–1167 (2017).

[256] A. P. Higginbotham, P. S. Burns, M. D. Urmey, R. W. Peterson, N. S. Kampel, B. M. Brubaker, G. Smith, K. W. Lehnert, and C. A. Regal, "Harnessing electro-optic correlations in an efficient mechanical converter," Nat. Phys. **14**, 1038–1042 (2018).

[257] M. Mitchell, D. P. Lake, and P. E. Barclay, "Demonstration of an optomechanically tunable optical buffer in diamond microcavities," in "Frontiers in Optics / Laser Science," (Optical Society of America, 2018), p. FW7A.6.

[258] G. Anetsberger, R. Riviere, A. Schliesser, O. Arcizet, and T. Kippenberg, "Ultra-low dissipation optomechanical resonators on a chip," Nat. Photon. **2**, 627–633 (2008).

[259] I. Aharonovich, D. Englund, and M. Toth, "Solid-state single-photon emitters," Nat. Photon. **10**, 631–641 (2016).

[260] M. Pfender, N. Aslam, P. Simon, D. Antonov, G. Thiering, S. Burk, F. Fávaro de Oliveira, A. Denisenko, H. Fedder, J. Meijer, J. A. Garrido, A. Gali, T. Teraji, J. Isoya, M. W. Doherty, A. Alkauskas, A. Gallo, A. Grüneis, P. Neumann, and J. Wrachtrup, "Protecting a diamond quantum memory by charge state control," Nano Lett. **17**, 5931–5937 (2017).

[261] D. D. Sukachev, A. Sipahigil, C. T. Nguyen, M. K. Bhaskar, R. E. Evans, F. Jelezko, and M. D. Lukin, "Silicon-vacancy spin qubit in diamond: A quantum memory exceeding 10 ms with single-shot state readout," Phys. Rev. Lett. **119**, 223,602 (2017).

[262] W. Pfaff, B. J. Hensen, H. Bernien, S. B. van Dam, M. S. Blok, T. H. Taminiau, M. J. Tiggelman, R. N. Schouten, M. Markham, D. J. Twitchen, and R. Hanson, "Unconditional quantum teleportation between distant solid-state quantum bits," Science **345**, 532–535 (2014).

[263] B. Hensen, H. Bernien, A. E. Dréau, A. Reiserer, N. Kalb, M. S. Blok, J. Ruitenberg, R. F. L. Vermeulen, R. N. Schouten, C. Abellán, W. Amaya, V. Pruneri, M. W. Mitchell, M. Markham, D. J. Twitchen, D. Elkouss, S. Wehner, T. H. Taminiau, and R. Hanson, "Loophole-free bell inequality violation using electron spins separated by 1.3 kilometres," Nature **526**, 682–686 (2015).

[264] I. Lekavicius, D. A. Golter, T. Oo, and H. Wang, "Transfer of phase information between microwave and optical fields via an electron spin," Phys. Rev. Lett. **119**, 063,601 (2017).

[265] A. H. Safavi-Naeini and O. Painter, "Proposal for an optomechanical traveling wave phonon-photon translator," New J. Phys. **13**, 013,017 (2011).

[266] A. Dréau, A. Tchebotareva, A. E. Mahdaoui, C. Bonato, and R. Hanson, "Quantum frequency conversion of single photons from a nitrogen-vacancy center in diamond to telecommunication wavelengths," Phys. Rev. Applied **9**, 064,031 (2018).

[267] P. Farrera, N. Maring, B. Albrecht, G. Heinze, and H. de Riedmatten, "Nonclassical correlations between a C-band telecom photon and a stored spin-wave," Optica **3**, 1019–1024 (2016).

[268] N. Maring, P. Farrera, K. Kutluer, M. Mazzera, G. Heinze, and H. de Riedmatten, "Photonic quantum state transfer between a cold atomic gas and a crystal," Nature **551**, 485–488 (2017).

[269] M. T. Rakher, L. Ma, O. Slattery, X. Tang, and K. Srinivasan, "Quantum transduction of telecommunications-band single photons from a quantum dot by frequency upconversion," Nat. Photon. **4**, 786–791 (2010). Article.

[270] J. S. Pelc, L. Yu, K. D. Greve, P. L. McMahon, C. M. Natarajan, V. Esfandyarpour, S. Maier, C. Schneider, M. Kamp, S. Höfling, R. H. Hadfield, A. Forchel, Y. Yamamoto, and M. M. Fejer, "Downconversion quantum interface for a single quantum dot spin and 1550-nm single-photon channel," Opt. Express **20**, 27,510–27,519 (2012).

[271] K. De Greve, L. Yu, P. L. McMahon, J. S. Pelc, C. M. Natarajan, N. Y. Kim, E. Abe, S. Maier, C. Schneider, M. Kamp, S. Höfling, R. H. Hadfield, A. Forchel, M. M. Fejer, and Y. Yamamoto, "Quantum-dot spin-photon entanglement via frequency downconversion to telecom wavelength," Nature **491**, 421–425 (2012).

[272] A. G. Radnaev, Y. O. Dudin, R. Zhao, H. H. Jen, S. D. Jenkins, A. Kuzmich, and T. A. B. Kennedy, "A quantum memory with telecom-wavelength conversion," Nat. Phys. **6**, 894–899 (2010).

[273] Q. Li, M. Davanço, and K. Srinivasan, "Efficient and low-noise single-photon-level frequency conversion interfaces using silicon nanophotonics," Nat. Photon. **10**, 406–414 (2016).

[274] F. Massel, T. T. Heikkilä, J.-M. Pirkkalainen, S. U. Cho, H. Saloniemi, P. J. Hakonen, and M. A. Sillanpää, "Microwave amplification with nanomechanical resonators," Nature **480**, 351–354 (2011).

[275] T. G. McRae and W. P. Bowen, "Near threshold all-optical backaction amplifier," Appl. Phys. Lett. **100**, 201,101 (2012).

[276] H. Li, Y. Chen, J. Noh, S. Tadesse, and M. Li, "Multichannel cavity optomechanics for all-optical amplification of radio frequency signals," Nat. Commun. **3**, 1091 (2012).

[277] M. Gorodetksy, A. Schliesser, G. Anetsberger, S. Deleglise, and T. Kippenberg, "Determination of the vacuum optomechanical coupling rate using frequency noise calibration," Opt. Express **18**, 23,236–23,246 (2010).

[278] Y. Zou, Y. Jiang, Y. Mei, X. Guo, and S. Du, "Quantum heat engine using electromagnetically induced transparency," Phys. Rev. Lett. **119**, 050,602 (2017).

[279] C. M. Caves, "Quantum limits on noise in linear amplifiers," Phys. Rev. D **26**, 1817–1839 (1982).

[280] V. Fiore, C. Dong, M. C. Kuzyk, and H. Wang, "Optomechanical light storage in a silica microresonator," Phys. Rev. A **87**, 023,812 (2013).

[281] H. Goldstein, *Classical Mechanics* (Addison Wesley, San Francisco, 2002).

[282] H. Xu, D. Mason, L. Jiang, and J. G. E. Harris, "Topological energy transfer in an optomechanical system with exceptional points," Nature **537**, 80–83 (2016).

[283] G. Patera, J. Shi, D. B. Horoshko, and M. I. Kolobov, "Quantum temporal imaging: application of a time lens to quantum optics," J. Opt. **19**, 054,001 (2017).

[284] M. Merklein, B. Stiller, K. Vu, S. J. Madden, and B. J. Eggleton, "A chip-integrated coherent photonic-phononic memory," Nat. Commun. **8**, 574 (2017).

[285] B. Stiller, M. Merklein, C. Wolff, K. Vu, P. Ma, S. J. Madden, and B. J. Eggleton, "Coherently refreshed acoustic phonons for extended light storage," arXiv:1904.13167 (2019).

[286] A. H. Safavi-Naeini, J. T. Hill, S. Meenehan, J. Chan, S. Gröblacher, and O. Painter, "Two-dimensional phononic-photonic band gap optomechanical crystal cavity," Phys. Rev. Lett. **112**, 153,603 (2014).

[287] C. R. Pollock and M. Lipson, *Integrated Photonics* (Springer, Boston, MA, 2003), 1st ed.

[288] C. Bond, D. Brown, A. Freise, and K. A. Strain, "Interferometer techniques for gravitational-wave detection," Living Rev. Relativ. **19**, 3 (2017).

[289] L.-S. Yan, Q. Yu, A. E. Willner, and Y. Shi, "Measurement of the chirp parameter of electro-optic modulators by comparison of the phase between two sidebands," Opt. Lett. **28**, 1114–1116 (2003).

[290] M. L. Boas, *Mathematical Methods in the Physical Sciences* (John Wiley and Sons, 2006).

Appendix A

List of publications

The following is a complete list of publications that I was involved in during my time as a graduate student. I have separated this list into publications closely related to the work presented in my thesis and those that are not.

Closely related publications

- D.P. Lake, **M. Mitchell**, Barry C. Sanders, and P.E. Barclay, "Two-color interferometry and switching through optomechanical dark mode excitation," arXiv:1906.10754, (2019).
- **M. Mitchell**, D.P. Lake, and P.E. Barclay, "Optomechanically amplified wavelength conversion in diamond microcavities," Optica, **6**, 832–838 (2019).
- **M. Mitchell**, D.P. Lake, and P.E. Barclay, "Realizing $Q > 300\,000$ in diamond microdisks for optomechanics via etch optimization," APL Photonics, **4**, 016101 (2019).
- D.P. Lake*, **M. Mitchell***, Y. Kamaliddin, and P.E. Barclay, " Optomechanically induced transparency and cooling in thermally stable diamond microcavities," ACS Photonics, **5**, 782-787 (2018).* **Authors contributed equally to this work.**
- **M. Mitchell**, B. Khanaliloo, D.P. Lake, T. Masuda, J.P. Hadden, and P.E. Barlcay, "Single-crystal diamond low-dissipation cavity optomechanics," Optica, **3**, 963-970 (2016).

- B. Khanaliloo, **M. Mitchell**, A.C. Hryciw, and P.E. Barclay, "High-Q/V monolithic diamond microdisks fabricated with quasi-isotropic etching," Nano Lett. **15**, 5131-5136 (2015).

- **M. Mitchell**, A.C. Hryciw, and P.E. Barclay, "Cavity optomechanics in gallium phosphide microdisks," Appl. Phys. Lett. **104**, 141104 (2014).

Other publications

- P.K. Shandilya, J.E. Fröch, **M. Mitchell**, D.P. Lake, S. Kim, M. Toth, B. Behera, C. Healey, I. Aharonovich, and P.E. Barclay, "Hexagonal boron nitride cavity optomechanics," Nano Lett. **19**, 1343-1350 (2019).

- D.P. Lake, **M. Mitchell**, H. Jayakumar, L.F. Dos Santos, D. Curic, and P.E. Barclay, "Efficient telecom to visible wavelength conversion in doubly resonant GaP Microdisks," Appl. Phys. Lett. **108**, 031109 (2016).

- C. Healey, H. Kaviani, M. Wu, B. Khanaliloo, **M. Mitchell**, A.C Hryciw, and P.E. Barlcay, "Design and experimental demonstration of optomechanical paddle nanocavities," Appl. Phys. Lett. **107**, 231107 (2015).

Appendix B

Approximate analytical solution for whispering gallery modes

This appendix is meant to serve as an overview for describing WGM's, and follows the analysis of Matthew Borselli [94]. Unfortunately, analytical solutions to Maxwell's equations for the disk geometry illustrated in Fig. B.1(a) have not been found due to the problem of matching boundary conditions near the corners of the structure as illustrated as the hatched regions in Fig. B.1(b), where these regions couple the x and y solutions of the field [287]. However, some assumptions and simplifications can be made in order to reach a solution with approximates the numerically computed solution. By assuming the microdisk thickness is greater than half the optical wavelength in the material, $d > \lambda_o/2n$ the field components near the corners can be taken to be small and the wave equation may be solved using the standard separation of variables method. This process is briefly outlined below, where the starting point is Maxwell's equations for the case of no free charges and currents in the material:

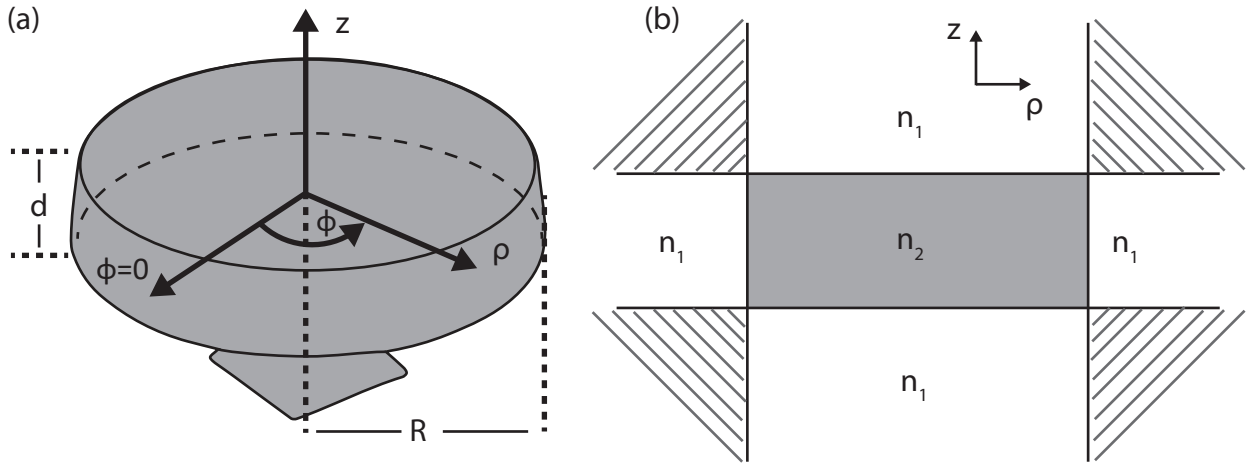

Figure B.1: Boundary value problem in dielectric disk structure (a), where boundary conditions can not be met in the hatched regions illustrated in (b).

$$\nabla \cdot \mathbf{D}(\mathbf{r},t) = 0 \qquad \nabla \times \mathbf{E}(\mathbf{r},t) = -\frac{\partial \mathbf{B}(\mathbf{r},t)}{\partial t}, \tag{B.1}$$

$$\nabla \cdot \mathbf{B}(\mathbf{r},t) = 0 \qquad \nabla \times \mathbf{H}(\mathbf{r},t) = \frac{\partial \mathbf{D}(\mathbf{r},t)}{\partial t},$$

where $\mathbf{D}(\mathbf{r},t) = \epsilon(\mathbf{r},t)\mathbf{E}(\mathbf{r},t)$ and $\mathbf{H}(\mathbf{r},t) = 1/\mu_0\mathbf{B}(\mathbf{r},t)$. In the absence of free current or charges the solutions to these equations are electromagnetic waves with an $e^{-i\omega t}$ time dependence. For the microdisk geometry the next assumption we can make is that the index of refraction is independent of the azimuthal position, i.e. $n(\mathbf{r}) = \mathbf{n}(\rho, \mathbf{z})$, and that the whole system is piecewise homogenous. This allows the writing of a master equation describing the system, which reduces to the Helmholtz equation in cylindrical coordinates:

$$\nabla^2\mathbf{F} + k_0^2 n^2(\rho, z)\mathbf{F}(\mathbf{r}) = 0, \tag{B.2}$$

where $\mathbf{F} = \{\mathbf{E}, \mathbf{H}\}$, $k_0 = \omega/c$ is the wave number in free space, and the speed of light $c = 1/\sqrt{\mu_0\epsilon_0}$. As the microdisk geometry provides vertical confinement such that light propagates in plane, the problem can effectively be reduced to two dimensions. Provided

that $d > \lambda_o/2n$ two sets of uncoupled optical modes with orthogonal polarizations can be described, namely TE and TM modes, where for the TM mode the electric field is polarized perpendicular to the disk plane and the magnetic field lies in the disk plane, i.e. $(H_r, H_\phi, E_z) \neq 0$ and $(E_r, E_\phi, H_z) = 0$. For the TE mode the electric field lies in the disk plane such that $(E_r, E_\phi, H_z) \neq 0$ and $(H_r, H_\phi, E_z) = 0$. Ignoring the corner regions as described above, Eqn. B can be solved via separation of variables, which gives differential equations for the vertical, $Z(z)$, azimuthal, $\Omega(\phi)$, and radial, $\Psi(\rho)$, field components in the disk ($\rho < R$) as:

$$\begin{aligned} \frac{\partial^2 Z}{\partial z^2} + k_0^2(n^2(z) - n_{\text{eff}}^2)Z = 0, \\ \frac{\partial^2 \Omega}{\partial \phi^2} + m^2\Omega = 0, \\ \frac{\partial^2 \Psi}{\partial \rho^2} + \frac{1}{\rho}\frac{\partial \Psi}{\partial \rho} + \left(k_0^2(n_{\text{eff}}^2(\rho) - \frac{m^2}{\rho^2}\right)\Psi = 0. \end{aligned} \tag{B.3}$$

The solution for $Z(z)$ follow that of a slab waveguide [103], whose vertical characteristics are described by the vertical number, q, which describes the number of nodes along the z-axis, where $\{q \in \mathbb{Z}, q > 1\}$. The solution for Ω is $\sim e^{im\phi}$ where m is the azimuthal number of the mode and describes the number of nodes along the circumference of the disk, where $\{m \in \mathbb{Z}, m > 1\}$. Lastly the solution for Ψ is given by Bessel functions inside the disk and Hankel functions outside the disk:

$$\Psi(\rho) = \begin{cases} J_m(k_0 n_{\text{eff}}\rho), & \rho \leq R. \\ J_m(k_0 n_{\text{eff}} R)e^{(-\alpha(\rho - R))}, & \rho > R. \end{cases} \tag{B.4}$$

where the Hankel function can be approximated with the exponential $e^{-\alpha(\rho - R)}$, where $\alpha = k_0(n_{\text{eff}}^2 - n_0)$. When solving for the resonant modes of the structure by enforcing that the tangential field components of $\mathbf{E}$ and $\mathbf{H}$ are continuous, it can be shown that for a fixed

value of m, multiple solutions may exist [94]. These multiple solutions correspond to modes with increasing radial order, labelled by n where $\{n \in \mathbb{Z}, n > 1\}$, such that modes of the microdisk may then be identified as $\mathrm{TE}_{m,n,q}$ or $\mathrm{TM}_{m,n,q}$. As these modes are not purely TE or TM polarized often they are referred to as TE-like and TM-like.

Appendix C

Optomechanically induced transparency and absorption

Here we follow the derivation presented by Safavi-Naeini et al. [111] starting with the following un-linearized Hamiltonian modelling the optomechanical system

$$\hat{H} = \hbar\omega_{\rm o}\hat{a}^\dagger\hat{a} + \hbar\omega_{\rm m}\hat{b}^\dagger\hat{b} + \hbar g_0\hat{a}^\dagger\hat{a}(\hat{b}^\dagger + \hat{b}) + \ ... \tag{C.1}$$

Here $\hat{a}$ is understood to describe the cavity fluctuations, $\delta\hat{a}$, described in the main text, where the δ has been dropped for convenience. The equations of motion for $\hat{a}$ and $\hat{b}$ are then

$$\dot{\hat{a}} = -(i\omega_{\rm o} + \frac{\kappa}{2})\hat{a} - ig_0\hat{a}(\hat{b} + \hat{b}^\dagger) + \sqrt{\frac{\kappa_{\rm ex}}{2}}\alpha_{\rm in}e^{-i\omega_c t}, \tag{C.2}$$

$$\dot{\hat{b}} = -\left(i\omega_{\rm m} + \frac{\Gamma_{\rm m}}{2}\right)\hat{b} - ig_0(\hat{a}^\dagger\hat{a}) + \sqrt{\Gamma_{\rm m}}\hat{b}_{\rm in}(t). \tag{C.3}$$

Where $\alpha_{\rm in}$ is the amplitude of the input control laser field oscillating at frequency $\omega_{\rm c}$. Next we can linearize these equations about a steady state given by the intracavity photon amplitude

α_0 and static phonon shift β_0. The interaction of pump photons at ω_c and probe photons at $\omega_\mathrm{p} = \omega_\mathrm{c} \pm \Delta_\mathrm{p}$ with the mechanics is then modelled by making the following substitutions

$$\hat{a} \rightarrow \alpha_0 e^{-i\omega_\mathrm{c} t} + (\alpha_- e^{-i(\omega_\mathrm{c}+\Delta_\mathrm{p})t} + \alpha_+ e^{-i(\omega_\mathrm{c}-\Delta_\mathrm{p})t}), \tag{C.4}$$

$$\hat{b} \rightarrow \beta_0 + \beta_- e^{-i\Delta_\mathrm{p} t} + \beta_+ e^{i\Delta_\mathrm{p} t}. \tag{C.5}$$

As we are generating our probe field by weakly driving an electro-optic modulator at frequency Δ_p we include two sidebands of amplitude α_- and α_+, which are defined such that the α_- and α_+ sidebands are the probe fields for OMIT and OMIA, respectively. In addition to the static radiation pressure frequency shift, the mechanical motion will also experience a time varying force at Δ_p, and thus the phonon amplitude will also have a time varying part at frequency $\pm\Delta_\mathrm{p}$. We start by subbing Eqn. C.4 into Eqn. C.2

$$\begin{aligned} &- i\omega_\mathrm{c}\alpha_0 e^{-i\omega_\mathrm{c} t} - i(\omega_\mathrm{c} - \Delta_\mathrm{p})\alpha_+ e^{-i(\omega_\mathrm{c}-\Delta_\mathrm{p} t)} - i(\omega_\mathrm{c} + \Delta_\mathrm{p})\alpha_- e^{-i(\omega_\mathrm{c}+\Delta_\mathrm{p})t} \\ &\qquad = (\alpha_0 e^{-i\omega_\mathrm{c} t} + \alpha_- e^{-i(\omega_\mathrm{c}+\Delta_\mathrm{p})t} + \alpha_+ e^{-i(\omega_\mathrm{c}-\Delta_\mathrm{p})t})[-i\omega_\mathrm{o} - \kappa/2 - ig_0(\hat{b} + \hat{b}^\dagger) \\ &\qquad\qquad + \sqrt{\kappa_\mathrm{ex}/2}(\alpha_{\mathrm{in},0} + \alpha_{\mathrm{in},+} e^{i\Delta_\mathrm{p} t} + \alpha_{\mathrm{in},-} e^{-i\Delta_\mathrm{p} t}) e^{-i\omega_\mathrm{c} t}. \end{aligned} \tag{C.6}$$

To find the equations of motion for the sideband amplitudes we sub Eqn.C.5 into Eqn. C.6, and group like frequency terms to get

$$\pm\, i\Delta_\mathrm{p}\alpha_\pm = -\left(i\Delta_\mathrm{c} + \frac{\kappa}{2}\right)\alpha_\pm - ig\beta_\pm + \sqrt{\frac{\kappa_\mathrm{ex}}{2}}\alpha_{\mathrm{in},\pm}, \tag{C.7}$$

where $g = g_0\,|\alpha_0| = g_0\sqrt{N}$ is the photon assisted optomechanical coupling rate. Here we have also discarded the $\beta_\mp$ terms corresponding to $\alpha_\pm$ as they are non-resonant. To find the

equations of motion for $\beta_\pm$ we sub Eqn. C.5 into Eqn. C.3 and group like frequency terms to find.

$$-i\Delta_\mathrm{p}\beta_- = -\left(i\omega_\mathrm{m} + \frac{\Gamma_\mathrm{m}}{2}\right)\beta_- - ig_0\left(\alpha_0^*\alpha_- + \alpha_0\alpha_+^*\right) + \sqrt{\Gamma_\mathrm{m}}\beta_{\mathrm{in},-} \tag{C.8}$$

Where $\beta_+ = \beta_-^*$. In order to compute the reflection and transmission coefficients of the probe sidebands, $r(\Delta_\mathrm{p})$ and $t(\Delta_\mathrm{p})$, respectively, we use the input output relations, ($\hat{r} = -\sqrt{\kappa_\mathrm{ex}/2}\hat{a}$ and $\hat{t} = \hat{s} - \sqrt{\kappa_\mathrm{ex}/2}\hat{a}$) and sub β_- or β_+ into Eqn. C.7. Here we assume that the system is sufficiently in the sideband resolved regime such that the off-resonant sideband terms can be safely ignored. This allows for us to solve for the probe field's transmission and reflection coefficients used in the main text, normalized to the input sideband amplitudes, $\alpha_{\mathrm{in},\pm}$.

OMIT

$$t(\Delta_\mathrm{p}) = 1 - \sqrt{\frac{\kappa_\mathrm{ex}}{2}}\frac{\alpha_-}{\alpha_\mathrm{in}} = 1 - \frac{\kappa_\mathrm{ex}/2}{i(\Delta_\mathrm{c} - \Delta_\mathrm{p}) + \kappa/2 + \frac{Ng_0^2}{i(\omega_\mathrm{m} - \Delta_\mathrm{p}) + \Gamma_\mathrm{m}/2}}, \tag{C.9}$$

$$r(\Delta_\mathrm{p}) = \sqrt{\frac{\kappa_\mathrm{ex}}{2}}\frac{\alpha_-}{\alpha_\mathrm{in}} = -\frac{\kappa_\mathrm{ex}/2}{i(\Delta_\mathrm{c} - \Delta_\mathrm{p}) + \kappa/2 + \frac{Ng_0^2}{i(\omega_\mathrm{m} - \Delta_\mathrm{p}) + \Gamma_\mathrm{m}/2}}, \tag{C.10}$$

OMIA

$$t(\Delta_\mathrm{p}) = 1 - \sqrt{\frac{\kappa_\mathrm{ex}}{2}}\frac{\alpha_+}{\alpha_\mathrm{in}} = 1 - \frac{\kappa_\mathrm{ex}/2}{i(\Delta_\mathrm{c} + \Delta_\mathrm{p}) + \kappa/2 + \frac{Ng_0^2}{i(\omega_\mathrm{m} - \Delta_\mathrm{p}) - \Gamma_\mathrm{m}/2}}, \tag{C.11}$$

$$r(\Delta_\mathrm{p}) = \sqrt{\frac{\kappa_\mathrm{ex}}{2}}\frac{\alpha_+}{\alpha_\mathrm{in}} = -\frac{\kappa_\mathrm{ex}/2}{i(\Delta_\mathrm{c} + \Delta_\mathrm{p}) + \kappa/2 + \frac{Ng_0^2}{i(\omega_\mathrm{m} - \Delta_\mathrm{p}) - \Gamma_\mathrm{m}/2}}, \tag{C.12}$$

Appendix D

Electro–optic modulator model

When modelling the predicted output spectra of the optomechanical cavities studied in this work the details of how the probe fields are generated are vital, due to the sensitivity of the cavity to both phase and amplitude fluctuations. A variety of constructions exist for implementing an optical phase or amplitude modulator. The $LiNbO_3$ electro–optic modulators (EOM) utilized in this work were purchased from EOSpace where the amplitude modulator used is Z–cut (pre–chirp) with an alpha chirp parameter of $\alpha_{\text{chirp}} \sim 0.6 - 0.8$. In practice this results in both amplitude and phase modulation which must be taken into account when considering the optical transmission and reflection by the optical cavity.

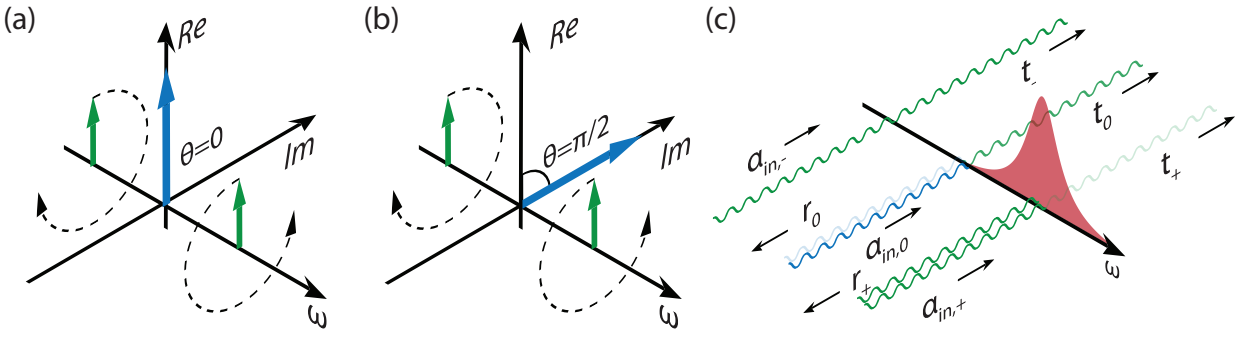

Figure D.1: (a) Frequency components of pure amplitude modulation in a frame rotating at the carrier frequency. The two sidebands are placed at $\pm\omega_{\text{m}}$, where ω_{m} is the frequency of modulation. Here the modulation is in a direction parallel to the carrier tone. (b) Frequency components of a pure phase modulation. Unlike the case of amplitude modulation, the modulation occurs in a direction perpendicular to the carrier tone. (c) Illustration of the expected reflected and transmitted signals for the case of a red detuned pump laser modulated such that one sideband is near resonance with the cavity.

A phasor picture can prove useful when visualizing the differences between pure phase and amplitude modulation as illustrated in Fig. D.1, where inspiration was taken from Ref. [288]. Here a frame rotating with the carrier frequency is used such that the electric field vector appears stationary. We observe from this animation that for pure phase modulation the generated sidebands are out of phase when re–phasing in the real plane leading to no amplitude modulation, while for the pure amplitude modulation case they are π out of phase when re–phasing in the real plane. In practice our amplitude modulator does not provide pure amplitude modulation. To account for this, we allow the phase of the carrier to be a variable dependent on the type of EOM used to develop a model capable of describing an EOM operating between the pure amplitude and phase modulation regime. First we describe optical field amplitude generated by the EOM and then input to the cavity α_{in} as:

$$\alpha_{\text{in}} = \alpha \left(e^{i\phi} + \frac{\beta}{2} e^{i\omega t} + \frac{\beta}{2} e^{-i\omega t} \right), \tag{D.1}$$

where α is the carrier optical field amplitude, β is the modulation index, and ω is the modulation frequency. When $\phi = 0 \pm n\pi$ the field for a pure amplitude modulator is described and for $\phi = \pi/2 \pm n\pi$ a pure phase modulator. To use this model to predict the observed cavity output spectra in this work we begin by writing the input optical field frequency components as $\alpha_{\text{in}}^{0} = \alpha e^{i\phi}$, $\alpha_{\text{in}}^{+} = \frac{\alpha\beta}{2} e^{i\omega t}$, and $\alpha_{\text{in}}^{-} = \frac{\alpha\beta}{2} e^{-i\omega t}$. Then the cavity transmission and reflection amplitudes are given by:

$$t_{\text{out}} = t_{\text{out}}^{+} + t_{\text{out}}^{0} + t_{\text{out}}^{-} \tag{D.2}$$

and

$$r_{\text{out}} = r_{\text{out}}^{+} + r_{\text{out}}^{0} + r_{\text{out}}^{-} \tag{D.3}$$

where

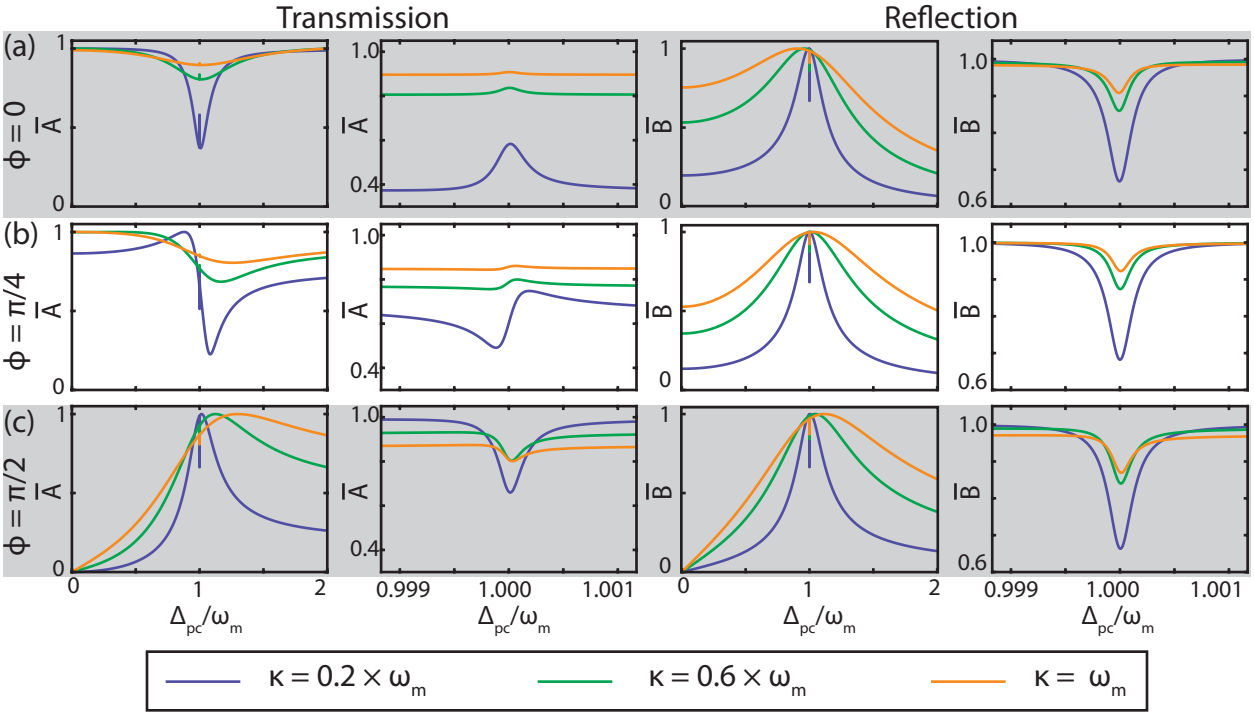

Figure D.2: Model for reflection and transmission spectra as a function of probe field detuning, Δ_p and sideband phase parameter ϕ for a red–detuned control field with $\Delta_\mathrm{c} = \omega_\mathrm{m}$, $Q_\mathrm{m} = 5000$, $G = 4.78$ MHz, $\kappa_\mathrm{ex} = 0.25 \cdot \kappa$, and varying sideband resolution shown in the legend.

$$t^+_\mathrm{out} = t^+\alpha^+_\mathrm{in}, \quad t^0_\mathrm{out} = t^0\alpha^0_\mathrm{in}, \quad t^-_\mathrm{out} = t^-\alpha^-_\mathrm{in} \tag{D.4}$$

and

$$r^+_\mathrm{out} = r^+\alpha^+_\mathrm{in}, \quad r^0_\mathrm{out} = r^0\alpha^0_\mathrm{in}, \; r^-_\mathrm{out} = r^-\alpha^-_\mathrm{in}. \tag{D.5}$$

Here the terms (t^+, t^0, t^-) and (r^+, r^0, r^-) describe the cavity transmission or reflection amplitude, respectively, as seen by each frequency component of the input field, defined as follows. We now consider the power measured by the photodetector in transmission and reflection, $|t_\mathrm{out}|^2 = t^*_\mathrm{out}t_\mathrm{out}$, and $|r_\mathrm{out}|^2 = r^*_\mathrm{out}r_\mathrm{out}$:

$$|t_\mathrm{out}|^2 = |t^0|^2|\alpha^0_\mathrm{in}|^2 + t^{0*}t^+\alpha^{0*}_\mathrm{in}\alpha^+_\mathrm{in} + t^0t^{-*}\alpha^0_\mathrm{in}\alpha^{-*}_\mathrm{in} + c.c \tag{D.6}$$

and

$$|r_{\text{out}}|^2 = |r^0|^2|\alpha_{\text{in}}^0|^2 + r^{0*}r^+\alpha_{\text{in}}^{0*}\alpha_{\text{in}}^+ + r^0r^{-*}\alpha_{\text{in}}^0\alpha_{\text{in}}^{-*} + c.c, \tag{D.7}$$

where we have neglected terms that are of $\mathcal{O}(\beta^2)$. Substituting our expressions for the input fields gives:

$$|t_{\text{out}}|^2 = |t^0|^2\alpha^2 + \alpha^2\frac{\beta}{2}[t^{0*}t^+e^{-i\phi} + t^0t^{-*}e^{i\phi}]e^{i\omega t} + \alpha^2\frac{\beta}{2}[t^0t^{+*}e^{i\phi} + t^{0*}t^-e^{-i\phi}]e^{-i\omega t} \tag{D.8}$$

and

$$|r_{\text{out}}|^2 = |r^0|^2\alpha^2 + \alpha^2\frac{\beta}{2}[r^{0*}r^+e^{-i\phi} + r^0r^{-*}e^{i\phi}]e^{i\omega t} + \alpha^2\frac{\beta}{2}[r^0r^{+*}e^{i\phi} + r^{0*}r^-e^{-i\phi}]e^{-i\omega t}. \tag{D.9}$$

In general the above may be written as

$$|t_{\text{out}}|^2 = |t^0|^2\alpha^2 + \alpha^2\beta|A|\cos(\omega t - \arg\{A\}) \tag{D.10}$$

and

$$|r_{\text{out}}|^2 = |r^0|^2\alpha^2 + \alpha^2\beta|B|\cos(\omega t - \arg\{B\}), \tag{D.11}$$

where

$$A = (t^{0*}t^+e^{-i\phi} + t^0t^{-*}e^{i\phi}) \tag{D.12}$$

and

$$B = (r^{0*}r^+e^{-i\phi} + r^0r^{-*}e^{i\phi}). \tag{D.13}$$

The measured vector network analyzer (VNA) signal for the phase and amplitude quadra-

ture are modeled by $\arg\{A\}$ ($\arg\{B\}$) and $|A|$ ($|B|$), respectively, for transmission (reflection) by the cavity. Additionally, by selecting the proper value of ϕ the response for a phase EOM, amplitude EOM, or mixture of both may be modelled. The bare cavity transmission amplitude $t^0(\Delta_c)$ is given by:

$$t^0(\Delta_c) = 1 - \frac{\kappa_{ex}/2}{i(\Delta_c) + \kappa/2} \tag{D.14}$$

and for a red–detuned control field, the sideband transmission amplitudes as a function of Δ_p are given by:

$$t^{\pm}(\pm\Delta_p) = 1 - \frac{\kappa_{ex}/2}{i(\Delta_c - (\pm\Delta_p)) + \kappa/2 + \frac{Ng_0^2}{i(\omega_m - (\pm\Delta_p)) + \Gamma_m/2}}. \tag{D.15}$$

In the main text the reflected amplitude measured on the VNA is fit to $|B|$ by taking $r = t - 1$, and substituting Eqns. D.14 and D.15 into Eqn. D.13, and choosing the appropriate value of ϕ depending on the EOM used. In order to determine ϕ for the amplitude EOM used in this work the phase difference (2θ) between the sidebands was determined from the chirp parameter, α_{chirp}, as:

$$\tan\theta \approx \alpha_{chirp}\cot\left(\frac{\varphi}{2}\right) \tag{D.16}$$

assuming a small–modulation amplitude ($\beta \ll 1$), where φ is the constant phase delay between the two interferometer arms, and $\varphi = \pi/2$ when biased at quadrature [289]. Through fitting the OMIT spectra obtained with the amplitude EOM in both the main text and in the following section, $\alpha_{chirp} \sim 0.70$ was found to provide the best fit; this value is within the bounds provided by the manufacturer.

For reference, the behavior of the model described above is shown in Fig. D.2 for various ϕ and degree to which the system is sideband resolved. In particular it can be seen that for a non–pure amplitude modulator the observed VNA transmission spectra, $\bar{A} = |A|/\max(|A|)$ can a resemble that of the reflection spectra, $\bar{B} = |B|/\max(|B|)$.

Appendix E

Transduction coefficient

Here we show how to extract the optomechanical transduction coefficient for light that is transmitted through the cavity, and detected directly on a high speed photodetector. We follow the derivation presented by Gorodetsky et al.[277] and adapt it to the doublet modes used in this work. We start by modelling the mechanical mode amplitude as $x(t) = x_{\mathrm{th}}\cos(\omega_{\mathrm{m}}t)$, where x_{th} is the thermally driven amplitude of the mechanical mode. These oscillations will produce a periodic change in the optical mode's frequency, and as a result the phase of the intracavity field, with magnitude $\phi = Gx_{\mathrm{th}}/\omega_{\mathrm{m}}$. The usual classical equations of motion for a double-sided optomechanical cavity are,

$$\dot{\alpha}(t) = \left[i\left(\Delta + Gx\right) - \frac{\kappa}{2}\right]\alpha(t) + \sqrt{\frac{\kappa_{\mathrm{ext}}}{2}}\alpha_{\mathrm{in}}(t) \tag{E.1}$$

$$\ddot{x}(t) = -\Gamma_{\mathrm{m}}\dot{x}(t) - \omega_{\mathrm{m}}^2 x(t) + \frac{\hbar G|a|^2}{m_{\mathrm{eff}}}, \tag{E.2}$$

which for zero optomechanical coupling results in an intracavity field amplitude given by $\alpha(\omega) = \alpha_{\mathrm{in}}\sqrt{\kappa_{\mathrm{ex}}/2}\chi(\omega)$ where $\chi^{-1}(\omega) = [-i(\omega+\Delta)+\kappa/2]$ is the optical susceptibility and ω denotes the Fourier frequency of fluctuations of the input field around its laser frequency ω_{l} [18]. We then model the optomechanically induced phase modulation of the intracavity field as

$$\alpha(t) = \alpha_{\mathrm{in}}(t)\sqrt{\frac{\kappa_{\mathrm{ex}}}{2}}\chi(0)e^{-iGx_{\mathrm{th}}\cos(\omega_{\mathrm{m}}t)}, \tag{E.3}$$

and use the Jacobi-Anger expansion,

$$e^{iz\cos(\theta)} \equiv \sum_{n=1}^{\infty} i^n J_n(x)e^{in\theta}, \tag{E.4}$$

where J_n are Bessel functions of the first kind of order n. We can then assume weak modulation ($Gx_{\mathrm{th}} \ll \omega_{\mathrm{m}}$) such that the small-$x$ approximation [290] of the Bessel function can be made:

$$J_n = \frac{1}{n!}\left(\frac{x}{2}\right)^n + \mathcal{O}(x^{n+2}). \tag{E.5}$$

Combining this approximation with the relation $J_{-n}(z) = (-1)^n J_n(z)$ allows us to write the intracavity field amplitude as

$$\alpha(t) = \alpha_{\mathrm{in}}(t)\sqrt{\frac{\kappa_{\mathrm{ex}}}{2}}\chi(0)\left[1 - i\frac{Gx_{\mathrm{th}}}{2}\chi(\omega_{\mathrm{m}})e^{-i\omega_{\mathrm{m}}t} - i\frac{Gx_{\mathrm{th}}}{2}\chi(-\omega_{\mathrm{m}})e^{i\omega_{\mathrm{m}}t}\right]. \tag{E.6}$$

We can then write the intracavity field amplitude for each doublet mode, $\alpha_{\mathrm{s,a}}(t)$, following using the same formalism given in Appendix D as

$$\alpha_{\mathrm{s,a}}(t) = \alpha_{\mathrm{in}}(t)\sqrt{\frac{\kappa_{\mathrm{ex}}}{2}}\chi_{\mathrm{s,a}}(0)\left[1 - i\frac{Gx_{\mathrm{th}}}{2}\chi_{\mathrm{s,a}}(\omega_{\mathrm{m}})e^{-i\omega_{\mathrm{m}}t} - i\frac{Gx_{\mathrm{th}}}{2}\chi_{\mathrm{s,a}}(-\omega_{\mathrm{m}})e^{i\omega_{\mathrm{m}}t}\right] \tag{E.7}$$

where κ_{ex} is the external coupling rate to the fiber, $|\alpha_{\mathrm{in}}|^2 = P_{\mathrm{in}}$, and

$$\chi_{\mathrm{s,a}}(\omega) = \frac{1}{-i\left(\omega \pm \gamma_\beta/2 + \Delta\right) + \kappa_{\mathrm{s,a}}/2}. \tag{E.8}$$

The reflected signal from the cavity, R, is given by Eqn. 2.23b,

$$R = \left|\sqrt{\frac{\kappa_{\mathrm{ex}}}{2}}\left(a_{\mathrm{s}} - \alpha_{\mathrm{a}}\right)\right|^2 P_{\mathrm{in}}. \tag{E.9}$$

where $\alpha_{\mathrm{s,a}} = \alpha_{\mathrm{s,a}}/\alpha_{\mathrm{in}}$, as we have pulled the common factor out to isolate P_{in}. Solving for the power spectral density of the reflected signal, S_{RR} in terms of the power spectral density of the driven harmonic mechanics signal, S_{xx}, according to Section 2.4.3, and ignoring small terms we can find the transduction coefficients $K(\Delta)$ which satisfies the expression:

$$\frac{S_{\mathrm{RR}}(\omega)}{P_{\mathrm{in}}^2} = |K(\Delta)|^2 \, S_{xx}. \tag{E.10}$$

where,

$$S_{xx} = 2\pi x_{\mathrm{th}}^2 \left[\delta(\omega - \omega_{\mathrm{m}}) + \delta(\omega + \omega_{\mathrm{m}})\right]. \tag{E.11}$$

Here the transduction coefficient can be computed via

$$K(\Delta) = (\chi_{\mathrm{s}}^0 - \chi_{\mathrm{a}}^0)^* \cdot (\chi_{\mathrm{s}}^0 \chi_{\mathrm{s}}^+ - \chi_{\mathrm{a}}^0 \chi_{\mathrm{a}}^+) + (\chi_{\mathrm{s}}^0 - \chi_{\mathrm{a}}^0) \cdot (\chi_{\mathrm{s}}^0 \chi_{\mathrm{s}}^- - \chi_{\mathrm{a}}^0 \chi_{\mathrm{a}}^-)^*, \tag{E.12}$$

where

$$\chi_{\mathrm{s}}^0 = \frac{\kappa_{\mathrm{ex}}}{2}\chi_{\mathrm{s}}(0), \qquad \chi_{\mathrm{s}}^+ = i\frac{Gx_{\mathrm{th}}}{2}\chi_{\mathrm{s}}(\omega_{\mathrm{m}}), \qquad \chi_{\mathrm{s}}^- = i\frac{Gx_{\mathrm{th}}}{2}\chi_{\mathrm{s}}(-\omega_{\mathrm{m}}), \tag{E.13}$$

$$\chi_{\mathrm{a}}^0 = \frac{\kappa_{\mathrm{ex}}}{2}\chi_{\mathrm{a}}(0), \qquad \chi_{\mathrm{a}}^+ = i\frac{Gx_{\mathrm{th}}}{2}\chi_{\mathrm{a}}(\omega_{\mathrm{m}}), \qquad \chi_{\mathrm{a}}^- = i\frac{Gx_{\mathrm{th}}}{2}\chi_{\mathrm{a}}(-\omega_{\mathrm{m}}). \tag{E.14}$$

$$\tag{E.15}$$

This coefficient is extracted from fits to the optical transmission spectrum, which can then be used to account for optomechanical transduction when measuring mode temperature or phonon occupation as a function of laser-cavity detuning.

Appendix F

List of equipment

The following is a list of the major commercial equipment used for the work presented in this thesis.

Measurement equipment

Part name	**Model**
Amplitude electro-optic phase modulator	EOSpace AZ-0K5-10-PFA-SFA
Arbitrary waveform generator (AWG)	Tektronix AWG70002A
Digital serial analyzer (DSA)	Tektronix DSA70804B
Erbium doped fiber amplifier (EDFA)	Pritel LNHPFA-30-IO
Fiber optic cable	SMF-28e+
Fiber polarization controller (FPC)	Thorlabs FPC 560
Heat transfer block	Ace Glass 9594-16
Horizontal bubbler	Airfree AF-0514-02
Optical power meter	Newport 2936-R
Optical spectrum analyzer (OSA)	Ando AQ6317B
Optical variable attenuator	Exfo FVA-3100
Phase electro-optic phase modulator	EOSpace PM-5S5-20-PFA-PFA-UV-UL
Photodetector	NewFocus 1621
Real-time spectrum analyzer (RSA)	Tektronix RSA5106A

Reflux system tubing	Tygon S3 ACF00024-V
Reflux condenser coil	Chemglass CG-1213-05
Round bottom flask	Glassco 057.470.55B
RF amplifier	SHF 100 AP
Thermoelectric temperature controller (TEC)	LDT-5910B
TEC element	Thorlabs TEC3–6
Tunable diode lasers	Newport TLB-6700
Tunable band pass filter	Optoplex C-band, 2-port
Vector network analyzer (VNA)	Keysight E5063A
Wavelength division multiplexer (WDM)	Montclair Optics MFT-MC-51-30 AFC/AFC-1
90/10 Waveguide couplers	Newport F-CPL-L22351-A
50/50 Waveguide couplers	Newport F-CPL-L22351-A
12 GHz Photoreciever	Newfocus 1554-B

Fabrication equipment

Part name	**Model**
EBPVD	Johnson Ultravac load locked e-beam evaporator
EBL	Raith 150-TWO
ICPRIE - NINT	Oxford PlasmaLab Pro 100
ICPRIE - nanoFAB - Si_3N_4 etching	Oxford Estrelas
ICPRIE - nanoFAB - SCD etching	Oxford PlamsaLab Cobra
Oven	Yamato DX302
PECVD	Trion
Resist spinner and hotplate	Brewer Cee
SEM	Hitachi S-4800
UV/ozone bonder	nanoFAB home built - 5 mW/cm^2 at 254 nm

Appendix G

Diamond fabrication tips and tricks

Here I will outline each step of the diamond fabrication process and any tricks that we developed in working with the SCD samples. This is meant to be a more practical guide to help reproduce the results shown in this work. While a lot of what we do in this process is standard cleanroom process, we constantly have to deal with the fact that our samples are quite small. This leads to having to modify quite a few of these standard processes, as detailed here. The procedures outlined in this Appendix are not necessarily the 'right' way to do things, but hopefully provides a baseline for future users of the process. Before going into detail on each steps there are some general rules we try to follow:

- Use the group's labware for all chemical processing steps.
- Be consistent in how you handle and process the samples so it will be easier to troubleshoot if something goes wrong or turns out differently.
- Take notes and update the groups shared notebook so the group and future generations can see what you did.

G.1 General preparation

To date, our SCD samples have been purchased exclusively from Element 6, which have $\langle 100 \rangle$ top surfaces and are grown using chemical vapor deposition. We typically purchase either optical, or electronic grade material which is differentiated by the number of impurities in the material, with electronic grade being the most pure. These are either single side or double side polished, and there is no visual difference between these two grades. Typically the SCD chips are 3 mm long x 3 mm wide, and vary in thickness from 0.3 to 0.5 mm.

Old samples that have failed fabrication attempts on them can be reused by having them mechanically polished. These are to be sent out for mechanical polishing by Delaware Diamond Knives, where ~ 50 μm of diamond per polished side is removed. Historically we have found that if any sample gets to the first nitride etch step, or beyond, it will require mechanical polishing in order to get a pristine surface free from surface contaminants that cause the 'grass' shown in Fig. G.1 when etching into the diamond layer in a future fabrication run.

If working with an electronic grade sample that will have nitrogen or silicon implanted into the top surface layer then extra etching steps can be taken to create a more pristine surface. After a mechanical polish, the top, highly stressed layer of diamond can be removed using an Ar/Cl_2 etch (Table G.1) to clean and etch the top surface away (~ 3 μm) followed by an anisotropic O_2 diamond etch to remove an additional ~ 1 μm of diamond. This second etch is done to remove any Cl_2 that might be present in the surface of the diamond, as this has been linked to harming the coherence properties of the color centers. A more aggressive, tri-acid clean can also be performed to remove any graphite that has formed on the surface of the diamond (see Section 6.5).

T [°C]	Pressure [mTorr]	RF [W]	Bias [V]	ICP [W]	Ar [sccm]	Cl_2 [sccm]
15	2.5	250	463	1500	25	40

Table G.1: Nominal etch parameters used for the surface removal Ar/Cl_2 etch using the Oxford PlasmaLab Pro 100. This results in an etch rate of ~ 111 nm/min for SCD, measured via optical profilometry.

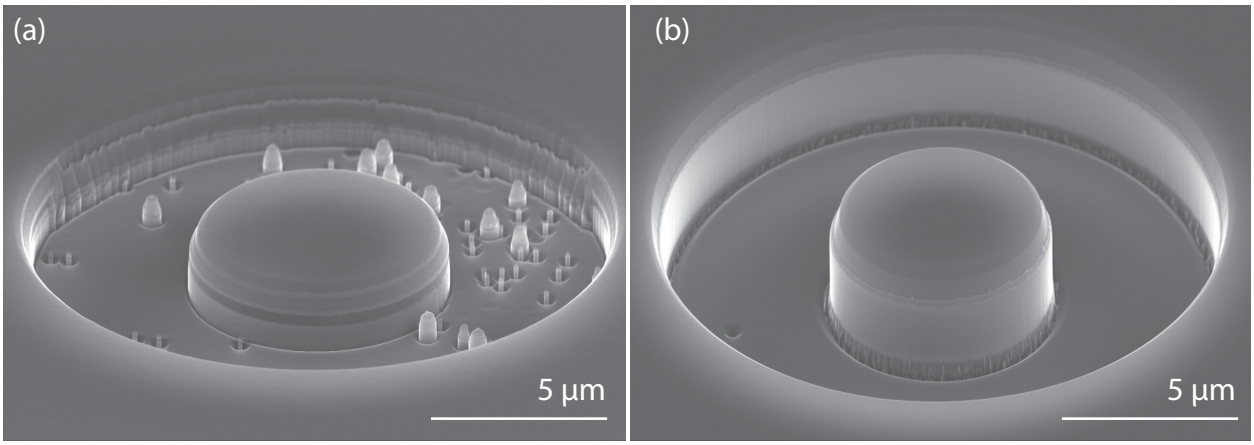

Figure G.1: Scanning electron micrographs comparing SCD samples after the anisotropic O_2 etch for a dirty (a) and clean (b) SCD surface.

G.2 Manipulating a sample

As the SCD samples are small and expensive, care has to be taken while handling them. To pick up a sample from a surface, we tend to use metal tweezers with a broad tip where possible. Metal tweezers are less susceptible to bending than their plastic-tip counterparts, and the broad tip makes it less likely that the sample with pivot in place. Metal tweezers should always be used on hot surfaces such as hotplates, and plastic tip tweezers should be used where scratching would be an issue, such as the sample mount for EBL or SEM. As I can have shaky hands I find that holding the tweezers in one hand and placing my pointer finger on top of the tweezers and pushing my hands towards each other helps alleviate some of this shakiness.

Take your time to level the tweezers, we find it helps to splay the tweezers out wider than the sample and push down on the surface you are working on in order to mechanically level your tweezers. After this you should be able to maintain the angle on the tweezers and pick up the sample. If you are picking up a sample from a cleanroom wipe, is helps to place the napkin such that the grooves are perpendicular to your tweezers. This prevents the tweezers getting caught, and threads from getting on to your sample.

G.3 Mounting and dismounting a sample on a carrier wafer

If you are mounting a sample onto a Si carrier wafer with grease, which we have done for all the plasma etches as well as for the Ti deposition, be sure to clean and N_2-dry the carrier wafer before mounting. There should be no visible dust on the carrier when viewed at a glancing angle. To apply grease, we insert a paperclip into a tube of grease and pull it out as shown in Fig. G.2. This should form a small filament of grease on the end of the paperclip, which you can apply to the carrier wafer. It is important not to use too much grease as it will flow out from under the sample when mounting it, and potentially contaminate the surface of the chip.

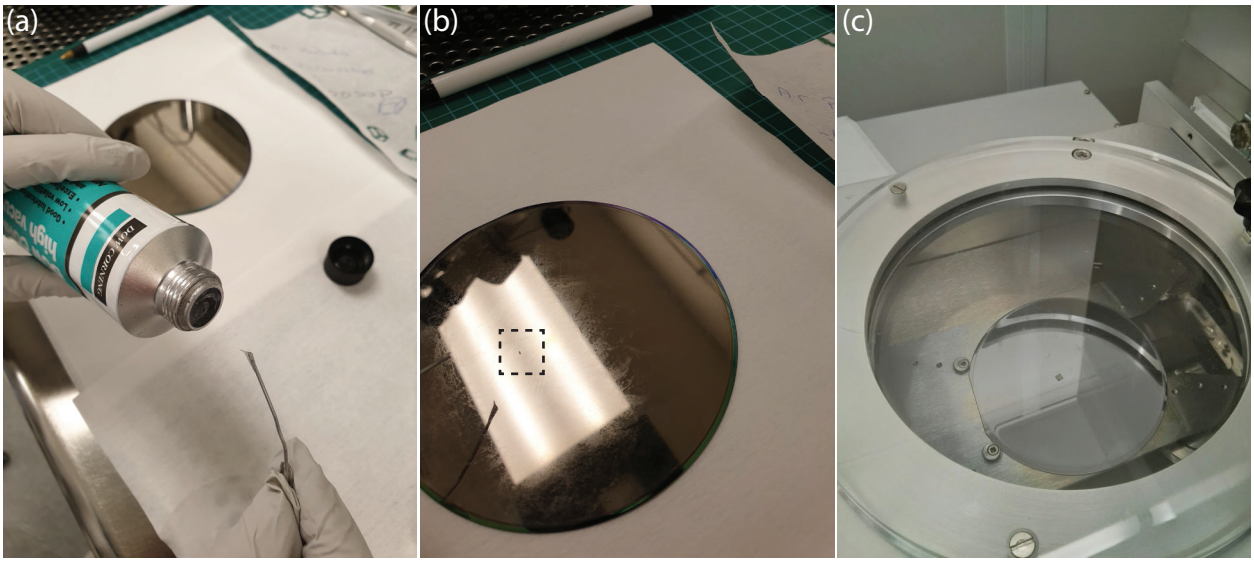

Figure G.2: Mounting a sample with vacuum grease to a Si carrier wafer. (a) A very small amount of vacuum grease is required for mounting the SCD chips to the Si carrier wafer, highlighted in (b). (c) Example of SCD sample mounted on the Si carrier and loaded into the loadlock of the PlasmaLab Pro 100.

Place your diamond sample on the grease and center it with your tweezers. Level your tweezers and push down on one set of opposite corners on your chip, and then on the other pair of opposite corners. This prevents your tweezers from touching the parts of the surface we will use for patterning. With this complete, check your sample from a glancing angle to make sure that it is flush with the carrier surface, and adjust if needed. Blow your carrier

and sample off with the N_2 gun and check for dust.

When dismounting a sample try not to squeeze your tweezers really tight and pull up, or you will most likely end up scratching the top surface of the sample. Also avoid sliding the sample since this can get grease on the side of the sample, again potentially leading to contamination. We have found that rotating and wiggling the sample until it releases from the grease below works best. When the sample is dismounted you'll want to clean the back with IPA to remove the remaining grease. To minimize surface contamination either wet the cleanroom wipe before you bring your sample out of the etcher, or cover your sample with a beaker while you spay IPA onto your wipe. To wipe the back off, pick up the sample with the tweezers, and then pinch and crease the wet cleanroom wipe between your fingers to create a ridge that you can wipe the back of the sample with.

G.4 Mounting a sample in the blue polypropylene forceps

Whenever you immerse a sample into liquid you will need to mount it into the blue polypropylene forceps (except for cleaning in acids: see following section). Pick up the sample with the metal tweezers, and place it in the palm of your other hand. It helps to wear double gloves for this, so your glove forms a trampoline in the center of your palm. Now take the blue forceps, pick up the sample, and lock the top of the tweezers, as shown in Fig. G.3(a).

At this point if you look as the sample closely, chances are it will not be sitting perfectly in the grooves of the tweezers. To fix this, pull back your gloves so they are tight over your fingertips, and then pinch the sides of the sample and wiggle the sample until you hear a snapping sound (Fig. G.3(b)), which indicates that the sample is now sitting well in the grooves of the forceps Fig. G.3(c).

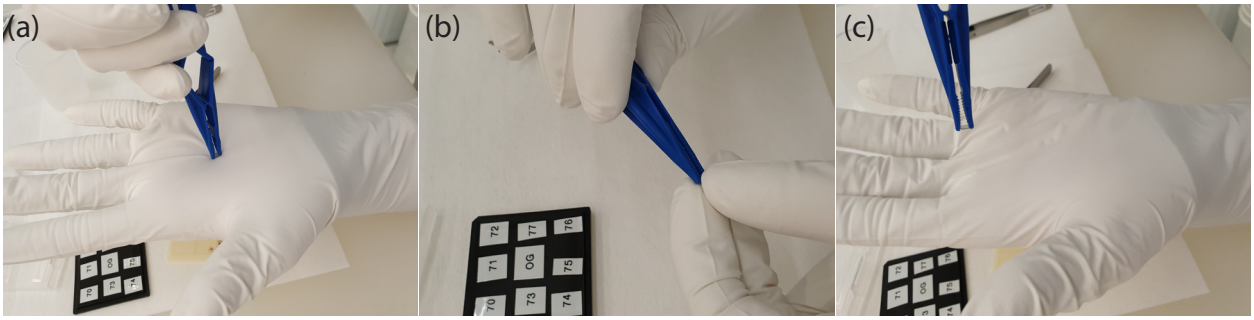

Figure G.3: Mounting a SCD sample in the blue polypropelene forceps. (a) A very small amount of vacuum grease is required for mounting the SCD chips to the Si carrier wafer, highlighted in (b). (c) Example of SCD sample mounted on the Si carrier and loaded into the loadlock of the PlasmaLab Pro 100.

G.5 Piranha cleaning

Typically we aim to make 200 mL of solution (50 mL H_2O_2:150 mL H_2SO_4, which allows us to hang the tweezers in the beaker such that the sample is just submerged, and a minimal amount of the tweezers are in the piranha. There is some debate if we should be using the polypropelyne forceps in piranha, as H_2O_2 and H_2SO_4 are known to attack polypropylene at high temperatures. All of the results presented in this thesis used the blue forceps, but we have noticed small particles present on our samples at the end of each fabrication run which could be from using these forceps. The PFTE tweezers we currently have introduce more chance for error, as they do not lock, and the grooves are quite deep which covers a significant portion of the chip, preventing cleaning by piranha. In the future a better PFTE sample carrier should be used.

Samples are left undisturbed in freshly mixed piranha for 15 minutes (Fig. G.4(a)). To stop the clean, the forceps are dipped in a beaker of water to a greater depth than they were in the piranha beaker, as shown in Fig. G.4(b). The sample is then rinsed with water from the wetdeck supply , and then immediately dried with the N_2 gun ((Fig. G.4(c)). At this point you should check for watermarks on the sample using a microscope, and repeat the rinsing step if there is anything noticeable. In order to prevent watermarks, start drying the sample at an angle nearly parallel to the surface in order to quickly drive off the water, followed by the backside of the sample, and the surface of the sample once more. Try not to

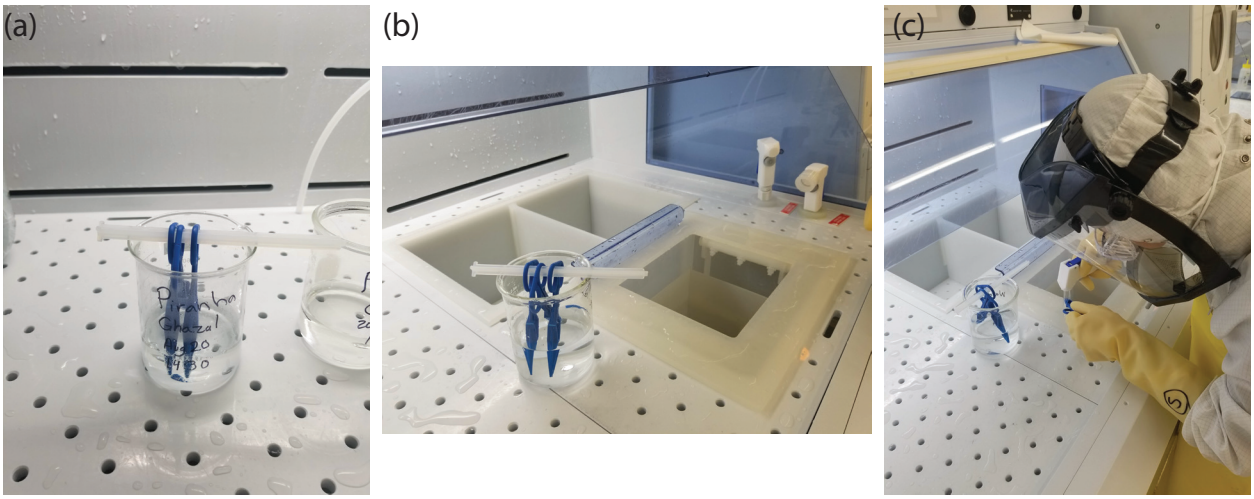

Figure G.4: Cleaning SCD samples in piranha with blue polypropelene forceps. (a) A piranha solution of 200 mL in a 500 mL beaker provides a good amount such that when hanging the blue forceps from the top only a small section of the forceps are in the solution. (b) To end the cleaning the forceps are dunked in a beaker of water. (c) After swirling the sample in water for 30 seconds it is rinsed with the DI water gun, and dried with the N_2 gun.

dry from above as contaminants from the forceps might drop down on to the sample.

G.6 PECVD SiNx deposition

For this step we use the Trion PECVD at nanoFAB, which historically would pull vacuum very quickly when set to run. This leads to turbulence inside the chamber, resulting in wafers skating across the heated chuck inside. To mitigate this we mount the diamond sample to a carrier wafer using double sided Kapton tape, and surround the carrier with additional Si pieces. Before each deposition we also made it a habit to do a physical clean of the chamber as described in the nanoFAB SOP.

We were using dedicated Si pieces for mounting both the SCD sample and some Si pieces to use for measuring the deposited film thickness and etch tests. It is important that the Si carrier wafer is flat and not warped (which we noticed happening for Si carrier wafers that were used many times). We then cut a long, narrow piece of Kapton tape with room to mount 3-4 Si pieces. As we measure the thickness using a FILMETRICS ellipsometer with a relatively large spot size, we infer the thickness of the nitride on the diamond from the

nitride on these Si pieces. Place the tape on the carrier wafer, sticky side down, then firmly press down the tape with a pair of tweezers. Then peel off the backing from the tape and place the Si samples such that the butt up against each other, and no tape is exposed. View the mounted samples from the side to check they are perfectly parallel to the carrier wafer, and adjust accordingly, as shown in Fig. G.5

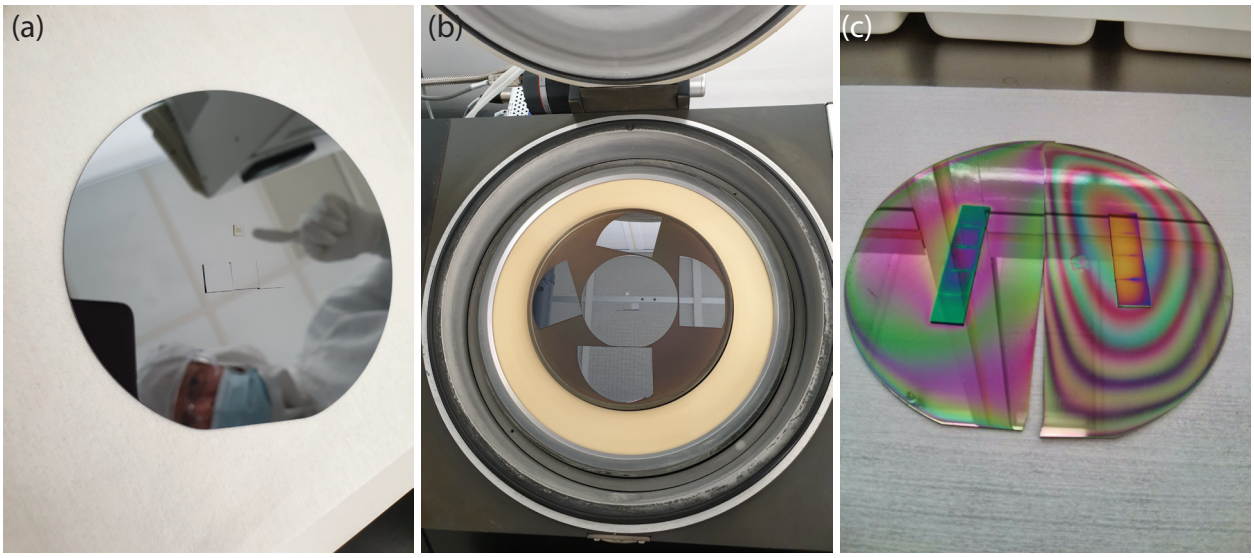

Figure G.5: (a) Mounting SCD and Si samples for PECVD Si_3N_4 on a Si carrier wafer. (b) The carrier is surrounded by Si wafer pieces to prevent the carrier from moving during the pumpdown. (c) Example of what the Si test pieces look like after deposition. Uniformity from sample to sample is an issue that is exacerbated by the Kapton tape mounting method.

Next, mount the diamond sample on a small square of tape. Again, make sure no tape is exposed (only about 25% of the sample has tape under it), and make sure that the sample is level. Since the diamond is clear, you can see which sections of tape have adhered to the sample by a change in colour. Place the carrier wafer into the middle of the chamber. Make sure to note the position so that you can replicate it. Surround the carrier wafer with the smaller pieces we have in the box, such that the carrier will not drift as shown in as shown in Fig. G.5.

Deposit the required amount of nitride, and then check the thickness of the Si test pieces. If the layer is not as thick as desired a second deposition will be necessary. When using the FILMETRICS be sure that you get a good fit to the curve. You can improve this by giving

it a good initial guess. Large errors in the fit, or drastic changes in deposition rate could indicate issues with the nitride, which would require intervention by the nanoFAB staff. Consistency is key with this step as any variation in the taping can lead to a different deposition rate, as this is tied very closely to the temperature of the sample.

To dismount the samples, it helps to start with the diamond, which eliminates the possibility of Si dust getting on the diamond when you try and move the other samples. Open your tweezers, and use one side to carefully dig under the sample using circular 'sawing' motions, to remove the tape. Once most of the tape has come unstuck from the sample, you can remove the diamond piece using twisting motions. If there is no tape on the back of the sample, you can simply clean the back with IPA in the usual way. If some tape is still stuck, it helps you mount the sample into blue forceps and then scrape off the back.

G.7 EBPVD Ti and SiO_2eposition

We follow the standard operating procedure at NRC-NANO for depositing Ti and SiO_2 on the SCD samples. To mount the sample we use vacuum grease, using the method described above. As the carriers are mounted upside down in the EBPVD tool, it is nice to check that the samples will hold by flipping the carrier upside-down and giving it a shake over a cleanroom wipe.

G.8 ZEP 520A spin coating and baking

With spin coating it is useful to gather all of the supplies you will need into the spinning area before you begin. You'll need your electron beam resist (ZEP 520A), parafilm, pipette (more if you are doing multiple samples), pipette bulbs, a small beaker of acetone, a few small q-tips, and metal tweezers.

Find the appropriate chuck, and ensure that it is clean, and the rubber O-ring is removed. Load the spin recipe you will use and carefully place and center the chip on the chuck. Turn

on the vacuum backing, and ensure that the chip is centered (the centering function on the Brewer Cee spinner is useful for this). Ensure that the tip of the pipette you are using is clean by spraying it with the N_2 gun and don't let it touch anything after this point. Then draw a very small amount of resist from the middle of the resist in the bottle, and avoid touching the sides a bottom. Squeeze a couple of drops out beside the chuck, and then place a drop onto the sample and start the spin cycle. Try to close the lid and start the spin as quickly as possible after dropping the ZEP.

When the spin cycle is finished, carefully remove the sample from the chuck with metal tweezers. Turn the sample upside down and check that the underside is completely clear of resist. Do not place it down onto the cleanroom wipe, as this can soak up resist and cause it to flow off the sample. If this is not the case (and this happens quite a bit), then wipe off the back with a q-tip that has been dipped in acetone. Make sure to touch the q-tip to a clean room wipe before wiping the back of your sample to avoid excess acetone or acetone vapor interfering with the top surface of the chip. Once you are satisfied that the back of the sample is completely clean, inspect the chip in one of the microscopes in the lithography area. You are looking for a large, flat 'diamond" shape in the middle of the sample. If at this point the resist does not look good, or if the sample was dropped or flipped, it's probably a good idea to remove the resist using Remover PG, and then repeat the spin steps from the beginning. Very stubborn resist can be removed with piranha, but this will also remove the titanium anti-charging layer.

If the spin coating looks acceptable, place it on the 180°C hotplate to bake for five minutes. It is very important that the back is clean so that it will be flat underneath clip in the EBL, permitting a good beam write. After baking, let the sample cool down, and then inspect again if any side looks particularly good, then make a note of it, and ensure that this area will be where you write the EBL pattern.

Finally, after a successful spin coat we will need to create some small particles on the thin part of the resist that we can use for imaging. While products such as gold and carbon

nanoparticles exist to help with this, we want to avoid contaminating the surface of the sample, and have found success creating small particles to focus on by scribing the surface of the resist with a diamond scribe. Place the scribe just past the bead of the resist such that the scratch will start in a uniform section of the ZEP, and extend down and over to the edge of the sample. This will break off some resist, which we will use to focus the EBL, and also leaves a trail from the edge of the sample, making it much easier to find.

G.9 EBL

As EBL is one of the more complex tools to use, we won't go into extreme detail on the procedure for using the tool and the buttons to push, as this is covered under the nanoFAB's SOP. Instead, we will mention some of the more practical tips and tricks we have found to be useful during beam writes.

When loading your sample on the sample holder shown in Fig. G.6 make sure to use plastic tweezers, never metal, as this can scratch the sample holder. The chip locations for driving to your sample are given in the table below and are on the group's Evernote notebook for your reference. The listed coordinates will place you near the curved edge of the clamp, which should be off or near the edge of the sample. Note that one of the clips is not to be used and is rotated backwards so that it is not used accidentally. When mounting the sample in this holder it is important to clamp down on enough of the chip so that it lies flat, but not so much that you cover the writable area with the clamp. Check that the sample is flat by holding the sample holder up you your eye and examine it from multiple angles. This is a reason why it is important to have a clean backside of the chip.

After the sample is loaded and you have driven to your chip location perform a rough focus on the edge of the chip. For diamond we use a 30 kV accelerating voltage and 15 μm aperture, so make sure you are using the SE2 detector for the best image quality. Find the bottom left corner of the chip, this will be the (0,0) point for the chip coordinate system

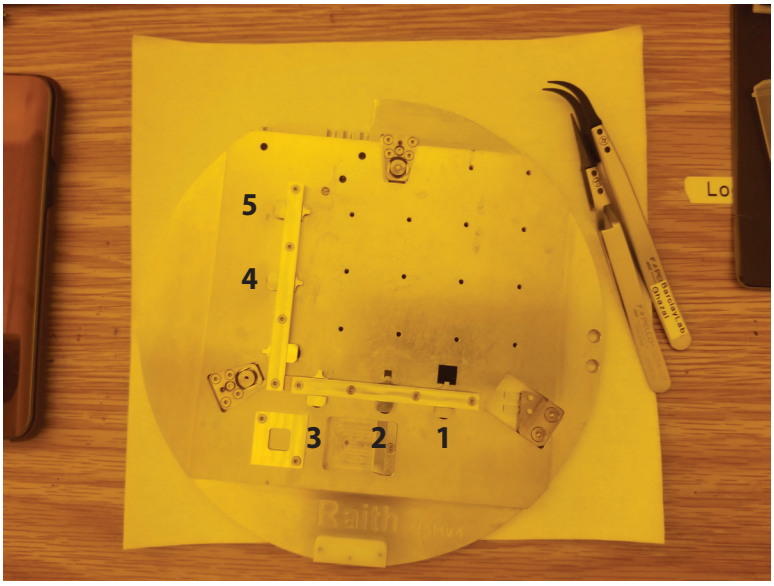

Figure G.6: Sample mount with corresponding XY clip coordinates for the Raith 150-TWO given in Table G.2

	X [mm]	Y [mm]	Z [mm]
Clip 1	-31.56	-29.67	20.00
Clip 2	-31.56	-4.52	20.00
Clip 3	-31.56	24.43	20.00
Clip 4	4.55	38.96	20.00
Clip 5	35.56	38.96	20.00

Table G.2: Raith 150-TWO sample holder clamp locations, with clamp numbers defined in Fig. G.6

(U,V). After performing the origin adjustment and angle adjustment it is time to perform alignment. Start by finding the scratch you made in the previous section. You can drive along the bottom of the chip to find it. You might have to make your scan speed slower to see the scratch. Then you want to drive up the scratch until you find the start of the scratch. This should be in a uniform region of the ZEP such that your focus and alignment is done on the surface of the ZEP.

Now find a small particle to perform your fine focus and alignment on. This should be $\sim$ 100 nm, but the smaller the better. A circular particle is ideal as this will make it easier to correct for stigmation, but these are usually hard to come by with the scratch method. You should not choose a particle in the scratch as you want to be focusing/aligning on the top of the ZEP layer. The procedure for focus and alignment that we follow is listed below:

1. Adjust the working distance to focus the particle as best you can.
2. Adjust stigmation such that the particle does not look skewed or stretched.
3. Iterate between 1 and 2 to get a decent focus but don't spend a lot of time at this stage.
4. Perform the aperture alignment by first turning on focus wobble and adjusting the aperture X and Y settings so that the particle focuses and defocuses in place, without translating across the screen.
5. Turn off focus wobble and adjust working distance again to focus the particle as best you can.
6. Check aperture alignment again. You can use focus wobble again and/or choose a fast scan speed and manually focus and defocus by adjusting your working distance to ensure that the particle does not translate across the screen as you do so.
7. Now tweak stigmation to try to improve the focus and ensure that the particle does not stretch or skew as you focus and de-focus. Iterate between working distance and stigmation correction a few times. These fine adjustments are best done with slow scan speeds and high averaging.
8. Test your alignment by burning a contamination dot. Set the magnification so that your scale bar is < 100 nm. Blank the beam and move to a new area of ZEP that has not been imaged. Select a slow scan speed, un-blank the beam, and press the contamination dot button (these steps need to be performed quickly as you don't want to raster the beam across the ZEP area that you are burning the dot on).

G.10 Cold Development

Approximately 30 minutes before the anticipated end of the EBL session, it is a good idea to begin setting up the cold development to allow the ZED-N50 and IPA to reach -15°C. When finished with EBL, mount the sample in the blue forceps. It also helps to grab a stopwatch

to use with timings, and to ensure the N_2 gun is in an easy location to grab. When ready dip the sample into the developer. We usually lightly swirl it around during this time, and lift it out at 19 seconds, giving it single shake to remove excess developer and immediately dip it into the IPA. Repeat this procedure in the IPA and then immediately dry the sample with the N_2 gun.

Finally you can examine the developed pattern under the optical microscope. What you are looking for at this point is to be sure that there is no debris in the exposed areas of your pattern, and that all features are clear and well defined. If patterns are not well defined you will probably want to adjust your dose factors or other parameters in the EBL process on your next fabrication run.

G.11 ICP-RIE

Depending on the etch step, or which machines are working well, you may end up performing ICP-RIE on the Estrelas, Cobra, or PlasmaLab Pro 100 etchers. Fortunately these are all Oxford Instruments products, so the general procedure and user interface is quite similar for all etches. Over the course of the diamond fabrication process you will need three different etches: a Si_3N_4 etch, an anisotropic O_2 or AR/Cl_2 diamond etch, and an isotropic O_2 diamond etch.

The Si_3N_4 etch can be done either on Estrelas or PlasmaLab Pro 100. In both cases we have our own carrier wafer, 150 mm for Estrelas and 100 mm for PlasmaLab Pro 100. You'll want these wafers to be as pristine, clean, and shiny as possible. On Estrelas you will also want to uncheck the automatic interwafer cleaning option, especially after performing the chamber conditioning. Over time, markings can show up from clamps or bad etches, or the middle of the carrier will no longer be totally flat as the Si wafer is etched down. If this is the case, you can get a wafer from the nanoFAB office. Be sure to get 'test grade' as 'electronic grade' has a different electrical conductivity and will not give you the bias that

the etch recipes has been optimized for. When you have your wafer, clean it, and check that there is no dust on either the front or back.

Since these machines are used with a variety of materials, it's good to do a very long clean of at least 1 hr. Each etcher has a different cleaning recipie, but they all use some combination of O_2 and SF_6. On Estrelas you'll run the recipe "Extended Chamber Clean with Wafer" and on PlasmaLab you'll run "OPT Clean at 20C". When this is done, we usually condition for at least 15 minutes.

To track the health of the etch over time, it's a good idea to log all the relevant parameters on the group's Evernote notebook, and note drifts over time. When the etch starts, you'll want to keep a close eye on a few parameters:

- Helium backing: an excessively high flow rate indicates that your wafer warped, or dusty on the back, or could indicate a misalignment in mounting, or buildup of debris / misalignment in the chamber clamps.
- Reflected power: this is a measure of how well tuned the etch is. You want as little reflected power as possible. This value is not always 0 and depends on the etch recipe. Just make sure it is consistent with the history of the etch.
- Bias: this is a good indication of the overall health of your etch. Changes in the bias might be due to change in conductivity of the sample due to contamination, backing, or changes in the tool itself.

Before doing the Si_3N_4 etch on the diamond sample, we usually do the etch on the Si test pieces you deposited nitride on earlier using the Trion. Using old etch parameters, and the Si_3N_4 thickness as measured, we do a etches for slightly different lengths of time on each sample to determine when the nitride is totally cleared. For very thin layers of nitride, you won't be able to accurately measure the thickness but residual nitride should be visible as darker area in the middle of the sample. Once we establish the length of time needed to clear the nitride, we etch the diamond by an additional 20% to ensure that the smaller features on the mask will be fully etched.

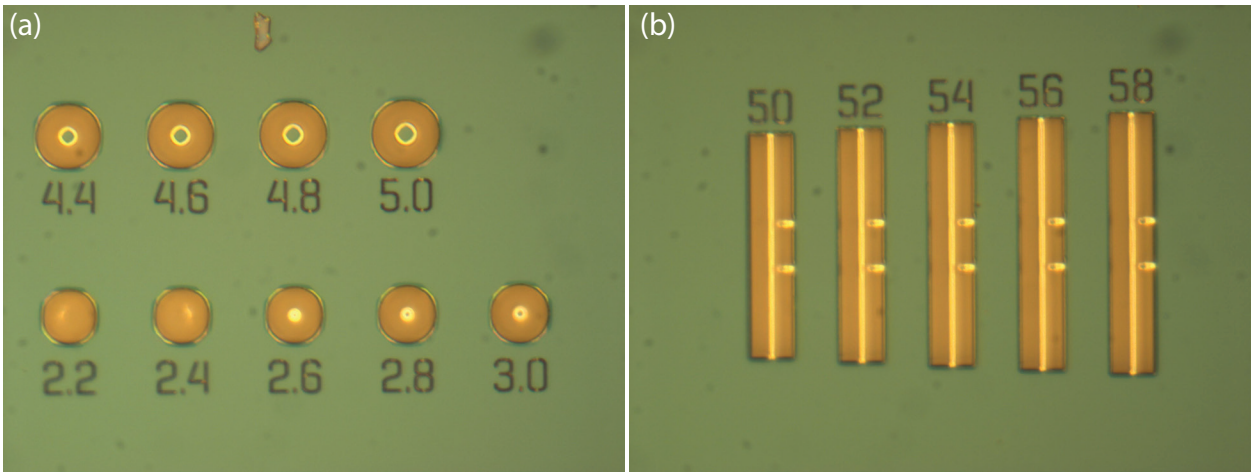

Figure G.7: Optical micrograph of SCD sample after performing the quasi-isotropic O_2 etch. (a) Microdisks of varying diameter, as labelled, where the lighter areas are a good indication of the amount of undercutting that has occured, compared to the darker regions which are still solid SCD. (b) For this length of undercut the nanobeam structures have been completely undercut, hence why there is no darker region in the center.

The anisotropic O_2 and Ar/Cl_2 diamond etches may be performed on either the Cobra or PlasmaLab Pro 100. Once again we'll clean for at least an hour, and condition for at least 15 minutes.

The final, isotropic etch, is a bit unusual. It uses no forward power (except on the strike step), and consequently has no preferred etch direction. Because the etch rate is slow, we raise the temperature of the sample to accelerate the etch rate as much as possible. This etch has always done on PlasmaLab Pro 100 at NRC, mainly because it is less busy so we can book it for the long hours required to undercut the device. For the clean step, run the 'pre-SCD iso clean' recipe, as this will raise the temperature of the chamber at the end of the cleaning step. About ten minutes or so before the cleaning step finishes (as in, the process is still runing), turn off the liquid nitrogen supply to PlasmaLab Pro 100, as it will no longer require active cooling. As usual, do a conditioning step after the clean before etching the sample.

When etching/undercutting SCD structures such as microdisks with varying diameter you can observe how the undercut is progressing by examining the sample under an optical microscope. This is useful for trying to minimize pedestal diameters, for example, as you can observe when the smaller microdisks pedestals are completely undercut, such that the

microdisk falls over (Fig. G.7). For structures like these it is a good idea to under-shoot the expected undercut time, and then do shorter etches (30 minutes to 1 hour) until satisfied with the degree of undercut.

G.12 Stripping the Si_3N_4ard mask with HF

As hydrofluoric acid (HF) will etch glass so do not use glass beakers for this step, but the teflon and plastic beakers shown in Fig. G.8 for HF and water, respectively. HF is quite dangerous, so we use as little of it as possible: just enough to submerge the diamond sample ($\sim$ 10 mL). We have been using the Teflon basket shown in Fig. G.8 for holding the SCD sample during the HF and water rinsing steps.

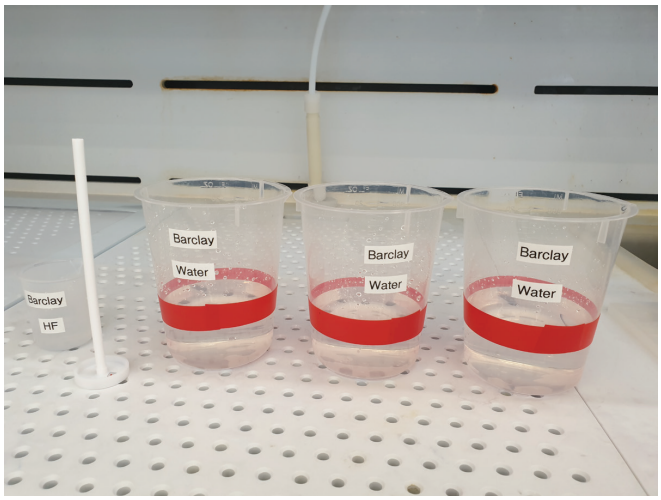

Figure G.8: Labware for stripping Si_3N_4 hard mask with HF. A teflon beaker and basket is used for the HF and SCD sample, while polypropylene plastic beakers are used for the three following water rinses.

We first pour the HF into the Teflon beaker and set up the 3 water beakers. Then place the sample in the Teflon basket, and place it in the Teflon beaker containing HF. After soaking the sample for $\sim$45 mins we remove the basket from the HF and let the HF drain through the small holes in the basket. You might have to use the second Teflon basket we have to break the surface tension in the holes to allow drainage. The basket is then transferred to the first water bath and swirled for 30 s before placing it in the second and third water

baths, swirling for 30 s each time. Finally, we bring the basket over to a cleanroom wipe, and transfer the sample to a pair of blue forceps for a final DI water rinse and N_2 dry.

G.13 Suggested schedule for booking tools

Note that this is a compressed schedule, and can be expanded if SEM or other characterization between steps is needed.

Day 1

- Piranha clean (1 hr)
- PECVD Si_3N_4 hard mask deposition (4–5 hrs if including clean & cool)
- JUV Ti deposition (1 hr)
- Spin and bake resist (1 hr)
- EBL (3 hr minimum, longer if doing multiple samples. Works well to do after hours.)
- Cold development (1 hr)
- Si_3N_4 hard mask etch (2–3 hrs, again depends on the number of samples)

Day 2

- Anisotropic diamond etch (2-3 hrs, again depends on the number of samples)
- PECVD Si_3N_4 sidewall deposition (4–5 hrs if including clean & cool)
- Short Si_3N_4 etch to clear bottom of 'wells' (2–3 hrs, again depends on the number of samples)
- Overnight quasi-isotropic diamond etch (> 6 hrs)

Day 3

- Potentially more quasi-isotropic etching (1-3 hrs)
- Si_3N_4 removal in HF (2 hrs)
- Final piranha clean (1 hr)

Appendix H

Copyright permissions

H.1 Journal permissions

Chapter 3

Portions of Chapter 3 contain content that was published in Applied Physics Letters (Ref. [1]). From the website of the American Institute of Physics (AIP), publisher of Applied Physics Letters:

Authors do **not** need permission from AIP Publishing to:

- quote from a publication (please include the material in quotation marks and provide the customary acknowledgment of the source)
- reuse any materials that are licensed under a Creative Commons CC BY license (please format your credit line: "Author names, Journal Titles, Vol.#, Article ID#, Year of Publication; licensed under a Creative Commons Attribution (CC BY) license.")
- reuse your own AIP Publishing article in your thesis or dissertation (please format your credit line: "Reproduced from [FULL CITATION], with the permission of AIP Publishing")
- reuse content that appears in an AIP Publishing journal for republication in another AIP Publishing journal (please format your credit line: "Reproduced from [FULL CITATION], with the permission of AIP Publishing")
- make multiple copies of articles–although you must contact the Copyright Clearance Center (CCC) at www.copyright.com to do this

Figure H.1: Screenshot capture of the American Institute of Physics website pertaining to copyright permission for use of manuscript in a thesis. Retrieved: November 19, 2019.

Chapter 4

Portions of Chapter 4 contain content that was published in Nano Letters (Ref. [3]). From the website of the American Chemical Society (ACS), publisher of Nano Letters:

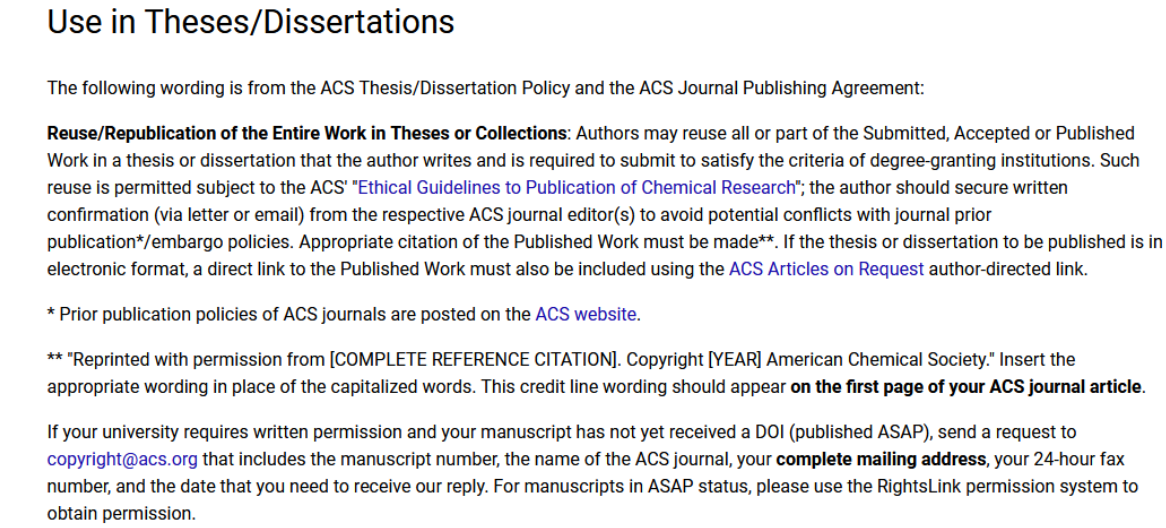

Use in Theses/Dissertations

The following wording is from the ACS Thesis/Dissertation Policy and the ACS Journal Publishing Agreement:

Reuse/Republication of the Entire Work in Theses or Collections: Authors may reuse all or part of the Submitted, Accepted or Published Work in a thesis or dissertation that the author writes and is required to submit to satisfy the criteria of degree-granting institutions. Such reuse is permitted subject to the ACS' "Ethical Guidelines to Publication of Chemical Research"; the author should secure written confirmation (via letter or email) from the respective ACS journal editor(s) to avoid potential conflicts with journal prior publication*/embargo policies. Appropriate citation of the Published Work must be made**. If the thesis or dissertation to be published is in electronic format, a direct link to the Published Work must also be included using the ACS Articles on Request author-directed link.

* Prior publication policies of ACS journals are posted on the ACS website.

** "Reprinted with permission from [COMPLETE REFERENCE CITATION]. Copyright [YEAR] American Chemical Society." Insert the appropriate wording in place of the capitalized words. This credit line wording should appear **on the first page of your ACS journal article**.

If your university requires written permission and your manuscript has not yet received a DOI (published ASAP), send a request to copyright@acs.org that includes the manuscript number, the name of the ACS journal, your **complete mailing address**, your 24-hour fax number, and the date that you need to receive our reply. For manuscripts in ASAP status, please use the RightsLink permission system to obtain permission.

Figure H.2: Screenshot capture of the American Chemical Society website pertaining to copyright permission for use of manuscript in a thesis. Retrieved: November 19, 2019.

Chapter 5

Portions of Chapter 5 contain content that was published in the open-access journal Optica (Ref. [4]). From the website of the Optical Society of America (OSA), publisher of Optica:

Open Access Licenses

Open Access Publishing Agreement

OSA's "Copyright Transfer and Open Access Publishing Agreement" (OAPA) is the default option for most authors when publishing in one of our fully open access journals or when opting for open access in our hybrid journals. All articles published under our OAPA are freely accessible, while copyright is transferred to OSA. Authors may post the published version of their article to their personal website, institutional repository, or a repository required by their funding agency. Authors and readers may use, reuse, and build upon the article, or use it for text or data mining, as long as the purpose is non-commercial and appropriate attribution is maintained.

Figure H.3: Screenshot capture of the Optical Society of America website pertaining to copyright permission for use of manuscript for a non-commercial purpose. Retrieved: November 19, 2019.

Chapter 6

Portions of Chapter 6 contain content that was published in the APL Photonics (Ref. [6]).

From the website of the American Institute of Physics (AIP), publisher of APL Photonics:

Authors do **not** need permission from AIP Publishing to:

- quote from a publication (please include the material in quotation marks and provide the customary acknowledgment of the source)
- reuse any materials that are licensed under a Creative Commons CC BY license (please format your credit line: "Author names, Journal Titles, Vol.#, Article ID#, Year of Publication; licensed under a Creative Commons Attribution (CC BY) license.")
- reuse your own AIP Publishing article in your thesis or dissertation (please format your credit line: "Reproduced from [FULL CITATION], with the permission of AIP Publishing")
- reuse content that appears in an AIP Publishing journal for republication in another AIP Publishing journal (please format your credit line: "Reproduced from [FULL CITATION], with the permission of AIP Publishing")
- make multiple copies of articles–although you must contact the Copyright Clearance Center (CCC) at www.copyright.com to do this

Figure H.4: Screenshot capture of the American Institute of Physics website pertaining to copyright permission for use of manuscript in a thesis. Retrieved: November 19, 2019.

Portions of Chapter 6 contain content that was published in the ACS Photonics (Ref. [5]).

From the website of the American Chemical Society (ACS), publisher of ACS Photonics:

Use in Theses/Dissertations

The following wording is from the ACS Thesis/Dissertation Policy and the ACS Journal Publishing Agreement:

Reuse/Republication of the Entire Work in Theses or Collections: Authors may reuse all or part of the Submitted, Accepted or Published Work in a thesis or dissertation that the author writes and is required to submit to satisfy the criteria of degree-granting institutions. Such reuse is permitted subject to the ACS' "Ethical Guidelines to Publication of Chemical Research"; the author should secure written confirmation (via letter or email) from the respective ACS journal editor(s) to avoid potential conflicts with journal prior publication*/embargo policies. Appropriate citation of the Published Work must be made**. If the thesis or dissertation to be published is in electronic format, a direct link to the Published Work must also be included using the ACS Articles on Request author-directed link.

* Prior publication policies of ACS journals are posted on the ACS website.

** "Reprinted with permission from [COMPLETE REFERENCE CITATION]. Copyright [YEAR] American Chemical Society." Insert the appropriate wording in place of the capitalized words. This credit line wording should appear **on the first page of your ACS journal article**.

If your university requires written permission and your manuscript has not yet received a DOI (published ASAP), send a request to copyright@acs.org that includes the manuscript number, the name of the ACS journal, your **complete mailing address**, your 24-hour fax number, and the date that you need to receive our reply. For manuscripts in ASAP status, please use the RightsLink permission system to obtain permission.

Figure H.5: Screenshot capture of the American Chemical Society website pertaining to copyright permission for use of manuscript in a thesis. Retrieved: November 19, 2019.

Chapter 7

Portions of Chapter 7 contain content that was published in the ACS Photonics (Ref. [5]). From the website of the American Chemical Society (ACS), publisher of ACS Photonics:

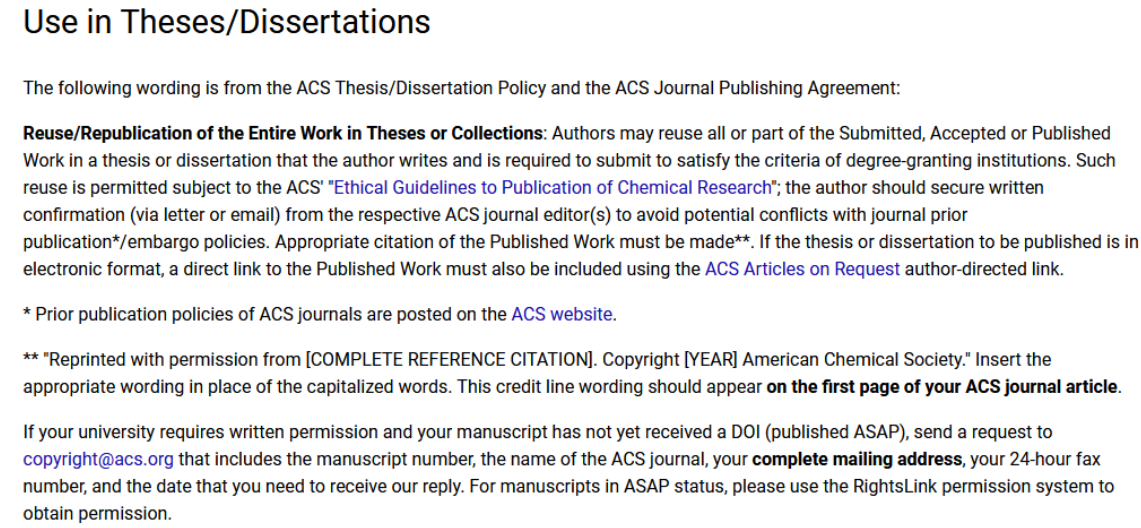

Use in Theses/Dissertations

The following wording is from the ACS Thesis/Dissertation Policy and the ACS Journal Publishing Agreement:

Reuse/Republication of the Entire Work in Theses or Collections: Authors may reuse all or part of the Submitted, Accepted or Published Work in a thesis or dissertation that the author writes and is required to submit to satisfy the criteria of degree-granting institutions. Such reuse is permitted subject to the ACS' "Ethical Guidelines to Publication of Chemical Research"; the author should secure written confirmation (via letter or email) from the respective ACS journal editor(s) to avoid potential conflicts with journal prior publication*/embargo policies. Appropriate citation of the Published Work must be made**. If the thesis or dissertation to be published is in electronic format, a direct link to the Published Work must also be included using the ACS Articles on Request author-directed link.

* Prior publication policies of ACS journals are posted on the ACS website.

** "Reprinted with permission from [COMPLETE REFERENCE CITATION]. Copyright [YEAR] American Chemical Society." Insert the appropriate wording in place of the capitalized words. This credit line wording should appear **on the first page of your ACS journal article**.

If your university requires written permission and your manuscript has not yet received a DOI (published ASAP), send a request to copyright@acs.org that includes the manuscript number, the name of the ACS journal, your **complete mailing address**, your 24-hour fax number, and the date that you need to receive our reply. For manuscripts in ASAP status, please use the RightsLink permission system to obtain permission.

Figure H.6: Screenshot capture of the American Chemical Society website pertaining to copyright permission for use of manuscript in a thesis. Retrieved: November 19, 2019.

Portions of Chapter 7 contain content that was published in the open-access journal Optica (Ref. [7]). From the website of the Optical Society of America (OSA), publisher of Optica:

Open Access Licenses

Open Access Publishing Agreement

OSA's "Copyright Transfer and Open Access Publishing Agreement" (OAPA) is the default option for most authors when publishing in one of our fully open access journals or when opting for open access in our hybrid journals. All articles published under our OAPA are freely accessible, while copyright is transferred to OSA. Authors may post the published version of their article to their personal website, institutional repository, or a repository required by their funding agency. Authors and readers may use, reuse, and build upon the article, or use it for text or data mining, as long as the purpose is non-commercial and appropriate attribution is maintained.

Figure H.7: Screenshot capture of the Optical Society of America website pertaining to copyright permission for use of manuscript for a non-commercial purpose. Retrieved: November 19, 2019.

H.2 Co-author permissions

Co-Author Permission Letter

November 1, 2019

Matthew Mitchell
[redacted]

Dear Paul E. Barclay,

As a co-author, I would like your permission to include the following material in my PhD thesis entitled "Coherent cavity optomechanics in wide-band gap materials"

1. M. Mitchell, D.P. Lake, and P. E. Barclay, "Optomechanically amplified wavelength conversion in diamond microcavities," Optica, **6**, 832–838 (2019).

2. M. Mitchell, D.P. Lake, and P.E. Barclay, "Realizing Q > 300 000 in diamond microdisks for optomechanics via etch optimization," APL Photonics, **4**, 016101 (2019).

3. D.P. Lake*, M. Mitchell*, Y. Kamaliddin, and P.E. Barclay, "Optomechanically induced transparency and cooling in thermally stable diamond microcavities," ACS Photonics, 5, 782-787 (2018).*Authors contributed equally to this work.

4. M. Mitchell, B. Khanaliloo, D. P. Lake, T. Masuda, J. P. Hadden, and P. E. Barclay, "Single-crystal diamond low-dissipation cavity optomechanics," Optica **3**, 963–970 (2016).

5. B. Khanaliloo, M. Mitchell, A.C. Hryciw, and P.E. Barclay, "High-Q/V monolithic diamond microdisks fabricated with quasi-isotropic etching," Nano Lett. **15**, 5131-5136 (2015).

6. M. Mitchell, A.C. Hryciw, and P.E. Barclay, "Cavity optomechanics in gallium phosphide microdisks," Appl. Phys. Lett. **104**, 141104 (2014).

Your permission gives me the right to include the manuscript in my thesis, understanding that my thesis will be added to the University of Calgary's Thesis Repository and the Library and Archives Canada repository.

Sincerely,

[redacted]

Matthew Mitchell

Permission granted for the use of the material as described above:

Signature: [redacted]

Name: Paul Barclay

Date: November 18, 2019

Co-Author Permission Letter

November 1, 2019

Matthew Mitchell
[redacted]

Dear David P. Lake,

As a co-author, I would like your permission to include the following material in my PhD thesis entitled "Coherent cavity optomechanics in wide-band gap materials"

1. M. Mitchell, D.P. Lake, and P. E. Barclay, "Optomechanically amplified wavelength conversion in diamond microcavities," Optica, 6, 832–838 (2019).

2. M. Mitchell, D.P. Lake, and P.E. Barclay, "Realizing Q > 300 000 in diamond microdisks for optomechanics via etch optimization," APL Photonics, 4, 016101 (2019).

3. D.P. Lake*, M. Mitchell*, Y. Kamaliddin, and P.E. Barclay, "Optomechanically induced transparency and cooling in thermally stable diamond microcavities," ACS Photonics, 5, 782-787 (2018).*Authors contributed equally to this work.

4. M. Mitchell, B. Khanaliloo, D. P. Lake, T. Masuda, J. P. Hadden, and P. E. Barclay, "Single-crystal diamond low-dissipation cavity optomechanics," Optica 3, 963–970 (2016).

Your permission gives me the right to include the manuscript in my thesis, understanding that my thesis will be added to the University of Calgary's Thesis Repository and the Library and Archives Canada repository.

Sincerely,

[redacted]

Matthew Mitchell

Permission granted for the use of the material as described above:

Signature: [redacted]

Name: David Lake

Date: 11/1/2019

Co-Author Permission Letter

November 1, 2019

Matthew Mitchell
[redacted]

Dear Yasmeen Kamaliddin,

As a co-author, I would like your permission to include the following material in my PhD thesis entitled "Coherent cavity optomechanics in wide-band gap materials"

1. D.P. Lake*, M. Mitchell*, Y. Kamaliddin, and P.E. Barclay, "Optomechanically induced transparency and cooling in thermally stable diamond microcavities," ACS Photonics, 5, 782-787 (2018).*Authors contributed equally to this work.

Your permission gives me the right to include the manuscript in my thesis, understanding that my thesis will be added to the University of Calgary's Thesis Repository and the Library and Archives Canada repository.

Sincerely,

[redacted]

Matthew Mitchell

Permission granted for the use of the material as described above:

Signature: [redacted]

Name: Yasmeen Kamaliddin

Date: Nov. 2 / 2019

Co-Author Permission Letter

November 1, 2019

Matthew Mitchell
[redacted]

Dear J.P. Hadden,

As a co-author, I would like your permission to include the following material in my PhD thesis entitled "Coherent cavity optomechanics in wide-band gap materials"

1. M. Mitchell, B. Khanaliloo, D. P. Lake, T. Masuda, J. P. Hadden, and P. E. Barclay, "Single-crystal diamond low-dissipation cavity optomechanics," Optica **3**, 963–970 (2016).

Your permission gives me the right to include the manuscript in my thesis, understanding that my thesis will be added to the University of Calgary's Thesis Repository and the Library and Archives Canada repository.

Sincerely,

[redacted]

Matthew Mitchell

Permission granted for the use of the material as described above:

Signature: [redacted]

Name: ___J.P. Hadden_____

Date: ___4 November 2019____

Co-Author Permission Letter

November 1, 2019

Matthew Mitchell
[redacted]

Dear Behzad Khanaliloo,

As a co-author, I would like your permission to include the following material in my PhD thesis entitled "Coherent cavity optomechanics in wide-band gap materials"

1. M. Mitchell, B. Khanaliloo, D. P. Lake, T. Masuda, J. P. Hadden, and P. E. Barclay, "Single-crystal diamond low-dissipation cavity optomechanics," Optica 3, 963–970 (2016).

2. B. Khanaliloo, M. Mitchell, A.C. Hryciw, and P.E. Barclay, "High-Q/V monolithic diamond microdisks fabricated with quasi-isotropic etching," Nano Lett. 15, 5131–5136 (2015).

Your permission gives me the right to include the manuscript in my thesis, understanding that my thesis will be added to the University of Calgary's Thesis Repository and the Library and Archives Canada repository.

Sincerely,

[redacted]

Matthew Mitchell

Permission granted for the use of the material as described above:

Signature: [redacted]

Name: Behzad Khanaliloo

Date: November 4, 2019

Co-author Permission Letter

November 1, 2019

Matthew Mitchell
[redacted]

Dear Aaron C. Hryciw,

As a co-author, I would like your permission to include the following material in my PhD thesis entitled "Coherent cavity optomechanics in wide-band gap materials"

1. B. Khanaliloo, M. Mitchell, A.C. Hryciw, and P.E. Barclay, "High-Q/V monolithic diamond microdisks fabricated with quasi-isotropic etching," Nano Lett. **15**, 5131-5136 (2015).

2. M. Mitchell, A.C. Hryciw, and P.E. Barclay, "Cavity optomechanics in gallium phosphide microdisks," Appl. Phys. Lett. **104**, 141104 (2014).

Your permission gives me the right to include the manuscript in my thesis, understanding that my thesis will be added to the University of Calgary's Thesis Repository and the Library and Archives Canada repository.

Sincerely,

[redacted]

Matthew Mitchell

Permission granted for the use of the material as described above:

Signature: [redacted]

Name: Aaron Hryciw

Date: 2019-11-01

Co-Author Permission Letter

November 1, 2019

Matthew Mitchell
[redacted]

Dear Tamiko Masuda,

As a co-author, I would like your permission to include the following material in my PhD thesis entitled "Coherent cavity optomechanics in wide-band gap materials"

1. M. Mitchell, B. Khanaliloo, D. P. Lake, T. Masuda, J. P. Hadden, and P. E. Barclay, "Single-crystal diamond low-dissipation cavity optomechanics," Optica 3, 963–970 (2016).

Your permission gives me the right to include the manuscript in my thesis, understanding that my thesis will be added to the University of Calgary's Thesis Repository and the Library and Archives Canada repository.

Sincerely,

[redacted]

Matthew Mitchell

Permission granted for the use of the material as described above:

Signature: [redacted]

Name: Tamiko Masuda

Date: November 11, 2019